MODELLING OF TRANSCEIVER PROPAGATION CHARACTERISTICS THROUGH AN ANALOGUE SiGe BiCMOS INTEGRATED CIRCUIT

by

Johannes Wynand Lambrechts

Submitted in partial fulfilment of the requirements for the degree

Philosophiae Doctor (Electronic Engineering)

in the

Department of Electrical, Electronic and Computer Engineering

Faculty of Engineering, Built Environment and Information Technology

UNIVERSITY OF PRETORIA

November 2013

SUMMARY

MODELLING OF TRANSCEIVER PROPAGATION CHARACTERISTICS THROUGH AN ANALOGUE SiGe BiCMOS INTEGRATED CIRCUIT

by

Johannes Wynand Lambrechts

Promoter:	Prof. S. Sinha
Department:	Electrical, Electronic and Computer Engineering
University:	University of Pretoria
Degree:	Philosophiae Doctor (Electronic Engineering)

Keywords: Dipole equivalent circuit, electromagnetism, impedance matching, mathematical model, millimeter-wave, passive component circuit model, propagation channel, SiGe integrated circuit, transmission loss, broadband

The necessity to model radio frequency (RF) transmission (with specific focus on wireless transmissions) is a determining factor to predict circuit operation prior to its implementation. The accuracy and effectiveness of these predictions are related to the circuit model and system parameters. At millimeter-wave frequencies (30 GHz to 300 GHz) the commonly used circuit models are insufficient and inaccurate due to parasitic variables. Improvement of these models to account for these additional parasitic effects enables better representation and prediction of circuit behaviour and transmission losses.

In this research a novel integrated circuit was proposed to model the transmission of a millimeter-wave (60 GHz) signal from a dipole antenna, accounting for attenuation due to free-space loss and non-line of sight (nLOS) components. The research estimates attenuation as factors of oxygen absorption, reflection, diffraction, and rain-rate and presents an integrated passive filter to represent these losses. The propagation of the transmitted signal from the dipole antenna ports is achieved through an equivalent circuit to eliminate the need for mathematical functions to represent the *Friis* transmission equations with parasitic effects. Theoretical investigation into current literature related to this study indicated that research is done on RF transmission and attenuation, but it has not been attempted to integrate such a system at millimeter-wave frequencies as a fully analogue system, eliminating the need for digital down-conversion.

An equivalent circuit for a dipole antenna (180° separation) was developed to account for parasitic effects that are present in millimeter-wave frequency operation. Based on the *Foster canonical form* for electrical antennas an improved circuit model is developed to represent a dipole antenna operating at 60 GHz, with broadband operation (57 GHz to 64 GHz) simulation profiles (with f_{min} = 40 GHz and f_{max} = 90 GHz in all simulations) to ensure compatibility over the entire spectrum.

A literature study towards signal attenuation as a result of commonly used materials and objects breaking the signal LOS was presented to estimate the attenuation of millimeter-wave signals. The proposed attenuation function estimates losses as a function of frequency, distance of the object from the source, distance between the transmitting and receiving antenna (free-space losses), oxygen absorption attenuation, reflection and diffraction losses as a result of objects breaking the LOS, as well as attenuation as a function of rain-rate, where rain-rate data specific to South Africa are used in this research. The proposed attenuation function indicated the required electric filter transfer function and attenuation at the operating frequency. The filter was designed using only passive components to eliminate active-device frequency limitations and up-converted noise.

The validity of the proposed techniques was verified through result comparison of electromagnetic simulations, electric circuit simulations, and the mathematical transfer functions presented as software automated designs. The dipole equivalent circuit and attenuation filters were fabricated and measurement results correlate well with simulations, verifying the accuracy and validity of the proposed models. Limitations due to technology nodes were identified and remarks on future improvements and applications are presented.

The simulation results of the *Foster canonical form* electrical antenna at 60 GHz presented a complex input impedance of Z_{11} = 34.5 – j89.6 Ω and an insertion loss of S_{11} = -16.6 dB compared to the electromagnetic dipole model (with substrate and matched to a 75 Ω load) input impedance of Z_{11} = 45.04 + j2.30 Ω and S_{11} = -12.81 dB at 60 GHz (with imaginary impedance of +j2.30 Ω less than 0.5 % of absolute maximum value). The proposed circuit model based on the *Foster canonical form* indicated significant improvement in the input impedance representation of a dipole antenna at 60 GHz, with Z_{11} = 21.7 + j2.40 Ω and S_{11} = -11.6 dB and accurate representation throughout the 40 GHz to 90 GHz spectrum. The imaginary impedance is sufficiently close to 0 Ω (1.46 % of absolute maximum imaginary impedance) indicating a good match ($X_C = |X_L|$) at 60 GHz. Upper and lower limitations on the complex (imaginary) impedance are due to technology node limitations (minimum component values) and can be improved in future works through implementing the circuit in a smaller node.

The proposed improved dipole equivalent circuit occupies 0.481 mm^2 of chip area compared to the 0.359 mm^2 footprint (27 % smaller) of the standard *Foster canonical form* circuit, with quality factor of 15 and 9 respectively. The *Butterworth*, *Chebyshev*, and *Bessel* filters occupy 0.771 mm^2, 0.931 mm^2 and 0.853 mm^2 of chip area respectively, with quality factors of 14, 11, and 13. The output buffer circuit occupies a chip area of 0.497 mm^2 and the matching network a chip area of 0.086 mm^2. On-chip short-open-line-through calibration structures occupy a chip area of 0.264 mm^2 each. Total die area is 6.278 mm^2.

OPSOMMING

MODELLERING VAN SENDER / ONTVANGERVOORTPLANTING-EIENSKAPPE DEUR MIDDEL VAN ’N ANALOOG- SiGe BiCMOS-GEÏNTEGREERDE KRINGBAAN

deur

Johannes Wynand Lambrechts

Promotor:	Prof. S. Sinha
Departement:	Elektriese, Elektroniese en Rekenaaringenieurswese
Universiteit:	Universiteit van Pretoria
Graad:	Philosophiae Doctor (Elektroniese Ingenieurswese)

Sleutelwoorde: Dipool-ekwivalente model, elektromagnetisme, impedansie-aanpassing, wiskundige model, millimetergolf, passiewekomponent-kringbaanmodel, transmissiekanaal, SiGe-geïntegreerde kringbaan, transmissieverliese, wyeband.

Die noodsaaklikheid om radio-frekwensie- (RF) transmissies te modelleer (met spesifieke fokus op draadlose versending) is ’n bepalende faktor in die voorspelling van ’n kringbaan se werking voordat dit geïmplementeer word. Die akkuraatheid en effektiwiteit van hierdie voorspellings is afhanklik van die kringbaanmodel, asook die stelsel se parameters. By millimetergolffrekwensies (30 GHz tot 300 GHz) is die algemeen gebruikte kringbaanmodelle onvoldoende en onakkuraat as gevolg van parasitiese veranderlikes. Verbetering van hierdie modelle om hierdie parasitiese veranderlikes in berekening te bring het beter voorstelling en voorspellings van die kringbaan se werking en versendingverliese tot gevolg.

In hierdie navorsing word ’‘n unieke geïntegreerde kringbaan voorgestel om die transmissie van ’n millimetergolf- (60 GHz) dipoolantenna te modelleer wat atmosferiese en obstruksieverliese in berekening bring. Die navorsing voorspel verliese as faktore van

suurstof-absorpsie, refleksie, diffraksie en die reënvalkoers en bied ’n geïntegreerde passiewe filter om hierdie verliese voor te stel. Die voortplanting van die oordragsein vanaf die dipool is bewerkstellig deur ’n ekwivalente kringbaan om die gebruik van wiskundige voorstelling van die *Friis*-transmissievergelykings met parasitiese effekte te elimineer. Teoretiese navorsing oor die huidige literatuur wat met hierdie studie verband hou, toon dat navorsing oor RF-versending gedoen word, maar daar is nog geen poging aangewend om so ’n sisteem by millimetergolffrekwensies te integreer om die afhanklikheid van frekwensieverminderingomskakeling uit te skakel nie.

’n Ekwivalente kringbaan vir ’n dipool-antenna (180° skeiding) is ontwikkel om parasitiese effekte by millimetergolffrekwensiewerking te verklaar. ’n Verbeterde kringbaanmodel gebaseer op die *Foster kanoniese vorm* vir elektriese antennas is ontwikkel om ’n dipool wat bedryf word by 60 GHz met wyebandwerking- (57 GHz tot 64 GHz) simulasieprofiel (met f_{min} = 40 GHz en f_{maks} = 90 GHz in alle simulasies) te skep om verenigbaarheid oor die hele spektrum te verseker.

’n Literatuurstudie oor seinverswakking as gevolg van algemeen gebruikte materiale, asook voorwerpe wat die lyn van sig breek, is aangebied om die verlies van millimetergolfseine te voorspel. Die voorgestelde funksie voorspel verliese as ’n funksie van frekwensie, afstand tussen die voorwerp en bron, afstand tussen die versending- en ontvangsantenna, suurstofabsorpsieverliese, refleksie en diffraksie as gevolg van die voorwerpe, asook reënvalkoersverliese spesifiek gefokus op gebiede in Suid Afrika. Hierdie funksie bepaal die elektriese filter se oordragskromme by die werkingsfrekwensie. Die filter is ontwerp deur slegs van passiewe komponente gebruik te maak om die frekwensiebeperkings en omgeskakelde ruis te verminder.

Die geldigheid van die voorgestelde tegniek is geverifieer deur die resultate van die elektromagnetiese simulasies, elektriese kringbaansimulasies en die wiskundige oordragskrommes te vergelyk. Die dipool-ekwivalente kringbaan en verliesfilters is vervaardig en die gemete resultate stem goed ooreen met simulasies wat die voorgestelde tegniek verifieer. Beperkings as gevolg van tegnologienodes is geïdentifiseer en opmerkings oor toekomstige verbeteringe is aangebied.

Die simulasieresultate van die *Foster kanoniese vorm*- elektriese antenna by 60 GHz het ’n komplekse impedansie van $Z_{11} =$ 34.5 – j89.6 Ω en ’n invoegingsverlies van $S_{11} =$ -16.6 dB, wat vergelykbaar is met die elektromagnetiese dipool (met substraat en aangepas tot ’n 75 Ω las) inset-impedansie van $Z_{11} =$ 45.04 + j2.30 Ω en $S_{11} =$ -12.81 dB by 60 GHz (met denkbeeldige impedansie van +j2.30 Ω minder as 0.5 % van die absolute maksimumwaarde). Die voorgestelde kringbaan gebaseer op die *Foster kanoniese vorm* wys ’n beduidende verbetering in inset-impedansie van ’n dipoolantenna by 60 GHz, met $Z_{11} =$ 21.7 + j2.40 Ω en $S_{11} =$ -11.6 dB en akkurate voorstelling deur die 40 GHz tot 90 GHz spektrum. Die denkbeeldige impedansie is na genoeg aan 0 Ω (1.46 % van die absolute maksimum), wat ’n goeie passing ($X_C = |X_L|$) by 60 GHz aandui. Die boonste en onderste limiete op die komplekse (denkbeeldige) impedansie is as gevolg van beperkings van tegnologie-nodes (minimumkomponentwaardes) en kan in die toekoms verbeter word deur die kringbaan in ’n kleiner node te implementeer.

Die voorgestelde verbeterde dipool-ekwivalente kringbaan beslaan 0.481 mm^2 van die skyf-area in vergelyking met die 0.359 mm^2 area (27% kleiner) van die standaard *Foster kanoniese vorm*-kringbaan, met kwaliteitsfaktor 15 en 9 onderskeidelik. Die *Butterworth*-, *Chebyshev*-, en *Bessel*-filters beslaan 0.771 mm^2, 0.931 mm^2 en 0.853 mm^2 vlokkie-area respektiewelik, met kwaliteitsfaktor 14, 11, en 13. Die uitsetbuffer beslaan 0.497 mm^2 vlokkie-area en die aanpassingsnetwerkvlokkie-area is 0.086 mm^2. Op-skyf ‘*short-open-line-through*’-kalibrasiestrukture beslaan 0.264 mm^2 elk. Die totale skyfarea is 6.278 mm^2.

ACKNOWLEDGEMENT

I would like to extend a special acknowledgement and thank you to my promoter and supervisor Prof. Saurabh Sinha for his countless hours spent on reviewing my research. Accept my utmost appreciation and gratitude towards Prof. Sinha's dedication and availability, abilities to secure funding and providing opportunities to liaison with international researchers and students, attention to detail, technical guidance, and friendship. I am privileged to have had the opportunity early in my career to have been assigned a mentor of such calibre and I am confident that his leadership and competence in engineering not only improved the quality of my research, but will influence my future career path immensely.

The time I spent at the Carl and Emily Fuchs Institute for Microelectronics allowed me to establish and secure friendships that I will value throughout my career. Thank you to Marius Goosen, Christo Janse van Rensburg, Dr Marnus Westrate, Dr Mladen Božanić, Alfons Bogalecki, and Jannes Venter for their availability to discuss and consider viable solutions to questions during the research. Thank you to Johan Schoeman for assisting in translating the summary of this thesis summary into Afrikaans. I enjoyed our social interactions and conference attendances which ensured for entertaining occasions. Your technical skills and valuable inputs are greatly appreciated and improved the quality of my work. A special thank you to Tilla Nel whose administrative skills and willingness to help me in any situation has not gone unnoticed and her dedication to all her colleagues is inspiring.

I would also like to thank my friends and colleagues Deepa George, Dr Alexandra Stefanescu, and Alina Bunea who helped me a lot with my software designs and made sure that the models and boundaries were sound and accurate. Their guidance assured me that I accounted and considered all variables and conditions that influenced my results.

Thank you to the National Research Foundation (NRF) of South Africa and IMT-Bucharest in Romania for supplying funding for my visit to the institution through a bilateral agreement between the University of Pretoria and IMT-Bucharest. My visit to IMT-Bucharest under guidance of Dr Alexandru Muller, Prof. Dan Neculoiu, and Dr Mircea Dragoman added

quality and relevance to my research and their experience and technical skills gave me a good perspective of my goals and overall relevance. I was guided by Valentin Buiculescu to conduct measurements on my prototypes at IMT-Bucharest, and I would like to thank Valentin for his valuable inputs and recommendations for improved results. Also accept my gratitude towards the institution for allowing me to complete my measurements using their specialized equipment and thank you for spending time with me to understand and use the equipment to its full potential and ensuring my results are correctly interpreted.

Finally I would like to thank my friends and family for their continual support, emotionally and financially to allow me to pursue my postgraduate studies. I appreciate the positive reinforcements and motivation pushing me to never give up and always do my best.

LIST OF ABBREVIATIONS

AC	Alternating current
ADE	Analog design environment
BiCMOS	Bipolar and CMOS
CAD	Computer aided design
CMOS	Complementary metal oxide semiconductor
CPW	Coplanar waveguide
DC	Direct current
DRC	Design rule check
DSP	Digital signal processor
DUT	Device under test
EM	Electromagnetic
FDTD	Finite difference time domain
FIT	Finite integration technique
GaAs	Gallium Arsenide
GBP	Gain-bandwidth product
GDS	Graphic data system
GSG	Ground-signal-ground
HBT	Heterojunction bipolar transistor
HDMI	High-definition multimedia interface
IC	Integrated circuit
IF	Impact factor
ISS	Impedance Standard Substrate
InP	Indium Phosphate
LOS	Line-of-sight

LPF	Low-pass filter
LVS	Layout versus schematic
MEMS	Microelectromechanical systems
MEP	MOSIS educational program
MIM	Metal-insulator-metal
MMIC	Monolithic microwave IC
mm-wave	Millimeter-wave
MOM	Metal-oxide-metal
MOS	Metal-oxide-semiconductor
MOSIS	MOS implementation service
MPW	Multi-project wafer
NDA	Non-disclosure agreement
nLOS	Non-line of sight
PCB	Printed circuit board
PDK	Process design kit
RF	Radio frequency
SAWS	South African Weather Service
SEM	Scanning electron microscope
SiGe	Silicon Germanium
SOLT	Short-open-load-thru
SPICE	Simulation program with integrated circuit emphasis
VCO	Voltage controlled oscillator
VNA	Vector network analyser

TABLE OF CONTENTS

CHAPTER 1: INTRODUCTION

1. CHAPTER OVERVIEW

This thesis investigates the possibility of an analogue path-loss prediction model for the attenuation of a millimeter-wave transmission as a function of distance between the transmitter and the receiver. This chapter outlines the background of the research and structures a concrete research question around this possibility. The justification of the importance of this research is presented and relevant objectives and goals are outlined to define and defend the contribution to the body of knowledge.

1.1 BACKGROUND TO THE RESEARCH

Millimeter-wave (mm-wave) (30 GHz to 300 GHz) communication offers unprecedented unlicensed bandwidth (up to 7 GHz bandwidth from 57 GHz to 64 GHz in North America and Korea, 59 GHz to 66 GHz in Europe and Japan [**1**], whereas South Africa is allowed 5 GHz bandwidth from 59 GHz to 64 GHz [**2**]) and offers wireless data communication in the Gbps range. This enables fast communication links to complement data transmission of high densities at much faster transfer times than previously possible. Continual performance enhancements and miniaturization offered through technology nodes allows for not only high-performance, but also cost-effective designs at mm-wave frequencies over short distances. Current wireless technologies lack these high-speed communications with wireless transmission (IEEE 802.11*n*) only reaching a theoretical maximum rate of 150 Mbps over a 40 MHz bandwidth (and up to 300 Mbps when channel-bonding is enabled); therefore a suitable replacement is needed. Broadband channels occupy 500 MHz of bandwidth around the 3.1 GHz to 10.6 GHz frequency bands, and can achieve theoretical data rates in excess of 675 Mbps. Possible mm-wave wireless links can reach maximum transfer rates of around 2.5 Gbps during line-of-sight (LOS) communications [**3**], with emerging standards such as WirelessHD, IEEE 802.15.3c, and ECMA[1]-387 targeting short-range wireless networks. Requirements for a high-definition multimedia interface (HDMI) with resolution of 1920 × 1080 pixels, at a frame rate of 25 frames per second is approximately 2.1 Gbps of bandwidth for transmission [**4**]. Obstructions that cause the link to lose LOS are detrimental to transfer

---

[1] The European Computer Manufacturers Association (ECMA) is an international, private, non-profit standards association for information and communication systems

speeds and signal integrity with recorded 20 dB losses when a person breaks the LOS [**3**]. The first study on the integration of 60 GHz broadband embedded antennas (broad-beam patch and switched-beam directive quasi-Yagi arrays) in wireless platforms (laptop computers) reports that only a small area (radius of 4λ centred around the antenna) of the chassis surface of the computer (can be extended to other mobile platforms) detrimentally affect the radiation performance, and presented good reflection coefficients (approximately -25 dB at 60 GHz), and resulting studies should drive the integration of mm-wave communication on wireless platforms in the near future.

Path-loss prediction models that analyse the propagation characteristics of a radio signal offer valuable information regarding the signal even before the hardware is deployed. Geometrical situations and environmental conditions add to signal degradation of a transceiver. Additional variables such as the height, distance, and orientation of the antennas, ground speed of the antenna (if mounted on a moving vehicle), and geographic and weather conditions influence the received signal [**5**]. The propagation loss (in dB) as a function of distance (m) provides a good estimation of signal integrity over distance and can be combined with the abovementioned variables to increase the accuracy of the model. These predictions are mostly analysed on a mathematical basis in computing software or digital signal processors, but are not performed in real-time due to processing limitations of digital equipment [**6**], [**7**].

Analogue components operating at mm-wave frequencies in order to achieve high-speed links translate directly to fast transistor switching speeds. Silicon Germanium (SiGe) BiCMOS processes, implemented with heterojunction bipolar transistors (HBTs), offer remarkable high frequency performance (with peak f_T currently at 350 GHz [**8**]) without large expense of noise performance (through trapping of hot carriers in the isolation between the emitter and extrinsic base). Low-cost implementation is possible and compatibility with very large scale integration processes is an advantage. High-speed, medium-voltage, SiGe HBT integration with f_T/f_{max} of 230/280 GHz have been implemented specifically for mm-wave applications in [**9**] where thick copper transmission lines are used to replace inductors. Doping of the Silicon (Si) transistor base-layer with a Germanium-graded composition lowers the thermal conductivity of the transistor and increases electron mobility resulting in faster switching speeds compared to the Si processes. The ability of these transistors to operate at these high frequencies facilitates the design of analogue circuits for the mm-wave spectrum. Passive components and interconnects have also been adapted for mm-wave applications to counteract for the increasing interconnect losses between signals. The number of metal layers has increased to reduce interconnect capacitance between signals, and reduced resistivity of metal interconnects limit resistive losses as a result of the smaller cross-sectional area. Thus, the implementation of passive components is becoming more practical due to the inverse proportionality between physical size and operating frequency.

1.2 HYPOTHESIS AND RESEARCH QUESTIONS

The use of analogue components operating at mm-wave frequencies could provide the ability to predict channel characteristics in real-time and use specialized schematic computer simulations to do predictions before the transceiver is physically implemented. Research conducted regarding path-loss prediction and signal integrity has been done in [**1**], [**10**], and [**11**], but these models are simulated in the digital domain, where frequency up- and down-conversion is applied. Passive components performance features of process technologies that facilitate designs at mm-wave frequencies enable possible analogue representations of these models.

Analysis of signals transmitted by radiating structures is commonly achieved through electromagnetic (EM) simulations. In this work, an analytical technique to model an EM centre-fed, half-wavelength dipole antenna operating in the 57 – 64 GHz unlicensed frequency band with a lumped element model is proposed to represent its operation in an analogue electrical circuit form. This equivalent electrical representation of the transmitting antenna provides an additional technique to observe and analyse antenna operation in real-time. Mathematical models describing antenna radiation do exist [**12**] and are combined with electrical network theory and represented on integrated circuit (IC) level to be compared to EM simulated results. This approach enables more accurate circuit representation of mm-wave antenna structures through characterization of parasitic effects within the structure and its immediate surroundings, leading to an overall improved circuit model in extremely wideband operation.

In addition, a passive filter, with variable transfer characteristics, could model the attenuation of the communication link, and it has been shown in [**13**] that passive filters with controlled attenuation in the stop-band are possible at mm-wave frequencies. On a single IC, combining antenna operation and variable estimated link-attenuation, provides integration of environmental effects on link integrity prior to the technology implementation and eliminates the requirement to digitize (and inevitably down-convert) the signal based *only* on mathematical predictions that do not necessarily account for all parasitic effects.

To summarize the abovementioned, the following research hypothesis was formulated:

> *If an equivalent electrical circuit model of a radiating antenna and a variable filter operating in the mm-wave spectrum, using only passive components can be combined, then it can be used as an analogue, real-time, path-loss prediction model that eliminates the need to down-convert signals for analysis in the digital domain.*

The first research question asks how to develop a model of an equivalent electronic circuit for an antenna operating at mm-wave frequencies in the 130 nm process? How can the resulting circuit be used to predict signal behaviour in real-time *and* eliminate the requirement to reconstruct environmental conditions such as the physical antenna, channel, and obstructions?

Secondly, how to define accurate mathematical path-loss prediction models or transfer functions at 60 GHz without increasing the complexity to an extent where circuit-modelling of these functions becomes mathematically cumbersome.

Thirdly, determining possible methods to derive these mathematical transfer functions into analogue IC theory using only passive components and standard library models of a 130 nm process? Should active devices such as transistors be used, depending on circuit structure, would the f_T and gain-bandwidth product (GBP) of the 130 nm transistors impact circuit operation and integrity?

Finally, how does interconnecting these models impact circuit integrity due to high frequency mismatches and resistive losses over a large bandwidth?

Measurements of the resulting prototype used to verify the research hypothesis will be investigated and compared to the transfer characteristics and distributions of the mathematical models. Any discrepancies between these are investigated and methods to increase the accuracy are proposed.

1.3 JUSTIFICATION FOR THE RESEARCH

Path-loss prediction is an active research field and depending on frequency of operation, the models derived for radio communications are relatively easy to apply. Significant work has been done in [**1**], [**3**], [**5**], [**10**], [**11**], and [**14**] regarding the measurement of signal losses in LOS and nLOS conditions, and some comparisons to statistical distributions have also been reported. Although it is difficult to derive a single model for all operating conditions, as the signal losses are heavily dependent on any change in environmental conditions, it is possible to create a *general* model which can be modified and improved to account for these conditions. This research aims to further generalize these models for 60 GHz radio-links in terms of *commonly experienced* environmental conditions related to the type and milieu of these links. To do this, it is vital to have significant measurement results to define losses based on material properties. Table 1.1 and Table 1.2 summarize significant work done on measurements and path-loss prediction models in the 60 GHz frequency range (all tables are listed at the end of Chapter 1).

This research will however aim to characterize signal losses mathematically, based on material and environmental properties, and use these predictions in investigating the possibility of an electronic analogue circuit to recreate the path of the signal in real-time. At the time of writing a similar application of these models has not yet been published, and to the author's knowledge this would be the first implementation of such a circuit. The significant contribution at 60 GHz would benefit researchers and designers to quantify losses at a frequency band that is experiencing increased popularity due to its large unlicensed bandwidth capabilities. Passive device sizes are getting smaller as a result of its indirect proportionality to operating frequency. It is now possible to use several inductive and capacitive components on one die without exceeding the size limits defined by the process.

The use of transmission lines is highly encouraged for this research. Transmission line modelling has been researched in [**15**], [**16**], and [**17**] for mm-wave CMOS applications. These models are summarized in Table 1.3 (also listed at the end of Chapter 1). Although measurements of transmission line performance characteristics are application-dependent,

Table 1.3 serves as a guide to the capabilities of transmission lines at mm-wave frequencies, based on general design parameters and the modelling approach followed in each reference. Improvement of transmission line quality factors (Q-factors) is not an objective of this research; therefore a basic modelling approach will be followed and adapted for the application proposed. Performance characteristics achieved in [**15**], [**16**], and [**17**] serves as a good guideline for expected values when implementing transmission lines at mm-wave frequencies.

To summarize the justification for this research, the main research aspects can be considered separately and the reasoning behind each outlined.

Firstly, conducting the research at 60 GHz was not chosen arbitrarily, and although this research could be applied to any band of mm-wave frequencies, 60 GHz received priority. The interest in the 60 GHz band is targeted mainly at multi-Gbps unlicensed wireless communication and non-intrusive imaging devices, whereas the 77 GHz band focuses more on automotive radar applications. This research aims to predict propagation losses in real-time for an indoor, wireless, data-transfer application for LOS and nLOS conditions, therefore 60 GHz signals will be analysed. An unprecedented unlicensed bandwidth of 5 GHz (in South Africa) at 60 GHz also facilitated in deciding on the band of interest. Increasing communication-link reliability by understanding (quantifying) losses is one of the benefits of this research. Similar research to quantify and predict these losses are summarized in Table 1.1 and Table 1.2.

Research regarding process technologies focuses on cost-effectiveness versus performance. SiGe BiCMOS technologies (refer to Table 1.5) provide a relatively low-cost alternative compared to Gallium Arsenide (GaAs) or Indium Phosphide (InP) technologies, with performance characteristics adequate for 60 GHz applications. This allows the antenna and filter structure to be integrated into a relatively low-cost IC representation where multiple instances of these building blocks, depending on physical size, can be placed on a single IC for analysis of the models. A comparative study between active and passive filters is also possible with SiGe HBTs having low r_b, high β_F, and high f_T properties. The use of active filters is suggested for future work in comparison with the passive filter option chosen in this thesis (since no gain is to be added to the propagating signal). Since the use of active devices is used in certain circumstances (as a control variable and not as a gain element), its characteristics are briefly outlined in Table 1.5.

Finally, the ability to model passive components using transmission lines (refer to Table 1.3) provides a variety of methods to implement the electronic filter on an IC. It also provides additional information regarding the structured approach to model passive components as electrical circuits at mm-wave frequencies, and these techniques can be adapted to better understand parasitic effects resulting from the immediate environment such as substrate effects.

The research methodology structures the approach of determining a hypothesis through investigating possible openings in the current body of knowledge and providing adequate reasoning through the justification of the research questions. Steps to define, model, and verify the proposed research are systematically outlined in the following section.

1.4 RESEARCH METHODOLOGY

The research methodology encourages a systematic procedure to the proposed research, and is outlined in Figure 1.1.

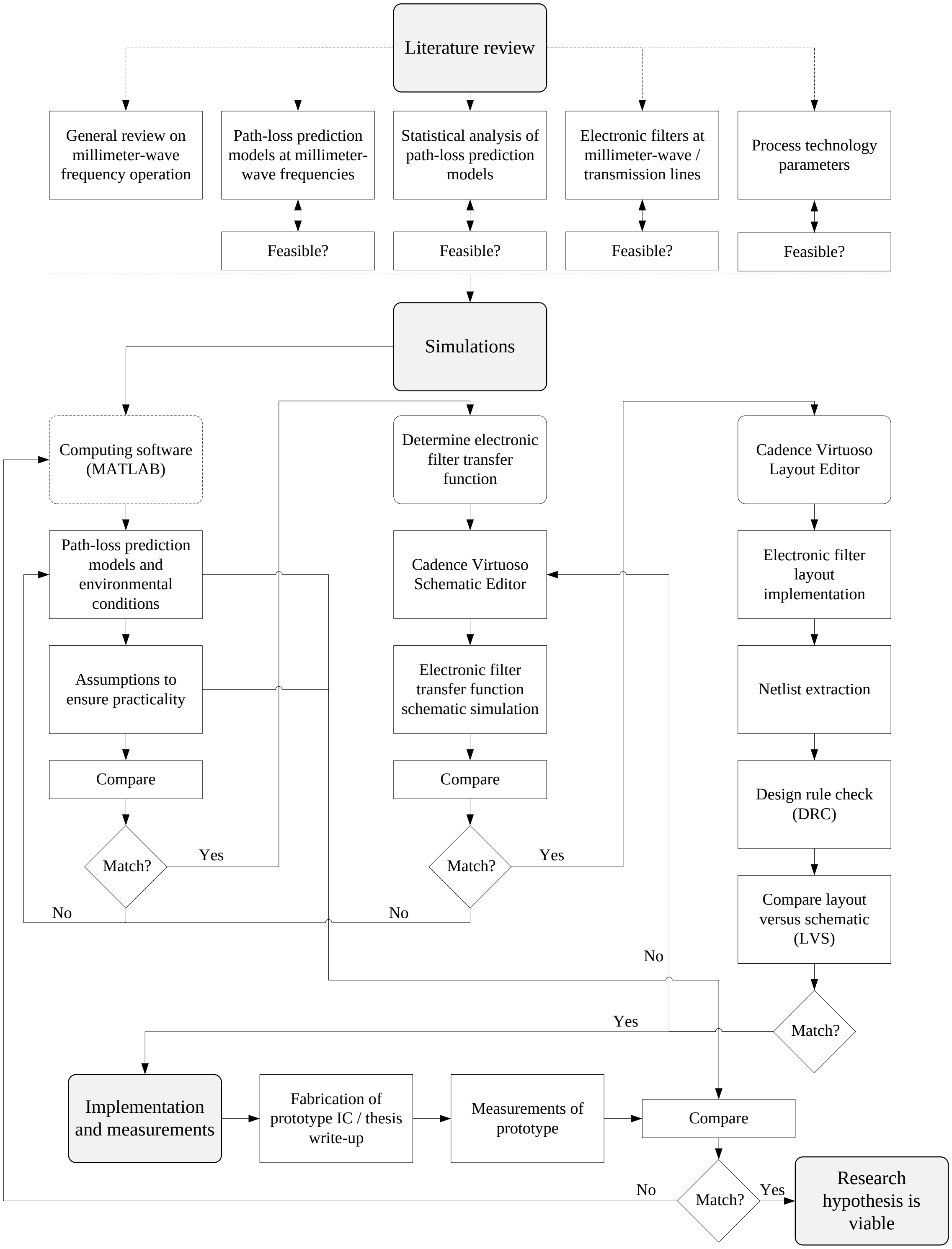

Figure 1.1: Research methodology followed for the proposed research.

From Figure 1.1, initially a thorough literature review on mm-wave frequency operation and its challenges and limitations was completed. A study on path-loss prediction models was done to get an understanding of how signals attenuate in free-space as well as within specific environments where LOS is broken. The study on mm-wave frequencies was then combined with the knowledge on prediction models, and gave an estimation on the amount of attenuation that can be expected at these high frequencies. Electronic passive filters were investigated together with specific process technology parameters of the 130 nm process to determine whether it would be possible to have circuit models at mm-wave frequencies.

These models were tested and modelled in MATLAB[2] and compared to electronic filter transfer functions to represent the free-space losses. The 130 nm process used for the designs has a f_T of 200 GHz and modelling was done in Cadence Virtuoso with component model libraries supplied by the vendor.

The layout of the schematic circuit was done in Cadence Layout Editor and design rule checks (DRCs) and Layout versus Schematic (LVS) tests confirmed that the layout and the schematic designs coincide and no design rules as specified by the 130 nm process were broken.

The layout was converted into a graphic data system (GDS) file and submitted for fabrication in the 130 nm process through the MOSIS Service[3]. The prototype was delivered and it was mounted on a printed circuit board (PCB) and measured using the Anritsu MS 2668C spectrum analyser and the Anritsu 37397D vector network analyser (VNA) connected to a probing station for on-wafer measurements.

The measurement results were then compared to the schematic simulations and the mathematical models and the accuracy of these models were verified. The measurement results were also documented and a conclusion on the hypothesis and research questions was drawn based on these results.

All aspects considered are interdependent, and during each phase these aspects and the effects on the research need to be revised. These aspects are shown in Figure 1.2.

---

[2] MATLAB is a technical computing software package supplied by Mathworks (www.mathworks.com)
[3] Information of scheduled multi-wafer project runs from The MOSIS Service is found at www.mosis.com

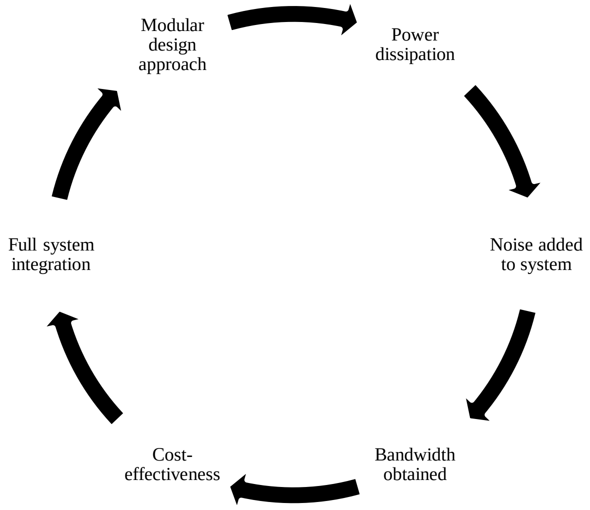

Figure 1.2: Key considerations during each phase of the research.

Starting from the middle left of Figure 1.2 (chosen arbitrarily) the full system integration must not interfere with the functions and purposes of each subsystem, therefore sufficient matching between subsystems is required. A modular design approach should still be adhered to, to allow for future research to be integrated without compromising the current structure. Power dissipation needs to be limited as mobile technologies benefit from low voltage supplies, and this also limits the amount of noise added to the system. The bandwidth of each subsystem is monitored to ensure optimal signal integrity during modulation. Low-cost process technologies and controlled complexity will allow a cost-effective implementation.

1.5 DELIMITATIONS AND ASSUMPTIONS

The concepts developed in this research are assumed to be transferable to other process technologies, although it would be a time-consuming and costly exercise to investigate these possibilities. Research regarding available passive components in alternative process technologies should be sufficient to make this assumption valid, however, correct operation cannot be guaranteed before measurement verifications.

The 130 nm process does provide passive components up to the required frequency range (60 GHz) but some of the component values are not small enough for direct use. For these values to be smaller, in some cases, devices are placed in series or in parallel to comply with technology rules, but this practice can influence transfer characteristics. Interconnects between the reduced (in physical size) components increased the layout size, but within acceptable limits (2 % to 4 % loss in area per passive component). Simulation results are necessary to prove that the effects are minimal.

In the cases where wire bonded connections are needed for the interconnecting bond pads with the external circuitry, the effect of the wire bonds are not simulated using electromagnetic simulations. The wire bonds are only coupled with direct current inputs and outputs for the circuitry to avoid uncontrollable parasitic components. Future works (refer to Chapter 6) would benefit from wire bond models to accurately predict these effects.

All measurements were assumed to be done at 279 K, constituting room temperature, with simulated results for varied temperature given in Appendix C. Equipment to vary the temperature of operation was not available during measurements; therefore the temperature effects cannot be measured, and are only simulated.

To ensure consistency throughout this thesis, all attenuation values are given as negative values. This approach allows attenuation values to be read directly from graphs and results that are labelled (on the *Y*-axis) as negative values. Positive gains have no sign (assumed +) and negative gain values are also assumed to be an attenuation. Variable change in attenuation has no sign and is assumed an absolute value.

1.6 CONTRIBUTION

This research proposes a technique to use schematic-driven, lumped circuit, analogue models to effectively predict propagation characteristics from a radiating structure and expected link-attenuation in real-time. These models can be used during schematic design of transceivers, as a separate building block in the schematic, or as a virtual channel during experimentations to eliminate the need to physically reconstruct each scenario. A prototyped IC could be connected between the transmitter and receiver with the ability to manually modify the scenario by externally manipulating component values. Figure 1.3 represents the system model to contextualize the research.

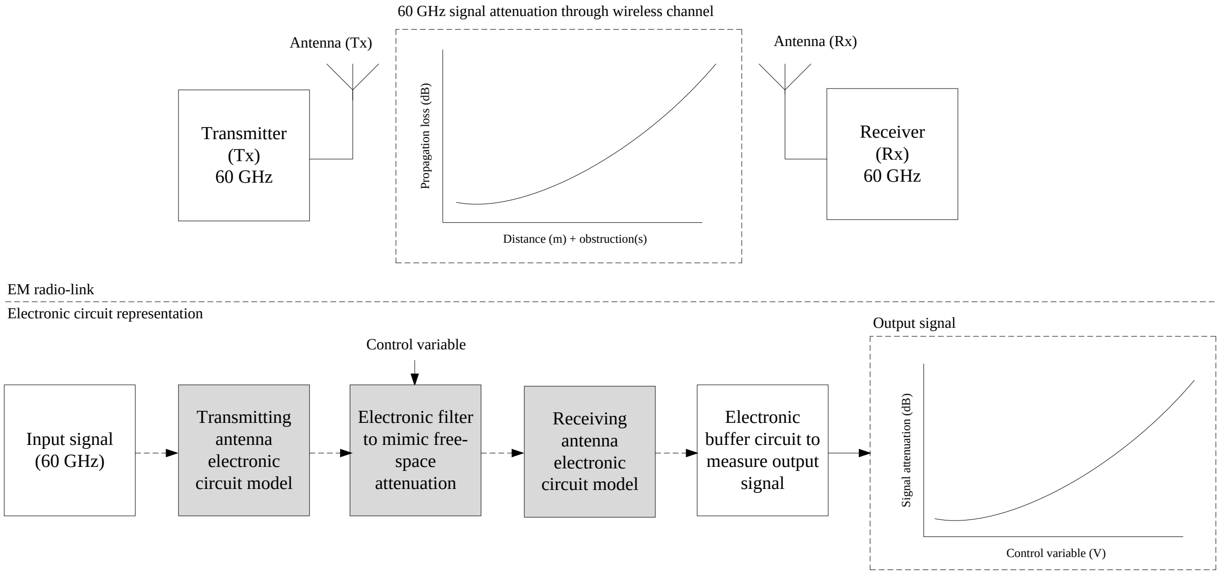

Figure 1.3: System model representing the proposed research contribution.

For this research (from Figure 1.3), to avoid the inaccurate antenna model, an EM simulation of the antenna was done at the desired operation frequency of 60 GHz. The transfer functions of the EM simulation were studied and an equivalent circuit was created to represent the antenna using S-parameter analytical analysis. Additional passive components related to substrate and parasitic effects were added to the *Foster canonical form* representation that added degrees of freedom to the design strategy. To avoid unwanted resonances and improve accuracy of the required complex impedance seen from the load, this strategy proved more effective compared to a more general approach of adding resonance circuits at the output. A guideline is given for designing these antenna types and is a contributory aspect of this research.

A MATLAB algorithm was developed to aid in determining component values during the design of an antenna equivalent circuit using the proposed model. This software uses user-specific inputs regarding the required transfer function for the antenna, and automatically computes a trend line from these specifications. The user can modify these results for improved accuracy, but the time consuming task of determining a first, good fit is eliminated.

The contribution to the current body of knowledge based on electrical circuit modelling of EM components as well as estimated link-attenuation is provided through identifying the considerations when modelling structures at mm-wave frequencies. EM simulations do provide modelling alternatives to account for high-frequency effects. This research work seeks to take forward the representation of these mm-wave effects from the perspective of circuit designers.

It was found that the standard library models of the variable nMOS capacitor models of the 130 nm process was insufficient to use in a variable filter topology at 60 GHz due to its low capacitance value and low variable capacitance at these frequencies. A novel filter based on a 7th order low-pass filter (LPF) topology combined with a common-base buffer amplifier with zero gain to limit active noise was developed to induce a variable filter transfer function using an external voltage which could achieve a maximum of 6.59 dB attenuation difference at 60 GHz using an external bias.

Contribution in the area of modelling transmission lines is achieved as a result of this research through a better understanding of parasitic effects on EM radiation. Inductors at mm-wave frequencies have become impractical to use, and can be replaced by more efficient and smaller transmission lines. Models for transmission lines are not commonly provided by foundries, and the investigation to find accurate and complete models for EM radiation can be directly applied to transmission lines at 60 GHz and contributes to the body of knowledge.

Publications that resulted from this research and contributed to the current body of knowledge are summarized in the following section. These include all peer-reviewed journal articles, co-authored works, and internationally peer-reviewed conference proceedings resulting from the research.

1.7 PUBLICATIONS FROM THIS RESEARCH

The following article has been published in the peer reviewed journal, Microwave and Optical Technology Letters. This journal is listed on the Thomson Reuters Web of Knowledge (formerly Institute for Scientific Information (ISI)):

J. W. Lambrechts and S. Sinha, “A BiCMOS lumped element model for a millimetre-wave dipole antenna,” published in *Microwave and Optical Technology Letters* (Wiley), Vol. 55, No. 12, pp. 2955-2965, December 2013.

The following article has been submitted for peer review. The selected journal is listed on the Thomson Reuters Web of Knowledge (formerly Institute for Scientific Information (ISI)):

J. W. Lambrechts and S. Sinha, “Estimation of signal attenuation in the 60 GHz band with an analogue BiCMOS passive filter,” submitted to *International Journal of Microwave and Wireless Technologies* (Cambridge University Press), submitted in July 2013.

1.8 OUTLINE OF THE THESIS

The outline and structure of this thesis are as follows:

Chapter 1 serves as the motivation for the proposed research and structures the research hypothesis with its justification. The research methodology is outlined and introduces the objectives, aims, and goals of the research. The contribution to the body of knowledge is given, and accompanied with a list of publications resulting from the research.

Chapter 2 is dedicated to the literature review of the relevant topics to investigate the research hypothesis. Reviews on propagation losses at mm-wave frequencies, component models, antenna design and modelling, and electronic (passive) filter design are done in this chapter.

Chapter 3 highlights the methodology undertaken to systematically describe the methods used to complete the research presented from the hypothesis phase up to the measurement and conclusion phase. Computer-aided design (CAD) tools used throughout these phases are briefly discussed, and the measurement set-up is given. A discussion on the design of a ceramic substrate to perform measurement results is given, and the measurement equipment and its functions are discussed.

Chapter 4 focuses on the mathematical modelling and EM / schematic simulations of the subsystems involved to investigate the research hypothesis and aims to verify these models. Subsystems include the EM modelling of mm-wave antennas, path-loss prediction models (mathematically), electronic (passive) filters (mathematically and in schematic simulations), and electronic matching networks (schematic simulations).

Chapter 5 is primarily dedicated to the measurement results of the prototyped circuit to verify the proposed research hypothesis. Chapter 5 also accounts for the practical considerations during the measurement phase, and highlights any modifications made to ensure accurate and precise results. A conclusion is drawn on the measurement results and any inconsistent results are analysed and discussed within this chapter, with further reference in Chapter 6.

Chapter 6 concludes this thesis and draws relationships between the mathematical, simulated, and measured results of the subsystems implemented to aid in proving the research hypothesis. It provides a critical analysis on discoveries within this thesis, provides a scope limitation and any assumptions made during the research, and provides some areas for future research.

1.9 CONCLUSION

This chapter of the thesis introduced an opening in the current body of knowledge and with supported background to the problem, formulated a research hypothesis (refer to section 1.2). The research hypothesis is justified, and the chapter summarized the research methodology. The following chapter provides the literature review regarding the research aspects of this thesis, and introduces required nomenclature to prove the hypothesis.

Table 1.1: Summary of journal impact factors (IFs) and *Cited half-life* for literature related to this research.

Reference	**Journal**	**Journal IF and *Cited Half-Life*[4]**	**Frequency band of interest**	**Contribution to body of scholarly knowledge**
[**1**]	*IEEE Transactions on Wireless Communications*	2.418 and 4.5	55GHz to 57 GHz	Model to calculate the capacity of mm-wave ICs – mathematically only. Angle of arrival method used to calculate capacity. Experiments designed to measure spatial MIMO[5] wireless channel transfer functions at mm-wave.
[**5**]	*IEEE Transactions on Vehicular Technology*	2.063 and 4.9	60 GHz	Propagation path losses affecting LOS and nLOS inter-vehicle communications defined – mathematically only. Data statistically processed to derive path-loss prediction model from experimental results.
[**10**]	*IEEE Transactions on Antennas and Propagation*	2.332 and 8.0	60 GHz	Physical measurements of propagation losses for different scenarios (LOS and nLOS). Data collected (measured) and statistically analysed to provide channel models – mathematically only. Fading statistics defined / compared briefly to coincide with *Rician* or *Rayleigh* distribution.
[**11**]	*IEEE Journal on Selected Areas in Communications*	3.121 and 7.4	RF-spectrum	Interactive software development to assist in transceiver placement. RF band but relevant propagation models defined for all frequency spectrums. General communication feasibility model and calculations of coverage regions provided (serves as a *classical* reference).

---

[4] Journal Impact Factor provided by the ISI Web of Knowledge (www.isiknowledge.com)

[5] MIMO – multiple-input multiple-output refers to the use of multiple antennas at the transmitter and receiver to increase communication performance

Table 1.2 (Table 1.1 continued)**:** Summary of journal IFs and *Cited half-life* for literature related to this research.

Reference	**Journal**	**Journal IF and *Cited Half-Life***	**Frequency band of interest**	**Contribution to body of scholarly knowledge**
[**14**]	*IEEE Transactions on Vehicular Technology*	2.063 and 4.9	60 GHz	Measurements of indoor environments for continuous-route and direction of arrival scenarios. Statistical parameters such as number of paths, RMS[6] delay spread, path loss, and shadowing determined. Reference to, and brief definition of, multipath propagation channels provided.
[This work]	*Microwave and Optical Technology Letters*	0.585 and 5.6	60 GHz	Electronic representation of mm-wave radiating structure, including substrate effects. Electromagnetic simulations of antenna propagation.

---

[6] RMS – root mean square is a statistical measure of the magnitude of a varying quantity

Table 1.3: Summary of previous works related to transmission line modelling at mm-wave.

Reference	Journal	Journal IF and *Cited Half-Life*	Technology	Frequency band of interest	Modelling approach	Comments
[**15**]	*IEEE Journal of Solid-State Circuits*	3.063 and 7.4	130 nm CMOS	40 GHz and 60 GHz	Measured transmission line data at optimized to fit mm-wave frequencies (and scalable).	Full amplifier design with peak values achieved at 60 GHz of $\|S_{21}\|$ = 12 dB and NF = 8.8 dB.
[**16**]	*IEEE Transactions on Electron Devices*	2.062 and 8.2	180 nm CMOS	30 GHz and 60 GHz	Inductively coupled plasma deep trench technology to selectively remove Si underneath transmission line.	Attainable Q-factor of 19.06 achieved at 60 GHz with NF_{min} improvement of 1.082 dB. Inductance of 162.2 pH achieved.
[**18**]	*IEEE Transactions on Plasma Science*	0.868 and 7.6	-	mm-wave frequencies	Numerical processing of paraxial beams and fields in oversized corrugated waveguides.	Corrugated waveguides used to overcome limitation of free-space model. Algorithm to determine amplitude distribution of paraxial mm-wave beam.

Table 1.4 (Table 1.3 continued)**:** Summary of previous works related to transmission line modelling at mm-wave.

Reference	**Journal**	**Journal IF and *Cited Half-Life***	**Technology**	**Frequency band of interest**	**Modelling approach**	**Comments**
[**19**]	*IEEE Transactions on Advanced Packaging*	1.261 and 6.8	180 nm CMOS	100 MHz to 50 GHz	Two-port open-short de-embedding technique and thru technique.	Coplanar waveguide approach with floating shields. Accuracy verified with full-wave simulations.
[**20**]	*IEEE Transactions on Microwave Theory and Techniques*	2.229 and 9.0	65 nm 45 nm 32 nm CMOS	up to 110 GHz	Non-quasi TEM mode modified Wheeler approach.	Improved thin-film microstrip line model for 65, 45, and 32 nm CMOS. Line length and line width constraints to avoid line resonance.
[**17**]	*IEEE Transactions on Microwave Theory and Techniques*	2.229 and 9.0	90 nm CMOS	up to 100 GHz	Scalable frequency-dependent *RLGC* parameters.	Scalability for CMOS processes up to 100 GHz. Measurement de-embedding methodology to reduce wafer size.
[This work]	*Microwave and Optical Technology Letters*	0.585 and 5.6	130 nm BiCMOS	60 GHz	*RLGC*-model parameter extractions for 60 GHz equivalent model	Electronic modelling of radiating structures. Analytical approach, passive components used.

Table 1.5: Summary of popular SiGe Process Technologies (130 – 350 nm). Shaded area shows the technology used for this thesis.

Manufacturer	**Process (BiCMOS)**	**Technology node**	**Active device parameters**					**Passive device parameters**			
			f_T (GHz)	**f_{max} (GHz)**	**BV_{ceo} (V)**	**β_F**	**Deep trench isolation**	**Metal layers (#)**	**I/O (V)**	**CMIM (fF/µm^2)**	**Poly resistor (Ω/□)**
AMS	SiGe	350 nm	60	70	2.7	160	×	4	3.3 / 5	1.05 - 1.45	Up to 1k1
IBM	SiGe (7WL)	180 nm	60	280	3.3	220	√	7	1.8	2.05 - 4.1	260 - 1k6
	SiGe (8HP)	130 nm	200	280	1.77	600	√	7	1.5	1	340 - 1k7
IHP	SiGe:C	250 nm	190	190	1.9	200	√	5	2.5	1	210 - 1k6
	SiGe:C	130 nm	250	300	1.7	500	√	5	1.2 / 3.3	1.5	335 - 750
Jazz Semiconductors	SiGe	350 nm	23 - 61	65 - 75	2.5	NA	√	3 or 4	3.3 / 5	1 - 4	95 - 1k1
	SiGe	180 nm	38 - 155	150 - 200	2.2	NA	√	3 - 6	1.8 / 3.3	1 - 5.6	235 - 1k
	SiGe	130 nm	40 - 200	150 - 200	2.2	NA	√	6	1.2 / 3.3	2.8 - 5.6	310 - 1k
STMicroelectronics	SiGe	350 nm	45	60	3.0	NA	√	5	3.3	5	1
	SiGe:C	250 nm	70	90	2.6	NA	√	5	2.5	5	1
	SiGe:C	130 nm	150	150	1.7	NA	√	6 - 8	1.2	5	1
TSMC	SiGe	180 nm	120	120	2.3	280	√	6	1.8 / 2.5 / 3.3	1 - 2	Up to 1k05
	SiGe	350 nm	62	70	2.5	155	√	4	3.3 / 5	1 - 2	NA

CHAPTER 2: LITERATURE REVIEW

2. CHAPTER OVERVIEW

This chapter elaborates on the research possibilities as proposed in Chapter 1. Each focus area is researched to determine the feasibility of the proposed hypothesis. This chapter investigates the possibility of generating a propagation loss function, consisting of existing models such as free-space, reflection, diffraction, and rain rate losses to determine the complexity of such a model. The transfer function of such a model (depending on its complexity) should then be re-produced by an analogue (passive) filter, and the chapter also investigates the possible filters that can be used on IC-level. The research proposes that an EM model of the transmitting and receiving antenna is investigated, and an equivalent circuit to represent transmission from the antenna is proposed. To integrate the abovementioned research areas on IC-level, matching networks are required (and researched) to compare performance characteristics of different topologies. A brief investigation into passive components is given, with reference to the technology process and its model library components.

2.1 PATH-LOSS PREDICTION MODELS

This section investigates propagation-loss functions and determines the validity of these functions at mm-wave frequencies. Research on free-space propagation loss, reflection, diffraction, and rain-rate attenuation is presented, and the section concludes with a propagation-loss model that accounts for these models. The proceeding research is based on this model, and the hypothesis that questions the possibility that an analogue circuit can be constructed to represent this model, hence follows. Figure 2.1 represents the considered loss functions to construct this loss model.

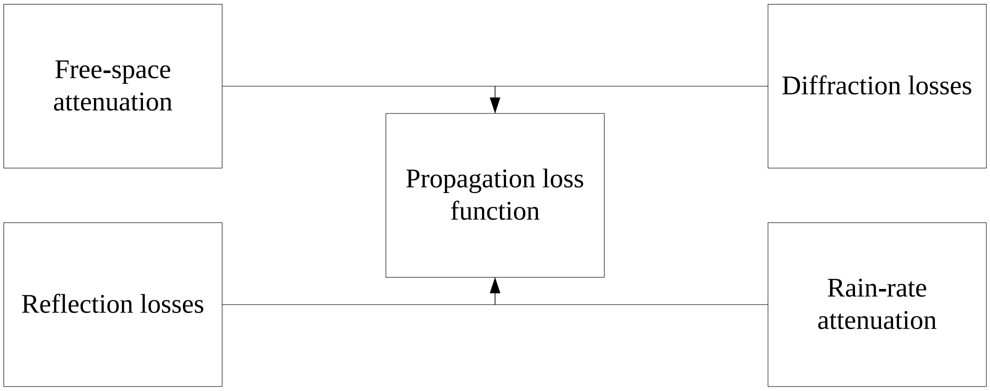

Figure 2.1: Summary of attenuation functions to estimate received power.

The three main mechanisms that account for losses in electromagnetic wave propagation are reflection, diffraction, and scattering [**21**]. Figure 2.1 summarizes the considered loss functions (free-space, diffraction, reflection, and rain-rate) that are considered to develop the proposed propagation loss function. Propagation models are divided into large-scale and small-scale models. Large-scale models predict the average received signal strength that is received by the transmitter, at a specified distance from the transmitting device. These predictions are useful in estimating the coverage area (or distance) of the transmitted radio wave. Fading models (small-scale) are used to characterize the rapid fluctuations of the received signal over short distances and short time intervals. The first attenuation function to be considered is the free-space loss model.

2.1.1 Free-space losses

Free-space propagation introduces losses in radio waves when travelling in LOS between the transmitter and the receiver. The free-space losses are proportional to the transmitted power and the distance that the signal travels towards the receiver. The *Friis* free-space equation [**22**] defines the power received at the receiver (antenna) and is given by

$$P_r(d) = \frac{P_t G_t G_r \lambda^2}{(4\pi)^2 d^2 L} \tag{2.1}$$

where $P_r(d)$ is the power received by the receiving antenna (in Watt) at distance d (in m), P_t is the amount of power transmitted (in Watt), G_t is the gain of the transmitter and G_r is the gain of the receiver (dimensionless), λ is the wavelength of the transmitted signal (in m), and L is the system loss factor ($L \geq 1$). A value of $L = 1$ would suggest that there are no losses in the system due to transmission line attenuation, filter losses, or arbitrary antenna losses. It is important to note that from (2.1) the received power is reduced (attenuated) proportionally to the square of the distance (d) between the transmitter and the receiver. The signal losses due to free-space propagation of a LOS signal can be represented by a positive quantity as the difference between the received power and the transmitted power. If it is assumed that the transmitter and receiver antenna gains are unity, to eliminate the antenna properties in the loss equation, the signal losses of a LOS signal becomes

$$PL(d)[dB] = 20\log_{10}\left(\frac{4\pi d}{\lambda}\right). \tag{2.2}$$

Equation (2.2) is *only* valid for values of d that exist in the far-field region (refer to section 2.3.3) and if $d \neq 0$. It is often preferred to determine the power received (or radiated in free-space) at a distance d as a power related to a known reference power at distance d_0. The reference power ($P_r(d_0)$) can be determined by (2.1) and the relationship of the power at d to the reference power (assuming both distances are within the far-field region) derived. It follows that a path-loss prediction model that is commonly used in [**5**], [**10**], and [**14**] for estimating the mean path loss ($\overline{PL}(d)$) of a signal and is defined by the following equation,

$$\overline{PL}(d)[dB] = PL(d_0)[dB] + 10n\log_{10}\frac{d}{d_0} \tag{2.3}$$

where $PL(d_0)[dB]$ is the path loss at reference distance d_0 in free-space and more importantly, n specifies the path-loss characteristics as a function of separation type between transmitter and receiver. Some values of n [**21**] are given in Table 2.1.

Table 2.1: Free-space path loss characteristics exponent $\boldsymbol{n}$.

Environment	**Path loss exponent**
Free-space	2
Urban area	2.7 – 3.5
Shadowed urban area	3 – 5
In building (LOS)	1.6 – 1.8
In building (nLOS)	4 – 6
Factory (nLOS)	2 – 3

From Table 2.1 it can be seen that the path-loss exponent of free-space is equal to 2, and the path-loss exponent inside a factory is approximated to be equal to this value (with maximum value approximated to n = 3. Urban areas and shadowed (high-density) urban areas have a path-loss exponent from n = 2.7 to a maximum value of n = 5. In-building LOS conditions present the lowest exponent values between 1.6 and 1.8 with in-building nLOS conditions path-loss exponents approximated between 4 and 6. The effect of n is noticeable from Figure 2.2, where the mean path loss of a 60 GHz communication signal over a distance of 30 m is simulated, for n = 1, 2, 3, and 4. For larger values of n, there is a significant difference in received power versus reference power at d_0.

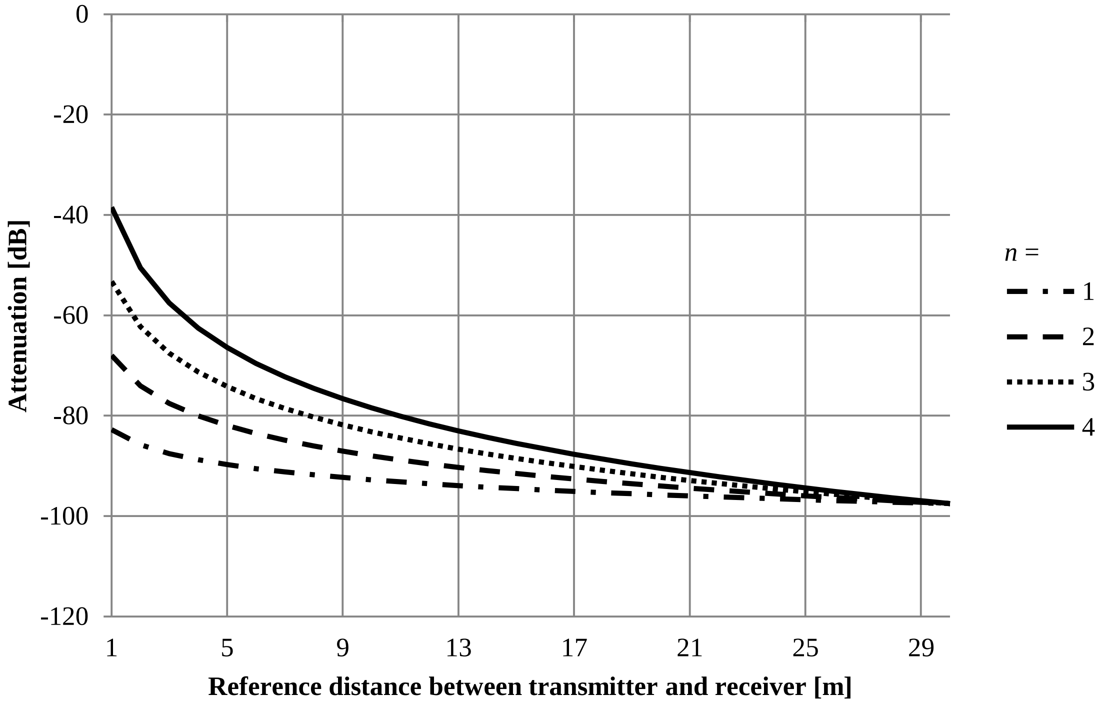

Figure 2.2: Signal attenuation with varying path-loss exponents (f = 60 GHz).

In Figure 2.2 the free-space attenuation frequency dependency for LOS can be illustrated through simulation of the mean path loss over a 30 m distance with path-loss exponent value of n = 2 (used mostly for indoor communications). The operating frequency is varied with values of f = 2.4 GHz, 10 GHz, 60 GHz, and 77 GHz, as seen in Figure 2.3.

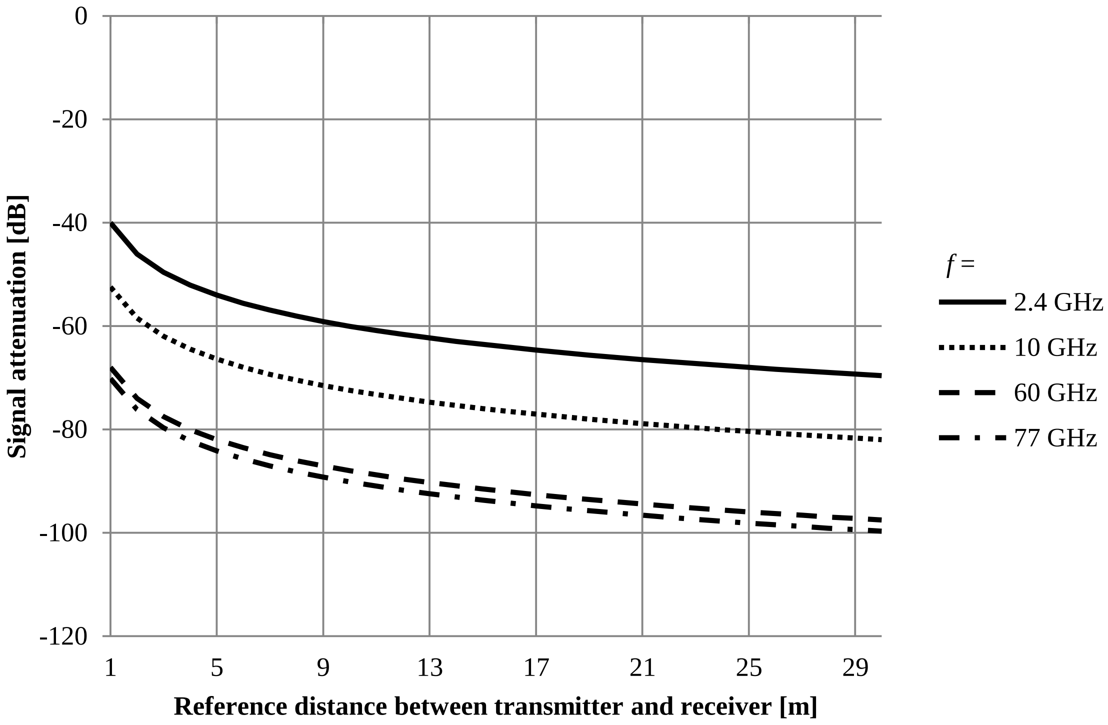

Figure 2.3: Signal attenuation with varying frequency (*n* = 2).

From Figure 2.3 it is evident that the amount of attenuation increases with increasing frequency, where at 2.4 GHz the attenuation at 30 m from the transmitter is -68.4 dB and at a frequency of *f* = 77 GHz the attenuation is increased (therefore a smaller negative value) to approximately -99.8 dB. The model in (2.3), however, only accounts for LOS communication, and needs to be expanded for cases where nLOS occurs, as this may often be the case. The mean path loss of the signal is therefore expanded to

$$\overline{PL}(d)[dB] = PL(d_0)[dB] + 10n\log_{10}\frac{d}{d_0} + \sum_i AF_i \qquad (2.4)$$

where AF_i is the attenuation in dB of the signal due to an intervening object that tends to break the LOS. Each attenuation (AF_i) is characterized as a function of thickness, density, as well as area; and experimental results can be used to obtain these values. A communication feasibility model used in [**11**] takes into account the receiver sensitivity and carrier-to-noise interference thresholds to determine if acceptable communication quality is achieved. In this research, it is assumed that the communication is defined acceptable as outlined in [**11**], as the proposed transmission is at a separation on less than 1 m at 60 GHz. In [**10**] and [**23**] measured attenuations for obstructions breaking LOS are given. Some of these measured attenuation values are given in Table 2.2.

Table 2.2: Attenuation values for LOS obstructions at 60 GHz measured in **[**10**]**.

Material	**Attenuation at 60 GHz [dB/cm]**
Plywood panels	0.12
Brick wall (with paint and plasterboards)	2.1
Drywall	2.4
Whiteboard	5.0
Ordinary glass	7.0
Double glass	11.3
Mesh glass	31.9
Iron door (with plywood panels)	49

From Table 2.2 the attenuation at 60 GHz (in dB/cm) is lowest for plywood panels at approximately (measured value) 0.12 dB/cm and highest for iron doors (49 dB/cm). Mesh glass also presents a relatively high attenuation at 31.9 dB/cm followed by double glass at 11.3 dB/cm. Brick walls, drywall, whiteboard, and ordinary glass all present attenuation values at 60 GHz lower than 10 dB/cm.

The measured values of attenuation for these materials are used in the propagation-loss models as variables to the specified environment, specifically with reference to objects breaking LOS.

Free-space losses for LOS and nLOS communications have been reported, and some of these results are tabulated in Table 2.3.

Table 2.3: Free-space losses at 60 GHz as reported in current literature.

Reference	Attenuation [dB] at 60 GHz	Distance between transmitter and receiver [m]	Comments
[23]	100 - 140	0 - 14	Losses calculated for different nLOS scenarios
[14]	105 - 115	15 - 30	nLOS communication
[14]	85 - 105	1 - 60	LOS communication in corridor environment
[23]	70 - 95	20	Losses calculated for LOS scenarios
[24]	82	5	EIRP estimated at 53 dBm Receiver NF assumed 7 dB
[5]	90-130	10 - 300	Inter-vehicle LOS communication Variation in vehicle height
[5]	105 – 135	10 – 400	Inter-vehicle nLOS communication 1 moving vehicle
[This Work]	70 – 120	0.1 – 30	nLOS including scattering and diffraction losses Rain-rate losses included

From the available literature in the current body of knowledge as summarized in Table 2.3, it is noticeable that the amount of attenuation of a LOS and nLOS signal at 60 GHz is around the 100 dB range. Also noticeable is the sharp rate of attenuation at distances closer than 10 m and the visible decrease in attenuation rate at increasing distance, as the signal quality reaches its minimum detectable signal. The 60 GHz spectrum lies within the oxygen absorption band, and is discussed in section 2.1.2.

2.1.2 Oxygen absorption

This research field was especially active during the 1960’s and 1970’s when satellite communications became popular, and many of the early findings still prove accurate today. Several methods of estimating atmospheric absorption exist, and these methods are briefly discussed in [**25**]. These methods are designed to be less computer intensive compared to the inversion of matrices [**26**]. The *Van Vleck* [**27**] absorption coefficient is an approximate formula for both the non-resonant absorption and the absorption by the tails of the 60 GHz band. The *Van Vleck* absorption coefficient estimates oxygen absorption attenuation at around 10 dB/km to 15 dB/km (0.01 dB/m to 0.015 dB/m) for a 60 GHz transmission [**28**] depending on the altitude.

Free-space losses and attenuation from the oxygen absorption band account for losses that occur regardless of the path followed by the signal (assuming LOS), and to account for reflection and refraction from objects breaking LOS, the following models are proposed.

2.1.3 Reflection losses

When a transmitted electromagnetic wave moves from one medium with a refractive index n_1 to a second medium with refractive index n_2, reflection (and refraction) will occur. The electric field intensity of the reflected and transmitted waves can be related to the incident wave in the medium of origin through the *Fresnel* reflection coefficient [**29**] and [**30**]. If the plane of incidence is defined as the plane containing the incident, reflected, and transmitted rays, then the electric field can be defined to have a vertical or horizontal polarization. The angle-of-incidence, reflection, and transmission can also be equated by applying sine, cosine, or tangential relationships to the electric or magnetic field incidence. The reflection coefficients for the vertical ($\mathit{\Gamma}_{\parallel}$) and horizontal ($\mathit{\Gamma}_{\perp}$) electric fields can be determined by boundary conditions using *Maxwell’s* equations [**31**], and results in

$$\mathit{\Gamma}_{\parallel} = \frac{E^-}{E^+} = \frac{\eta_2 \sin\theta_t - \eta_1 \sin\theta_i}{\eta_2 \sin\theta_t + \eta_1 \sin\theta_i} \tag{2.5}$$

$$\mathit{\Gamma}_{\perp} = \frac{E^-}{E^+} = \frac{\eta_2 \sin\theta_i - \eta_1 \sin\theta_t}{\eta_2 \sin\theta_i + \eta_1 \sin\theta_t} \tag{2.6}$$

where E^- and E^+ are the complex number ratio of the electric field strength of the reflected and incident wave, respectively, θ_t and θ_i are the angles of the transmitted and incident waves respectively, η_i is the intrinsic impedance of the ith medium (i = 1,2). The return losses, depending on the polarization, are given by

$$RL[dB] = -20\log\left|\Gamma_{\parallel}\right| \tag{2.7}$$

$$RL[dB] = -20\log\left|\Gamma_{\perp}\right|. \tag{2.8}$$

The reflection coefficients for three obstructive materials (paper, ordinary glass, and alumina) as a function of the angle of incidence for vertical (in plane) scattering losses at 60 GHz are given in Figure 2.4.

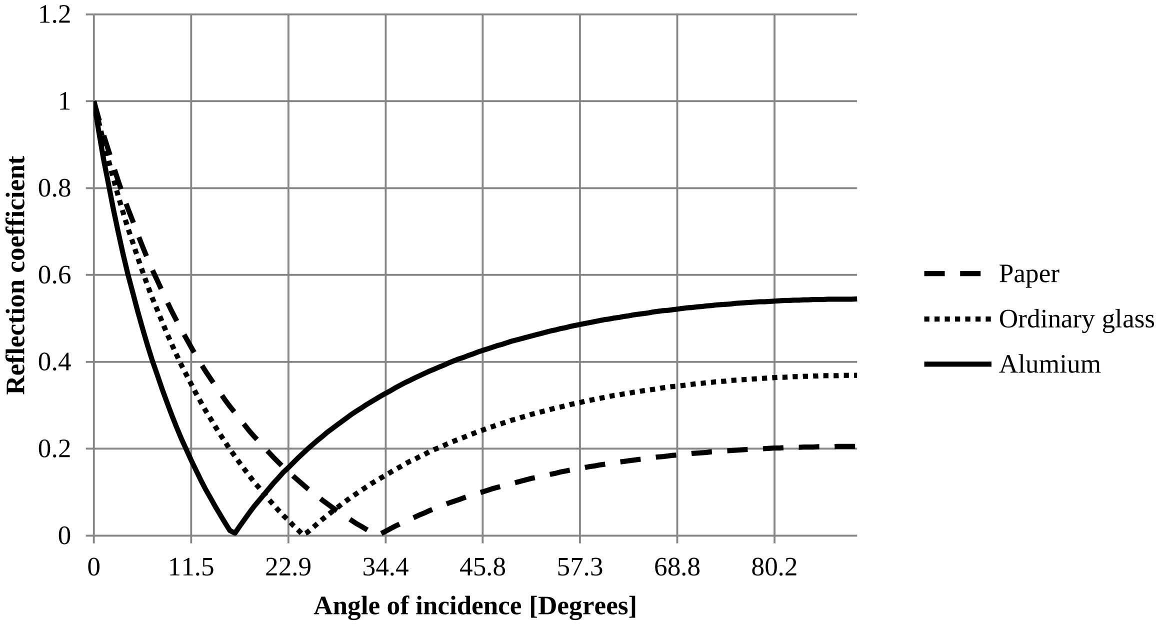

Figure 2.4: Reflection coefficient for paper, ordinary glass, and alumina.

From Figure 2.4 there exists an angle for each obstructive material where the reflection coefficient is 0; therefore none of the signal power passes through the material. This can be visually represented by plotting the return loss in (2.7) as a function of the angle-of-incidence for vertical polarization at 60 GHz, and is given in Figure 2.5.

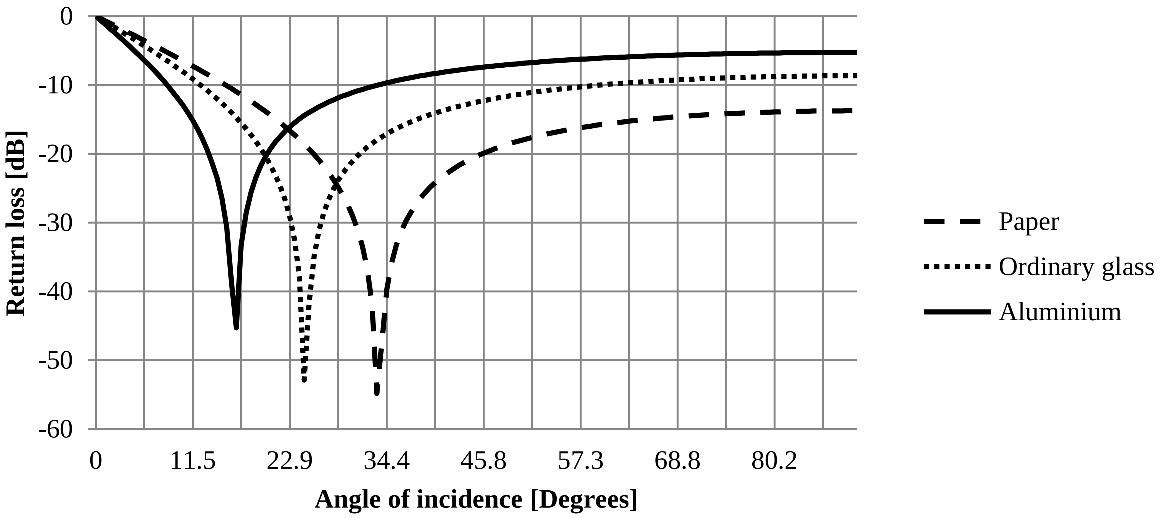

Figure 2.5: Return loss for paper, ordinary glass, and alumina.

Figure 2.5 represents a visual method of limiting the return loss (up to -5 dB for paper at 34^{o}) by ensuring that the angle of incidence does not fall within the high attenuation peak. Note that the least attenuation occurs at 0^{o} and then again at 90^{o} angle-of-incidence. If the incident power is a known variable, it is possible to equate the reflected power from this analysis. Measurements of reflection and transmission coefficients done in 1997 in [**32**] on walls, the floor, ceiling, and windows at 57.5 GHz (with 2 GHz to 3 GHz intermediate frequency) were compared to models based on the *Fresnel* reflection coefficient computations. It was shown that the position of inhomogeneity objects display variations in measured values versus mathematical models, but could be accounted for. Reflection coefficient as a function of angle-of-incidence measured results in [**32**] display similar tendencies to the obtained results in Figure 2.4 (where different materials were used). More recent works in [**33**] and [**34**] on reflection of high frequency signals are focused on future mm-wave (D-band and THz range) operation but similar procedures and analysis to measure reflection coefficient versus angle-of-incidence using simple structures and equipment persist.

To account for the bending of waves during transmission, diffraction losses are described in the following section.

2.1.4 Diffraction losses

Diffraction models [**35**] such as the electron diffraction model, *Fresnel* and *Fraunhofer* models, the knife-edge model, and *Schaefer–Bergmann* diffraction models exist to determine the amount of losses that occur due to diffraction. Complex and irregular terrains and environments generally make these computations complex and theoretical approximations and predictions, as well as empirical corrections and assumptions are applied for relatively accurate results. EM waves in general have limited ability to diffract around obstacles with physical size much larger than its wavelength. The wavelength of a 60 GHz radio signal (λ = 5 mm) is small compared to objects breaking LOS such as furniture and humans, commonly found in high data rate environments (over short distances). Decreases of the link budget up to 30 dB can be experienced with humans breaking LOS and can cause intermittent interferences of mm-wave radio links. Diffraction theories such as the uniform geometrical theory of diffraction rely on generalized reflection / diffraction coefficients depending on the geometry of the environment and its obstacles breaking LOS [**36**]. Analytical solutions exist for these geometries, however, it is required to determine the coefficients based on measurements and difficult to generalise the computational steps for other environments. Some less complex models (such as the knife-edge model described by the *Huygens-Fresnel* principle) are used to give a good first approximation of the magnitude of losses that can be expected from limited diffraction at these small wavelengths. A parameter simulation of the *Fresnel-Kirchoff* diffraction parameter (v) [**37**] with height of the obstructing object equal to 7.5 cm, λ set to 5 mm, and total distance between transmitter and receiver of 30 m is given in Figure 2.8.

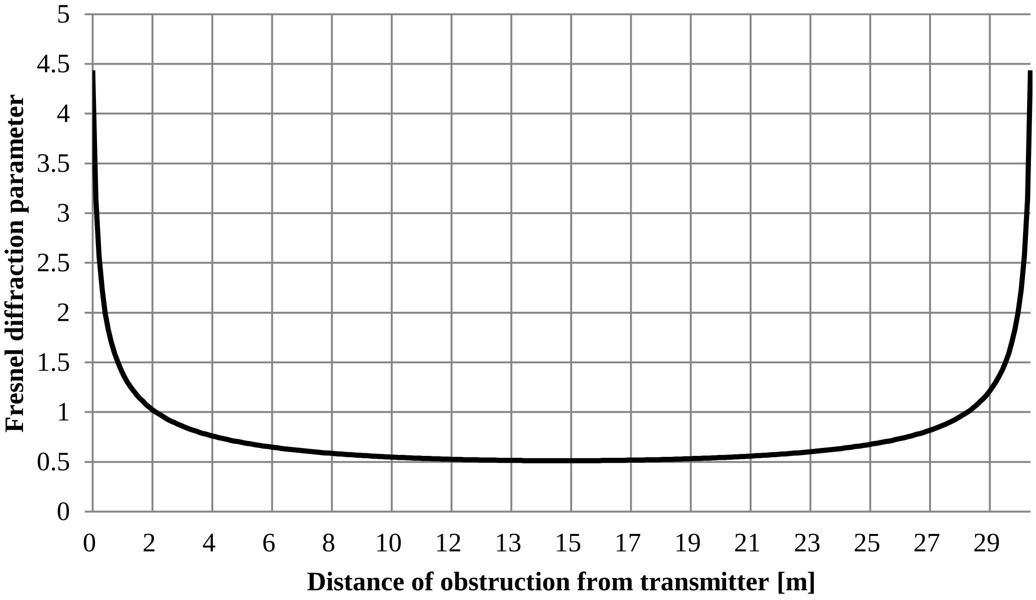

Figure 2.6. Simulation of *Fresnel-Kirchoff* diffraction parameter.

In Figure 2.8 the distance between the receiver and the obstruction is varied from 0 m to 30 m and the resulting *Fresnel-Kirchoff* diffraction parameter plotted. It is evident from the results displayed in Figure 2.8 that v is minimized with distance d_2 equal to 15 m (v = 0.511), therefore halfway between the transmitter and the receiver.

The diffraction gain (or attenuation) ($G_d[dB]$) as a result of a knife-edge modelled obstruction, is a logarithmic function of $F(v)$ where

$$F(v) = 6.9 + 20\log\left(\sqrt{(v-0.1)^2+1}+v-0.1\right) \tag{2.9}$$

for $v \geq 0.7$ and $F(v) = 0$ for $v < 0.7$. An approximate solution for $G_d[dB]$ is given in [12] and can also be displayed in a more convenient way as in Figure 2.7, representing the knife-edge diffraction gain as a function of the *Fresnel* diffraction parameter. The resulting knife-edge attenuation can therefore be minimized by moving the obstruction of constant height h in to halfway ($\frac{d_1+d_2}{2}$) between the transmitter and receiver.

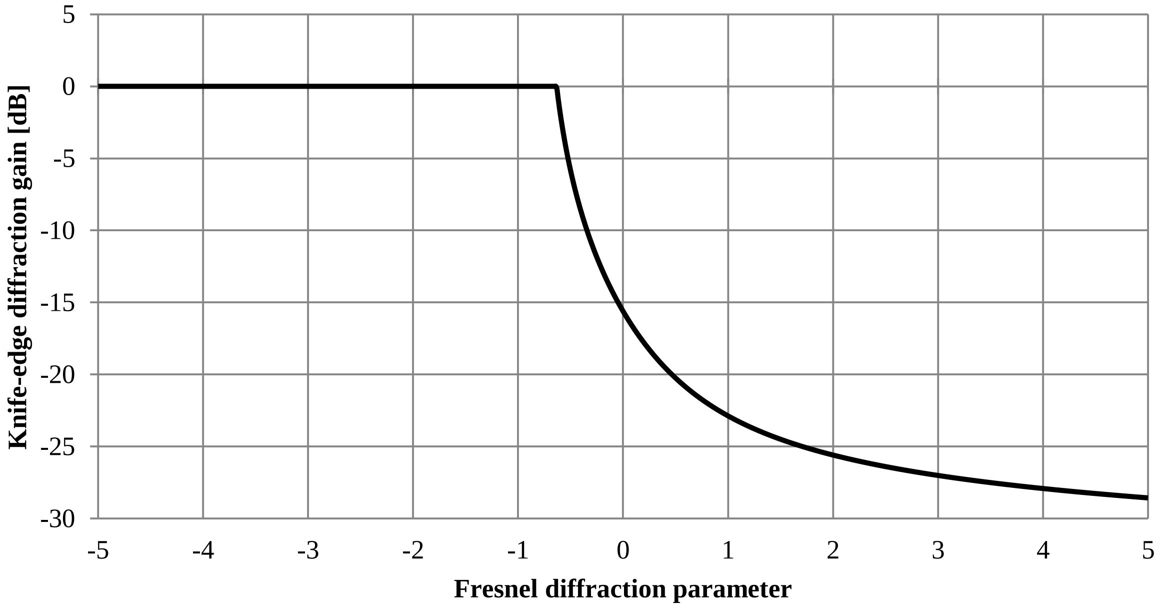

Figure 2.7. Diffraction gain as a function of *Fresnel* diffraction parameter.

Figure 2.7 therefore presents a convenient, graphical way of determining an estimated attenuation of the transmitted signal due to the knife-edge model, and is included in the final loss-function, assuming all variables can be determined. The diffraction gain follows an overshoot-type function (with theoretical positive gain) for *Fresnel* diffraction parameters below *v* = -0.75 (simplified to zero dB in Figure 2.7) and the gain decreases at approximately -5 dB per decade and reaches its asymptote at -28 dB for *v* > 5. The *Fresnel* diffraction parameter as a function of attenuation can be simulated by a LPF structure as proposed in section 1.2 depending on the maximum variable attenuation attainable by the filter structure (refer to section 4.6). Scattering losses occur due to the roughness of the obstructive material, and are discussed in the following section.

2.1.5 Scattering losses

Scattering occurs if an electromagnetic wave (or any form of radiation) deviates from a straight line trajectory due to non-uniformities in the medium through which it is passing. If the surface through which the wave is travelling is defined rough [**38**], the reflection coefficient needs to be adjusted by a scattering loss factor (ρ_S), such that

$$\Gamma_{rough} = \rho_S \Gamma \tag{2.10}$$

and the factor ρ_S is derived in [**38**]. The return loss is determined by the equation

$$RL[db] = -20\log\left|\Gamma_{rough}\right|. \tag{2.11}$$

The complexity of the scattering losses is considered high due to the use of the *Bessel* function, and is not included in the final loss-function. In [**39**] a technique is presented to estimate scattering effects from inhomogeneous objects breaking LOS through a 2.5D volume integral equation using a spatial *Fourier* transform of the fields along the invariant direction (assumed 2D). Combining the 2D fields using method of moments can estimate the 3D scattered field, however, computational complexity is beyond the scope of this research.

Rain-rate attenuation has an effect of transmitted signal if the range increases. To determine an estimation of the effect of rain over a short distance, the following section is presented.

2.1.6 Rain-rate attenuation

Rain-rate attenuation for terrestrial and earth-space paths can be determined by using uniformly distributed raindrops (modelled as spheres) or as more complex shapes depending on the type of rain considered (drizzle, thunderstorm, or hard rain). An empirical procedure for determining the attenuation constant (A) is defined in [**40**] as

$$A = aR^b \tag{2.12}$$

where a and b are functions dependent on frequency (f) of operation and rain temperature (T) in Kelvin, and R is the rain-rate (in mm/h) of the geographical location at a specified time. The attenuation constant is measured in dB/unit distance. Some estimation of rain-rate in climatic zones of South Africa for frequencies up to 50 GHz is given [**41**] with rainfall models in South Africa determined in [**42**]. The rain rates ($R_{0.01}$) are specified with an integration time of 1 min and a rainfall rate distribution probability of 0.01 %.

To determine the rain-rate attenuation in dB/m ($K(d_0)$), the following equation is proposed:

$$K(d_0)[dB/m] = \frac{aR^b \times d_0}{1000} \tag{2.13}$$

where d_0 is the distance where the attenuation is measured with reference to the transmitter (in m). From the derivatives determined in [**40**], an approximate solution for the terms a and b is given by (first the approximation for a)

$$a = G_a f^{E_a} \tag{2.14}$$

where $G_a = 4.09 \times 10^{-2}$, $E_a = 0.699$ at $54 \leq f \leq 180$ GHz. Similarly for the exponent b, where

$$b = G_b f^{E_b} \tag{2.15}$$

and $G_b = 2.63$ and $E_b = -0.272$ for $25 \leq f \leq 164$ GHz. From this, the following equation is prosed for this work.

$$K(d_0)[dB/m] = 1398.5R^{0.0031} \tag{2.16}$$

where the rain rate is specified at time-of-estimation. Figure 2.8 shows the rain-rate attenuation in dB/m as a function of the rain rate (at 60 GHz), for values of $R_{0.01}$ = 0 mm/h (no rain) up to $R_{0.01}$ = 150 mm/h (considered very hard, tropical rain).

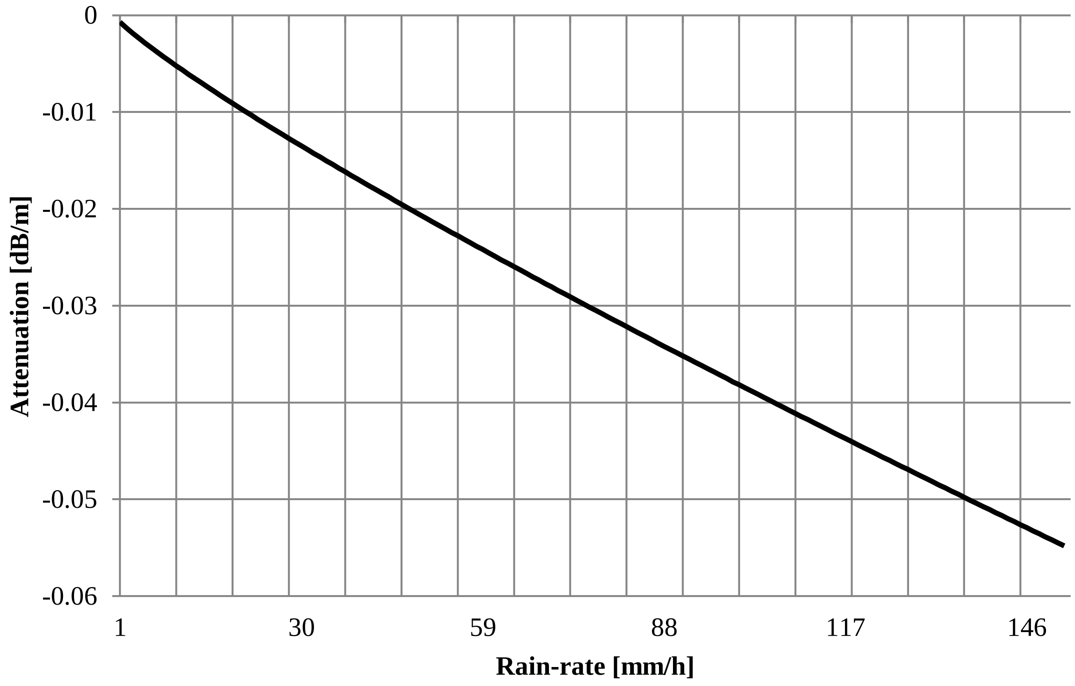

Figure 2.8. Rain-rate attenuation in dB/m as a function of rain rate.

From Figure 2.8 (with f = 60 GHz) it can be seen that the attenuation in dB/m increases almost linearly with increasing rain-rate (in mm/h). The rain-rate can also be illustrated as a function-of-distance from the transmitter, for different rain-rates (at 60 GHz), as illustrated in Figure 2.9.

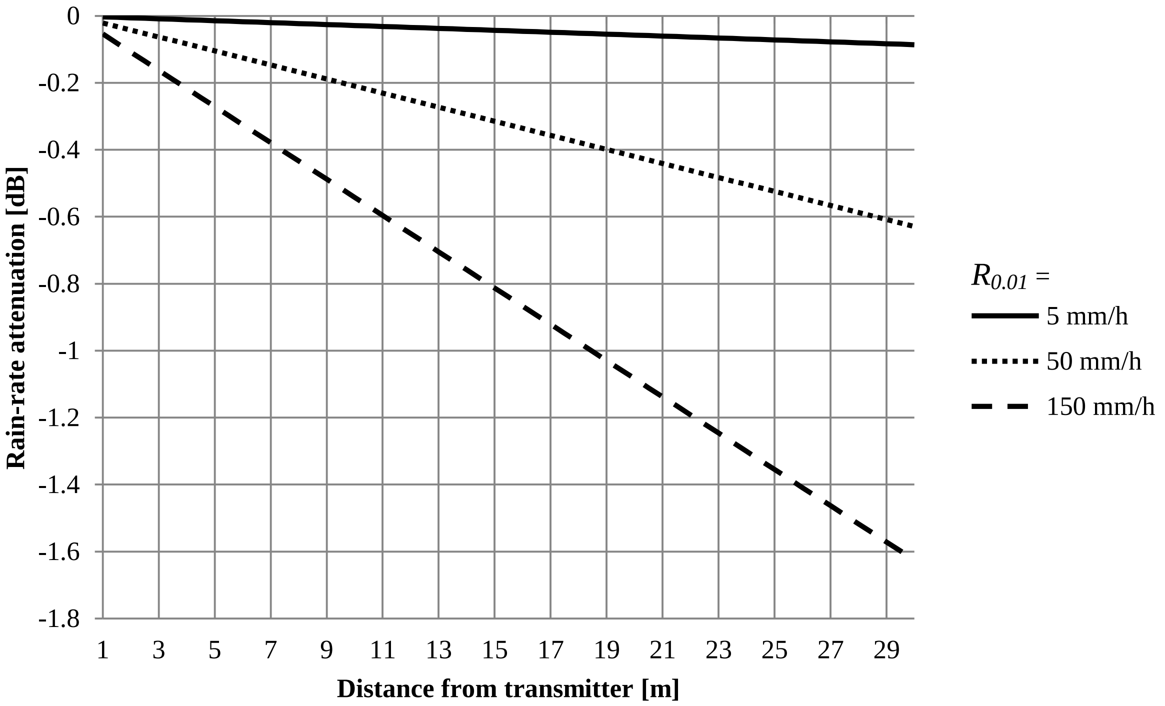

Figure 2.9. Rain-rate attenuation in dB as a function of distance for varied *R*.

Figure 2.9 represents attenuation (in dB) for rain rates of $R_{0.01}$ = 5, 50, and 150 mm/h respectively at 60 GHz. It can be seen from Figure 2.9 that at high rain rates ($R_{0.01}$ = 150 mm/h) the attenuation as a function of distance increases (becomes more negative) at a larger slope compared to lower rain-rates (such as $R_{0.01}$ = 5 mm/h) and has a detrimental effect on signal quality over large distances. The attenuation is used in the final loss-function and adds to the total attenuation that a 60 GHz signal encounters during transmission.

Considering the attenuation to a 60 GHz transmission incurred by free-space losses, oxygen absorption, reflection, diffraction, scattering, and rainfall, the following attenuation model is proposed. The research investigates if this model can be reproduced by an analogue electronic circuit model to analyse the attenuation in real-time, as opposed to computer-processed results which needs to be converted to the digital domain before analysis.

2.1.7 Proposed attenuation function

This section summarizes the results obtained in sections 2.1.1 to 2.1.6, and determines a loss-function that includes all loss mechanisms discussed up to this point. Each mechanism loss function is given, with all variables described in the respective sections and summarized in Table 2.4.

Table 2.4: Summary of attenuation mechanism functions.

Attenuation mechanism	**Attenuation function**
Free-space	$\overline{PL}(d)[dB] = PL(d_0)[dB] + 10n\log_{10}\frac{d}{d_0} + \sum_i AF_i$
Oxygen absorption	0.01 dB/m
Reflection	$RL[dB] = -20\log\lvert\Gamma\rvert$
Diffraction	$G_d[dB] = 20\log_{10}\lvert F(v)\rvert$
Rain-rate	$K(d_0)[dB] = 1398.5R^{0.0031} \times d_0$

From Table 2.4 (summarized results from sections 2.1.1 to 2.1.6), the final loss function that will be simulated is

$$TL(d_0)[dB] = PL(d_0)[dB] + 10n\log_{10}\frac{d}{d_0} + \sum_i AF_i + 0.01dB/m - 20\log\lvert\Gamma\rvert + 20\log_{10}\lvert F(v)\rvert + 1398.5R^{0.0031} \times d_0. \tag{2.17}$$

The function (2.17) is graphically represented using MATLAB (refer to section 4.1), with the variables chosen to represent the specified environmental condition. These variables can be modified in MATLAB (refer to Appendix A) to effectively alter the situation (environmental conditions and obstructions). The analogue electronic circuit representation should be able to reproduce the amount of attenuation obtained from (2.17), and the effects analysed in real-time.

The following section describes electronic filter theory, as an introduction to the types of electronic circuits and topologies available to represent the proposed transfer function. Digital and analogue, active and passive filters are compared to determine which type of filter would better suit this application, and the reasoning is also given.

2.2 ELECTRONIC FILTER THEORY

This section describes the basics of integrated electronic filter design, and filter specifications for different types of filters. The goal of the electronic filter is to represent the attenuation obtained from the loss-function in section 2.1.7.

2.2.1 Introduction to electronic filters

A filter is an electrical network that changes the amplitude or phase characteristics of a signal, with respect to frequency. Additional frequency components should ideally not be added to a signal by a filter, and it should only change the amplitude or phase characteristics of the existing frequency components. In this way, filters can be used to emphasize or reject certain frequency components, depending on the system specifications. This is done by altering the gain (or attenuation) of the filter at certain frequencies.

Typical requirements of filters are the frequency response, phase shift (group delay), and impulse response. A filter must be causal (only be dependent on current and past inputs) and stable (to prevent oscillation). The filter should not be computationally complex, and implemented in either software or hardware, depending on the application. Other considerations include whether the filter should be analogue, analogue-sampled, digital (finite impulse response or infinite impulse response), or mechanical. The linearity of the filter must be accounted for. Finally, the filter can be either active (introduce amplification) or passive (no amplification).

Several filter types exist, each with specific characteristics for amplitude response and phase shift (group delay). The choice of filter therefore depends on the application. *Butterworth*, *Chebyshev*, *Bessel*, *Elliptical*, and *Gaussian* filters are a few examples of filter types, with variations on each type also possible. *Butterworth* filters produce the flattest pass-band amplitude response of all the filters, but at the expense of a relatively slow roll-off between pass-band and stop-band. *Butterworth* filters also present an unwanted phase shift which can result in distortion of the output signal. *Chebyshev* filters improve somewhat on the sharpness of the roll-off of *Butterworth* filters, but at the expense of a small output ripple in the transfer characteristic amplitude response. *Bessel* filters address the maximum flatness of the time delay within it the pass-band (in contrast to the *Butterworth* filter maximum flatness of amplitude response) but again, at the expense of large ripples in the pass-band, and also a lower roll-off in the frequency domain.

Electronic filters can operate in the digital (digitized) domain and in the analogue (continuous-time) domain. Each domain has its own advantages and disadvantages depending on the application. Analogue filters are most commonly used in high-frequency, RF applications such as electronic frequency mixers and RF modulators, whereas digital filters are preferred for high precision and high-accuracy applications. Digital filters generally operate far below the f_T of the transistors used to design these filters to avoid aliasing. Analogue filters present higher bandwidth capabilities compared to its digital counterpart (as there is no need for analogue to digital conversion). Analogue filters are also relatively easier and cheaper to implement as there are less overhead circuitry needed. For this research, analogue filters are used due to its higher bandwidth capabilities.

Implementing a passive filter (or active filters, depending on the frequency of operation and limiting parameters of active components) on an IC requires knowledge of process parameters to determine the feasibility of designing these filters on-chip. Size, speed, and the addition of noise to these circuits are considered and comparisons to find the optimal process in terms of performance and cost-effectiveness are crucial.

2.2.2 Passive filters

A passive filter is a filter that uses only passive components (capacitors, inductors, and resistors) and has no amplification properties (gain), and ideally only attenuation outside the pass-band. Active filters employ amplification elements, such as transistors and operational amplifiers, and use the passive components in the feedback loop. The distinct advantage of passive filters over active filters is that it does not require any power supply to operate, and thus does not consume power. There are also no bandwidth limitations incurred from active components, and it can operate at higher frequencies compared to active filters, which suffer from gain-bandwidth limitations. Passive circuits generate low noise (only thermal noise is present from the resistive components) and no active noise is present, the circuits are reliable even under high-current operation as no active devices are present. The lack of gain in these circuits can in some applications be considered a disadvantage, where active filters might be more practical. Passive filters can also present too low input and too high output impedances, and additional buffer circuitry may be required. Active filters present high input impedance, low output impedance and can be designed to have almost any desirable gain. The use of inductors in passive filters increase the real-estate needed to implement the circuits (increased cost in IC fabrication). The fact that active filters do not need inductors is one of the more distinct advantages of these types of filters (especially at lower frequencies where inductor sizes tend to be physically impractical). Large order filters (to attain sharp roll-off and attenuation slopes) can become very time-consuming to design, and limit tuning due to its mathematical complexity. Active filters are generally easier to design compared to passive filters. In high-frequency applications, standard CMOS and BiCMOS integrated filters that employ on-chip passive devices suffer from large substrate losses and therefore exhibit generally low quality factors and hence low-bandwidth capabilities. To counter this effect, active filters can be used to enhance the quality factor of the circuit, but an increase in noise factor (NF), non-linearities, and direct current (DC) power consumption are exhibited. RF (on-chip) filters can also be implemented as digital or analogue filters.

Examples of passive filters include inductor-capacitor (LC) configurations, RF-micro-electromechanical systems (RF-MEMS), and electro-acoustic filters. LC filter configurations are the most generally used filters, however, at higher frequencies the bandwidth of the filter depends on the Q-factor of the inductor and capacitor, which could be a limiting factor depending on the technology process. Several new methods are being investigated to improve the quality of the passive components, such as the works presented in [**43**], [**44**], and [**45**]. RF-MEMS filters can be implemented on-chip as they have good linearity, low-power consumption, and low losses. RF-MEMS filters do, however, suffer from high thermal-mechanical noise due to *Brownian* motion [**46**], resulting in additional noise at the output of these circuits. A study on the linearity of RF-MEMS (tuneable) filters are done in [**47**] by using the pole-perturbation approach. Acoustic wave filters employ an acoustic component, not mounted on integrated level, and is not considered for this research application.

The following section is an introduction to antenna theory, with specific reference to equations used to design an equivalent circuit model used in this research. Important considerations such as the directivity and radiation intensity, definition-of-field regions, the gain and efficiency of an antenna, as well as the impedance and aperture characteristics of antennas are described here.

2.3 ANTENNA THEORY

Any electrical device that can convert electric currents into propagating radio waves can be classified as an antenna. Antennas form the basis of any radio transceiver, and are responsible for radiating the electric signal at a specified frequency. Antennas are used in radio-broadcasting, cellular telephones, two-way radios, radar systems, radio-frequency identification (RFID) tags, wireless computer networks (such as Bluetooth), satellite communications (for example global-positioning satellites (GPS)), and many other applications. Antennas generally fall into two categories namely; omni-directional antennas that radiate in all directions (dipole antennas), and directional antennas that radiate in a specified direction (horn antennas). Dipole antennas are relatively simple and inexpensive to construct, and can be considered the most popular type of antenna implementation in general applications. To add directivity (and gain) to a dipole antenna, more complex antennas (such as phased arrays) can be used. This section describes the performance parameters considered in general antenna design.

2.3.1 Introduction

The directional characteristics, the gain of an antenna, and the resonant frequency are considered the focal design considerations in antenna design. These parameters determine the possible types of antennas that can be used in the application, and the physical size of the antenna. The gain and efficiency are aspects that relate to the type of antenna and are to be determined as performance characteristics. Also considered here, is the impedance of the antenna (used in determining the equivalent electronic circuit) and the effective aperture that expresses the amount of power delivered to the terminal of the antenna, related to its effective area. A three-dimensional graph that plots the relative field strength in the radiating angles is also briefly discussed (as informative section to categorize the antenna pattern). The above-mentioned performance characteristics of an antenna are described in the following sections.

Table 2.5 summarizes equations used in antenna characterization, and each term is described in further detail in the following section. Undefined variables are referenced below Table 2.5.

Table 2.5: Antenna characterization parameters.

Parameter	**Equation**
Maximum directivity	$D_{max} = D_0 = \frac{4\pi U_{max}}{P_{rad}}$
Inner boundary of far-field region (outer boundary is infinity)	$R = 2D^2/\lambda$
Isotropically radiated gain	$G = 4\pi \frac{U}{P_{in}}$
Antenna efficiency	$\eta = \frac{R_r}{R_r + R_L}$
Effective aperture	$A_{em} = \frac{\lambda^2}{4\pi} D_0$
Radiation resistance	$R_r = \frac{2P_{rad}}{\lvert I_0\rvert^2}$
Electric field	$\lvert E\rvert = \sqrt{\frac{\eta \times P_r(d)}{A_{em}}}$

To determine the maximum directivity (D_{max}) in Table 2.5, the maximum radiation intensity (U_{max}) in W/unit solid angle, and the total radiated power (P_{rad}) in Watts are required. In the equation for the isotropically radiated gain, P_{in} is the power (in Watts) accepted (received) by the antenna. The current through the radiating structures is given by I_0. In the equation for the electric field, η is the intrinsic impedance of free-space (377 Ω), and $P_r(d)$ is the received power specified in Watts.

2.3.2 Directivity and radiation intensity

The directivity of an antenna is defined by [**53**] as the ratio of radiation intensity in a specified direction from the antenna to the average radiation intensity calculated in all directions around the same antenna, and is considered an important figure of merit in antenna design. This unit specifies that the maximum directivity is radiated in a specific direction and compared to the average directivity of an isotropic antenna, which radiates equally in all directions (Table 2.5).

Measurements of antenna electric and magnetic field propagation are done in specific field regions considered at a given distance from the antenna. These regions are usually divided into three categories namely the reactive near-field, radiating near-field (or *Fresnel* zone), and the far-field (*Fraunhofer*) regions. The boundaries that separate these regions are not unique, but there exist some techniques that identify these regions, discussed in the following section.

2.3.3 Field regions

Firstly, the reactive near-field region lies immediately in the area surrounding the antenna where the reactive field dominates. Strong inductive and capacitive effects occur from the currents and charges in the radiating source, and this behaviour is very different from effects in other regions. Absorption of radiated power in this region can be fed back to the transmitter and increase the impedance of the antenna that the transmitter sees, resulting in apparent mismatched conditions. The outer boundary of this region can be defined at a distance (R) from the radiating source, and is approximately $R < 0.62\sqrt{D^3/\lambda}$ from the antenna surface, where D is the largest physical dimension of the antenna, and λ is the wavelength.

The radiating near-field region (*Fresnel* zone [**54**]) lies between the reactive near-field and the far-field region. In this region, radiation fields predominate and the angular field distribution is dependent on the distance from the antenna. From [**53**], it is stated that if the antenna has a maximum physical dimension that is not large compared to the wavelength, this region may not exist. For the case where the maximum dimension of the antenna is large compared to the wavelength, the inner boundary of this region lies at a distance of $R \geq 0.62\sqrt{D^3/\lambda}$ and the outer boundary at a distance $R < 2D^2/\lambda$.

The far-field region (refer to Table 2.5) (*Fraunhofer*) is where the angular field distribution is essentially independent of the distance from the antenna. The field components are therefore essentially transverse and the angular distribution is independent of the radial distance where the measurements are made. In the far-field region, the total energy per unit area at a distance R is approximately proportional to $1/R^2$. Now that the field-regions are defined, the gain and the efficiency of the antenna are discussed. For this thesis, measurements are conducted in the *Fraunhofer* region.

2.3.4 Antenna gain

The gain (G) of the transmitting and receiving antenna is the ratio of power received through free-space at distance d, $P_r(d)$, and power received by the antenna transmission lines, P_{in}, such that the equation for the antenna gain is given as

$$G = 10\log_{10}\frac{P_r(d)}{P_{in}}. \tag{2.18}$$

The radiation intensity corresponding to the isotropically radiated power is equal to the power (in Watts) accepted by the antenna divided by 4π (refer to Table 2.5). The impedance and effective aperture is described in more detail in the following section. The impedance characteristics of the antenna are paramount in determining the electronic equivalent model, as proposed in this thesis. The effective aperture of the antenna is used to determine the directivity and hence the radiation patterns (and intensity) of the source.

2.3.5 Impedance, efficiency, and aperture

The input impedance of a radiating source is defined by [**53**] as the impedance presented by an antenna at its terminals or the ratio of the voltage to current at a pair of terminals. The impedance of the antenna (Z_A in Ω), with no load attached, is defined as

$$Z_A = R_A + jX_A \tag{2.19}$$

where R_A is the real impedance in Ω at the antenna terminals, and X_A is the complex antenna reactance also measured in Ω. The real impedance consists of two components, such that

$$R_A = R_r + R_L \tag{2.20}$$

where R_r is the radiation resistance of the antenna and R_L is the load loss resistance (both measured in Ω). Losses at the input terminals of the antenna and within the structure are taken into account to determine the efficiency of the antenna. These losses can occur due to reflections caused as a result of mismatches between the transmission line and the antenna. Conduction and dielectric losses (I^2R) also influence the efficiency of the antenna. The efficiency (η) of the antenna can be determined by the real impedance and the load loss resistance such that its relationship determines the antenna efficiency (refer to Table 2.5).

To describe the amount of power that an antenna can absorb if a wave impinges on it, the effective area, or effective aperture, of the antenna is defined. This area is defined as a ratio of the available power at the receiving terminals of the receiving antenna, to the power flux density of the incident wave. In general, the maximum effective aperture (A_{em}) of *any* antenna is directly related to its maximum directivity (refer to Table 2.5).

To determine and visually represent the electric field (E) as a result of the transmitted power, the equation is derived in [**21**] to relate the electric field to the distance travelled by the signal, and the effective aperture of the antenna (refer to Table 2.5).

The parameters discussed in sections 2.3.1 to 2.3.5 can be used to completely define and characterize the type of antenna and its radiating properties, important when investigating its electronic equivalent model. The equivalent model is, however, based on electronic circuit theory as well, and combining these two fields of research, at specific frequencies, is beneficial in analysing the antenna without having to physically create it.

This thesis proposes the use of a dipole antenna to prove the hypothesis, as dipole antennas are the driven element behind many other types of antennas such as the Yagi antenna, and the equations can be extended for more complex antennas in future works. These antennas are also compatible with many CMOS technologies. Antennas capable of operating in the 60 GHz frequency band have been introduced in [**55**], [**56**], [**57**], [**58**], [**59**], [**60**], and [**61**] with its performance parameters summarized in Table 2.6.

Table 2.6: Performance parameters of antennas operating in the 60 GHz band.

Ref.	**Type of antenna**	**Technology node**	**Simulated S_{11} at 60 GHz [dB]**	**Measured S_{11} at 60 GHz [dB]**	**Gain [dBi]**	**Efficiency (%)**
[55]	Post-wall waveguide and microstrip-line layers	CMOS	-20	-6	6	-
[56]	Rectangular Yagi-Uda patch	-	-32	-22	-	-
[57]	On-chip patch antenna	130 nm CMOS	-28	-15	-	-
[58]	Coplanar waveguide patch antenna	CMOS	-20	-15	6 - 7	91 estimated
[59]	Antenna-in-package (AiP) ceramic grid array	LTCC	-9.5	-7.7	9	94 estimated
[60]	Self-shielded microstrip Yagi-Uda	Teflon	-10	-15	12 - 14	-
[61]	Coplanar waveguide-fed dipole	Wafer transfer technology	-13	-11	5.1	-
[This work]	Rectangular dipole on silicon substrate	130 nm CMOS	-12.8	-		-

From Table 2.6 it is evident that antennas operating in the 60 GHz band of interest are capable of obtaining reflection coefficients of less than -10 dB (with the exception of [55] where measured and simulated results do not correspond at 60 GHz) and with gain factors of up to 14 dBi in the case of [**60**]. Some design possibilities for dipole modelling are described in the following section.

2.4 DIPOLE MODELLING

The input impedance and radiation characteristics (through full-wave analysis) are used to study an antenna [**62**]. Extraction of the equivalent circuit based on the input impedance of the antenna is used to analyse the antenna operation using electronic circuit theory (assuming no coupling between the antenna and the circuit it is connected to). The objective is to obtain the equivalent circuit of the structure and determine its multivariable components functions with the physical dimensions as their variables [**63**]. Characterization parameters of an antenna include losses due to coupling between the antenna and the substrate, resistive (ohmic) losses, and capacitive losses between the antenna and nearby conductive structures or elements. Parameters such as the input impedance, losses, radiation patterns, and radiation efficiency can be predicted using electromagnetic solvers, and the results are used in constructing the equivalent circuit [**12**].

The modelling of large bandwidth antennas presents several challenges [**12**]. Requirements of broad impedance bandwidth, high radiation efficiency, small size, omni-directional radiation patterns, and a broad radiation pattern bandwidth are some challenges observed in the design of these antennas. For constant radiation patterns over a broad-frequency range, electrically small antennas (always operates below the second resonance [**64**]) present poor impedance matching due to large quality factors. The converse is also true, where antennas operating close to the first resonance have good impedance matching but a weak radiation pattern (as a function of frequency), and methodologies of modelling these circuits are presented [**12**]. Operating the antenna well above the first resonance frequency presents a good impedance match but the radiation pattern changes rapidly with frequency [**12**]. To achieve simultaneous impedance matching over a large bandwidth and constant radiation patterns, the antenna must be shaped *around* the first resonance frequency.

The *Friis* transmission equation in large bandwidth systems cannot take into account waveform dispersion caused by the antenna itself, and single-value parameters such as the power gain, reflection coefficient, and input impedance become inaccurate when using the transmission equation (sufficient for narrow bandwidth systems). The phase responses of an antenna are constant and can be compensated for in narrow bandwidth systems, but cannot be ignored in large bandwidth systems due to its frequency dependence [**12**].

Extraction of circuit parameters of large bandwidth systems can be achieved by modelling the antenna circuit as a parallel RLC circuit, known as the degenerated (for small electrical antennas) *Foster canonical form*. This representation of electrical antennas in electrical circuit form has been used to model narrow-bandwidth dipoles [**64**] as well as wide-bandwidth dipoles [**12**]. The *Foster canonical form* is applicable for magnetic (for example loop antennas) and electric antennas (monopoles and dipoles), and the differences in circuit topology is outlined through in Figure 2.10. Omni-directional small antennas for ultra-wideband (UWB) applications are also modelled using the *Foster canonical form* in [**12**] and the radiated far-fields are estimated from the voltages across the radiation resistor in the network. In [**65**] a broadband equivalent circuit for a straight-line dipole antenna (SLDA) and meandered-line dipole antenna (MLDA) represents the electrical model in the *Foster canonical form* is verified through simulation in EMCoS Antenna Vlab[7] software. In [**62**] it is mentioned that combining several narrow bandwidth antenna models to form a wide bandwidth model is difficult and impractical since interpolation of dipole parameters is not applicable and presents a method to optimize this procedure.

Due to the limitations of the *Friis* transmission equation for wide-bandwidth operation, the frequency and angle-dependent transfer functions are determined by directly simulating the two-port *S*-parameters, the transmitting antenna as briefly mentioned in [**12**]. A preliminary circuit model for the electrical antenna (dipole) is created using a first-order *Foster canonical form* circuit model, and this model is then expanded (improved) to fit the wideband EM transfer functions of the dipole. A brief description of the *Foster canonical form* is given in section 2.4.1.

2.4.1 The foster canonical form

Dipole models can be represented by the *Foster canonical form* for electrical and magnetic antennas. Electrical antennas have a predominantly larger electric field distribution in the near

---

[7] EMCoS Antenna VLab is simulation software suited for antenna calculations (www.emcos.com/AVL)

field, whereas the magnetic radiation in the near field dominates for magnetic antennas. The radiation pattern in the far field is similar for electrical and magnetic antennas. Monopoles, dipoles, and stub antennas are examples of electrical antennas, whereas loop antennas fall under the category of magnetic antennas. It is possible for the near-field radiation to exhibit a combination of electrical and magnetic properties, as seen with helix antennas. Magnetic antennas can become complex structures and EM modelling of these structures quickly becomes mathematically cumbersome. The electrical antenna structure gives equal ability to accurately model and predict the behaviour of the radiated signal, without adding complexity in the antenna design. The *Foster canonical form* for the electrical antenna is given in Figure 2.10.

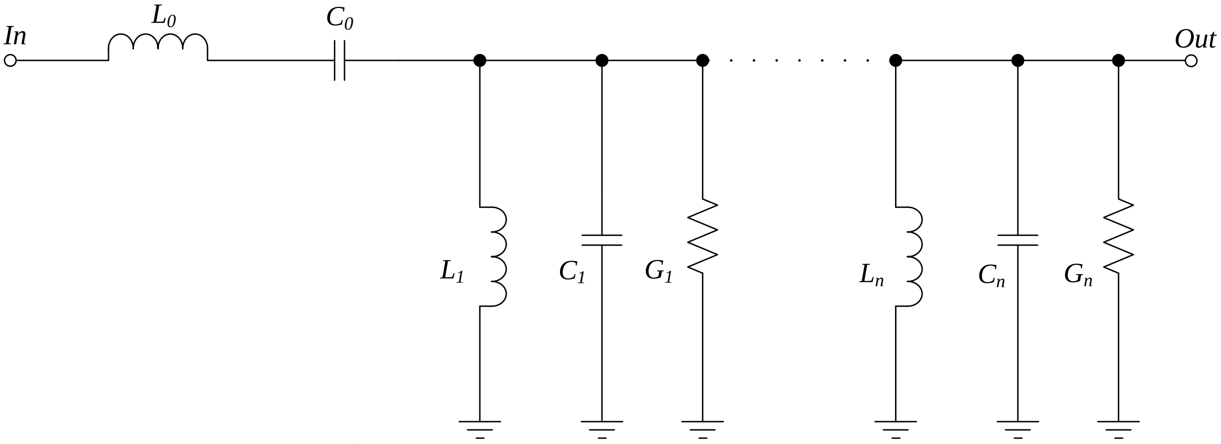

Figure 2.10. Foster canonical form for an electrical antenna **[**12**]** (© [2012] IEEE).

From Figure 2.10 L_n represents the inductive components for each resonant circuit in the electrical antenna equivalent circuit (where L_0 and C_0 represents the high- and low-frequency inductive and capacitive poles respectively), C_n represents the capacitive components, and G_n the resistive components in each resonant circuit. n can be any value and determines the order the transfer function, where complexity of the transfer function increases with increasing n. The resonant frequencies of an antenna are modelled through the RLC tanks. The specified bandwidth determines the amount of RLC tanks. Assuming the radiation pattern is constant at an operation frequency, then the antenna is operated below the second resonance frequency and the *Foster canonical form* in Figure 2.10 is reduced to only having one RLC tank circuit.

Since reactive components do not dissipate power, the instantaneous power radiated from the antenna is equal to the power dissipated in the resistive component (G_1). The transfer function for the single RLC tank circuit, $H(j\omega)$, can be derived by applying the *Laplace* transform, using *Kirchhoff's* voltage law around the circuit loop, collecting terms and rewriting the circuit equation, the system frequency response $H(s)$, is derived as

$$H(s) = sL_0 + \frac{1}{sC_0} + \left(sL_1 \parallel \frac{1}{sC_1} \parallel G_1\right) \tag{2.21}$$

Multiplying by the common denominator and collecting terms, substituting the complex number $s = \sigma + j\omega$, and applying the theorems for division of complex numbers, it follows (refer to Appendix A) that the imaginary part of the transfer function can be expressed as

$$H(j\omega)_{Im} = \frac{-\omega C_0 G_1\left(1-\omega^2 C_1 L_1\right)\times G_1\left(\omega^2 C_0 L_0\left(\omega^2 C_1 L_1 - 1\right) - \omega^2 L_1 (C_0 + C_1) + 1\right) + \omega^3 C_0 L_1^2 (1 - \omega^2 C_0 L_0)}{(\omega G_1 C_0 (1 - \omega^2 C_1 L_1))^2 + (\omega^2 C_0 L_1)^2} \tag{2.22}$$

In order to determine the exact component values for the imaginary transfer function in (2.22), it is necessary to differentiate the transfer function with respect to frequency. First principle mathematical calculations (such as setting the differential, or slope, of the transfer function equal to zero) can be used to completely define the transfer function of the circuit. The complexity of the calculations, however, reduces the practicality of this approach, as the amount of computation time becomes cumbersome. An analytical approach, combined with circuit theory and careful assumptions is used in this thesis to derive an accurate equivalent circuit, as a *Foster canonical form* first approach, and improving on this model to better fit the wideband transfer function as presented by the dipole EM simulations. This procedure is derived from adapting the principles outlined in [**12**] that provides insight into the *Foster canonical form* by dividing circuit operation into frequency ranges (low, high, and resonant). Techniques presented by [**66**] to electrically model an inductively coupled capacitive-loaded monopole antenna based on substrate and feeding pins are adapted as these techniques are verified in a circuit simulator (Advanced Design Systems 2009). Electrical circuit magnitudes are related to electric field magnitudes by [**12**]

$$E(\theta, \phi, r, t) = \frac{1}{r}\sqrt{\frac{\eta_0}{\beta R_{rad}}}\,\alpha(\theta, \phi) V_{rad}\left(t - \frac{r}{c}\right) \tag{2.23}$$

where $E(\theta,\phi,r,t)$ is the far-field electric field propagating in the direction (θ,ϕ), η_0 is the free-space characteristic impedance (377 Ω), β is a constant and $\alpha(\theta,\phi)$ is a direction-dependent scaling factor, R_{rad} is the radiating resistor (load) in the electrical circuit (measured in Ω) with voltage V_{rad} across its terminals, r is the observation distance from the antenna (in m), c is the speed of light (in m.s^{-1}), and from this equation it is possible to determine circuit parameters in the respective operating frequency regimes (refer to Chapter 4). Once the initial component values for the equivalent circuit is determined, an iterative process constructed in MATLAB (refer to Appendix A) is used to minimize the error (E) function given by

$$E = \frac{1}{2K}\sum_{i=1}^{K}\left[\left|S_{11}^{EM} - S_{11}^{cir}\right| + \left|S_{21}^{EM} - S_{21}^{cir}\right|\right]^2 \qquad (2.24)$$

where K is the amount of sampled frequencies in the band, S_{11}^{EM} and S_{21}^{EM} are the reflection coefficients and forward gain of the EM simulations respectively, and where S_{11}^{cir} and S_{21}^{cir} are the equivalent circuit reflection coefficients and forward gain, respectively. If the error is within a predefined limit (to reduce computational time) the equivalent circuit component values can be adjusted for optimum results.

2.5 MATCHING NETWORKS

The proposed research attains a modular approach to all sub-circuits to allow for future improvements and additional implementations. In order to successfully achieve this modular approach, it is important to discuss proper matching techniques between subsystems and equivalent models as described in sections 2.2 to 2.4. For minimal power loss between these circuits, the following approach to defining and implementing matching networks is proposed. Two- and three-components matching networks, micrsotrip-line, and stub-line matching networks are discussed, and reference to the *Smith* Chart is given.

2.5.1 Matching network types

To achieve maximum real-power to complex load impedances, the delivered source impedance should be equally (matched) to the complex conjugate of the load impedance. Two- and three-component matching networks offer easy and intuitive implementations for impedance matching. As circuit wavelengths are reducing and parasitic elements from lumped elements increase, microstrip-line matching networks are increasing in popularity. Stub-line matching networks remove all lumped elements and cancel the reactive part of the presented impedance depending on the length of the stub.

Matching networks are not only used to match complex source and load impedances. It also contributes to maximizing power-handling capabilities, linearizing the frequency response, and to minimize the noise added to the existing circuit. The impedance of the load (as in the case with transmitting antennas) can vary as a result of configuration, environmental characteristics, and operating frequency. Ensuring optimal power flow under all of these varying conditions is crucial and is achieved with matching networks.

The simplicity of a two-component matching network [**67**] allows that a unique solution can be found, but limits the capabilities of the network when designing not only for impedance matching (additional criteria could include bandwidth requirements). Forbidden regions exist for these networks and create conditions where matching to a 50 Ω source impedance is not possible. By including a third component an additional degree of freedom is introduced to the circuit. Through this, it is possible to also control (design for) a loaded quality factor (narrower bandwidth requirements), parasitic effects, or harmonic rejection which adds flexibility and additional design criteria. The number of possible solutions to match load and source impedances with these networks is not limited to one, making the networks difficult to tune over a range of frequencies.

If component values become a limitation for on-chip matching networks, and parasitic effects increase the complexity of these designs to the extent that its use becomes impractical, microstrip-line matching [**68**] can replace the use of lumped elements (assuming the wavelength is sufficiently small compared to circuit dimensions). The tuning capabilities of these types of networks (through capacitive tuning and component locations) ensure popularity of these circuits in prototyping. Single-stub matching networks eliminate the use of lumped elements, but placement at a variable distance from the load can be difficult to achieve in practice, confining its use to fixed networks, and matching is only done at one frequency. Double-stub matching networks remove this variable distance problem. These networks are often replaced in implemented designs with more compact and broadband applications. In CMOS power amplifier design, short-circuited, LC, on-chip stub-matching networks are preferred due to its low-loss [**69**], good noise performance (NF of 5.5 dB at 60 GHz reported in [**70**]), and attenuation of out-of-band components [**71**], and are generally used for input *and* output stage matching. Performance of matching networks is characterized by parameters such as the load reflection coefficient, nodal quality factor, bandwidth, and the standing wave ratio. The following section presents passive device modelling and essential design equations of these passive elements (with specific reference to elements used for this thesis).

2.6 PASSIVE DEVICE MODELLING

Passive elements are equally dependent on physical attributes and placement as it is to material properties, which is complex and expensive to alter to limit the addition of parasitic components, compared to changing its dimensional properties. Passive elements described in this section are transmission lines, capacitors, resistors, bonding pads, and interconnect lines.

2.6.1 Transmission lines

The small wavelength of mm-wave frequencies makes the use of transmission lines for on-chip designs suitable and practical. The quality factor of transmission lines are relatively high (compared to spiral inductors) as the radiation pattern surrounding the transmission line relates to that of a dipole, coupling less energy to the substrate. Quality factors of 19.06 at 60 GHz for transmission lines using compatible back-side inductively coupled-plasma deep-trench technology is achieved in [**16**]. In [**72**] stacked metal layers can achieve quality factors of up to 15 at 50 GHz for a designed inductance value of 400 pH. A well-defined ground-return path reduces magnetic and electric field coupling to adjacent structures. Given the quasi-transverse electromagnetic (quasi-TEM) mode of propagation, transmission lines are very scalable in length and capable of realizing accurate values of small reactances. Table 1.3 and Table 1.4 in Chapter 1: list currently available transmission line models for mm-wave frequencies. For convenience, the references referred to in the abovementioned tables are [**15**], [**16**], [**17**], [**18**], [**19**], and [**20**]. Figure 2.11 is used to characterize the frequency-dependent equivalent circuit model of a transmission line, based on the *RLGC*-distributed model.

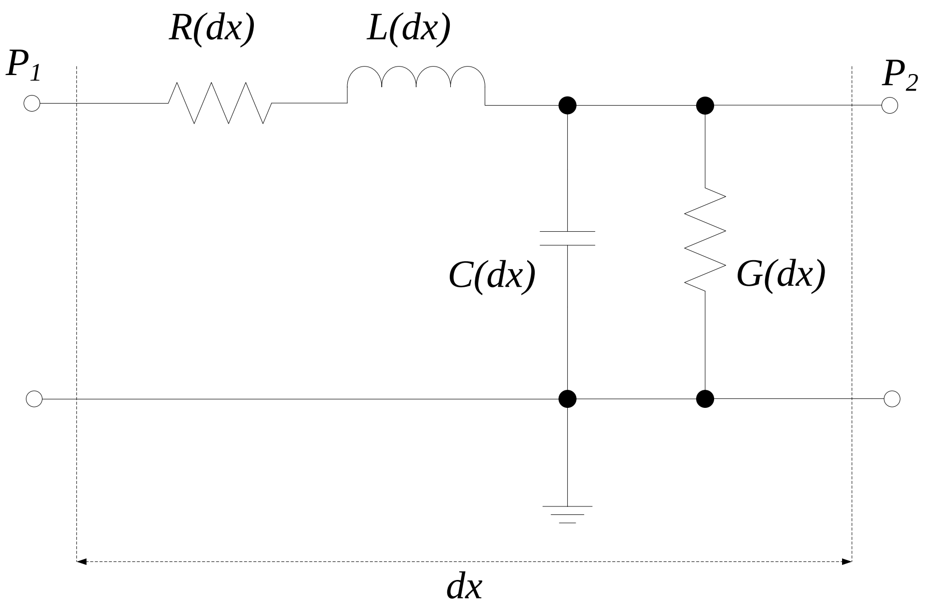

Figure 2.11: *RLGC*-distributed equivalent circuit model of a transmission line **[**15**]** (© [2012] IEEE).

From Figure 2.11 the parameter $R(dx)$ is the resistance per unit length dx, $L(dx)$ the inductance and $C(dx)$ the capacitance per unit length, and $G(dx)$ is the conductance (usually due to substrate and dielectric leakage losses) per unit length. The characteristic impedance (Z_0) of the equivalent model in Figure 2.11 is *not* a function of the propagating waveform, position on the line, or time.

If the transmission line is lossless $(R = G = 0)$ then the characteristic impedance is not a function of frequency. The quality factor is defined by the attenuation constant α, in Np/m, and the phase constant, β, in rad/m.

Two options of implementing transmission lines on BiCMOS technology are microstrip transmission lines and coplanar waveguides (CPW). Microstrip-lines on silicon are typically implemented using the top-layer metal line as the signal line, and the bottom-layer metal as the ground plane. These transmission lines are popular due to its ease of implementation and large range of applications. A drawback of using microstrip-lines on silicon technologies is the close proximity of the ground plane to the signal line which yields a small distributed inductance, degrading the inductive quality factor, Q_L. The use of a CPW allows the implementation of one signal line surrounded by two ground planes (on the same metal layer). The signal line width controls the conductor losses, and the spacing between the signal line and the ground planes controls the characteristic impedance and the trade-off between Q_L and Q_C.

CPWs are preferred above microstrip-lines when designing amplifiers and matching networks due to its higher Q_L values. In [**73**] a shielded CPW with quality factor of 42 at 60 GHz is presented, with low attenuation constant of 0.49 dB/mm. It is directly compared to a similar microstrip-line transmission line only achieving a quality factor of 20 at 60 GHz, with similar attenuation at 0.5 dB/mm. These high quality factors were achieved through identifying *eddy* current losses in the patterned shield, and hence optimizing the structures. Using an underpass lower metal level below a CPW can suppress the unwanted *odd* parasitic propagation mode in CPWs [**74**]. Variations of CPW structures and microstrip-line transmission lines include micro-coplanar striplines, CPW with ground plane, shielded CPW, asymmetric CPW, coplanar strips, asymmetrical coplanar strips, three coplanar strips, three coplanar strips with ground, covered CPW, covered CPW with ground plane, microstrip-line with truncated ground plane and dielectric, embedded microstrip-line, nonhomogeneous dielectric embedded microstrip-line, shielded microstrip-line, edge-compensated microstrip-line (ECM line), and covered microstrip-lines [**75**]. Although many variations even exist apart from the abovementioned, it is not in the scope of this research to investigate the properties of each variation. The standard model library microstrip-lines provided by the 130 nm process are used in this thesis.

Following transmission line analysis, a brief discussion on capacitors as passive elements is presented in the following section, again with reference to physical dimensions and design equations.

2.6.2 Capacitors

In general design practice, in mm-wave circuits lumped capacitors are typically used in alternating current (AC) coupling and to provide for DC bypass, whereas transmission lines are used to realize capacitors in matching networks and resonators. Modelling of lumped capacitors is important as these capacitors reside within the signal path. Ideally, any capacitor should have infinite impedance at DC and zero impedance at the frequency of interest, but this is rarely the case and therefore careful modelling is paramount.

Metal-oxide-metal (MOM) capacitors are parallel-fingered capacitor structures used as coupling capacitors in mm-wave circuits. These structures are relatively easy to implement in BiCMOS processes due to the possible high-packing density of metal layers in these processes. In order to decrease the resistance and increasing the quality factor, each parallel finger comprises of all metal layers stacked on top of each other and connected by using the maximum number of vias possible to take advantage of the additional via-to-via capacitance. A large number of small fingers or a small number of large fingers can be used to realize the desired capacitance. Smaller fingers have a lower resistance and inductance, but suffer from larger lead parasitic effects, whereas larger fingers have higher resistance and inductance, but present a smaller lead parasitic element. MOM capacitors are generally more cost-effective compared to metal-insulator-metal (MIM) capacitors with its thing high-K dielectric, but depending on the application and the size of the capacitor, MIM may be a more viable option in circuit design.

Large DC bypass capacitors have one port permanently connected to the circuit ground, usually the bottom plate of the capacitor to create a low inductance path towards ground and increases the self-resonance frequency when used in mm-wave circuits where a high capacitance value is required.

Extending the use of resonator circuit capacitors to voltage controlled oscillator (VCO) circuits, the use of variable capacitors (varactors) can be used. Such a component would also allow for a variable (tuneable) filter structure. Varying the capacitance of a varactor also influences the quality factor. As with all on-chip passive components, the quality factor is inversely proportional to the operating frequency. MOS varactors are readily used as the tuning voltage is applied to the gate-source input (V_{GS}) of the MOS varactor, resulting in a quality factor of

$$Q = \frac{\mu(V_{GS} - V_T)}{L^2} \tag{2.25}$$

where μ is the mobility, V_T the threshold voltage, and L the length of the fingers. A structure that is generally used is a pMOS transistor with its drain, source, and bulk nodes connected to for a single node of the capacitor, denoted $D = S = B$. This structure can operate in the accumulation, depletion, and inversion mode. Another possible structure is the inversion-mode MOS (I-MOS) capacitor, with its drain and source connected to from one node of the capacitor, while the poly-silicon gate forms the other node. The bulk of this structure is connected to the supply voltage, V_{DD}. This device can only operate in inversion. The C-V characteristic of this structure is non-linear and near-monotonic, but with a sharp transition from its minimum capacitance (C_{min}) to its maximum value (C_{max}). MOS varactors can also be designed to operate in accumulation mode (A-MOS) by replacing p-type diffusions of the drain and source with n-type regions, resulting in very large C_{min} to C_{max} ratios [**76**].

This thesis makes use of coupling capacitors, lumped capacitors, and varactors in the design of the circuit proposed to prove the hypothesis. The abovementioned models and equations aid in determining important variables and parameters of these components to verify correct implementation and operation. The following section describes passive resistors on integrated level.

2.6.3 Resistors

On-chip passive resistor values are calculated by determining the sheet resistivity of the material used to create the resistor. The sheet resistance accounts for the currents flowing along the plane of the sheet, as opposed to the perpendicular flow of currents, and considers the thin film (resistive material) as a two dimensional system. Resistance (R) of a three-dimensional conductor is given by

$$R = \rho \frac{L}{\pi W \delta} \tag{2.26}$$

where ρ is the resistivity of the sheet material, L the length and W the width of the sheet, and δ is the skin depth. The use of bonding pads to account for on-wafer probing measurements of the prototype IC adds a considerable amount of capacitance to the input and output of the circuit, and it is paramount to include these models in the circuit design and ensure that its effects are analysed and accounted for throughout simulated and measured results. The following section briefly describes bonding pads when used on ICs.

2.6.4 Bonding pads

Bonding pads are essential large square shape of predefined metal layers stacked on top of each other to allow for on-wafer probing measurement. This stack of metals induces a capacitance that needs to be accounted for during the simulation stages, to ensure accurate measurements. Bonding pads capacitance per unit area is process-specific and measured in oxide area capacitance for the amount of metal layer, with unit fF/µm^2. The oxide fringe capacitance unit around the fringes of the bonding pads has units fF/µm. The bottom metal layer of a bonding pad should always be grounded to avoid floating concerns.

2.6.5 Interconnect lines

Degraded interconnect performance as a result of the aspect ratio to component (like transmission lines) sizes, limits the performance, packaging, and yield of ICs. With scaling, interconnect delays increase and limit the length of global routing, and increased crosstalk is introduced in the circuit. Techniques have been developed in [**80**] to integrate transmitting or receiving chips operating at 60 GHz using flip-chip antenna-in-package technology using standard organic circuit boards to achieve data rates of 5.3 Gbps while retaining return losses and antenna gain of 10 dB and 5 dBi respectively, without severe loss in interconnect attenuation. An easily implementable and cost-effective technique for high density broadband monolithic microwave ICs (MMICs), termed silicon-metal-polyimide (SIMPOL), has been introduced in [**81**] to limit crosstalk and improve insertion loss (0.62 dB/mm) up to 30 GHz (which is extended to > 50 GHz in [**82**]). Some of the techniques introduced in [**81**], such as placement of interconnect lines with respect to vias, has been adapted in this thesis.

2.7 CONCLUSION

The research nomenclature required to prove the research hypothesis (refer to section 1.2) is introduced in this chapter and supporting references from current literature is supplied to compare the contribution of this thesis to the current body of knowledge. The following chapter is focused on the methodology followed to implement the different phases of research (modelling, simulation, and measurement) and outlines these phases with its supporting technical aspects.

CHAPTER 3: RESEARCH METHODOLOGY

3. CHAPTER OVERVIEW

The literature review presented in Chapter 2 investigates and researches attenuation models at mm-wave frequencies, passive device modelling (including antenna modelling and the design of matching networks) and electronic filter design. The nature of this research requires analysis of the research hypothesis (refer to section 1.2) on theoretical, simulated, and measured levels where the lack of integration could result in fragmentation, detrimental in formulating conclusions.

An outline of the proposed research hypothesis is given in section 1.2 with specific reference to Figure 1.1, and this chapter aims to expand on some of these considerations. Each phase is accomplished, or documented; using computer software and the chosen technical package for these phases is briefly presented. Measured results rely on specialized equipment that needs to be set up for the appropriate measurements depending on the application. Reference to the equipment required and the set-up procedures are discussed in this chapter.

The process that was selected for the implementation is the 130 nm IBM 8HP process. Due to a non-disclosure agreement (NDA) between the author and the foundry through the University of Pretoria, certain process parameters have been excluded from this thesis. The technology node was made available through the MOSIS Educational Program (MEP) that offered multi-project wafer (MPW) runs for the 130 nm IBM 8HP process. The process offers 5 metal layers with substrate resistivity of less than 20 Ω/cm. Modelled device structures of transmission lines, bond pads, RF interconnect lines, and distributed passive components are supplied. The maximum supply voltage for the IBM 8HP process is 1.5 V. Some of the device characteristics are given in the following section.

3.1 DEVICE SPECIFICATIONS

The devices used for this thesis are briefly discussed in this section, with reference to some of the most important specifications and considerations. The metal layers are given as M1, M2, and MQ, whereas the aluminium layers LY and AM are top-most layer in the structure. The QY layer is used in designing of capacitors.

3.1.1 Transmission lines

The 130 nm IBM 8HP process supports transmission lines consisting of an top metal layer (AM layer) over a DT lattice. The width of the transmission line can vary up to 25 µm. The length can vary up to 1500 µm. If a longer transmission line is needed (larger inductance with narrowest line width), multiple lines can be connected in series. A good practice is not to exceed 250 µm, and use series-connected transmission lines. The specifications for the transmission line are given in Table 3.1.

Table 3.1: 130 nm IBM 8HP transmission line specifications.

Specification	Value	Unit
Inductance	up to 2.20	nH
Oxide area capacitance	*removed (NDA)	fF/µm^2
Oxide fringe capacitance	*removed (NDA)	fF/µm
Supported lengths	up to 1500	µm
Supported widths	up to 25	µm

From Table 3.1 the inductance values for the 130 nm IBM 8HP technology node transmission line maximum value is 2.20 nH at (supported) length of 1500 µm. Proper connection to the ground node, connected to an ideal AC source, of the transmission line during simulation to reduce stray inductance. An important consideration during the layout of the transmission line is to ensure that all substrate contacts are placed at a minimum distance from the transmission line.

3.1.2 Capacitors

The 130 nm IBM 8HP process technology provides three types of capacitors. The first is a MOS varactor, consisting of a thick or thin oxide NFET-in-Nwell MOS capacitor. Also provided is a hyper abrupt junction diode varactor (HA varactor), and the third option is the single aluminium MIM capacitor. The area capacitances of the three available capacitors are given in Table 3.2

Table 3.2: Area capacitances of 130 nm IBM 8HP capacitors.

Model	**Area capacitance [fF/µm^2]**	**Bias voltage [V]**
Thin oxide MOS varactor	*removed (NDA)	1.2
Thick oxide MOS varactor	*removed (NDA)	1.25
HA varactor	*removed (NDA)	0
MIM capacitor	*removed (NDA)	-

From Table 3.2 the MIM capacitors in the 130 nm IBM 8HP technology node is used in this research to remove any unwanted RF noise from the DC supplies that may be up-converted to noise. Since varactors and constant capacitance values are considered in this research, both options were considered and some of the capacitance specifications are listed here. The MOS varactor nominal capacitance $C_{nom}(V)$ (in fF) at 25 ^{o}C is given by

$$C_{nom}(V) = (C_A(V)LWF) + (C_L 2LF) + (C_W 2WF) + (C_F F) \tag{3.1}$$

where $C_A(V)$ is the capacitance per unit area at a specified bias voltage, C_L, C_W, and C_F are fringe capacitance terms that are functions of the channel length (L), variation in width (W), and number of individual devices connected in parallel (F).

The HA varactor nominal capacitance (in fF) at 25 ^{o}C is similarly given by

$$C_{nom}(V) = (C_A(V)LWN) + \left(C_P(V)2N(W+L)\right) \tag{3.2}$$

where $C_P(V)$ are the standard junction capacitance as a function of the applied voltage, and N is the width of the n-type subcollector implant under the structure.

The MIM capacitor has a nominal capacitance, C_{nom} in fF, value at 25 ^{o}C of

$$C_{nom} = (C_A LW) + \left(C_P 2(W+L)\right) \tag{3.3}$$

where L is the design length, and W is the design width. Both quantities are measured in μm. The MIM capacitor is susceptible to electrostatic discharge (ESD) and ESD protection should be used to avoid damage to the MIM capacitor.

The MIM capacitor model includes a calculation for the parasitic capacitance from the bottom plate of the MIM capacitor to the substrate assuming the MIM is placed over a buried sub-collector (NS) plate. This parasitic capacitance could introduce unwanted resonances at mm-wave operation. The value of this parasitic capacitance ($C_{parasitic}$) can be determined by using (3.3) and the area parasitic capacitance (C_A) and perimeter parasitic capacitance (C_P).

3.1.3 Bond pads

The 130 nm IBM 8HP process offers bond pad models that simulate the loading effect of an pad over an metal layer ground plane, as well as a layer ground plane. The specifications for the two types of bond pads are given in Table 3.3.

Table 3.3: 130 nm IBM 8HP bond pad specifications.

Model	**Oxide area capacitance [fF/μm^2]**	**Oxide fringe capacitance [fF/μm]**
Bond pad over metal	< 0.0040	< 0.0400
Bond pad over ground	< 0.0040	< 0.0400

The bond pads used in this work (over metal in Table 3.3) were specified as 100 μm × 100 μm to comply with the wafer-probing station used for on-wafer measurements.

3.1.4 Resistors

The 130 nm IBM 8HP process technology provides 4 types of resistors, namely OP P+ polysilicon resistors (opppcres), RR polysilicon resistors (oprrpres), NS diffusion resistors (nsres), and KQ BEOL resistors (kqres). The resistor model parameters specified by the technology node is given in Table 3.4.

Table 3.4: 130 nm IBM 8HP resistor model parameters.

Parameter	**Unit**	**opppcres resistor**	**oprrpres resistor**	**kqres resistor**	**nsres resistor**
Sheet resistance	Ω/□	< 400	< 2000	< 70	< 10
End resistance	Ω-μm	< 30	< 30	< 30	< 30
Poly-sheet resistance	Ω/□	-	*removed (NDA)	-	-
Minimum width	μm	0.20	0.74	5.92	2.00
Minimum length	μm	1.60	1.10	5.00	2.60
Sheet resistance tolerance	Ω/□	51.0	340	4.8	20.0
End resistance tolerance	Ω-μm	16.0	16.0	10.0	16.0

The oprrpres resistor from Table 3.4 has the highest sheet resistance and is appropriate in creating shorter length resistors. The tolerance is 20 % compared to 14 % for the opppcres resistor and 8 % for the kqres resistor (large tolerances in nsres make it less viable). The nominal resistance at 25 °C for all types of resistance can be determined by

$$R_{nom} = \left(R_S \frac{L}{W}\right) + \left(2 \frac{R_{end}}{W}\right) \tag{3.4}$$

where R_S and R_{end} are the sheet resistance and end resistance respectively, and L and W are the length and width of the resistor respectively. The nominal resistance is measured in kΩ.

The software that was chosen to implement each phase of this thesis is briefly described in the following section.

3.2 TECHNICAL PACKAGES

Each implementation phase is dependent on a technical package to aid in providing tangible results of the proposed research questions. Accuracy of these results is not only dependent on the software of choice, but also the understanding of the software, and the integrity of the models used in the software (also applicable if the models are supplied by a third party). The technical packages chosen as an aid in structuring the hypothesis and its results are given in Table 3.5.

Table 3.5: Software packages used to formulate and prove research hypothesis.

Software	Version	Functionality
MATLAB	R2010b version 7.11.0.584 (64-bit)	Mathematical computing
Cadence Virtuoso Schematic Editor	IC6.1.3.500.13	Schematic composer
Cadence Virtuoso Analog Design Environment (ADE)	IC6.1.3.500.13	SPICE-based simulator
Cadence Virtuoso Layout Editor	IC6.1.3.500.13	IC layout composer
IBM 8HP Process Development Kit	*removed (NDA)	DRC, LVS and layer density checks
CST Microwave Studio	2010 with SP3	EM simulations
Agilent Advanced Design System (ADS)	2011	Schematic composer

The software packages presented in Table 3.5 are listed with version numbers to ensure compatibility. Cadence Virtuoso was updated to version IC6.1.3.500.13 with the process design kit (PDK) version 1.2.1.0HP used to complete DRC and LVS tests. MATLAB R2010b was used for mathematical modelling and extraction of circuit transfer functions. The EM dipole was modelled and simulated in CST Microwave Studio, version 2010 with SP3 to improve stability. Agilent ADS 2011 was used to determine adjusted circuit component values from measured results in Chapter 5. A diagram that represents the technical packages used during each research phase is given in Figure 3.1.

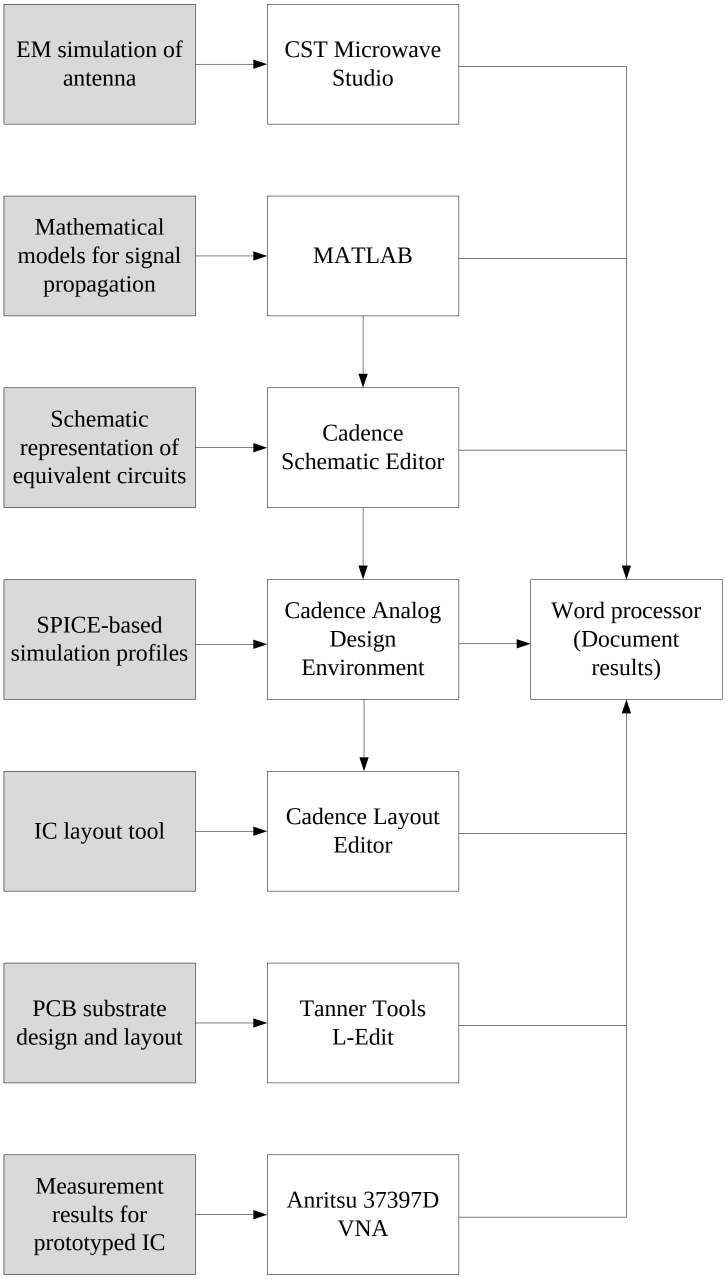

Figure 3.1: Technical packages used during each phase of the research.

In Figure 3.1 the grey blocks represent the research phases. These phases include EM simulations of the antenna in CST Microwave Studio, mathematical modelling of propagation attenuation equations in MATLAB, schematic and layout simulations using Cadence Virtuoso, and measurements of the prototype (substrate mask designed in Tanner Tools L-Edit). A description of each phase, with reference to Table 3.5 and Figure 3.1 is given in sections 3.3 to 3.8. The substrate mask is defined and described in section 3.7.

3.3 MATHEMATICAL MODELLING

Mathematical models of path-loss prediction functions were created in MATLAB to obtain a visual representation of the estimated attenuation of a 60 GHz transmission. This research made extensive use of MATLAB not only for creating path-loss prediction models, but also to create scripts (m-files) to determine first order estimations of electronic equivalent circuits using theoretical design equations. These scripts were used to get initial component values for equivalent circuits, and improvements to the accuracy of these results could then commence in the SPICE-based simulation software. Each *ideal* electronic passive circuit (filters, antenna, matching networks) was represented as a mathematical transfer function in MATLAB as a first-level verification of the design equations (refer to Appendix A). It was then compared to the SPICE results. This aided in determining optimized component values numerically, allowing scripting to obtain thousands of possible circuit structures, and determine the optimum structure.

3.4 ELECTROMAGNETIC SIMULATIONS

To improve the accuracy and integrity of the electronic simulation and measurement results, it was chosen to do an EM simulation of the transmitting and receiving antenna and not only use mathematical representations. EM-simulation profiles were designed in CST Microwave Studio, and the S-parameters were obtained to create an equivalent circuit model. The CST Microwave Studio provides specialist 3D EM simulations of high-frequency components. The behaviour of high-frequency components such as planar and multi-layer structures, antennas, filters, and couplers can be determined under various circumstances using the CST Microwave Studio. The software suite uses a finite integration technique in its transient solver to improve efficiency.

Antenna theory and design equations were adapted from [**53**] to design a (dipole) antenna operating at 60 GHz. The S-parameters were analyzed and used to determine an equivalent electronic circuit model that presents similar transfer functions compared to the EM simulation results. Brief reference to the electric field distribution is also given, but with the majority of focus on the scattering parameters and the impedance distributions. Design equations are discussed in detail in Chapter 4 and simulation results given in Chapter 5.

3.5 SCHEMATIC DESIGNS AND SPICE SIMULATIONS

The electronic circuits were represented in Cadence Virtuoso Schematic Editor and the simulation profiles (time and frequency domain) in the Virtuoso Analogue Design Environment (ADE). The Cadence circuit simulator provides RF performance simulations with S-parameter models using the 130 nm IBM 8HP PDK supplied by IBM. The simulation environment enables fast and accurate design verification, with additional functions to improve efficiency, such as its script-driven mode.

The simulation results obtained with Virtuoso ADE were compared to the mathematical models before further steps (towards layout) were undertaken. Each sub-circuit was designed separately to allow for a modular approach during integration. This approach ensured that the testing and verification phases were efficient. As each subsystem represented a single entity of the IC, comparison with the MATLAB structures also proved to be resourceful. A large number of simulation profiles, including corner analysis (worst power, worst speed, and typical mean), Monte Carlo analysis, and optimization techniques were done to improve the quality and integrity of the prototype and these results are given in Chapter 5.

The software suite ADS (refer to Table 3.5) by Agilent Technologies was used to determine the component values that resulted due to the difference in measurement results in comparison with the simulated results in Cadence Virtuoso. The *Tuning* ability in ADS was helpful in this case and provided the ability to determine possible changes in circuit component values to further investigate the changes in results. These adjusted values and an analysis on the changes are given in section 5.1.

The following section discusses the circuit layout and verification phase.

3.6 CIRCUIT LAYOUT AND VERIFICATIONS

The Cadence Virtuoso Layout Suite supports physical IC layout for digital, mixed-signal, and analogue designs on device, cell, and block level. The 130 nm IBM 8HP device libraries are used and can be directly imported from the schematic editor for easier verification. These verifications include the DRC and LVS checks, where the DRC rules are supplied by IBM. Also supplied by IBM are the layer density check rules that must pass, together with the DRC and LVS checks, before submission to the foundry was possible. Post-layout simulations could not be verified in the Cadence suite since the post-layout tool license was not included in the Cadence Academic Network EMEA[8] university software package. As a result, parasitic effects of layout structures could not be analysed before the prototyped was manufactured.

Several structures, including test structures of subsystems, and calibration structures were placed on the layout of the IC. The test structures were used to measure the results of each subsystem and compare these results with simulation, and theoretical results. This procedure ensured that if the full system did not operate as expected, that quick and efficient fault-finding was possible. Additional test points within the circuit are an alternative to the test structures, but would require additional bonding pads that could influence measurement results. Bonding pads require large areas on the IC, and present a practical challenge during implementation, as die real-estate is limited. The calibration structures are needed to calibrate the circuit with the wafer-probing equipment before attempting measurements. The calibration technique followed was the short-open-load-thru (SOLT) technique, and the layout of these structures is given in Chapter 5. The following section describes the set-up used during the measurement phase.

3.7 PCB DESIGN AND LAYOUT

The device under test (DUT) (IBM 8HP IC prototype) was designed to facilitate on-wafer probe measurements of the passive circuit structures with bonding wire connections only required for DC connections. This measurement set-up is depicted in Figure 3.2.

---

[8] Cadence Academic Network for Europe, Middle-East, and Africa (EMEA) university software tools for educational institutions (http://www.cadence.com/support/Pages/academic_network.aspx)

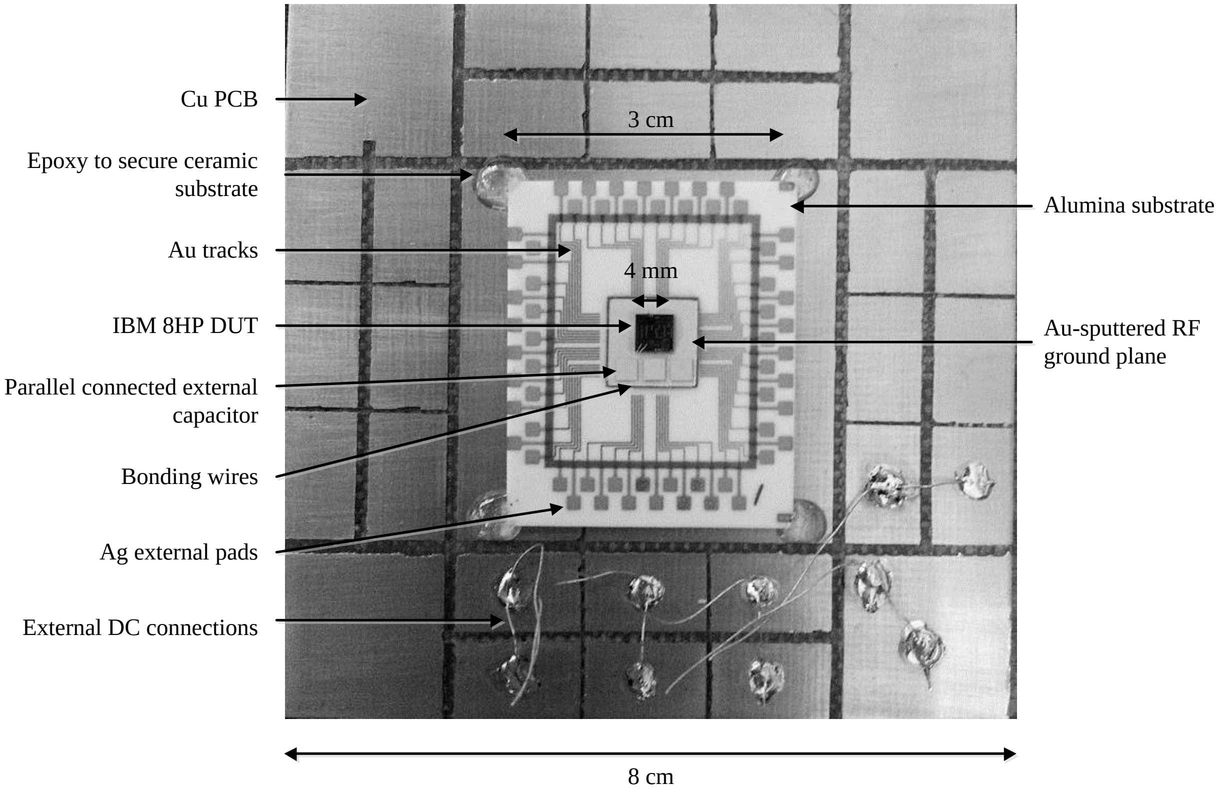

Figure 3.2: IC prototype mounted on the ceramic substrate and secured to the Cu PCB.

This method, as illustrated in Figure 3.2, eliminates the requirement for high-frequency modelling of inductive behaviour of the bonding wires. The DUT was secured to an Al_2O_3 (alumina) ceramic substrate with gold (Au)-plated ground plane using conductive epoxy. The alumina ceramic substrate is commonly used at cryogenic temperatures (down to 77 K) to house Indium Antimonite (InSb) chips as it has a thermal expansion coefficient (α = 6 - 7 × 10^{-6} /°C) similar to that of InSb (α = 5.37 × 10^{-6} /°C). The thermal expansion coefficient of Silicon (α = 2.7 × 10^{-6} /°C) is in the same range as the alumina and since the measurement set-up would not be exposed to extremely high or low temperatures, the use of the ceramic substrate could be implemented. This method also proved the most cost-effective as the equipment for machining and coating (sputtering) the substrates was available at no cost for this research project.

The Au tracks (2 μm thickness) on the alumina substrate were deposited onto a layer of 40 nm titanium tungsten (TiW) (ρ = ~95 × 10^{-6} Ω/cm) and 500 nm nickel (Ni) (ρ = 6.99 × 10^{-8} Ω/cm) with physical vapour deposition. These Au conductive tracks have a low resistivity of ρ = 2.44 × 10^{-8} Ω/cm. The bonding pads at the ends of the Au tracks were not Au-sputtered, as it was easier to solder to silver (Ag) compared to Au as Au is soluble in solder. Ag is more susceptible to oxide formation (tarnish) that can degrade low-voltage / current signals and therefore not used as the full length of the tracks. Although the DC signals applied to the tracks were high enough (1.8 V at approximately 130 mA, refer to Chapter 5), this method was still followed since it was available at the time. The external DC connections were bonded to the Ag pads using an Ag conductive epoxy (adhesive with ρ = 0.017 Ω/cm) and cured at 80 ^{o}C for 40 min. Wire bonding from the DC bias pads to Au tracks was performed to facilitate soldering of external DC connections (as opposed to probing the DUT at the required bias points) to simplify the measurement strategy by limiting the amount of external probes that need to be fed to the DUT during a measurement. These connections included a parallel-connected 1000 pF external capacitor to provide a low-impedance path of less than 10 Ω for spurious RF signals starting at around 150 MHz. The lowest possible RF input from the VNA is 40 MHz and this capacitor was chosen in-line with this frequency. A low-impedance path (less than 10 Ω) for spurious signals ranging from about 20 GHz and higher was provided by the integrated shunt capacitor of 1.2 pF. Further improvements on the robustness of the measurement set-up were made by mounting the ceramic substrate on a Cu PCB since the Ag pads on the ceramic substrate were at risk of lifting off if handled on multiple occasions.

The DUT was placed in the centre of the substrate (refer to Figure 3.2) with bonding wires leading out to the Au tracks, where wires were soldered to the end of the tracks and connected to the power supply (refer to section 3.8). The bottom surface of the Cu PCB was secured to the probing station by means of a vacuum applied to the flat surface, and this restricted movement of the PCB during measurements.

3.8 MEASUREMENTS

To avoid signal mismatches and performance degradation from unaccounted parasitic components in IC packaging and bonding wires, it was decided to perform on-wafer probe measurements for the passive filters and dipole models integrated on the DUT. Specialized equipment was required to enable such measurements such as the 40 MHz to 65 GHz Anritsu 37397D VNA with an externally added frequency conversion up to 110 GHz for full-band measurements with Picoprobe 67a DP-type probe needles (refer to Figure 3.3 and Figure 3.4).

Figure 3.3: Anritsu 37379D VNA.

The Anritsu 37379D VNA (refer to Figure 3.3) has a multiple source control mode, gain compression application, and a 1 Hz frequency resolution. The VNA was able to measure *S*-parameters of the proposed passive circuit with sufficient resolution (100 MHz) for this research since extremely wideband operation was analysed. The nature of the required measurements allowed for less stringent requirements on the VNA resolution and its ability to analyse signals up to 110 GHz was more desired to analyse the frequency response over the entire circuit spectrum. The VNA was calibrated using CS-5 structures for the frequency range of 40 MHz up to 110 GHz with a 0 dBm input level to ensure a high enough input signal and linear operation of the active components. For circuits consisting of passive components only (dipole equivalent circuits) the same input power of 0 dBm was used. The wafer probe station connected to the Anritsu 37397D VNA (PM5 / Suss MicroTec AG) used the high performance Picoprobe 67a DP-type probe needle as depicted in Figure 3.4.

Figure 3.4: Picoprobe 67a DP-type probe needle.

The Picoprobe 67a DP-type probe needle (refer to Figure 3.4) is manufactured using Tungsten coplanar probe tips. It has a minimum pitch of 50 µm and is able to perform measurements of up to 67 GHz (from DC). The probes could be operated up to 110 GHz with careful calibration using the SOLT-method to compensate for losses at frequencies higher than 67 GHz with reference to the VNA input parameters. It had an insertion loss of less than 1.1 dB and return loss greater than 14 dB. The ground-signal-ground (GSG) pads on the DUT were designed to adhere to the specifications of the probes. The measurement set-up is depicted in Figure 3.5.

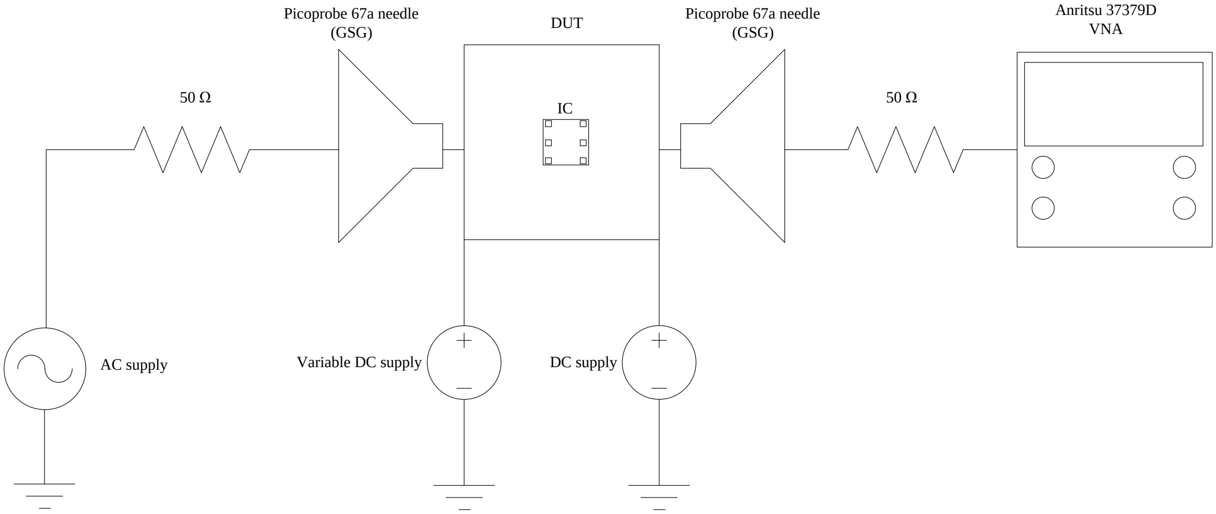

Figure 3.5: Measurement set-up for on-wafer probing measurements.

From Figure 3.5, the DUT is situated between the signal generator GSG probe needle of the Anritsu ME7838A VNA and its GSG output probe. The probe needles were matched to the internal circuit with a 50 Ω load impedance. The passive filters on the DUT were supplied with a DC signal to the base of the transistor (refer to section 4.6.5) from a GW Instek GPS-

2303 (refer to Figure 3.6) linear power supply, as well as a variable DC supply to represent the changing environment of the transmission (refer to section 2.1.7).

Figure 3.6: GW Instek GPS-2303 linear power supply.

The GW Instek GPS-2303 presented low noise and low ripple (< $1 \mathrm{mV}_{\mathrm{RMS}}$, 5 Hz ~ 1 MHz) to supply a DC signal acceptable for the application, since the DC signal to bias the active devices on the DUT was not noise- or ripple-sensitive. The DC supply only allowed for a 0.1 V resolution and since the DUT did not require a finer resolution for the bias circuitry, this was sufficient. Measurement results are documented in Chapter 5.

3.9 CONCLUSION

The methodology described in Chapter 1 completely describes the important considerations during each phase of the research and the tools used to complete each phase. If CAD software is involved in a phase, priority should be given to the choice of software, and the version number. This chapter describes the software used for the theoretical, electromagnetic, circuit schematic, circuit layout modelling, and PCB design, and describes the measurement set-up, considerations, and challenges.

Consideration during the layout of the passive circuits for this research included layout techniques that would provide *ease of measurements* of the circuits and provide a *variety of results* to defend the research hypothesis in the case of incorrect and inevitable design errors during the layout itself (such as grounding strategies and component placements). These techniques included reducing the numbers of cascaded circuits to avoid interconnect resistance, reduced number of external connections to ensure predominantly wafer-probed measurements, and careful design of the PCBs to save on cost by avoiding the need for a large number of PCBs through placement of the ICs and wire bonds. In summary, many of the design considerations during the schematic and layout design phases took into account the available measurement equipment that would be used which ensured that the equipment could be used as effectively as possible. The 40 MHz to 65 GHz Anritsu 37397D VNA with an externally added frequency conversion up to 110 GHz provided the ability to measure the circuit performance up to the required ISM bandwidth (57 GHz to 64 GHz) and provided a glimpse into the operation at much higher frequencies and thus aided in circuit performance enhancements improving operation within these bands. These decisions during the design phase also ensured less stringent requirements on the DC supply and the inclusion of coupling capacitors on the DC lines removed unwanted spurious frequency components.

It was therefore possible to verify the research hypothesis using the suggested measurement set-up at it ensured full-band frequency measurements of the passive circuits. On-wafer probing was possible with the bonding pads designed on the IC and measurements up to 110 GHz was also possible through calibration of the probes. The design of the ceramic substrate for placement of the IC followed a design practise that ensured low-losses and low-noise measurements, and in conjunction with considerations during layout (external connections are all DC connections) this technique complemented to verifying the research hypothesis through simplified measurements.

CHAPTER 4: MATHEMATICAL MODELLING AND SIMULATIONS

4. CHAPTER OVERVIEW

This chapter describes the mathematical modelling followed from the literature study provided in Chapter 2. Mathematical modelling is verified in MATLAB and the results are compared to the simulation results performed in CST Microwave Studio for the EM simulations and Cadence Virtuoso for the electrical circuit simulations.

The procedure in determining the transfer characteristics of a dipole operating in the mm-wave spectrum is presented in section 4.1.

4.1 DIPOLE DESIGN

Section 2.4 stated procedures that can be used to determine the transfer function of narrow- and wide-band antennas, where alternative methods to using the *Friis* transmission equation is presented, as wide-band operation modelling is not accurate using this approach. The method that is implemented for this thesis is using antenna design equations to simulate the operation of the antenna using EM software. The complexity of the signal propagation equations for large bandwidth operation and the amount of uncertainty of the propagation estimated over the entire bandwidth originated the initiative to not rely fully on the transmission equations and design the antenna using CST Microwave Studio. The equations used to construct the dipole in the software are adapted from fundamental antenna design equations and presented in this section.

The design and verification procedure of the dipole antenna was related to the research hypothesis (refer to section 1.4). The accuracy of purely mathematical models depends on its complexity as a function of considered variables. The risk of not accounting for parameters such as substrate effects and scattering is eliminated by using EM simulations instead. The research hypothesis, quoted that *"If an equivalent electrical circuit model of a radiating antenna and a variable filter operating in the mm-wave spectrum, using only passive components can be combined…"* states the requirement for an equivalent electrical circuit of a radiating antenna, therefore a defined transfer function of the radiating antenna is firstly required, either purely mathematically or as a simulated model to fully describe the operation of the antenna. The following considerations provide a guideline for the design of the dipole antenna using mathematical design equations, and interpreting the results of the simulated model.

- This section provides a working model of a dipole antenna operating in the mm-wave frequency band, with resonance at 60 GHz, and simulated using an EM simulator software package.
- Design equations to mathematically represent the geometry of the dipole antenna as a two-port network were used as an initial model for the antenna.
- Mathematical derivations and equations were used to determine the theoretical results for the antenna without increasing the complexity to account for parasitic effects.
- Simulated results were analysed and compared to the theoretical results to determine the accuracy of the design equations. Errors smaller than 2 % for input impedance and reflection coefficient could be considered negligible as the mathematical equations used assume ideal environmental circumstances.
- Inclusion of a silicon substrate to the dipole antenna simulation profile provided a better representation of the antenna behaviour in practical applications (with substrate geometric and radiating parameters matched to the 130 nm technology).

Once the design and operation (results) of the dipole antenna in the mm-wave frequency band are verified, these results can be used as a reference point to determine if this operation can be represented by electrical (passive) components. The limitations of the process in terms of components size, geometry, and placement will determine if an antenna (resonating at 60 GHz) can exist using a specific node. Quoting the last part of the research hypothesis in section 1.4 as *"...then it can be used as an analogue, real-time, path-loss prediction model that eliminates the need to down-convert signals for analysis in the digital domain,"* it is evident that if the antenna can be represented by an electrical equivalent circuit it could prove a cost-effective technique to create an analogue (real-time) prediction model. Implementation in the 130 nm technology node would expose limitations as a result of component values and parasitic effects that could be addressed within the node, or by implementing the strategies in a smaller, compatible, node.

This section aimed to construct a working EM antenna to be used as reference for this procedure.

The theoretical derivations are computed with reference to Figure 4.1 (with variables adapted from section 2.3).

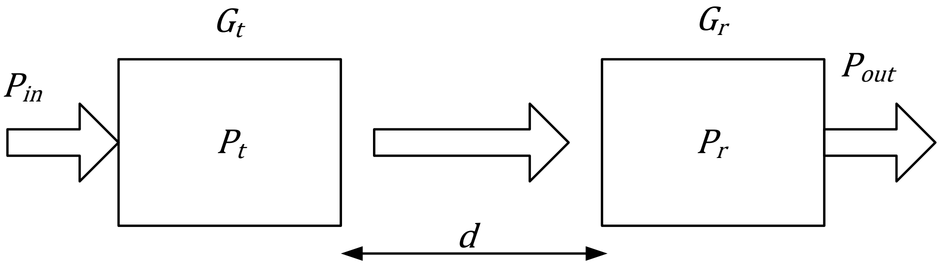

Figure 4.1: Antenna diagram with reference to the *Friis* equation.

From Figure 4.1, P_{in} is the input power from the source, P_t is the power of the transmitted signal from the transmitting antenna with gain G_t. The distance between the transmitting antenna and the receiving antenna is d. The receiving antenna receives a signal with power P_r and has a gain of G_r. The power distributed to the load is P_{out}.

The dipole is simulated as aluminium conductors on a silicon substrate surrounded by air (free space, as opposed to operation in a vacuum). These materials are used in the 130 nm process. The dipole can therefore also be created with the 130 nm process and measurement results of such a structure can be verified and compared to the simulated structure in EM software (material properties listed in Table 4.1).

Table 4.1: Material properties used for the dipole EM simulations.

Property	**Unit**	**Aluminium**	**Silicon**	**Air**
Relative permittivity (ε)	-	-	11.9	1.00059
Relative permeability (μ)	-	1	1	1
Conductivity (σ)	S/m	3.56×10^{7}	2.5×10^{-4}	-
Thermal conductivity (k)	W/K/m	237	148	0.026
Young's modulus (E)	kN/mm^2	69	112	-
Poisson ratio (ν)	-	0.33	0.28	-
Thermal expansion (α_V)	1e^{-6}/K	23	5.1	-

As described in Table 4.1, the relative permittivity of silicon is ε =11.9 F/m, and its relative permeability μ = 1 H/m (as with aluminium). Aluminium (σ = 3.56 × 10^{7} S/m) is a good conductor at 293 K whereas silicon is a weak conductor (σ = 2.5 × 10^{-4} S/m), and air does not conduct electricity. Silicon is a relatively good conductor of heat (k) whereas Aluminium has about 1.6 times the ability compared to silicon. The measure of stiffness (tensile / Young's modulus) of silicon is rated at E = 112 kN/mm^2 and for aluminium it is E = 69 kN/mm^2 (both values rated at 300 K). Aluminium has an almost 5 times larger thermal expansion coefficient (α_V) compared to silicon.

The dipole is constructed as a half-wavelength dipole ($\lambda/2$). Choosing the dipole as a half-wavelength device has several advantages during the analysis. Advantages include the fact that a half-wavelength dipole has a radiation pattern that is omni-directional in the H-plane, ensuring relevance of proposed simulated results to practical applications (this type of radiation pattern is required for mobile applications). It has a directivity of 1.64 dBi or 2.15 dBi and is larger than short dipoles directivity (although smaller than a full-wavelength dipole). The full-wavelength dipole, however, is much larger in size therefore this is a good trade-off between size and directivity. The input impedance of the half-wavelength dipole is 73 Ω (real) and this is matched with a standard transmission line with characteristic input impedance of 75 Ω or 73 Ω (resulting in a VSWR of less than 2).

4.1.1 Dipole geometry

To determine the wavelength (therefore the physical length of the dipole), the refractive index of the medium through which the signal is passing has to be determined first. The refractive index is given by $n = \sqrt{\varepsilon_0\varepsilon_r\mu_0\mu_r}$ where ε_0 is the permittivity of free space (8.854 × 10^{-12} F/m), ε_r is the relative permittivity of the medium (ε_r is equal to 1 in free space), μ_0 is the permeability of free space (4π × 10^{-7} N/A^2), and μ_r is the relative permeability of the medium (usually μ_r is equal to 1). Therefore, the wavelength can be determined by taking into account the refractive index, the speed of light in a vacuum (c = 300 × 10^{6} m/s in free space), and the frequency of operation (f = 60 GHz). The wavelength is defined by

$$\lambda = \frac{n \times c}{f} \tag{4.1}$$

$$= \frac{1 \times 300 \times 10^{6}}{60 \times 10^{9}}$$

and is equal to 5 mm (or 5000 µm as used in the EM software). The intrinsic impedance (η) of free space is approximately equal to 120π Ω (377 Ω). Dipoles are typically constructed by two back-to-back conductors of quarter-wavelength length to form a node and an anti-node, with total length of $L = \lambda/2$. This topology yields the largest differential voltage therefore generating the largest current. The length of the dipole is therefore $L = \lambda/2$ and is equal to 2.5 mm. Thus, each lobe of the dipole should be equal to 1.25 mm ($\lambda/4$). Figure 4.2 is a representation of the dipole in CST Microwave Studio, consisting of two $\lambda/4$ conductors, connected through a port in the centre (centre-fed dipole).

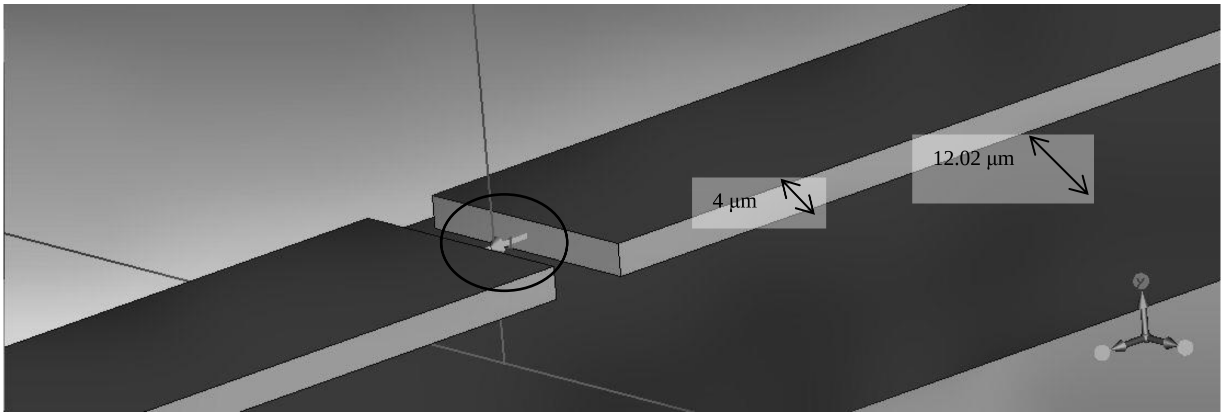

Figure 4.2: Dipole geometry at the centre port.

Figure 4.2 represents the simulated dipole and shows the thickness of the top-metal (aluminium) layer to be 4 µm at a distance of 12.02 µm from the silicon substrate. This information relates directly to the layer heights and thicknesses of the 130 nm technology. The two metal strips are connected by a centre-fed excitation port (highlighted in Figure 4.2).

Two dipoles are designed, to act as transmitting and receiving antennas (ports). The distance between the two antennas (R) is chosen to ensure operation in the far-field region (refer to section 2.3.3) (for this design, $D = \lambda/2 = 2.5$ mm). The design of the radiation box around the dipole antennas should extend to at least $\lambda/4 = 1.25$ mm from all radiating surfaces. Figure 4.3 depicts the entire length of the dipole, with the port situated in the centre of the two conducting strips.

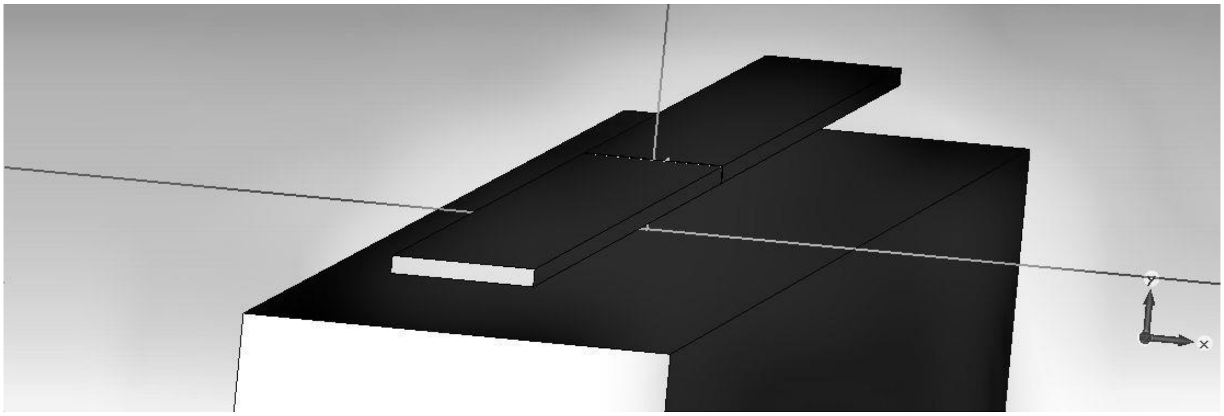

Figure 4.3: Dipole geometry of two conducting aluminium strips.

In Figure 4.3 the aluminium metal layer on top of the silicon substrate is visible, with the centre-fed dipole constructed using two metal strips of equal length ($\lambda/4$) and excited with electrical energy at the port situated in the middle of the strips (the port is situated where the two metal strips in Figure 4.3 join).

The following section describes the theoretical dipole parameters mathematically computed based on the length of the dipole at 60 GHz.

4.1.2 Theoretical dipole parameters

The maximum directivity of the finite length, half-wavelength dipole is determined from [**53**] to be equal to 1.643. The maximum effective aperture area (refer to Table 2.5) is equal to

$$A_{em} = \frac{0.005^2}{4\pi}(1.643) \tag{4.2}$$

and therefore the effective aperture (area) was calculated to be 3.27 µm. The effective aperture result is used to determine the electric field of the dipole. The radiation resistance (refer to Table 2.5) for the dipole antennas for operation in free space, which has to be matched to the source impedance, is calculated as approximately 73 **Ω**. In reality, for a dipole length of exactly $\lambda/2$, there exists a reactive impedance of *j*42.5 **Ω**. Therefore, the total impedance of the dipole is in reality a complex value (following the form $Z_A = R_A + jX_A$) and was equal to 73 + *j*42.5 **Ω**, which has to be properly matched to the source to ensure minimum reflection between the load (antenna) and the source (generator). To account for this reactive impedance in simulation, the length of the dipole was adjusted to approximately 0.47λ - 0.48λ (as opposed to $\lambda/2$) which removed the reactive part of the total radiation resistance.

The gain of the dipoles in the direction of maximum directivity was computed by (2.18) and was also equal to 1.643 (the same as the maximum directivity D_{max}).

The electric field at the specified distance from the transmitting dipole antenna was equated using the *Friis* transmission equation. Therefore, from this equation,

$$P_r(d) = \left(\frac{\lambda}{4\pi d}\right)^2 G_t G_r P_t \tag{4.3}$$

where d is the distance where the electric field is measured (10 mm), G_t and G_r are the gains of the transmitting and receiving dipoles respectively (both G_t and G_r are equal to 1.643), and P_t is the reference transmitted power of the dipole, chosen as 1 W. Assuming that the dipole is properly matched to the source at the frequency of operation, the value for P_t of 1 W could be assumed without any losses. This value had to be adjusted to account for the mismatches that occurred due to the reflection coefficient of the port. Thus, the theoretical received power at a distance of 10 mm from the transmitting antenna, was calculated as

$$P_r(d) = \left(\frac{0.005}{4\pi(0.01)}\right)^2 (1.643)(1.643)(1) \tag{4.4}$$

and was approximately 4.3 mW (6.3 dBm). From the received power (refer to Table 2.5) the electric field (E) was calculated by

$$|E| = \sqrt{\frac{120\pi \times 4.3 \times 10^{-3}}{3.27 \times 10^{-6}}} \tag{4.5}$$

and was equal to 704.2 V/m. The electric field was found to be ($A_{em} = 1$)

$$\begin{aligned} |E| &= \eta \times P_r(d) \\ &= 120\pi \times 4.3 \times 10^{-3} \end{aligned} \tag{4.6}$$

equal to 1.62 V/m. This value of electric field was, however, slightly higher than the calculated value, as mathematical results did take into account the reflection losses, and scattering parameters.

4.2 SIMULATION RESULTS

This section presents the simulation results of the dipole antenna. These results are separated into two different simulation environments to allow a structured and logical approach for interpreting substrate effects in EM simulations. Section 4.2.1 presents the simulated dipole antenna when not placed on a substrate. These results are used to determine the effectiveness and accuracy of the geometrical parameters presented in section 4.1 as these parameters assume no external parasitic effects in the operation of the structure. Section 4.2.2 presents the results, of the same dipole structure, but accounts for parasitic effects introduced by placing a substrate below the device, as is more the practical approach when using integrated antennas. The results can therefore be used to compare with section 4.2.1 and provide a comparative analysis of the same structure, but with differences in its EM operation. Evaluating these differences allows for the analytical approach to improve the equivalent circuit. In practise the geometry of the antenna can be altered to represent the required operation without fully comprehending the reasons for these changes.

4.2.1 Simulation results (no substrate)

Through simulation results, the real and complex impedance of the dipole antenna at 60 GHz, with the physical characteristics of the dipole specified in sections 4.1.1 and 4.1.2, were determined. Using the physical properties computed in section 4.1.1, the dipole was first simulated using no substrate below the conducting strips. The simulation therefore only took into account transmission through air, and no substrate effects of scattered parameters were accounted for. This simulation confirmed that the parameters determined in the theoretical design were accurate at 60 GHz. The radiation resistance, real and imaginary part, is depicted in Figure 4.4.

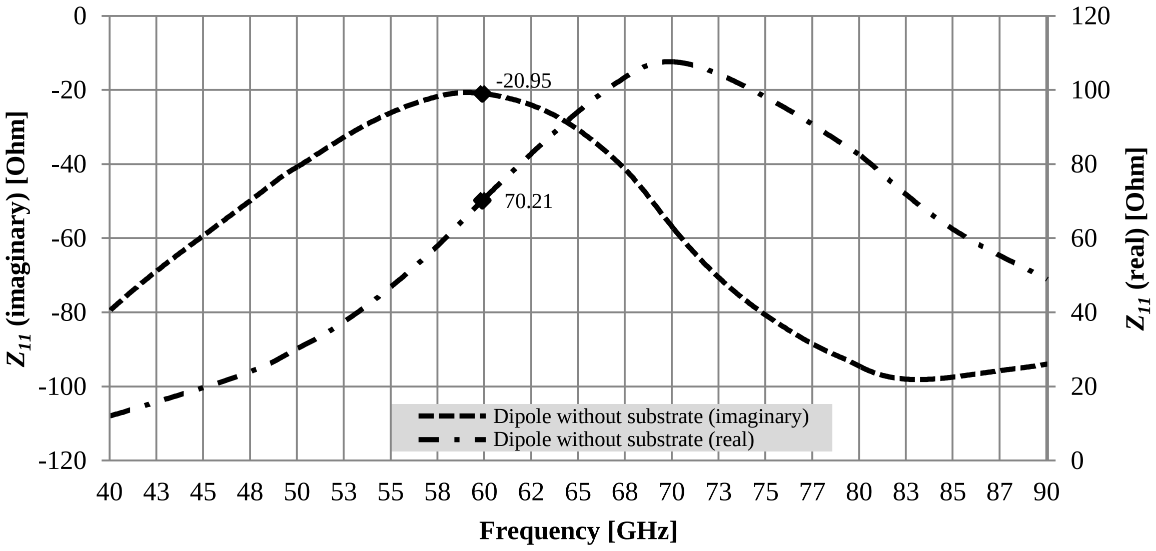

Figure 4.4: Real and imaginary impedance of dipole without substrate.

From Figure 4.4 the radiation resistance of the dipole at 60 GHz was

$$R_r = 70.21 - j20.95\ \Omega \tag{4.7}$$

and the magnitude of the radiation resistance ($|R_r|$) was 73.27 Ω. This value of the impedance magnitude was confirmed from Figure 4.5. The value represented in the impedance magnitude of the dipole without a substrate in Figure 4.5 (73.77 Ω) fell within a 0.6 % error compared to the derived value of 73.27 Ω. The value of the impedance, as determined by CST Microwave Studio, therefore confirmed that the initial design of the dipole was correct, as the impedance is within 10 % of the theoretical value for dipole antennas, which was 73 Ω. The magnitude of the input impedance of the dipole without a substrate is given in Figure 4.5.

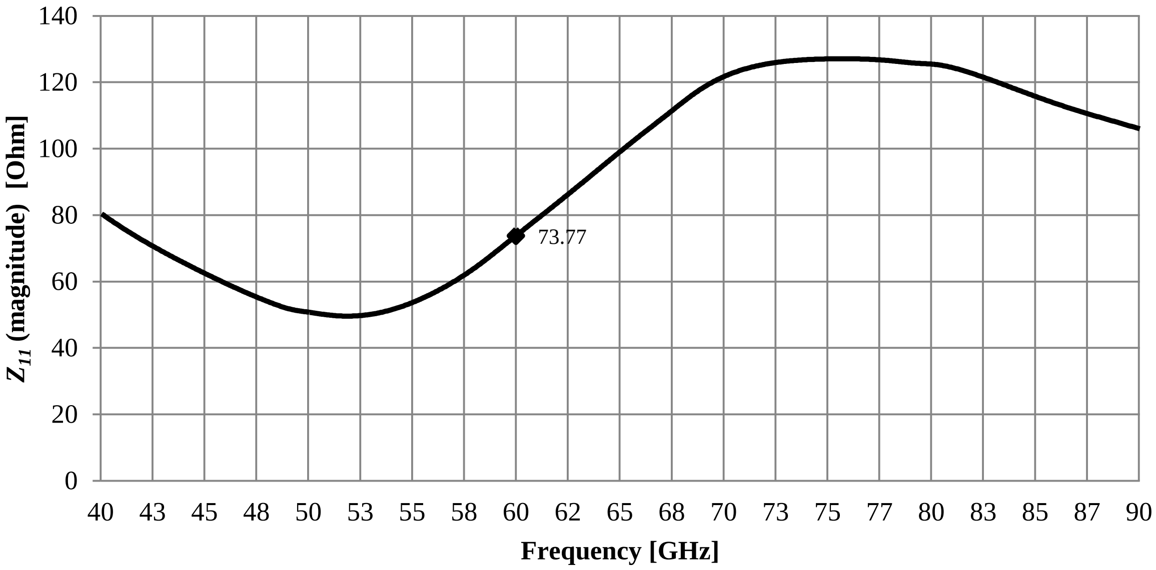

Figure 4.5: Magnitude of impedance of dipole without substrate.

From Figure 4.5 the magnitude of the impedance at 60 GHz is 73.77 Ω with minimum value of 49.58 Ω at 51.85 GHz and maximum value of 127.1 Ω at 75.70 GHz. From the radiation resistance (R_r), it was possible to calculate the input reflection coefficient (Γ) if the dipole was connected to a 75 Ω source impedance. The input reflection coefficient of the dipole antenna at 60 GHz was determined to be

$$\Gamma = \frac{75-(70.21-j20.95)}{75+(70.21-j20.95)} \tag{4.8}$$

equal to 0.0119 + j0.1460, and $|\Gamma|$ was equal to 0.1465 (-16.68 dB). The reflection coefficient was also the parameter used to determine the value of the insertion loss of the dipole antenna S_{11}, as $|S_{11}| = |\Gamma|$ = -16.68 dB.

This result was also obtained with a dipole length of not exactly 5 mm, but an optimized dipole length of 4.177 mm – to ensure optimal efficiency at 60 GHz, taking into account reflection, diffraction, and scattering losses of the overall system. Several techniques can be used for this optimization process, such as the placement and the orientation of the port(s), varied height of the substrate, and the thickness and width of the conducting material used as the dipole. No substrate was added in this simulation, and the thickness of the conducting material was constant as determined by the 130 nm process, the option of varying the length of the dipole was implemented. By varying the length of the dipole, the minimum value of the insertion loss shifted away from 60 GHz, and through optimization the resonant point of the insertion loss was kept at 60 GHz.

The reflection coefficient and therefore the insertion loss of the dipole without a substrate is depicted in Figure 4.6.

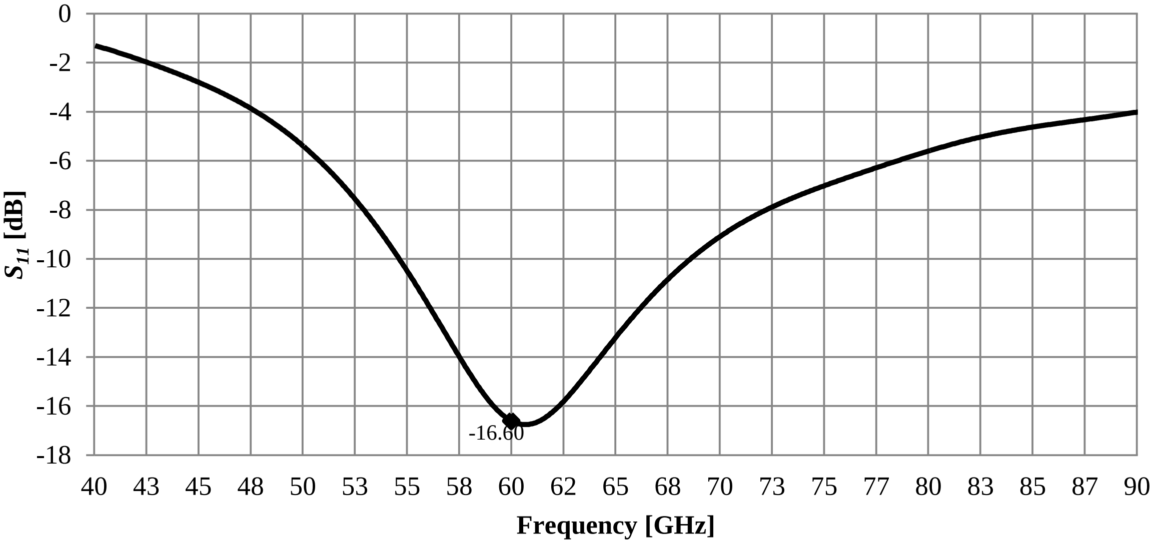

Figure 4.6: Reflection coefficient of dipole without a substrate.

The reflection was minimized at 60 GHz, with a value of -16.6 dB at 60 GHz visible in Figure 4.6. This value translated to a unitless value of 0.1463, constituting that 85 % of the incident amplitude was received within the dipole. Optimization of the radiation resistance through varied dipole length also influenced the insertion loss and -16.60 dB was the best obtainable value during simulation.

The actual power radiated from the transmitting antenna at 60 GHz when taking into account the mismatched conditions and the antenna gain was determined from the equation

$$\begin{aligned} P_{t\_actual} &= G_t P_t \times (1 - {S_{11}}^2) \\ &= (1.643)(1) \times (1 - 0.1463^2) \end{aligned} \tag{4.9}$$

and was equal to 1.60 W (32.06 dBm). The actual power available at the port, as a result of mismatches in the radiation resistance, was available through

$$P_{r\_actual}(d) = \frac{P_r(d)}{1 - S_{11}{}^2} \tag{4.10}$$

which was equal to 4.4 mW (6.43 dBm). These equations were implemented in conjunction with the reflection coefficient simulated results to determine the actual power characteristics of the dipole as a result of mismatches. To determine the VSWR of the transmission;

$$\begin{aligned} \text{VSWR} &= \frac{1+\Gamma}{1-\Gamma} \\ &= \frac{1+0.1463}{1-0.1463} \end{aligned} \tag{4.11}$$

resulted in a VSWR of 1.35:1 at 60 GHz. The VSWR for the dipole was determined and shown in Figure 4.7 and it is evident from Figure 4.7 that the VSWR had a minimum value (as required) at 60 GHz.

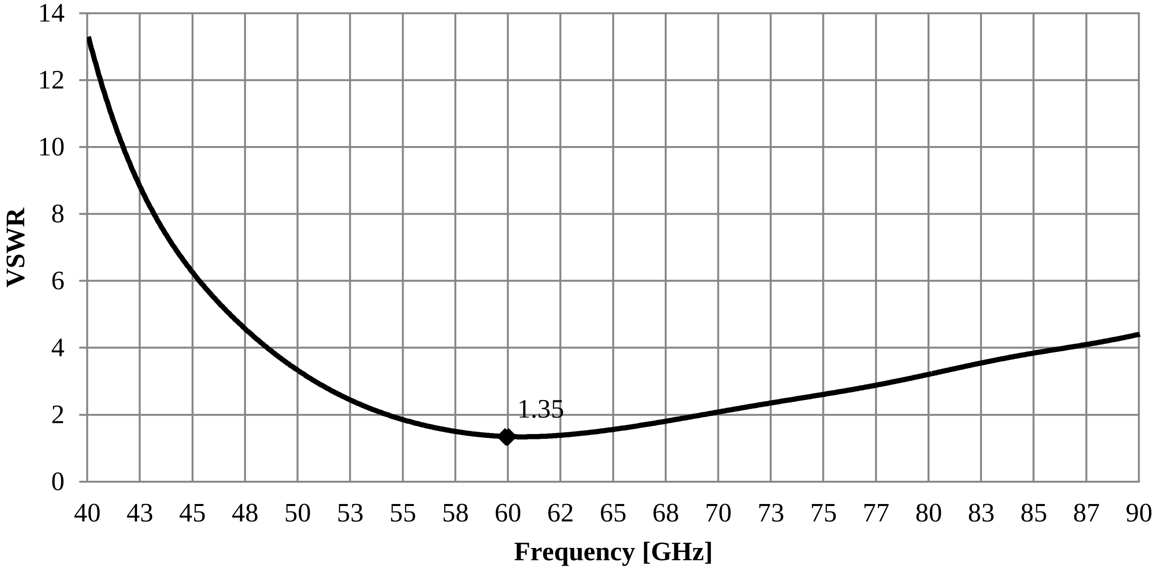

Figure 4.7: VSWR of dipole without a substrate.

The VSWR of 1.35:1 (2.6 dB) in Figure 4.7 was less than 2:1 and this related to an acceptable level for radiating structures [**83**]. Less than 4 % of the source transmission was reflected (not transmitted) by the antenna.

As an initial result to the simulation of the dipole without the addition of the substrate, the results correlated well with the theoretical values determined in section 4.1.2. However, since the application of the dipole was based on measurements on a silicon substrate comparable to the 130 nm process, the addition of the substrate could influence the obtained results and needed to be simulated and optimized before the electrical equivalent circuit was obtained. The results and optimizations are documented in section 4.2.2.

4.2.2 Simulation results (with substrate)

To represent the dipole as two conducting strips machined onto a wafer, the EM simulation was adapted to represent this procedure. For the improved simulation profile, a silicon substrate was simulated at a height similar to the aluminium metal layer of the 130 nm process (refer to section 3.1). Introducing the substrate below the dipole, however, changed the transfer characteristics and radiation resistance of the dipole. The geometrical parameters of the conductive metal strips remained similar allowing for a comparative analysis of the effects introduced by the substrate. The parasitic substrate effects had to be accounted for in the equivalent electrical circuit of the dipole, therefore the EM simulation results are depicted in this section. The real and imaginary impedance of the dipole mounted on the silicon substrate is depicted in Figure 4.8.

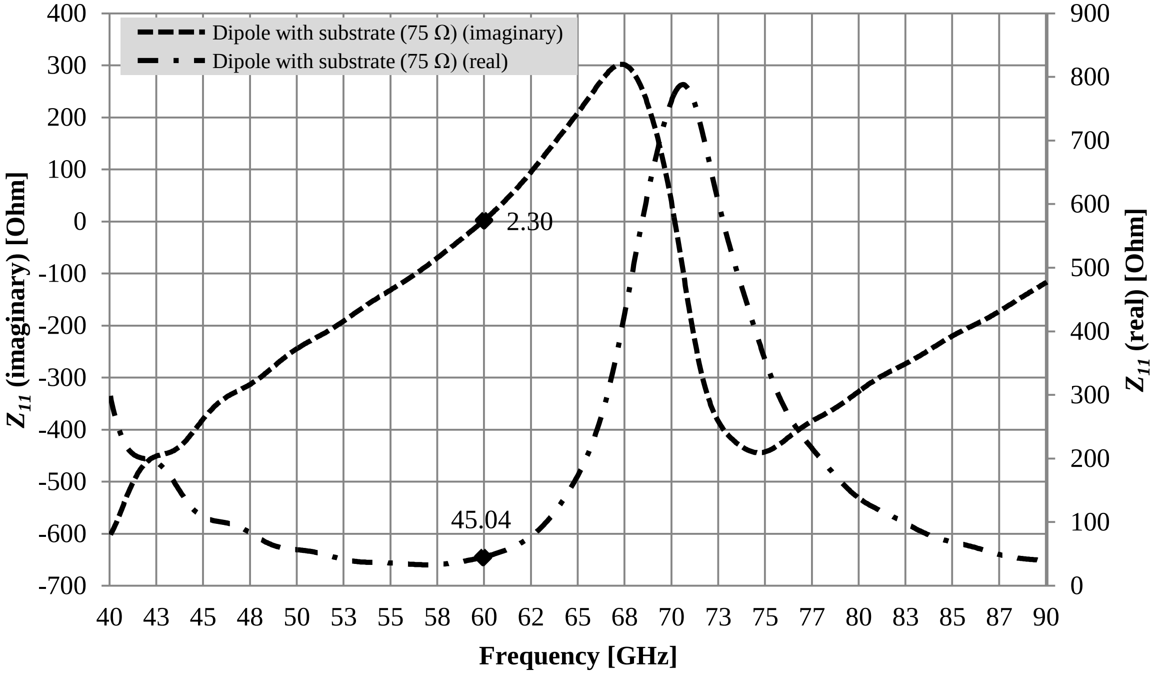

Figure 4.8: Real and imaginary impedance of dipole with substrate (75 Ω).

In Figure 4.8 the radiation resistance of the dipole at 60 GHz matched to a 75 Ω load was

$$R_r = 45.04 + j2.30\ \Omega \tag{4.12}$$

and the magnitude of the radiation resistance ($|R_r|$) was 45.1 Ω. This value of the impedance magnitude is confirmed from Figure 4.9. The radiation resistance (impedance) of the dipole therefore changed considerably as a result of the addition of the substrate, and proved to be inductive ($j2.30$ Ω). The magnitude of the input impedance of the dipole with a substrate and matched to a 75 Ω load is given in Figure 4.9.

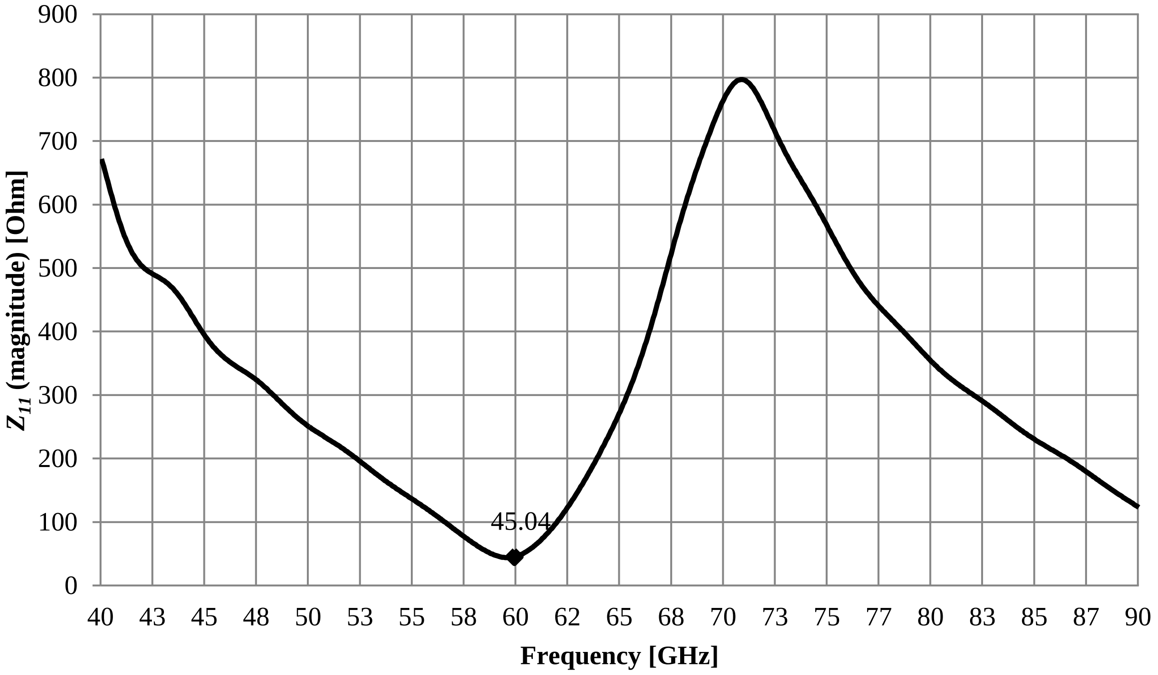

Figure 4.9: Magnitude of impedance of dipole with substrate.

Although the impedance (magnitude) of the dipole changed from 73.27 Ω to 45.1 Ω by adding the substrate in Figure 4.5, the emphasis of this simulation was to maintain resonance at 60 GHz rather than optimizing the radiation resistance. The original impedance of 73.27 Ω could be matched to a 75 Ω load, and the 45.1 Ω radiation resistance could be matched to a 50 Ω load, therefore the choice of the load resistance could be modified during the electrical simulations. The effect of adding the substrate to the insertion loss and resonant frequency was analysed. The simulation profile was not changed in this case to be matched to a 50 Ω load, and still remained set using a 75 Ω load to ensure comparable results with regard to the results where no substrate was added. The results of the simulation using a 50 Ω load are also added for the reflection coefficient and VSWR for comparative analysis.

Mathematically it could be verified that the input reflection coefficient of the dipole antenna at 60 GHz, used with a 75 Ω load impedance was determined to be

$$\Gamma = \frac{75-(45.04+j2.30)}{75+(45.04+j2.30)} \tag{4.13}$$

equal to 0.2491 – *j*0.0239, and the insertion loss $|\Gamma|$ (refer to Figure 4.10) was equal to a calculated value of 0.2503 (-13.85 dB). This value was sufficiently close to the graphically depicted value in Figure 4.10 of -12.81 dB. The reflection coefficient was also the parameter used to determine the mathematical value of S_{11}, as $|S_{11}| = |\Gamma|$ = -13.85 dB.

The input reflection coefficient of the dipole antenna at 60 GHz, used with a 50 Ω load impedance was mathematically determined to be

$$\Gamma = \frac{50-(45.04+j2.30)}{50+(45.04+j2.30)} \tag{4.14}$$

equal to 0.0516 – *j*0.0254, and the insertion loss $|\Gamma|$ (refer to Figure 4.10) was equal to a calculated value of 0.0575 (-28.55 dB). This value was sufficiently close to the graphically depicted value in Figure 4.10 of -25.55 dB. The reflection coefficient was also the parameter used to determine the mathematical value of S_{11}, as $|S_{11}| = |\Gamma|$ = -28.55 dB.

The reflection coefficient ($|\Gamma|$) of the dipole with a substrate (matched to 75 Ω and to 50 Ω) is depicted in Figure 4.10.

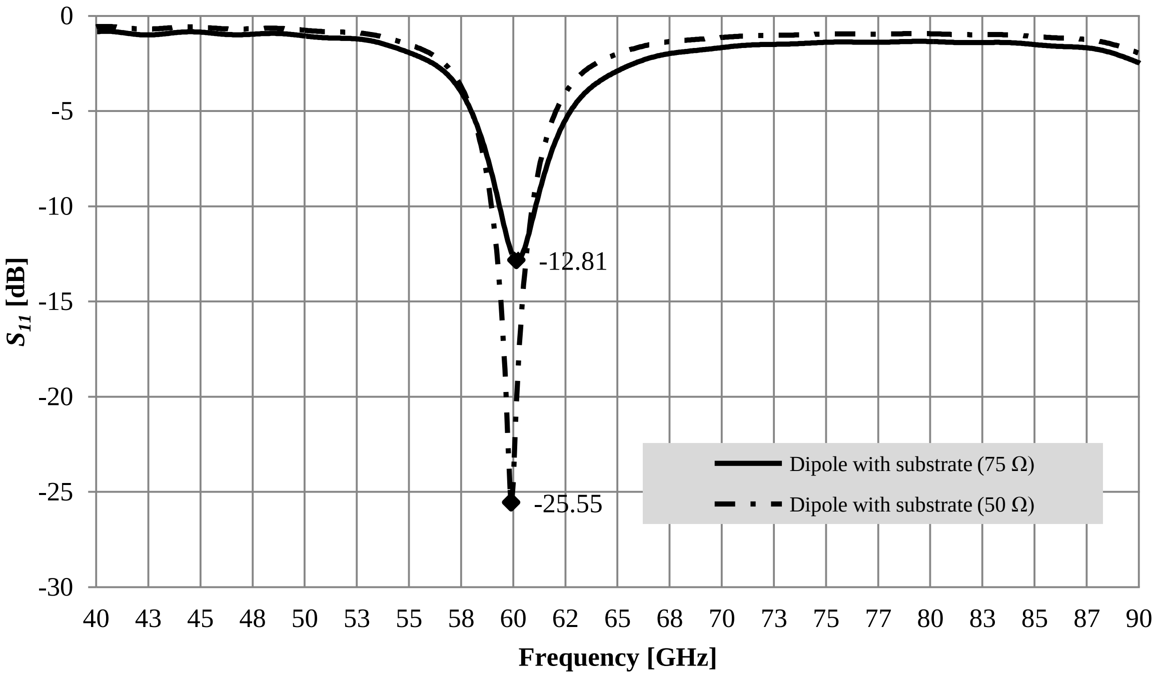

Figure 4.10: Reflection coefficient of dipole with a substrate matched to 75 Ω and 50 Ω.

From Figure 4.10 the reflection was minimized at 60 GHz, with a value of -12.81 dB for the 75 Ω load, and -25.55 dB for the 50 Ω load at 60 GHz. The value of $|\Gamma|$ changed from -16.25 dB with no substrate to -12.81 dB (or -25.55 dB matched to 50 Ω) through introduction of the substrate. The simulated reflection coefficient was used to determine the insertion loss S_{11}, as $|\Gamma| = S_{11} =$ -12.81 dB (0.2287) for the 75 Ω load or -25.55 dB (0.053) if matched to a 50 Ω load.

The result for the VSWR is valid when the substrate was added, and the connected load was rated at 75 Ω.

$$VSWR = \frac{1+0.2503}{1-0.2503} \tag{4.15}$$

resulted in a VSWR of 1.67:1 at 60 GHz matched to a 75 Ω load. The following result is valid when the substrate is added, and the connected load was rated at 50 Ω.

$$VSWR = \frac{1+0.0575}{1-0.0575} \tag{4.16}$$

resulted in a VSWR of 1.12:1 at 60 GHz matched to a 50 Ω load. These results were verified with the values obtained through simulation in Figure 4.11.

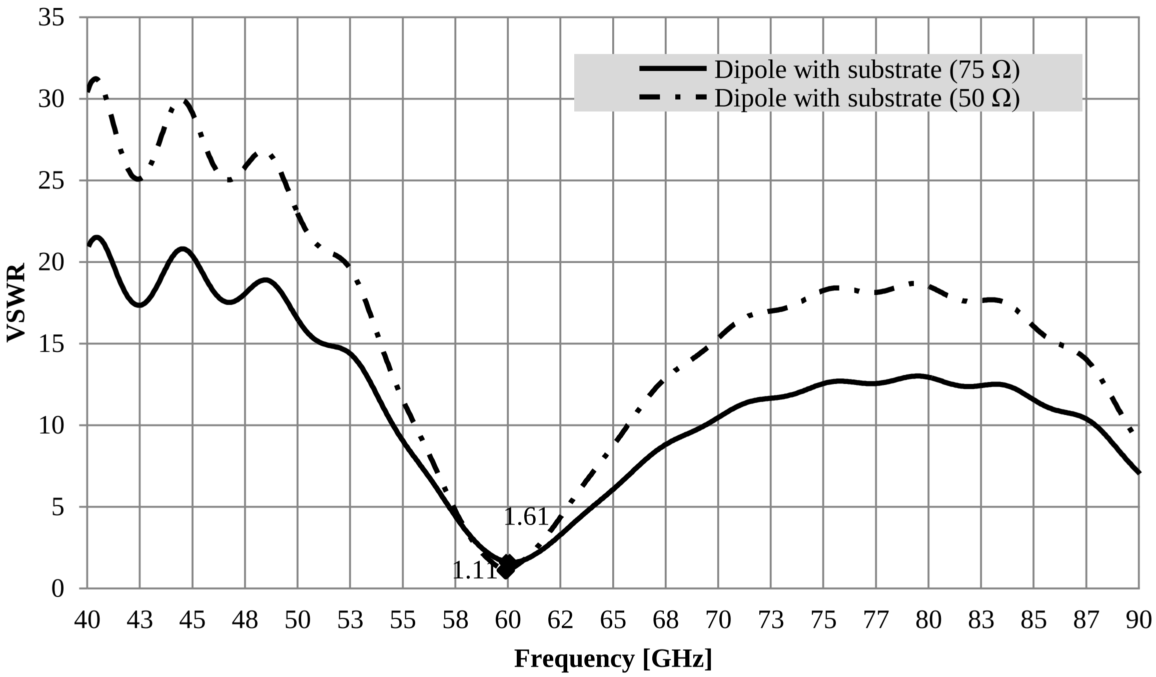

Figure 4.11: VSWR of dipole antenna with a substrate.

The VSWR (refer to Figure 4.11) of the dipole with the substrate (match to 50 Ω and 75 Ω respectively) from the simulation results (refer to Figure 4.11) shows an 18 % and 16 % error respectively. These errors can be accounted to the fact that the mathematical derived value does not account for parasitic variances as a result of substrate effects. The ripple effects evident in Figure 4.11 at lower and higher frequencies are also testament to frequency-dependent parasitic effects that are not visible in theoretical results displayed in Figure 4.7.

4.2.3 Simulation results (comparison)

This section briefly outlines relevant changes in radiation resistance, insertion loss, VSWR, and the phase of the radiation resistance of the dipole antenna under conditions that there is no substrate added to the design, and the addition of the substrate (matched to 50 Ω and 75 Ω, respectively). The documented results show that the substrate parasitic effects weakens the radiation efficiency of the antenna when the matched load is 75 Ω. Although the value of the load resistor could be changed to 50 Ω without affecting the design, it was chosen to adhere to the 75 Ω load resistor and model the electrical equivalent circuit based on the initail design, chosen with the 75 Ω load and the parasitic effects of the substrate. Figure 4.12 depicts the change in the imaginary impedance (radiation resistance) of the dipole antenna with and without the addition of the substrate. The choice of matched load did not influence the results where the substrate was added, therefore only two lines are visible.

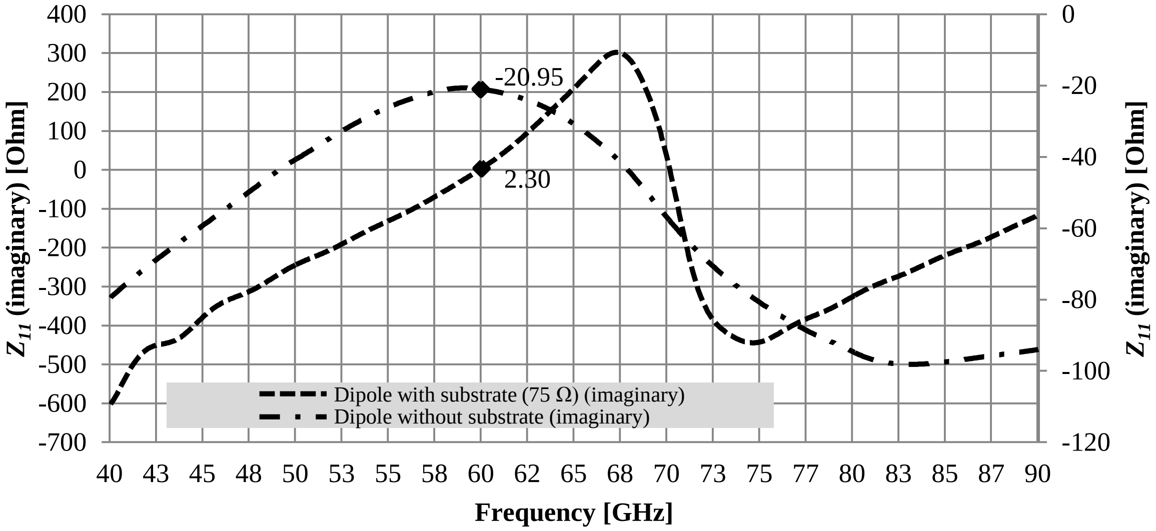

Figure 4.12: Dipole Z_{11} Imaginary impedance with and without substrate.

From Figure 4.12 it was noted that the imaginary impedance, when the substrate was added, proved inductive and the bandwidth of the transmission decreased, evident from the increased slopes in Figure 4.12. This effect is better described in Figure 4.13 where the insertion loss of the dipole was compared.

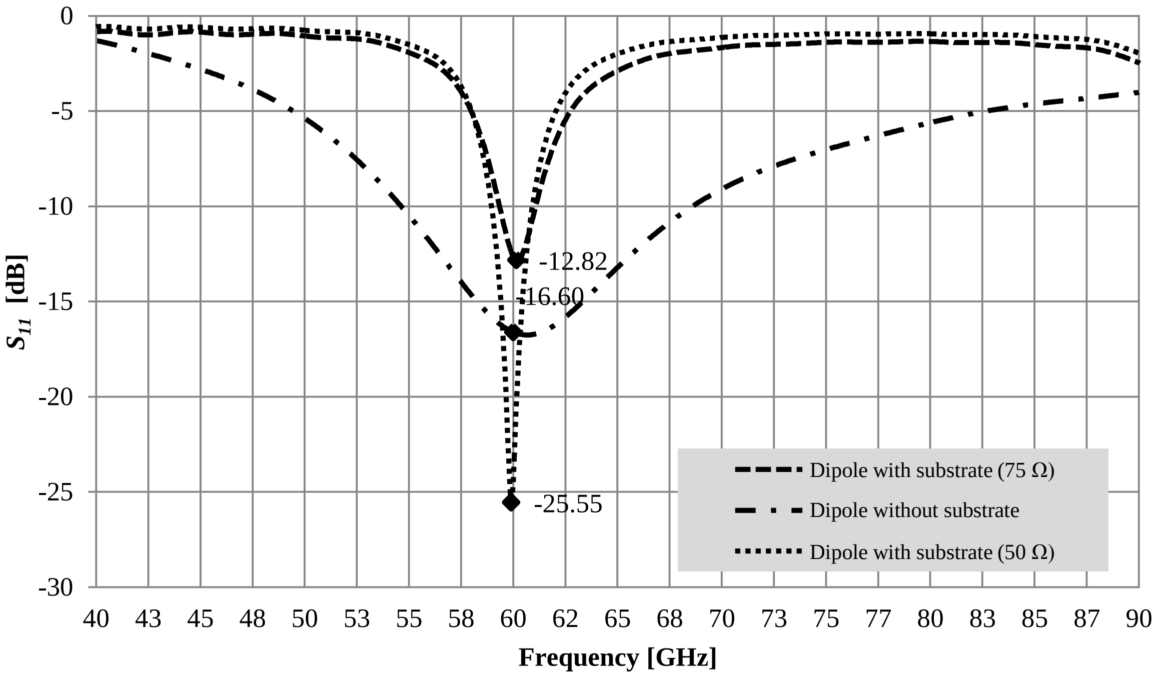

Figure 4.13: Dipole S_{11} reflection coefficient with and without substrate.

From Figure 4.13, the insertion loss without a substrate had a large -3 dB bandwidth with a value of -16.60 dB at 60 GHz, close to resonance. The bandwidth of the insertion loss decreased with the addition of the substrate, and the insertion loss also increased (degraded) to -12.82 dB, however, this value is calculated when mismatched to the 75 Ω load. If the value of the load resistance in CST Microwave Studio changed to 50 Ω, a better match was obtained with the insertion loss decreased (improved) to -25.55 dB, with a further decrease in bandwidth. Figure 4.14 shows the VSWR of the dipole antenna as the substrate characteristics changed.

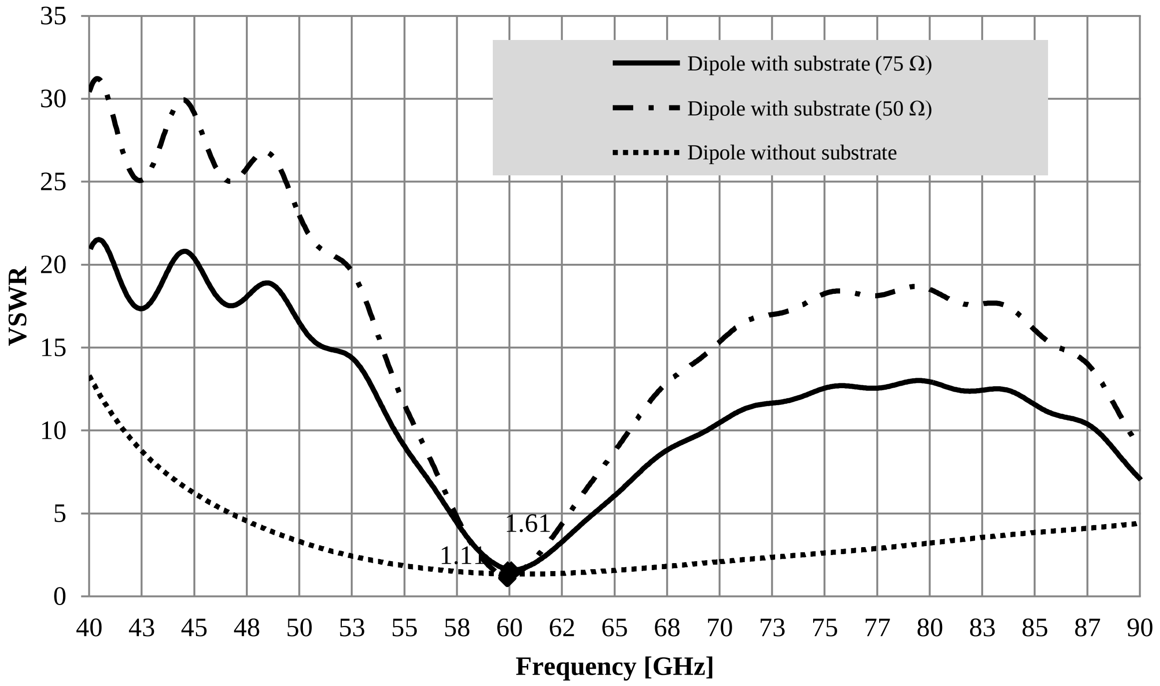

Figure 4.14: Dipole VSWR with and without substrate.

From Figure 4.14, the initial VSWR when no substrate was added had a minimum ratio of 1.35:1 at 60 GHz, with a relatively consistent form factor. With the addition of the substrate, and a matched load of 75 Ω, the VSWR is higher (degraded), at 1.61:1, and the minimum value was unchanged at 60 GHz, however, the included parasitic elements from the substrate was evident in the lower (< 50 GHz) and higher (> 70 GHz) frequency spectrums, where the value of the VSWR became inconsistent and unpredictable (when looking at narrow bandwidth applications). The 50 Ω matched load antenna showed similar characteristics, although the VSWR was improved to 1.11:1 at 60 GHz due to the closer match with its input impedance. The phase of the radiation resistance is depicted in Figure 4.15. Only the phase of the dipole with and without the substrate is shown, as the phase did not change regardless of the load connected to the dipole.

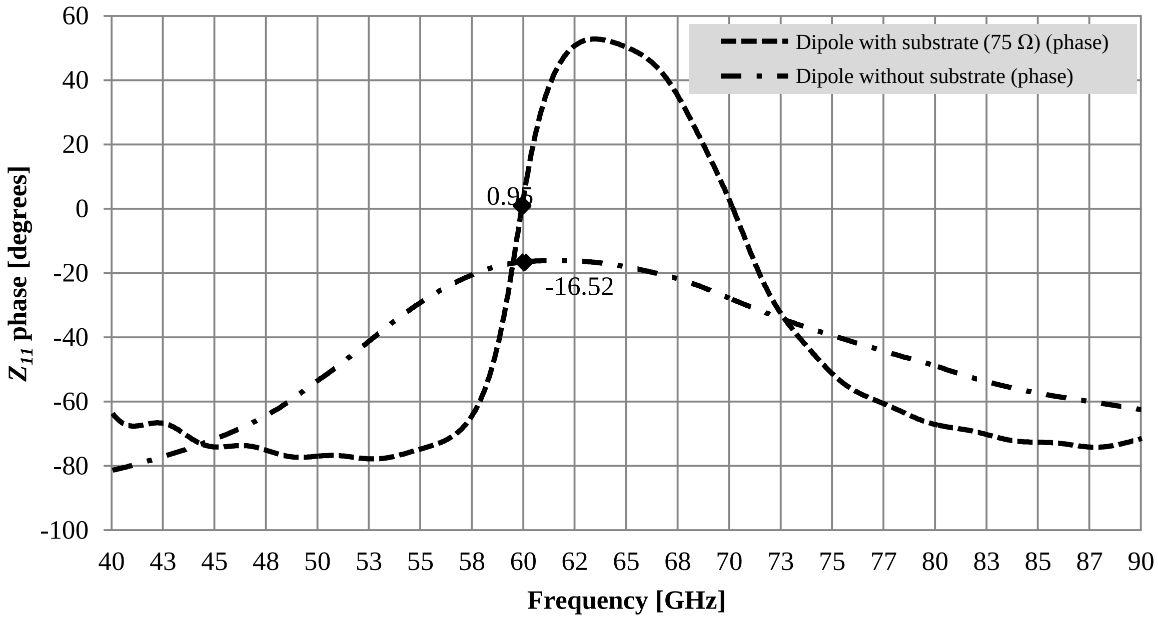

Figure 4.15: Dipole Z_{11} impedance phase with and without substrate.

Figure 4.15 confirms that the simulated dipole antenna was optimized to have a (close to) zero degrees (0.95°) phase shift at the input port at 60 GHz with the silicon substrate added. The input has a -16.52° phase shift without the addition of the substrate, but this value could be optimized by modifying the length (or width) of the dipole.

A brief summary of the results obtained in sections 4.1.2 to 4.2.3 is given in Table 4.2.

Table 4.2: Simulation results for the EM dipole antenna at 60 GHz.

Simulated results	**Radiation resistance**	**Reflection coefficient**	**Voltage standing-wave ratio**	**Actual transmitted power**
(Theoretical)	70.21 Ω	-	-	6.3 dBm
Without substrate	70.21 – j20.95 Ω	-16.68 dB	1.35:1	6.43 dBm
With substrate (match 75 Ω)	45.04 + j2.30 Ω	-12.82 dB	1.61:1	6.72 dBm
With substrate (match 50 Ω)	45.04 + j2.30 Ω	-25.55 dB	1.11:1	6.32 dBm

From Table 4.2 it can be seen how the real part of the radiation resistance decreased from a theoretical value of 70.21 Ω (as confirmed by the dipole simulation without the substrate) to 45.04 Ω through the addition of the substrate below the dipole. This research could use these results to confirm the hypothesis since the equivalent circuit for the dipole would be based on the results obtained through EM simulations at 60 GHz where these parasitic components could not be ignored. The imaginary part of the radiation resistance should in theory be equal to 0 Ω, and the simulated results presented an imaginary impedance (with substrates) of approximately +j2.30 Ω. The reflection coefficient of the dipole without the substrate was -16.68 dB compared to the theoretical value of -16.60 dB. This value increased to -12.82 dB for the dipole when the substrate was added and it was matched to 75 Ω. When matched to 50 Ω, the reflection coefficient decreased (improved) to -25.55 dB due to the closer match to the real radiation resistance of the dipole. The *SWR* values followed the same pattern with an improved ratio of 1.11:1 for the dipole matched to 50 Ω. The actual transmitted power varied within 2 % from the theoretical value when no substrate was added, and 6 % and 0.5 % with the substrate added and matched to the 75 Ω and 50 Ω load respectively. The simulation results presented in this section were used as the fundamental results for modelling an electrical equivalent circuit model of a dipole antenna operating at 60 GHz. The equivalent circuit was based on first iteration on the design of the dipole antenna where no substrate is added, and an improved model is used to represent the parasitic effect of the silicon substrate it is placed on.

4.3 DIPOLE MODEL

The design of the equivalent circuit for the dipole antenna operating at 60 GHz was based on the analysis of the real and imaginary impedance simulations given in section 4.1. Analysing the complex impedance of the dipole antenna contains sufficient data to represent the antenna using an electrical circuit [**12**]. Operation in the frequency domain and characteristics of its capacitive, inductive, or purely resistive behaviour is contained in this data. Scattering parameters were also analysed to determine the resonant frequency of the proposed equivalent circuit.

The outcome of this section provides an analysis on the results obtained to highlight the possibility of an equivalent electrical circuit in the 130 nm technology that completely represents the operation and characteristics of the dipole antenna simulated in section 4.1.

Successful representation of the antenna could provide the opportunity to use this equivalent circuit as a path-loss prediction model, and quoting from the hypothesis: *"If an equivalent electrical circuit model of a radiating antenna…in the mm-wave spectrum, using only passive components…"* the implementation should be possible using only passive components in the mm-wave spectrum. Key considerations in this section include:

- To use existing techniques as a *control* to represent an antenna transfer function with an equivalent electrical circuit, and determining the validity of these techniques in the mm-wave spectrum using the 130 nm technology.
- To determine the accuracy and limitations of the *control* circuit, and if these limitations prevent accurate representation of the antenna, finding a solution to improve accuracy through electrical circuit theory.
- To obtain an imaginary input impedance of the *control* circuit that represents the EM dipole antenna with at least 5 % accuracy at 60 GHz and broadband accuracy with average error less than or equal to 10 %.
- To ensure that the analytical representation of the imaginary impedance over a broad band accurately represents the *operation* of the EM with *frequency* errors of less than 5 %.
- If the accuracy for the imaginary input impedance can be reached, this should inherently ensure that the error of the reflection coefficient of the equivalent circuit compared to the EM dipole should be less than 5 %.
- To implement an analytical technique in software to determine component values for the equivalent circuits as opposed to using computer intensive techniques to solve cumbersome transfer functions.
- If such solutions exist, using it to represent the antenna as an IC and verifying its operation through simulated and measured results.

A technique to determine the frequency and phase-dependent transfer functions is to directly measure or simulate the S-parameters of the transmitting and receiving antenna pair, where the poles and residues can be extracted from this data to express the transfer function in the frequency domain. In [**12**] it was attempted to simultaneously model the antenna input impedance and the transfer function, however, only the input impedance was modelled by the circuit elements and the transfer function was not, making this technique complex when designing circuits with desired resonant frequency. Correlating the input impedance and the transfer function was done in [**12**], however, at lower frequencies (up to 6 GHz) and the analysis did not take into account any parasitic elements that may incur changes on the EM antenna. This work aimed to use the techniques presented in [**12**] but extended for mm-wave frequency operation, while including parasitic effects and limitations of the proposed technology node. The complex input impedance at low frequencies, near the resonant frequency, and at high frequencies were analysed and used to determine component values.

As a preliminary approximation of the dipole antenna, the technique presented in section 4.2.1 was followed.

4.3.1 Preliminary dipole equivalent circuit

To determine a preliminary approximation for the dipole equivalent circuit, the transfer curve of Figure 4.4 was combined with the electrical properties of the circuit in Figure 2.10, the *Foster canonical form* for an electrical antenna. Analysis on the frequency band between 40 GHz and 90 GHz was chosen to ensure that the equivalent circuit operated correctly within a large enough band, but without taking into consideration frequencies where the capacitive or inductive behaviour of the antenna was beyond the limitations of the process.

To determine the low frequency operation ($f < 40$ GHz) of the circuit presented in Figure 4.4, (2.27) in section 2.4.1 is rewritten in [**12**] to calculate the output voltage ($V_{out}(s)$) of the electrical antenna (assuming operation below the second resonance) as

$$V_{out}(s) = \frac{sC_0Z_T}{1+sC_0Z_T} L_{eff}E_{in} \tag{4.17}$$

where Z_T is the impedance of the circuit, L_{eff} is a frequency *independent* constant [**12**] and E_{in} is the incident electric field. The antenna impedance is dominated by C_0 and if the circuit load is small, the transfer function follows a first-derivative relation. If the load is large (in relation to C_0) the transfer function approached a linear relation without any dispersion. Relating this analysis of the lower frequency operation of the antenna to the results obtained in Figure 4.4, it seemed that the (capacitive) complex input impedance of the antenna was determined mainly by the value of capacitor C_0 and that the inductor L_0 acted as a short-circuit. Since the parallel combination of L_1 and C_1 (refer to Figure 2.10) operated below its resonance, the value of C_0 was assumed to dominate the circuit input impedance. The value of C_0 was determined by

$$C_0 = \frac{1}{2\pi f|X_{C_0}|} \tag{4.18}$$

where f was 40 GHz and X_{C_0} was -j80 Ω (obtained from the EM results in Figure 4.4). The value for the capacitance was therefore calculated to be 50 fF.

The higher frequency operation ($f \geq 90$ GHz) was analysed in a similar way, and the positive increase in complex impedance as a function of frequency proved predominantly inductive (with C_0 now operating as a short circuit). Therefore, L_0 was calculated as $L_0 = 2\pi f\left|X_{L_0}\right|$ to be 53 pH.

The transfer function for the complex input impedance of the dipole antenna in the frequency band of $40 \leq f \leq 90$ GHz was analysed differently in this work compared to the techniques presented in [**12**] and offer an intuitive and analytical approach combined with first principle circuit theory as mentioned in section 2.4.1. Analysing Figure 4.4 with respect to (2.26) containing 6 variables (for the initial circuit), becomes computationally cumbersome and therefore a more analytical approach was proposed. The proposed technique involved analysing the differential (slope) of Figure 4.4 and identifying points on the curve that can be related to the electronic circuit components. The slope of Figure 4.4 is defined as

$$\frac{d(X_C(f)+X_L(f))}{df} \tag{4.19}$$

where $X_C(f)$ and $X_L(f)$ are the frequency (in Hz) dependent complex capacitive and inductive reactances respectively, differentiated with respect to f.

From Figure 4.4 it can be seen that there exist a local maximum and a local minimum at frequencies of 59 GHz and 83.2 GHz respectively. These points could be defined mathematically as

$$\frac{d(X_C(f)+X_L(f))}{df} = 0 \tag{4.20}$$

and comparing this results to electrical circuit behaviour, it was deducted that at the local maximum (59 GHz) the transfer function reached a point of maximum capacitive reactance and the inductive reactance started dominating the circuit. Therefore at this point, the frequency could be estimated by

$$f = \frac{1}{2\pi\sqrt{L_1(C_0+C_1)}} \tag{4.21}$$

whereas at this point L_1 dominated the inductive reactance and L_0 was thus neglected. Similarly, at the local minimum (83.2 GHz), the capacitive reactance was at its minimum and the inductive reactance completely dominated the circuit (as parallel resonance was already reached), and through this the frequency was estimated at

$$f = \frac{1}{2\pi\sqrt{L_1(|C_0-C_1|)}} \tag{4.22}$$

and the output impedance was also dominated by L_1 (the parallel combination with the real load impedance). The point in between the local minimum and local maximum where the slope reached its maximum negative value, was mathematically described by

$$\frac{d(X_C(f-\Delta f)+X_L(f-\Delta f))}{df} < \frac{d(X_C(f+\Delta f)+X_L(f+\Delta f))}{df} \tag{4.23}$$

and this point represented the parallel resonance of the circuit, at the frequency

$$f = \frac{1}{2\pi\sqrt{L_1C_1}} \tag{4.24}$$

where $X_C = |X_L|$ and the output impedance seen from the load is at its minimum absolute (real) value. In Figure 4.4 this point is at a frequency of 70.6 GHz. From this analytical approach, a MATLAB script (refer to Appendix A) was developed to determine the optimum component values. The upper and lower limits of the component values were related to the limitations incurred by the 130 nm process. These component values, estimated parasitic capacitances, and simulated results are given in Appendix A (Table A.1 and Figure A.1) and can be referenced to as a comparison to the 130 nm circuit simulations.

To improve the performance (obtain accurate impedance values while maintaining circuit operation) of the electrical circuit, an improved dipole model based on the *Foster canonical form* was introduced to overcome the component limitations. The initial circuit (with ideal circuit components) was transferred to a 130 nm technology node (using the supplied library models) to represent the IC performance. The results are depicted in Figure 4.16.

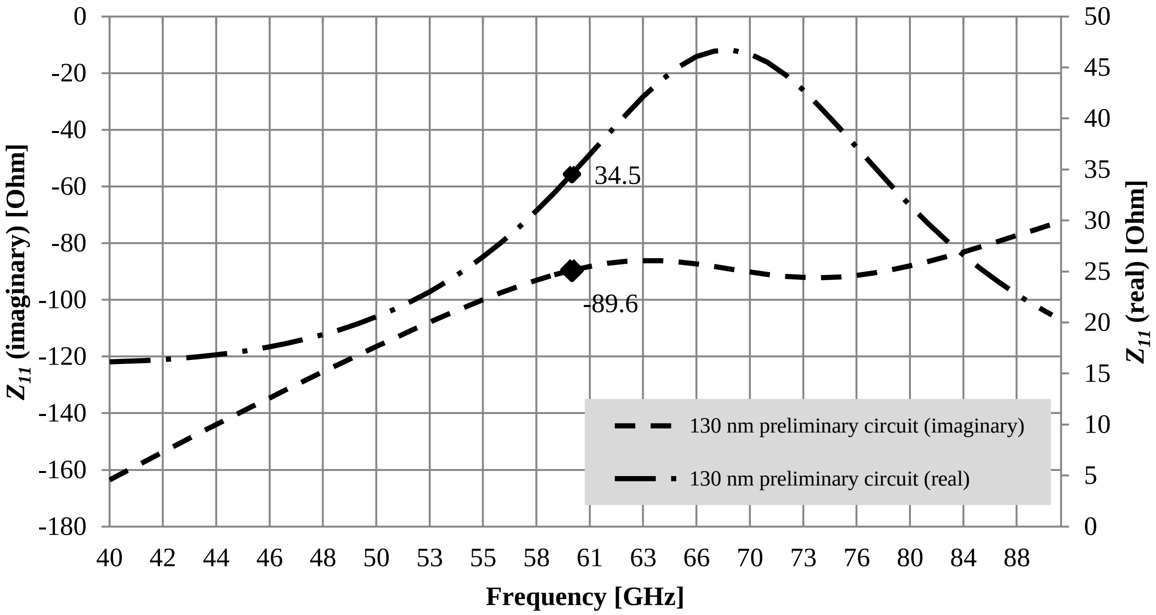

Figure 4.16: Initial electrical circuit Z_{11} real and imaginary impedance (130 nm).

From Figure 4.16 the imaginary impedance of the 130 nm circuit (-j89.6 Ω at 60 GHz), although it still conforms to the design approach in terms of circuit operation, it does flatten in its response and displays a smaller difference in capacitive and inductive reactances between 40 GHz and 90 GHz. The real impedance at 60 GHz is again lower (at 34.5 Ω) as the 130 nm circuit components introduce parasitic impedances in parallel and lowers the overall output impedance seen from the load. The imaginary impedances of the dipole without a substrate, ideal initial electrical circuit, as well as the imaginary impedance of the 130 nm initial circuits are given in Figure 4.17.

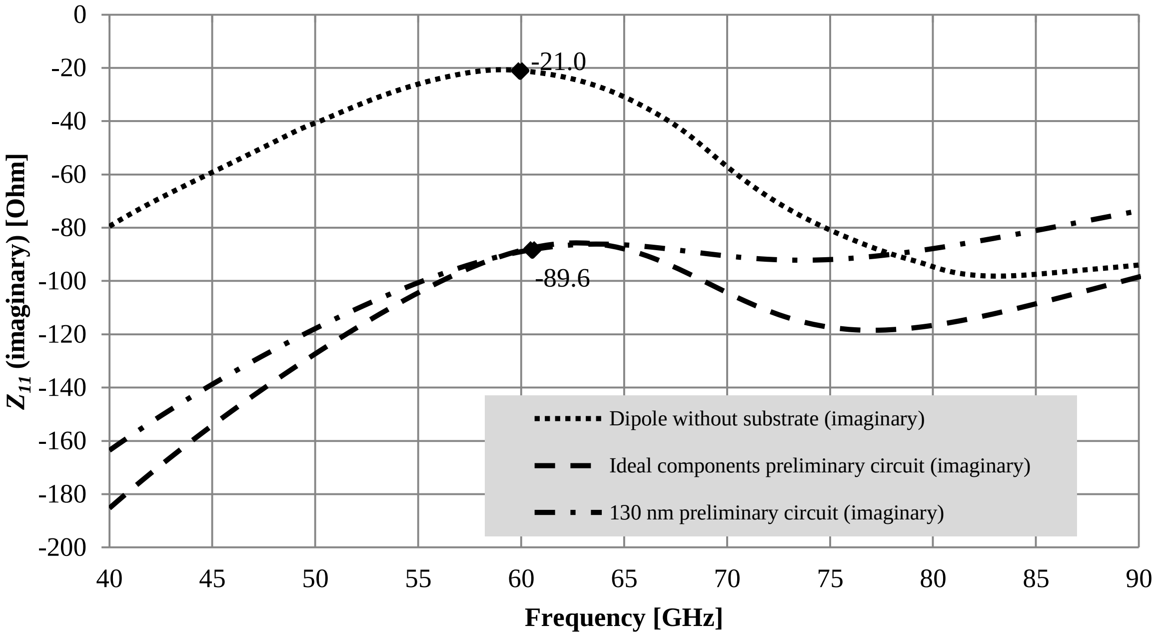

Figure 4.17: Imaginary impedance of dipole without substrate, and preliminary (ideal and non-ideal components) electrical circuits.

Comparing the results obtained in Figure 4.17 it was evident that the circuit operation of the electrical equivalent circuits represented the operation of the dipole antenna without a substrate; however, the values of the impedance were limited by the component values of the 130 nm process. An improved equivalent circuit was needed to better represent the operation of the dipole, as was also evident from the real impedance values in Figure 4.18.

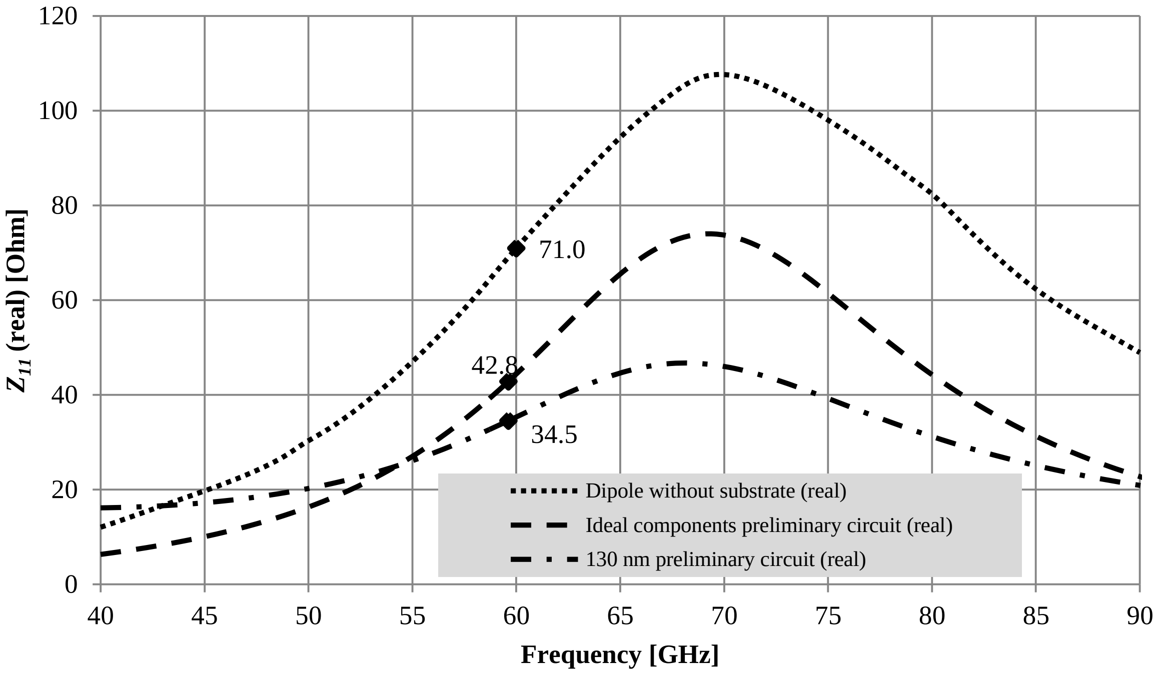

Figure 4.18: Real impedance of dipole without substrate, and preliminary (ideal and non-ideal components) electrical circuits.

The real impedance of the dipole without the substrate, and the ideal and non-ideal (130 nm) electrical circuits displayed similar results, as the operation of the circuits was similar but the real value of the impedance lowered with the introduction of parasitic elements in the non-ideal equivalent circuit, and the limiting component values in the ideal circuit. The resonance of the circuit was depicted by plotting the insertion losses of the dipole, and the ideal and non-ideal component equivalent circuit, as depicted in Figure 4.19.

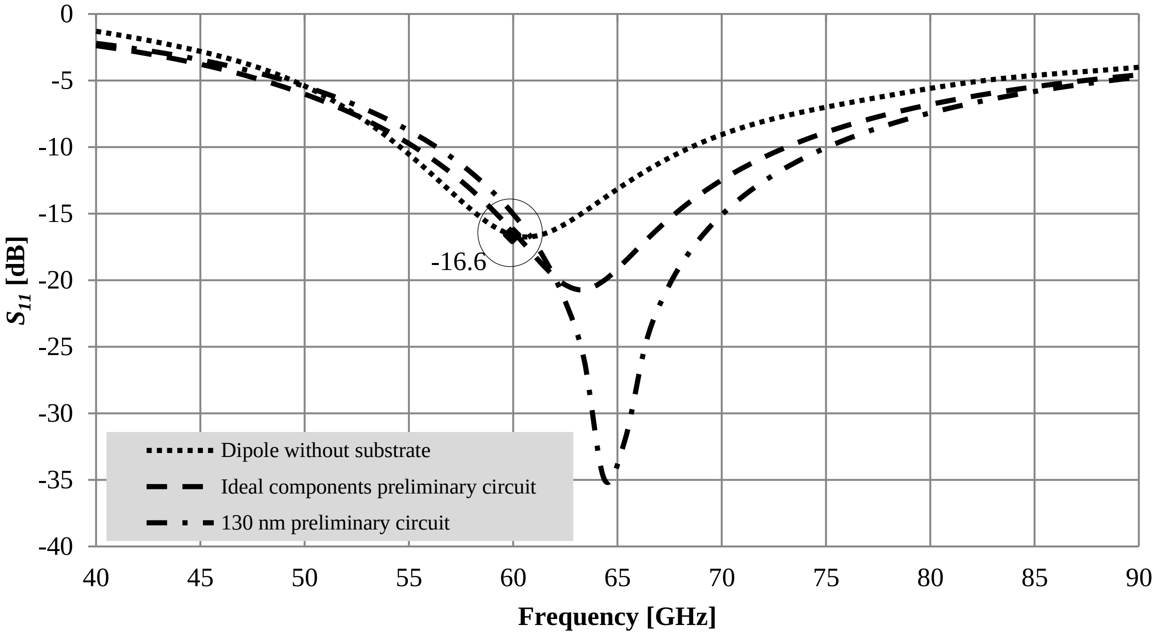

Figure 4.19: Reflection coefficient of the dipole without substrate, and preliminary (ideal and non-ideal components) electrical circuits.

The insertion losses as given in Figure 4.19 seemed to have a similar value at the operating frequency of 60 GHz (-16.6 dB), however, the point of resonance moved away from the required 60 GHz, with resonance occurring at around 64 GHz for the initial 130 nm equivalent circuit, displaying a reflection loss of -35 dB at 64.3 GHz. The initial *Foster canonical form* electrical equivalent circuit could potentially represent the dipole at mm-wave frequencies; however, implementing this equivalent circuit using non-ideal component models (supplied by the technology process) introduced parasitic components that shifted resonance.

4.3.2 Improved dipole equivalent circuit

The addition of the substrate to the EM dipole antenna during simulations added a degree of freedom to the results, as the scattering and absorption of the transmitted signals in the substrate (matched to 75 Ω) displayed that the depth of the substrate could be modified to completely match the dipole itself, and therefore resonate at the desired frequency without having to change the length of the dipole to accommodate for the parasitic and intrinsic effects of the added substrate. The addition of the substrate also required a modified equivalent electrical circuit to account for these parasitic elements, together with additional components to improve the results obtained from the initial circuit. The improved equivalent electrical circuit is displayed in Figure 4.20.

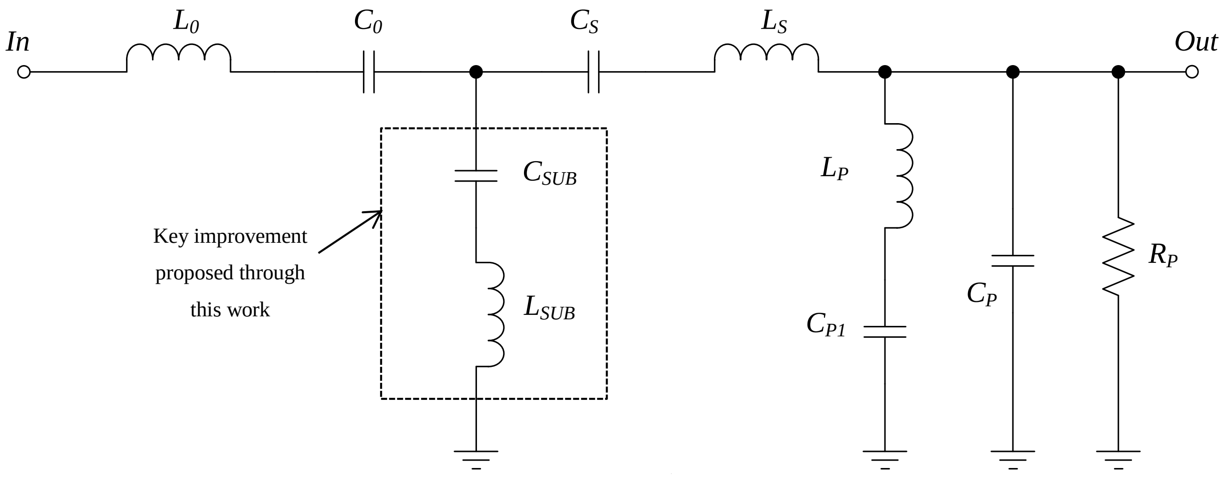

Figure 4.20: Improved equivalent electrical circuit based on the *Foster canonical form* for electrical antennas.

From Figure 4.20, the addition of parallel resonance through C_{SUB} and L_{SUB} accounted for the parasitic elements introduced by adding the substrate to electromagnetically simulated dipole antenna. C_S and L_S are series resonant capacitive and inductive elements introduced between the parallel networks for the substrate effects and the output of the antenna, and these elements added two degrees of freedom to the circuit design to account for the limitations incurred by designing the equivalent circuit based on component limitations of the 130 nm process. This novel approach moved away from the general approach to add resonant circuits at the output of the *Foster canonical form* as this added unwanted circuit resonances not evident in the results obtained in EM simulations, and also lowered the minimum and maximum obtainable complex impedances as seen from the load, to effectively and accurately represent the transfer functions. The addition of the inductor L_P also added the ability to increase the range between the minimum and maximum imaginary impedance in the frequency band between 40 GHz and 90 GHz without having a large effect on the impedance at lower or higher frequencies. L_P was used to fine-tune the resonant frequency around the operation frequency. The simulated results for these component values, using ideal components, are presented in Appendix A (Table A.2 and Figure A.2) as reference to the changes occurring when implemented using 130 nm components.

The improved equivalent electrical circuit using the 130 nm process results of the real and imaginary impedance is depicted in Figure 4.21.

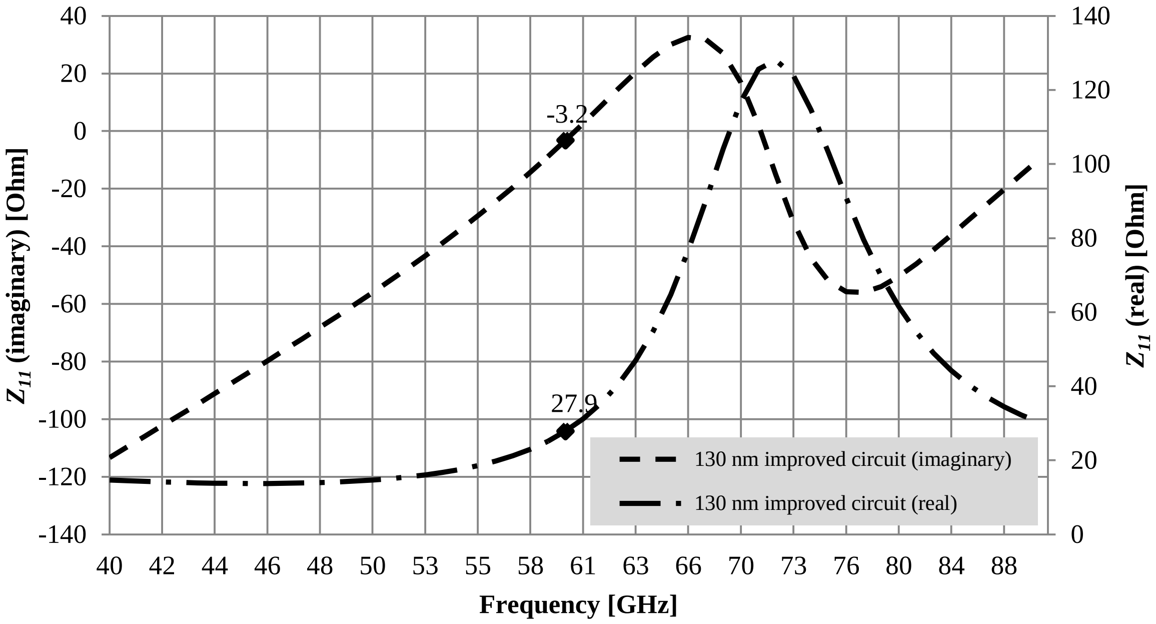

Figure 4.21: Improved electrical circuit Z_{11} real / imaginary impedance (130 nm).

The results of implementing the 130 nm process for the improved equivalent electrical circuit in Figure 4.21 showed that although the circuit operation remained similar to that of the EM dipole antenna, some changes to the operation of the improved circuit was in fact noticeable. The local maximum and minimum of the imaginary impedance shifted somewhat in frequency (to 67.4 GHz and 78.5 GHz respectively), and the mid-point (maximum real impedance) shifted to 72.7 GHz. The real impedance at 60 GHz changed due to the parasitic elements introduced at the circuit output, to 27.9 Ω as opposed to 21.7 Ω for the ideal circuit. At 60 GHz the circuit was now also slightly capacitive with imaginary impedance of –j3.2 Ω as opposed to +j2.4 Ω although this value was still within ±j5 Ω of the required value (+j2.30 Ω from Figure 4.8).

To effectively compare the circuit operation of the EM dipole antenna with a substrate to the ideal and non-ideal component (130 nm) electrical circuits, Figure 4.22 and Figure 4.23 graph the imaginary and real impedances of these three simulations respectively.

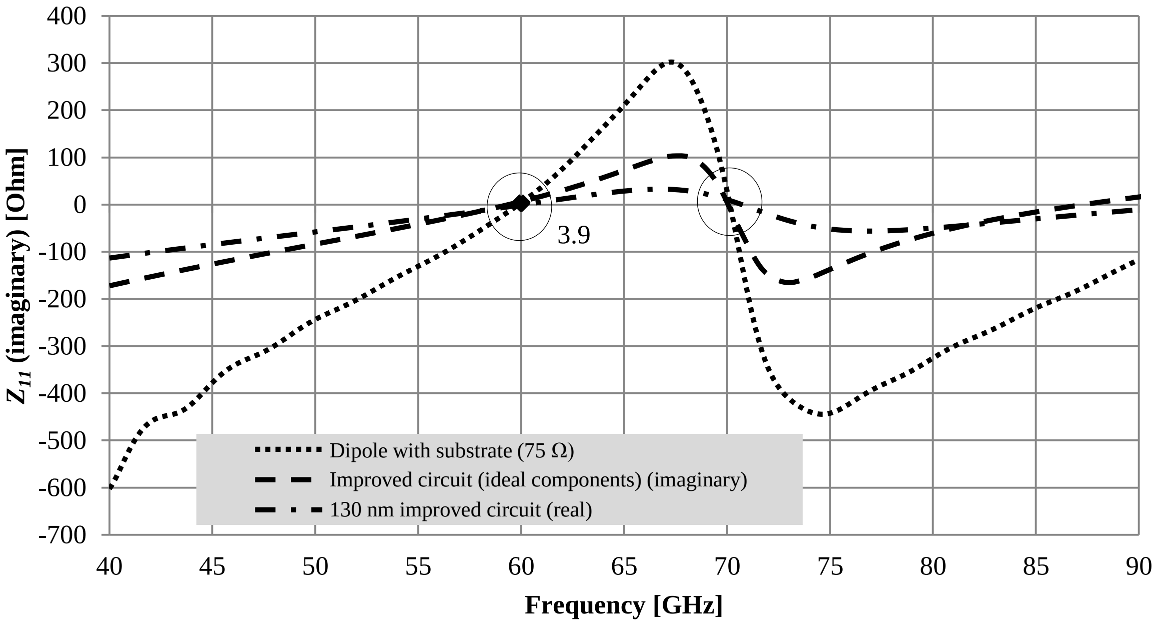

Figure 4.22: Imaginary impedance of dipole with substrate (75 Ω), improved (ideal and non-ideal components) electrical circuits.

From Figure 4.22, since the circuit operation could be entirely described by the form factor of the imaginary impedance of a circuit [**12**], it was evident that although the values of the imaginary impedance does not necessarily peak at the maximum and minimum values of the EM dipole antenna due to limitations incurred by the 130 nm component values, the dipole antenna operation between 40 GHz and 90 GHz can be represented by the improved equivalent electrical circuit of Figure 4.20 by accounting for the substrate parasitic effects (C_{SUB} and L_{SUB}) and adding degrees of freedom through C_S, L_S, and C_{P1}. A similar comparison for the real impedances between 40 GHz and 90 GHz is given in Figure 4.23.

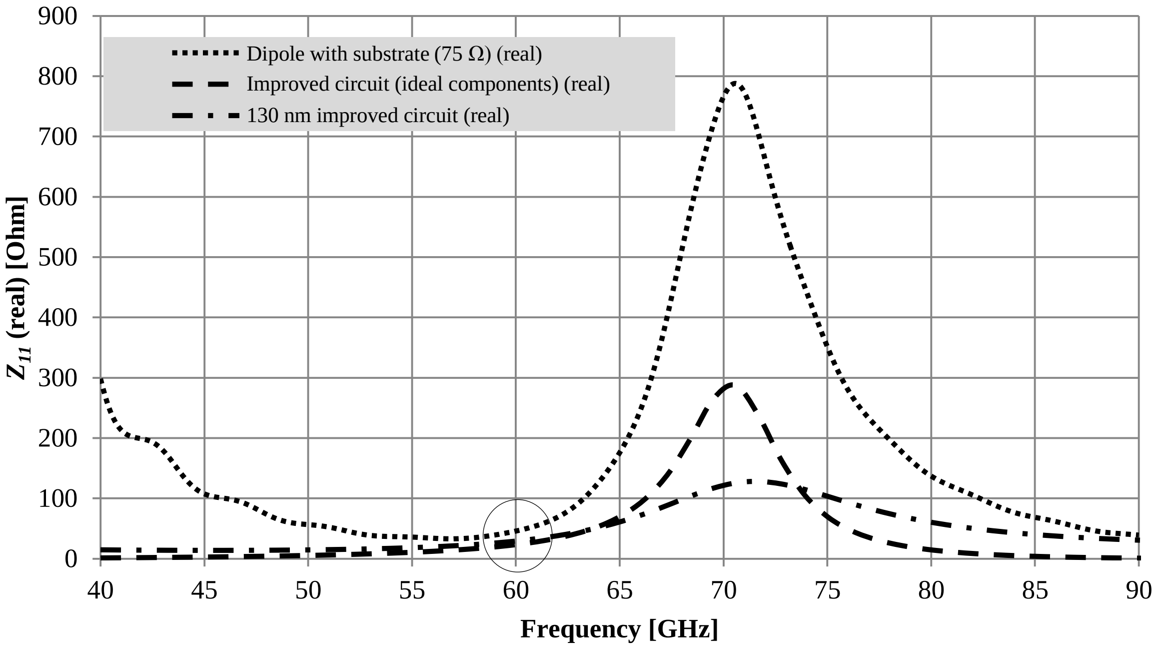

Figure 4.23: Real impedance of dipole with substrate (75 Ω), improved (ideal and non-ideal components) electrical circuits.

Figure 4.23 again outlined the fact that although the (large) real impedance value at resonance cannot be achieved as a result of component value limitations, the operation of the dipole antenna (thus the transfer function) can be represented by the improved equivalent electrical circuit. It could also be seen that the real impedance at the required frequency (60 GHz) was represented well with the electrical circuit (close to the 45.04 Ω of the dipole with substrate and matched to 75 Ω).

A comparison of the reflection coefficient of the dipole antenna and the improved 130 nm electrical circuit is given in Figure 4.24.

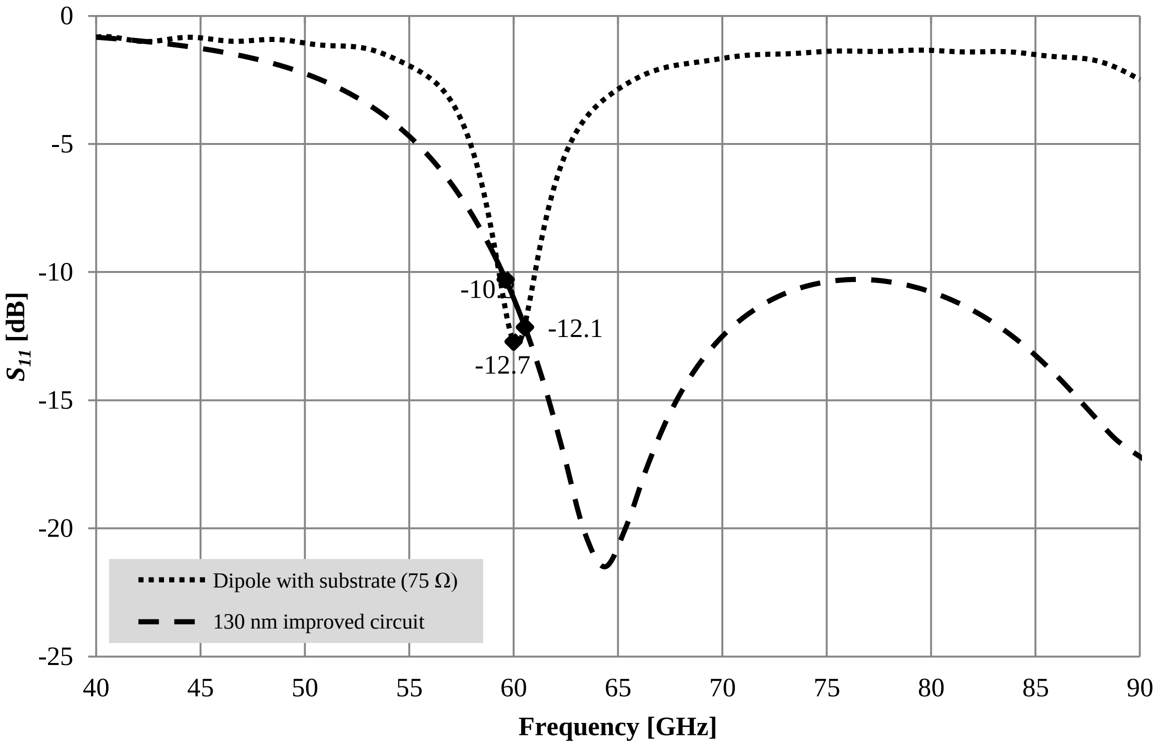

Figure 4.24: Reflection coefficient of dipole with substrate (75 Ω), improved (ideal and non-ideal components) electrical circuits.

The reflection coefficient at 60 GHz of the dipole antenna was -12.7 dB, and the value for the improved electrical circuit was ±-11 dB (between -10 dB and -12.1 dB – averaged as a result of the default step-size in the simulation profile). The resonant point of the reflection coefficient for the 130 nm electrical circuit shifted away from 60 GHz to ±64 GHz (-21.8 dB) as a result of parasitic reactances of the components at high frequencies.

Overall comparisons of the imaginary and real impedances for the electrical circuits (initial ideal and non-ideal components and improved circuit with ideal and non-ideal components) are given in Figure 4.25 and Figure 4.26 respectively.

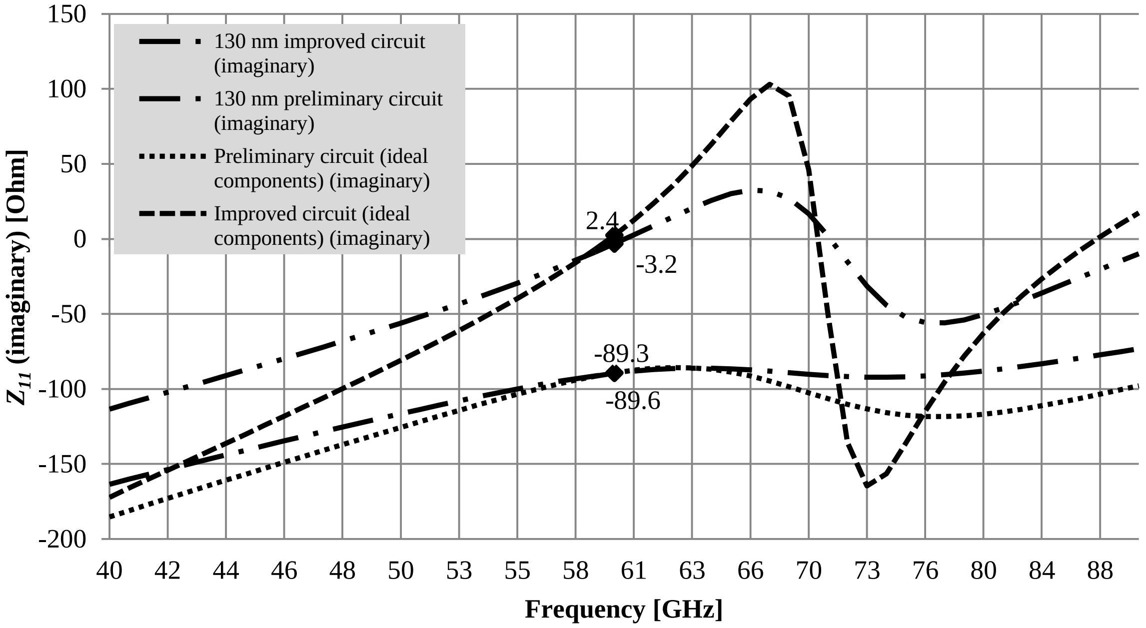

Figure 4.25: Imaginary impedance of initial and improved (ideal and non-ideal components) electrical circuits.

From Figure 4.25 the difference between the imaginary input impedance of the preliminary *Foster canonical form* electrical circuit and the improved dipole model is evident. At 60 GHz, both circuits (preliminary and improved) show good correlation between the circuit proposed using ideal component values and the 130 nm based circuits, with a j0.3 Ω mismatch at 60 GHz for the preliminary circuits, and a j5.6 Ω difference between the improved circuits. Figure 4.25 also depicts the increased ratio between capacitive and inductive behaviour of the improved circuit compared to the preliminary equivalent circuit, and compared to Figure 4.8, the improved circuit shows good correlation with the EM dipole over a large bandwidth (refer to Figure 4.22). A similar comparison between the preliminary equivalent circuit and the improved circuit, based on its real impedances over a large bandwidth, is shown in Figure 4.26.

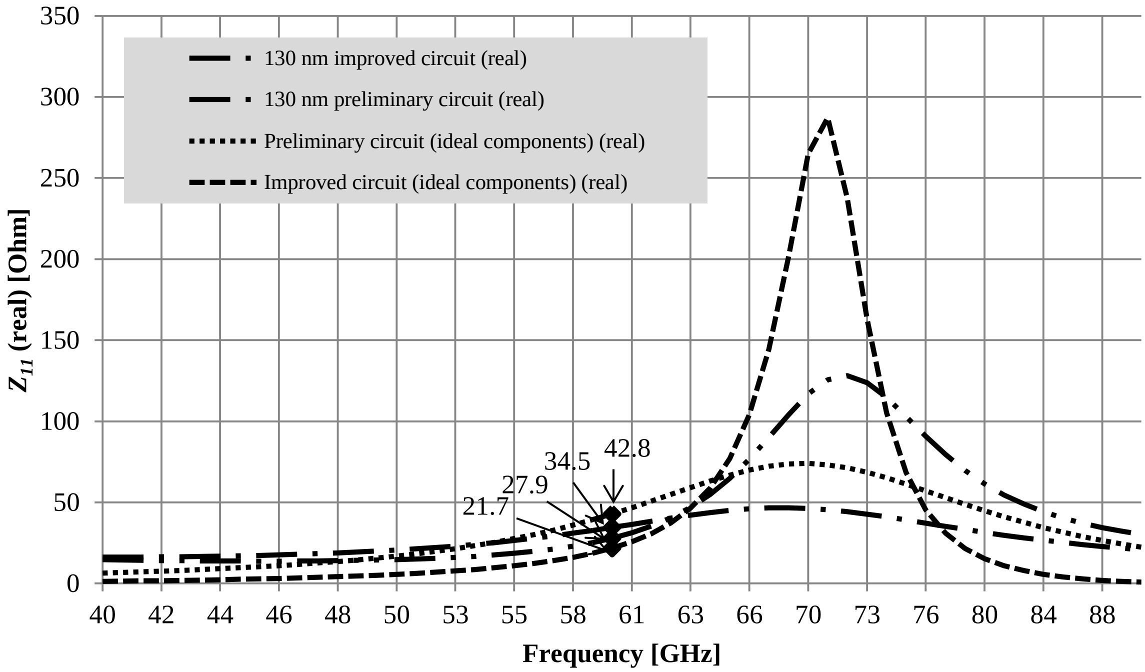

Figure 4.26: Real impedance of initial and improved (ideal and non-ideal components) electrical circuits.

From Figure 4.26 the real impedance behaviour at the output of the preliminary and improved circuits is evident. The real impedance at 60 GHz lowers with the addition of passive components to the equivalent circuit due to increased parasitic losses of non-ideal components at mm-wave frequencies, but circuit operation is maintained throughout the frequency range. The improved equivalent circuit using ideal components displays the largest resonant peak for the real impedance at 70.58 GHz with impedance 287.20 Ω, which decreases to 125.62 Ω when implemented using the 130 nm process. This change in impedance near the series resonant frequency compared to the preliminary circuit is due to the addition of the series resonant capacitive and inductive element the C_S and L_S as shown in Figure 4.20. This effect is briefly described with regards to the simplified capacitor and inductor model for the process in Figure 4.27.

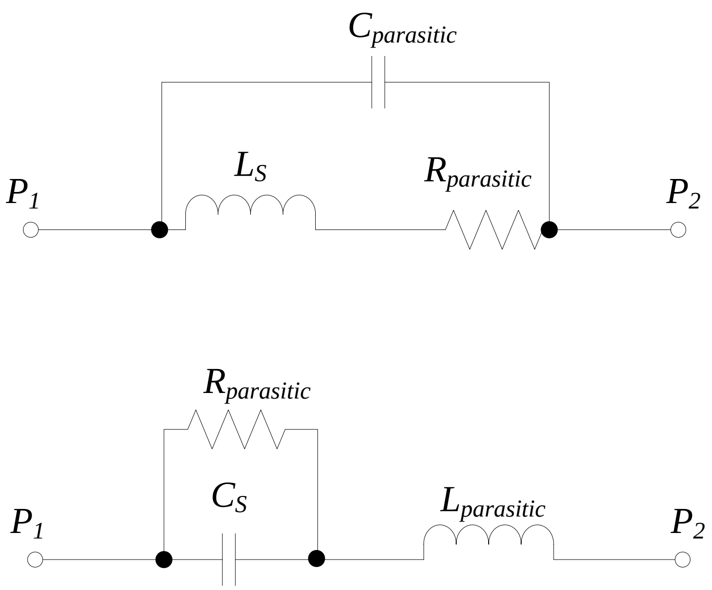

Figure 4.27: Simple inductor L_S (top) and capacitor C_S (bottom) model.

From Figure 4.27, $C_{parasitic}$, $R_{parasitic}$, and $L_{parasitic}$ represent parasitic capacitance, resistance, and inductance respectively, whereas C_S and L_S are the required capacitance and inductance values. At frequencies below the series resonant frequency, in the inductor model (top circuit in Figure 4.27), the parasitic resistance $R_{parasitic}$ dominates and is generally a low value of smaller than 25 Ω. At high frequencies, the signal passes through the parasitic capacitor $C_{parasitic}$ (refer to sections 3.1.1 and 3.1.2 for approximate values) and the parasitic resistance is also minimized, therefore the largest effect of increased parasitic resistance occurs near the resonant frequency where X_L is large. Similarly, for the capacitor model (bottom of Figure 4.27), at low frequencies, $R_{parasitic}$ (generally a small parasitic value of less than 25 Ω) dominates the circuit impedance, and at high frequencies the impedance of $L_{parasitic}$ (refer to section 3.1.2) dominates. Therefore at frequencies near the resonant frequency, the impedance is dependent on C_S, $R_{parasitic}$, and $L_{parasitic}$ and is largest at these frequencies.

4.4 PATH-LOSS MODELS

The mechanisms that introduce attenuation and loss of signal integrity at 60 GHz are discussed in section 2.1. The mechanisms are applied to the 60 GHz frequency band and three scenarios of communication systems in common working environments are modelled. This section aims to introduce the three scenarios, with relevant reference to section 2.1 and provides transfer functions of signal attenuation as a function of distance for each scenario. Table 4.3 provides values for parameters applicable to each scenario.

Table 4.3: Mathematically modelled attenuation for communication environments.

Attenuation mechanism	**Scenario 1**	**Scenario 2**	**Scenario 3**
	Varied parameter	**Varied parameter**	**Varied parameter**
Free-space loss	$n = 1.6$	$n = 2.0$	$n = 3.5$
Oxygen absorption	-	-	-
Reflection loss ($\theta_i = 80^{o}$)	Paper	Ordinary glass	Aluminium
Diffraction loss	$v = -1$	$v = 0$	$v = +1$
Rain-rate attenuation	$R_{0.01}$ = 5 mm/h	$R_{0.01}$ = 50 mm/h	$R_{0.01}$ = 150 mm/h

From Table 4.3 three scenarios were chosen to represent a 60 GHz transmission, based on environmental conditions that are commonly experienced. The first scenario represented a transmission over 30 m where the free-space loss exponent $n = 1.6$ (in building LOS). A thin sheet of paper halfway between the transmitter and the receiver resulted in reflection losses and a *Fresnel* diffraction loss parameter of $v = -1$ was chosen. A rain-rate of $R_{0.01}$ = 5 mm/h (estimated rain-rate for a climatic zone designated as desert by the South African Weather Service (SAWS) such as Brandvlei [**42**]) also contributed to the total losses of the signal. The second scenario represented a transmission over 30 m where $n = 2.0$ (free space). Ordinary glass halfway between the transmitter and the receiver resulted in reflection losses and a *Fresnel* diffraction loss parameter of $v = 0$ was chosen. A rain-rate of $R_{0.01}$ = 50 mm/h (estimated rain-rate for a climatic zone designated as Mediterranean by the SAWS such as Cape Town [**42**]) also contributed to the total losses of the signal. The third scenario represented a transmission over 30 m where $n = 3.5$ (urban area). Aluminium halfway between the transmitter and the receiver resulted in reflection losses and a *Fresnel* diffraction loss parameter of $v = +1$ was chosen. A rain-rate of $R_{0.01}$ = 150 mm/h (estimated rain-rate for a climatic zone designated as temperate by the SAWS such as Pretoria [**42**]) also contributed to the total losses of the signal.

The proposed attenuation function (2.17) for each scenario is displayed in Figure 4.28. The attenuation of each scenario is given for a distance of up to 30 m from the transmitting antenna, and attenuation is given in dB.

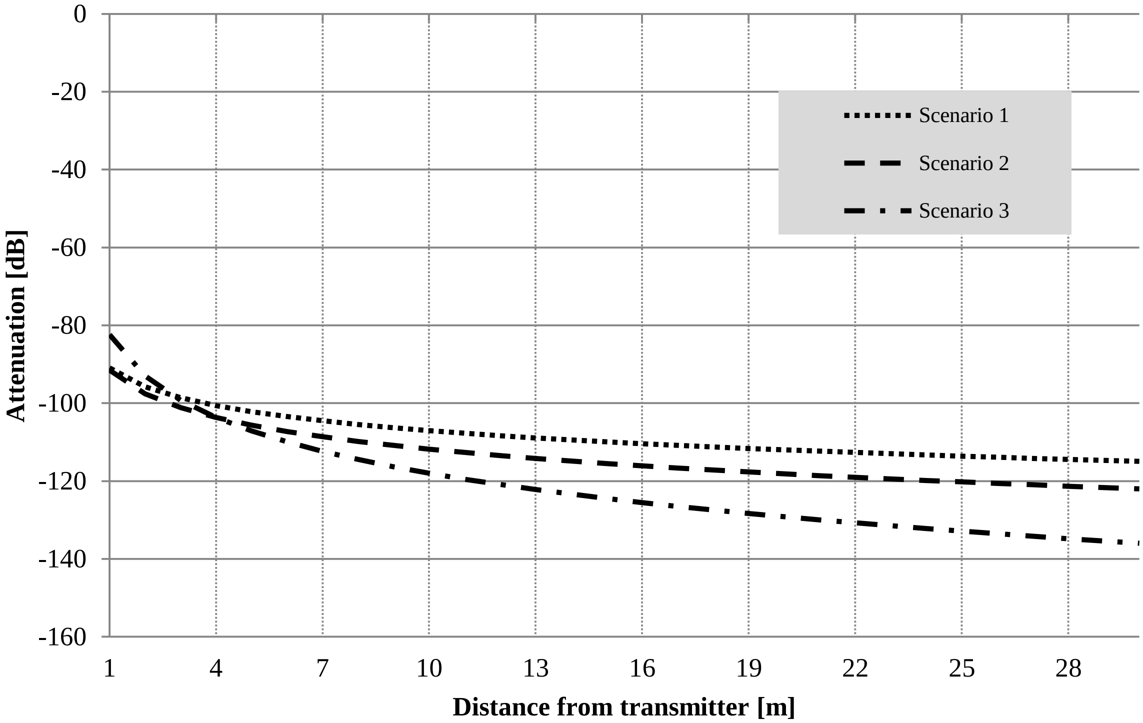

Figure 4.28: Proposed attenuation function for three different scenarios.

From Figure 4.28, it can be noted that the amount of attenuation for each scenario reaches a value of -100 dB already at a distance of only 2 m from the transmitter. The attenuation drops significantly at distances up to about 8 m, and then slowly reaches -120 dB at 30 m. For this work, measurements are obtained within the far-field region (refer to section 2.3.3). For practical purposes in terms of physical measurement set-up and limiting the amount of noise added to the measurements at high separation distances, the measurements are done within 2 m of the transmitting antenna. Variation of the electronic passive filter attenuation between -75 dB and -100 dB ($\Delta = 25$ dB) also reduces the complexity of the circuit design as compared to a variation between -75 dB and -120 dB ($\Delta = 45$ dB). Figure 4.28 therefore gives an approximation of expected attenuation for a 60 GHz signal at a range of distances from the transmitter, and can be used to investigate the research hypothesis (refer to section 1.2). The MATLAB functions created to determine the overall attenuation from the proposed attenuation function (2.17) are given in Appendix A. Each term (free-space losses, reflection, diffraction, and rain-rate attenuation) in (2.17) is accounted for separately (as a function of distance and / or nLOS material) and combined (oxygen absorption (10 dB/km or 0.01 dB/m at high altitude) is included) over the specified distance (30 m).

The expected amount of attenuation at 60 GHz for different scenarios have now been established, and in order to prove the research hypothesis that electronic circuits can represent this signal attenuation, the electronic filter is mathematically modelled to ensure that the amount of attenuation (approximately -100 dB) is in fact possible with existing passive filter models and technology limitations. Circuit complexity and size can become an issue if the filter order becomes impractically high, and attenuation of the signal using a lower order filter is preferred.

4.5 PASSIVE FILTER DESIGN (MATHEMATICAL APPROXIMATION)

The mathematical approximations for the *Butterworth*, *Chebyshev*, and *Bessel* passive filters are given in this section. Simulated results in MATLAB are also presented. These mathematical estimates are designed to have an attenuation of -100 dB (from Figure 4.28) at 60 GHz and serves as a first approximation of the expected transfer characteristics of the proposed electronic filters.

4.5.1 *Butterworth* filter

MATLAB simulation results for the proposed *Butterworth* filter are presented in Figure 4.29 and Figure 4.30. These simulations assumed ideal components and gave a first order representation of the attainable results without taking parasitic losses into account. Figure 4.29 represents the amplitude transfer function of the *Butterworth* 7th order LPF. The amplitude response (A_{dB}) of the *Butterworth* filter was determined by

$$A_{dB} = 10\log_{10}\left[1 + \left(\frac{\omega}{\omega_c}\right)^{2n}\right] \tag{4.25}$$

where n is the chosen order of the filter (for this work n = 7), ω and ω_c are the operating frequency and cut-off frequency (10 GHz) respectively.

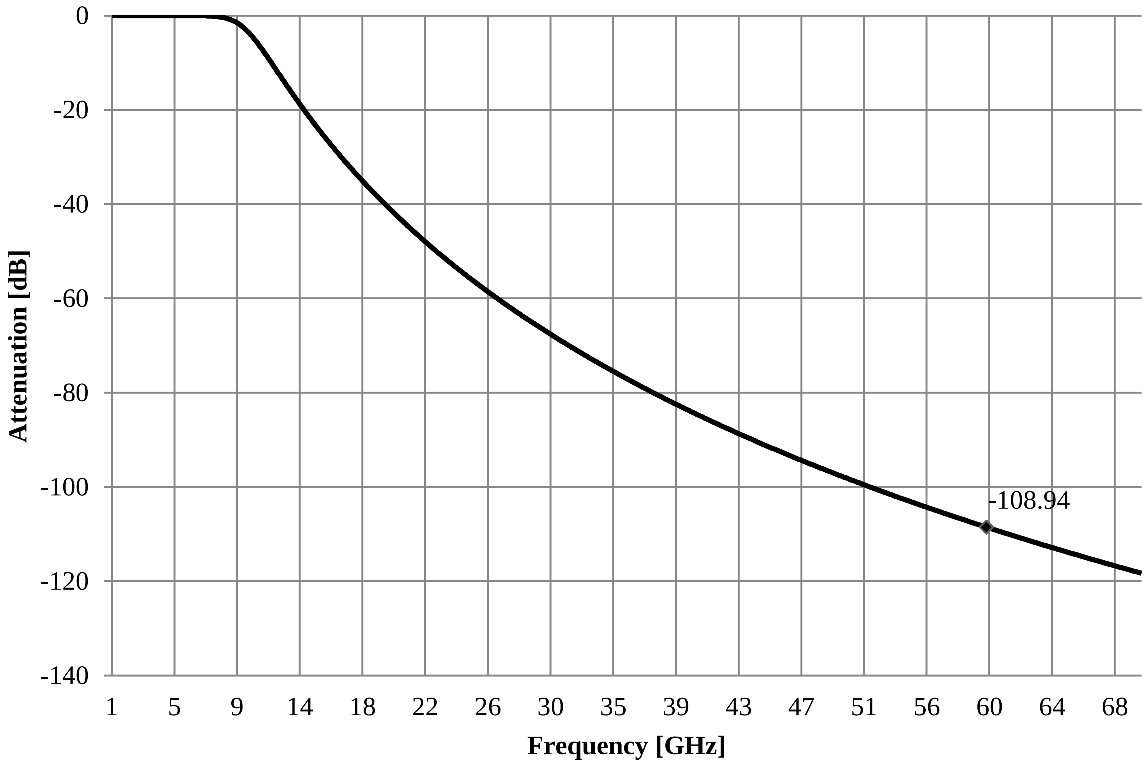

Figure 4.29: Amplitude response of 7th order *Butterworth* LPF.

The cut-off frequency of the 7th order *Butterworth* LPF was designed to be 10 GHz. Figure 4.30 represents a closer view of this frequency, adapted from Figure 4.29. The filter attenuation from 8 GHz up to 12 GHz is depicted, with the -3 dB crossing visible at 10 GHz.

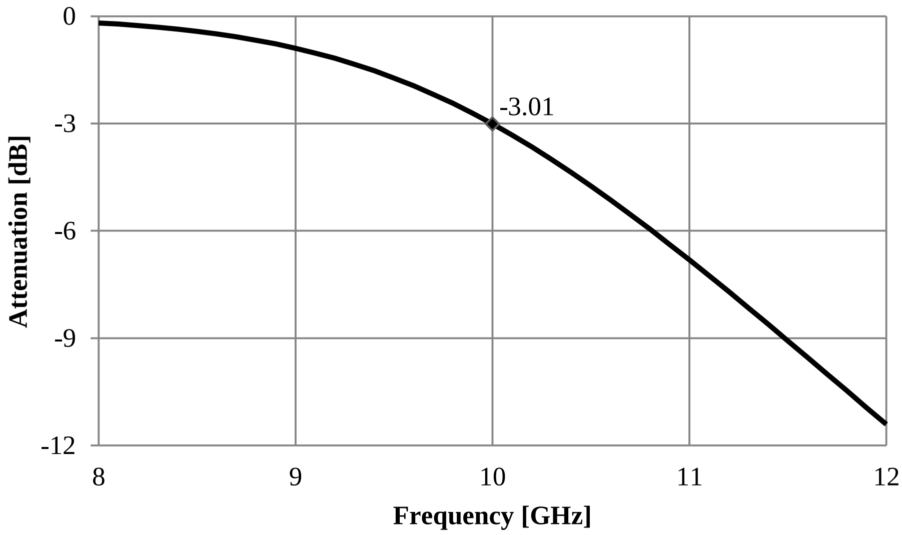

Figure 4.30: -3 dB attenuation of 7th order *Butterworth* LPF.

Figure 4.30 confirmed the cut-off frequency of 10 GHz for the *Butterworth* filter, and shows that the theoretical design of the proposed filter operated as required, and schematic design and simulations could be conducted. These simulations provided numerical representations of the filter transfer functions. The same procedure for the *Chebyshev* LPF is followed in section 4.5.2.

4.5.2 *Chebyshev* filter

The proposed *Chebyshev* LPF simulations gave a good representation of the attainable results without taking parasitic losses into account. Figure 4.31 represents the amplitude response of the *Chebyshev* 7th order LPF.

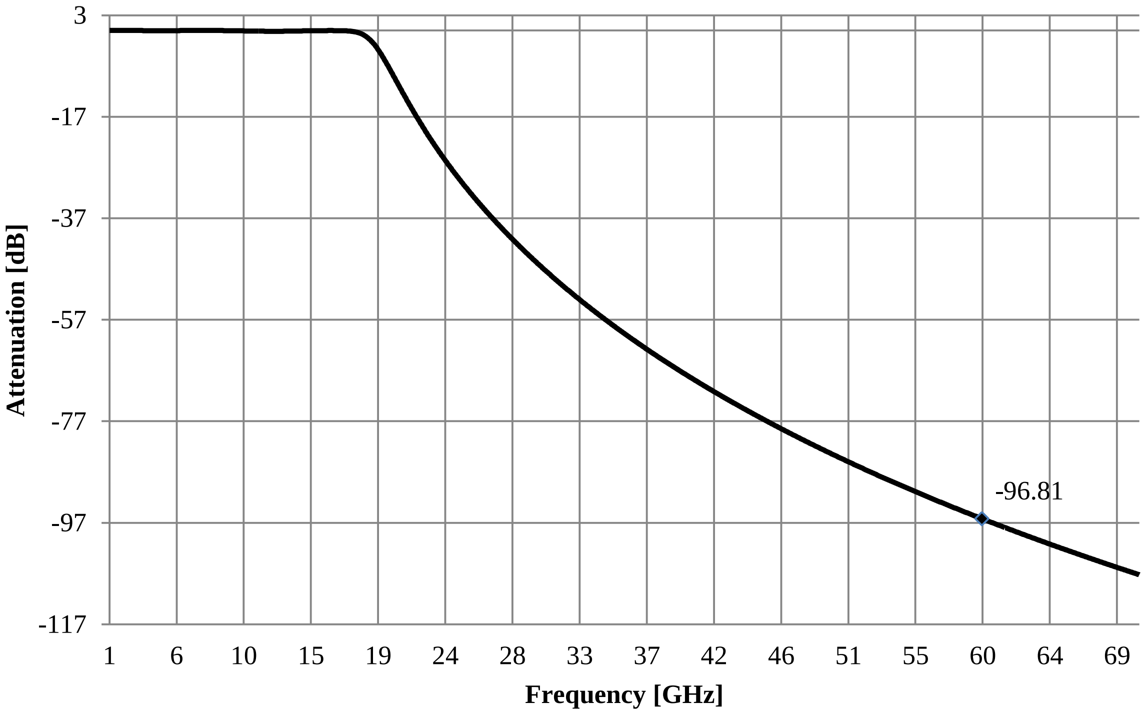

Figure 4.31: Amplitude response of 7th order *Chebyshev* LPF.

From Figure 4.31 it was not possible to measure the amount of ripple of the *Chebyshev* LPF as specified (0.01 dB). It was, however, possible to note that at frequency ranges of between 60 GHz and 64 GHz, an attenuation of -100 dB was achieved. The mathematical estimation of the maximum amount of ripple for the *Chebyshev* LPF was about 0.15 dB (absolute value) at 12 GHz, which was a value acceptably close to the specified value of 0.01 dB, considering the following ripple design bracket is at 0.1 dB. The -3 dB frequency was close to 19 GHz, whereas it was designed for 18 GHz (within 95 % of the designed value). The final LPF that was used in as a comparative measure was the *Bessel* LPF, as described in section 4.5.3.

4.5.3 *Bessel* filter

The normalization procedure provided in [**84**] for a n-th order *Bessel* filter transfer function provides accurate roots and delay parameters for the filter. For this thesis, the accuracy of the filter at 60 GHz is controlled by circuit enhancements as described in section 4.6. In [**68**] it is stated that at high frequencies (above the cut-off frequency) the transfer function should be represented as a straight line with 20 dB/octave attenuation. From simulation results it was validated that at 60 GHz, an attenuation of -106.2 dB is achieved. Up to the cut-off frequency (10 GHz), the numerical representation is valid, and is given in Figure 4.32.

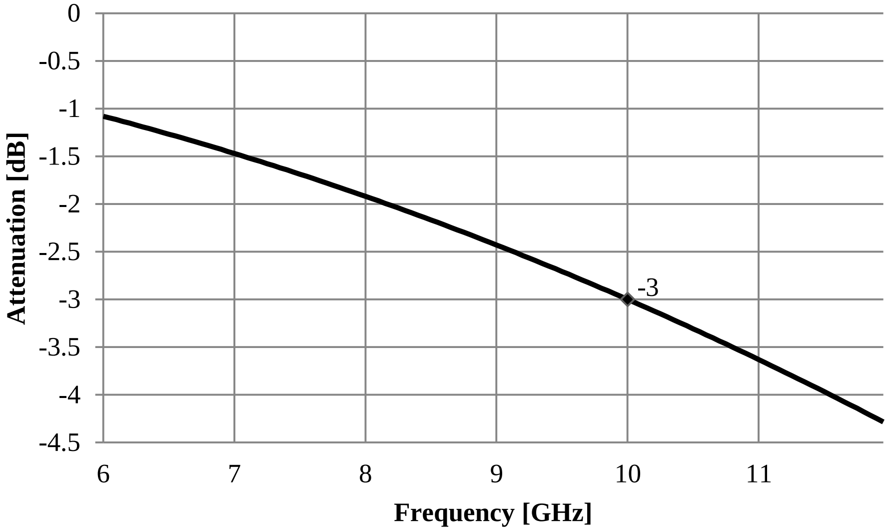

Figure 4.32: -3 dB attenuation of 7th order *Bessel* LPF.

From Figure 4.32 it is evident that the -3 dB cut-off frequency for the *Bessel* 7th order LPF is at 10 GHz as specified. The mathematical analysis for the design equations of the dipole operating at 60 GHz is given in section 4.3.

This section concludes that it is possible to obtain a signal attenuation of -100 dB using passive filters of order not exceeding 7. This is advantageous as higher order filter coefficient tables are not as readily available as for filter orders up to 7. All three filter types allow attenuation of -100 dB through a 7th order filter, and since all filters are therefore chosen to of an order 7, the circuit design complexity is decreased through reproducibility.

Simulation results using the 130 nm circuit components for -100 dB attenuation at 60 GHz required transmission lines of large geometries and therefore *W/L* ratios exceeding 100.

Implementing such large aspect ratios required dividing the transmission lines into subsections since the self-inductance of a long straight transmission line is not a linear function of its length. Cascading these sections could yield an equivalent transmission line. Skin effect losses are increased in longer transmission lines resulting in low quality factors.

One means of accounting for this frequency-dependent loss mechanism in the model is to use frequency dependent lumped elements (the resistive component increasing with frequency and the inductance decreasing). This approach has a large disadvantage due to the fact that general circuit simulators can only calculate the frequency dependent element value at one frequency point per simulation. This means that a frequency at which to calculate the element values is specified at simulation run-time and that value will be used for the entire simulation, even for broadband, multi-frequency, or transient simulations.

Relaxing circuit performance to an attenuation of -60 dB at 60 GHz proved to overcome this limitation by ensuring aspect ratios of 100 or less. It was still possible to verify the hypothesis of changing circuit parameters to represent changing environmental conditions with these relaxed specifications.

4.6 PASSIVE FILTER DESIGN (SIMULATED RESULTS)

The simulated results for the passive filters are summarized in this section. These results include the schematic simulations using ideal circuit components (no parasitic losses), followed by the simulated results obtained by implementing the 130 nm circuit library components. Parasitic effects of the 130 nm components are analysed and limitations to circuit performance identified. The following sections (sections 4.6.1 to 4.6.3) apply a common 7th order LC filter structure to realize the applicable filter (*Butterworth*, *Chebyshev*, and *Bessel*) where only the component ratios for each type of filter differ. The common circuit diagram is given in Figure 4.33, and can be referenced to in each of these sections.

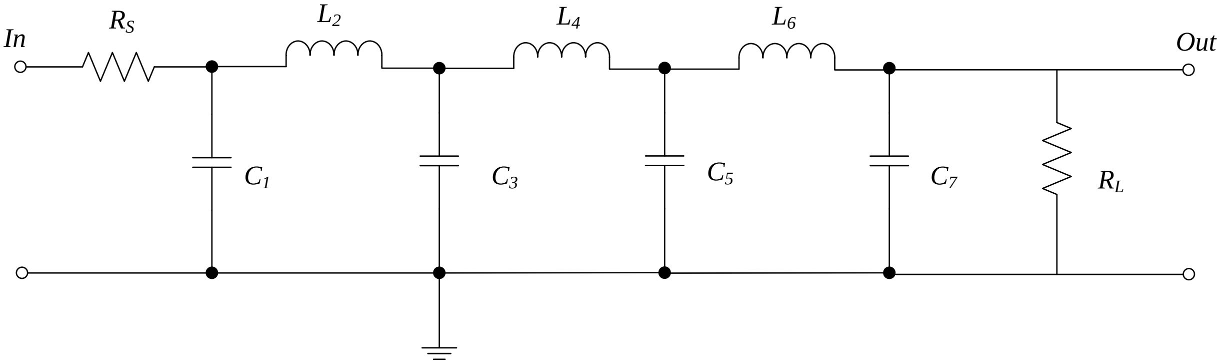

Figure 4.33: Schematic representation of 7th order LC LPF.

Figure 4.33 consists of 4 capacitors (C_1, C_3, C_5, and C_7), each commonly connected to the circuit ground and 3 inductors (L_2, L_4, and L_6) placed between these parallel-placed capacitor combinations. The series, source resistance R_S and load resistance R_L is also included in the circuit and its ratio is a determining factor for the LC component values and ratios.

4.6.1 *Butterworth* filter

The first step in the design of the *Butterworth* passive LPF was determining the cut-off frequency (f_c) that would enable an average of 60 dB (refer to section 2.1.7) attenuation at an operating frequency of 60 GHz (f). The attenuation at 60 GHz must be variable, and the circuit design to achieve this is outlined in this section. In order to achieve -60 dB attenuation a 7th order filter was chosen as this would allow for high attenuation closer to the cut-off frequency (steep roll-off). From [**68**], for a 7th order filter with attenuation of -60 dB to be possible, a frequency ratio f/f_c of 6 was obtained graphically.

From this ratio, a cut-off frequency of 10 GHz was required. With a normalized resistance value of $R_S/R_L = 0.7$ where the source resistance (R_S) was 50 Ω and the load resistance (R_L) was 73 Ω (equal to the output impedance of the dipole antenna), the following values were obtained for the 7th order filter circuit. The circuit is represented in Figure 4.33 and the obtained component values are given in Table 4.4.

The low-pass prototype circuit element values normalized to R_L = 1 Ω (C_n and L_n) are obtained in [**68**] with

$$A_k = 2\sin\frac{(2k-1)\pi}{2n} \tag{4.26}$$

where n is the number of elements in the filter structure, and A_k is the k^{th} reactance (k = 1, 2,…n) (capacitive or inductive). To determine the component values (C and L) for the 7th order *Butterworth* LPF, the following equations are used.

$$C = \frac{C_n}{2\pi f_c R_L} \tag{4.27}$$

$$L = \frac{L_n R_L}{2\pi f_c} \tag{4.28}$$

The capacitance and inductance values are given on the right-hand column of Table 4.4.

Table 4.4: Component values for the *Butterworth* LPF.

Component	**Element values (C_n and L_n)**	**Component values (C and L)**
C_1	0.151	33 fF
L_2	0.229	266 pH
C_3	0.713	155.5 fF
L_4	0.484	562 pH
C_5	1.106	241.18 fF
L_6	0.401	465.58 pH
C_7	0.774	168.86 fF

The component values obtained in Table 4.4 are within the attainable component values of the 130 nm technology node. The inductive values were large relative to the technology node specifications (L > 450 pH) and therefore the transmission lines used in the circuit layout were separated into smaller sections. Distributed passive connection guidelines are supplied within the 130 nm design rules to ensure coupling factors of less than 30 dB between adjacent passive components through interconnects. Large planes or closed loops of metal, close to the transmission lines, are avoided to limit losses due to *Eddy* currents. Adjacent metal areas that are connected to AC ground are spaced within a minimum distance (84 µm) to decrease capacitance coupling to ground. Capacitors were sized based on the supplied (simulated and tested) capacitance per unit area (refer to section 3.1.2 within

Table 3.2). Simulated results are given in section 4.6.4.

4.6.2 *Chebyshev* filter

An additional specification for the *Chebyshev* LPF was the ripple (in dB) at low frequencies. The pass-band filter gain is given by $G = 1/\sqrt{1+\varepsilon^2}$ (where ε is the ripple factor). To maximize the gain (closest to 0 dB) in the pass-band, the smallest obtainable ripple for this topology was chosen, at $20\log_{10}\sqrt{1+\varepsilon^2}$ = 0.01 dB. A 7th order LPF structure with a f/f_c ratio of 3.5 (taking into account the ripple) was required to achieve -60 dB attenuation at 60 GHz.

From this ratio, a cut-off frequency of 18 GHz was required. With a normalized resistance value of $R_S/R_L = 0.7$, the following values were obtained for the 7th order LPF circuit. The circuit is represented in Figure 4.33 and the obtained component values are given in Table 4.1.

The element values (C_n and L_n) obtained in [**68**] were normalized by (4.27) and (4.28) to determine the component values (C and L) for the 7th order *Chebyshev* LPF circuit given in Figure 4.33. Table 4.5 represents the component values for the Chebyshev LPF.

Table 4.5: Component values for the *Chebyshev* LPF.

Component	**Element values (C_n and L_n)**	**Component values (C and L)**
C_1	0.540	65.45 fF
L_2	0.970	626.16 pH
C_3	1.184	143.5 fF
L_4	1.137	734.12 pH
C_5	1.184	143.5 fF
L_6	0.970	626.16 pH
C_7	0.540	65.45 fF

The component values obtained in Table 4.5 presented lower capacitance values which translated into better and more reliable simulation results (refer to section 4.6.2) as circuit components could be designed without breaching geometry limitations of the 130 nm technology node. Another advantage of the *Chebyshev* circuit was the symmetry of component values (repeated values) which made the design, implementation, and placement (layout) of the individual components efficient for this type of circuit. Although the inductance values were generally higher than that of the *Butterworth* filter (refer to Table 4.4), it presented less of a problem compared to high capacitance values, as the transmission lines could be reduced in size and connected in series with short interconnect lines to reduce parasitic effects. This technique ensured that the proposed circuits were able to be implemented on the IC (as layout space is a limitation factor and a function of overall cost) without influencing circuit operation and therefore results based on the research hypothesis. A similar analysis based on the research hypothesis was done for the *Chebyshev* filter, but with these layout advantages implemented during the design.

4.6.3 *Bessel* filter

The *Bessel* LPF design also required specifying the amount of attenuation at 60 GHz, which is again -60 dB. Achieving this with a *Bessel* filter, a 7th order filter is again chosen, although this amount of attenuation was almost on the limit for a 7th order filter. The ratio f/f_c of 9 (almost 10) was required.

With this ratio, a cut-off frequency of around 10 GHz was required. With a normalized resistance value of $R_S/R_L = 0.7$ the following values were obtained for the 7th order LPF circuit. The circuit is represented in Figure 4.33 and the obtained component values are given in Table 4.6.

The element values (C_n and L_n) are normalized by (4.27) and (4.28) to determine the component values (C and L) for the 7th order *Bessel* LPF circuit (Figure 4.33) and given in Table 4.6.

Table 4.6: Component values for the *Bessel* LPF.

Component	**Element values (C_n and L_n)**	**Component values (C and L)**
C_1	0.091	19.89 fF
L_2	0.275	319.95 pH
C_3	0.431	94.09 fF
L_4	0.593	688.98 pH
C_5	0.714	155.74 fF
L_6	0.868	1.08 nH
C_7	1.862	406.13 fF

The component values for the Bessel LPF presented the least ideal component values as these values were relatively large (L_6 and C_7 in Table 4.6) which compromised the geometry limitations incurred by the 130 nm technology node.

4.6.4 LPF simulation results

The component values obtained in sections 4.6.1, 4.6.2, and 4.6.3 were used to create similar circuit structures for the LPFs using schematic simulation software. A similar circuit topology as depicted in Figure 4.33 was implemented, firstly using ideal component values, and secondly using the library components for the 130 nm process. Simulations of the frequency-domain transfer functions were performed and these results are depicted in Figure 4.34.

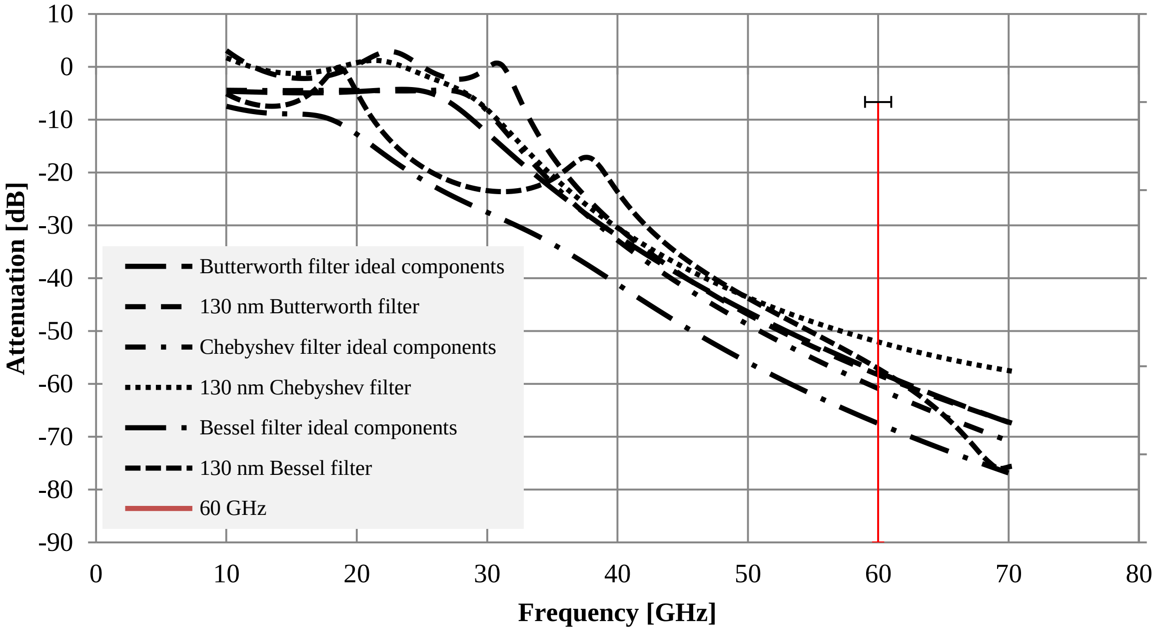

Figure 4.34: LPF simulated results for ideal circuit components and 130 nm components.

The results depicted in Figure 4.34 show the attenuation of each LPF circuit (*Butterworth*, *Chebyshev*, and *Bessel*) from 10 GHz to 70 GHz (λ = 30 mm to ~4.3 mm). Noticeable from Figure 4.34 is that the transfer functions for the circuits implemented with ideal components, have attenuation at 60 GHz very close to -60 dB as it was proposed, with relatively flat response at lower frequencies. Implementing similar circuits using the 130 nm components, introduced an error in attenuation at 60 GHz, where the *Chebyshev* LPF presented decreased attenuation (-52.23 dB at 60 GHz). The *Bessel* LPF (ideal circuit components) presented an increased attenuation at 60 GHz (-67.75 dB), however, the attenuation of its 130 nm counterpart presented an attenuation closer to the proposed -60 dB of -57.48 dB. Also evident from the results in Figure 4.34 is the resonant peaks introduced by the 130 nm circuit components at frequencies lower than 40 GHz. These resonant peaks are functions of the introduced parasitic capacitance (refer to section 3.1.2) and inductance values of the non-ideal circuit components, evident from the simplified capacitor model (Figure 4.35) for this node.

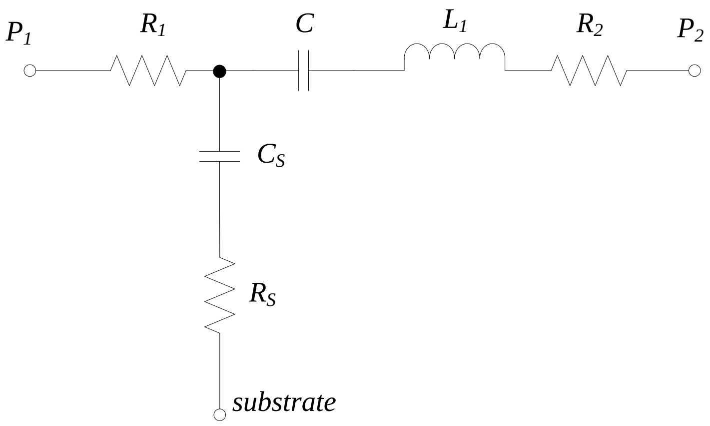

Figure 4.35: Simplified capacitor model for the 130 nm process.

From Figure 4.35, C represents the desired capacitance between P_1 and P_2, whereas C_S and L_1 represent parasitic capacitance and inductance values as a result of substrate effects and high-frequency coupling respectively. Skin effect losses and substrate losses are represented by R_1, R_2, and R_S respectively. Data simulated by the vendor based on this model showed a sudden increasing 'spike' in quality factor (as opposed to an expected decrease for ideal models) for frequencies between 20 GHz and 30 GHz, which proved consistent with results obtained in Figure 4.34. From section 3.1.2, the parasitic capacitance C_S introduced by the bottom plate of the capacitor ranges from 0.7 fF (for an 18 fF required capacitance C) to 2.5 fF (for a 143.5 fF capacitor C). Parasitic resistance R_S is less than 25 Ω.

4.6.5 Variable attenuation simulation results

To change the environmental conditions as proposed in section 2.1.7, varactors allowed only an 18 pF change in capacitance between 0 V and 1.8 V DC input. This limited the use of varactors as variable attenuation components within the passive filter structures. Also, the fixed capacitance from circuit parasitics increases at mm-wave frequencies, thus lowering the $\Delta C/C$ ratio and reducing the range of variable attenuation of the LPF. In a 7th order LPF structure the attenuation at 60 GHz did not vary by more than ± 0.4 dB between 0 V and 1.8 V DC input. From Figure 4.28 the difference in attenuation up to 30 m can reach -20 dB in the proposed scenarios. The hyperabrupt junction varactor frequency response only presented a constant capacitance (at constant DC input) up to 20 GHz. Beyond this point, the capacitance displayed an exponential increase and from 25 GHz its capacitance decreased to 0 F. For this reason, it was not possible to vary the attenuation of the proposed filter structures enough to investigate changes in transmission losses as proposed in section 1.2.

An alternative approach was to introduce an active component to attenuate the transmitted signal and present zero gain within its passband. For maximum bandwidth (no gain maximises the GBP), the common-base transistor amplifier (generally proposed for low-noise amplifiers) was used. The common-base amplifier is commonly used in high-frequency applications since the *Miller* effect is not present at its input, maximizing bandwidth and high-frequency parasitic losses (as opposed to a more limited bandwidth capability of the common-emitter amplifier due to this effect). Additionally, the increased isolation between the input and output node increased stability (also not present in common-collector amplifier configuration) by limiting feedback from the circuit output (on-wafer probe measurements). The common-base configuration is shown in Figure 4.36.

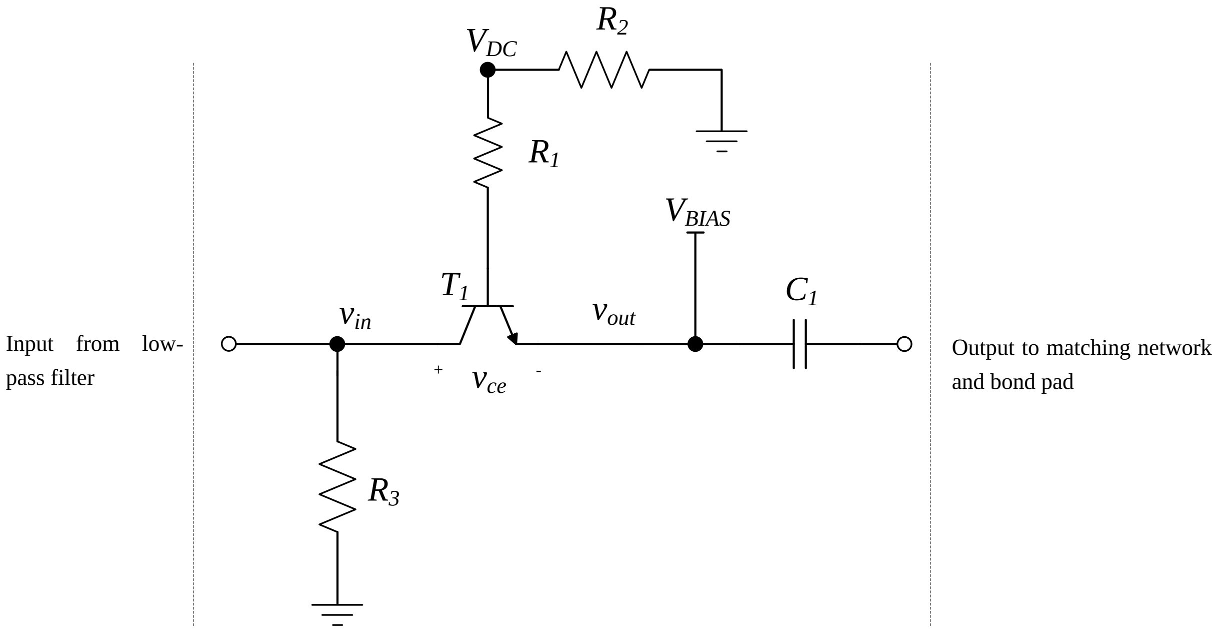

Figure 4.36: Common-base transistor amplifier to simulate changes in environmental conditions.

From Figure 4.36, transistor T_1 was used to decrease the filter attenuation from unity gain (g_mR_3). The voltage V_{DC} is applied to the base of T_1 through a (small) resistor R_1 (100 Ω) to achieve the desired on-biasing for the transistor across its base and emitter. In order to establish a flow of current through the collector, resistors R_2 (4.7 kΩ) and R_3 (1 kΩ) are placed between the source (V_{DC}) and the (DC) ground, since T_1 would be negatively biased with these components omitted. The variable input voltage (V_{BIAS}) is externally introduced at the emitter of T_1 to allow a more positive voltage (varied) to be applied with respect to the transistor base, allowing significant attenuation of the input (from the preceding LPF) AC signal. The additional DC-offset to the AC signal at this stage is removed through capacitor C_1 placed between the common-base active circuit and the following matching circuit and finally the bond pads where the measurements are taken. The results for the *Butterworth* LPF, with input supply (V_{BIAS}) ranging from 100 mV to 1.8 V are depicted in Figure 4.37.

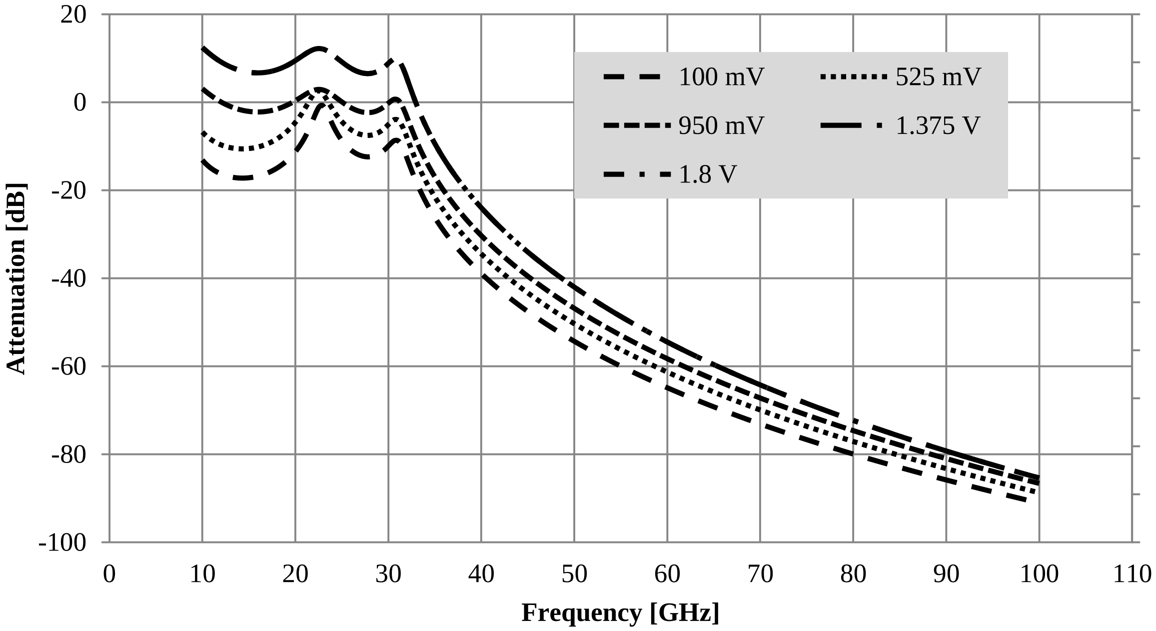

Figure 4.37: *Butterworth* LPF variable transfer function with input DC supply varying from 100 mV to 1.8 V.

From Figure 4.37 it can be seen that at lowest input supply (100 mV) the highest attenuation (-65.12 dB at 60 GHz) occurs as the transistor base current is at its lowest and implies an off transistor. The attenuation decreases to a value of -58.53 dB (60 GHz) at 1.375 V and higher (up to 1.8 V) when the transistor is fully on. This implies a change of 6.59 dB (using the hyperabrupt junction capacitor, a change of only 0.4 dB could be achieved) throughout the range of the input voltage. A large change in signal attenuation translates to more possibilities for changing environmental conditions that influence signal integrity, and increases the accuracy through an enlarged resolution. From Figure 4.28 in section 4.4, a variable attenuation of 6.59 dB translates to simulating the differences in path-loss models for the three scenarios up to 7 m (assuming stationary objects). These conditions imply stationary objects, therefore a constant distance during analysis. The differences between scenario 1 and scenario 2 can be tracked up to a distance of 30 m since $|s_{1,dB} - s_{2,dB}| < 6.59$ dB where $s_{1,dB}$ and $s_{2,dB}$ are the attenuation at any given distance (up to 30 m) for scenario 1 and scenario 2 respectively. Section 4.6.6 discusses other possible applications of using the results obtained in Figure 4.37, based on the information provided in section 4.4.

The results for the *Chebyshev* LPF with variable DC input are given in Figure 4.38.

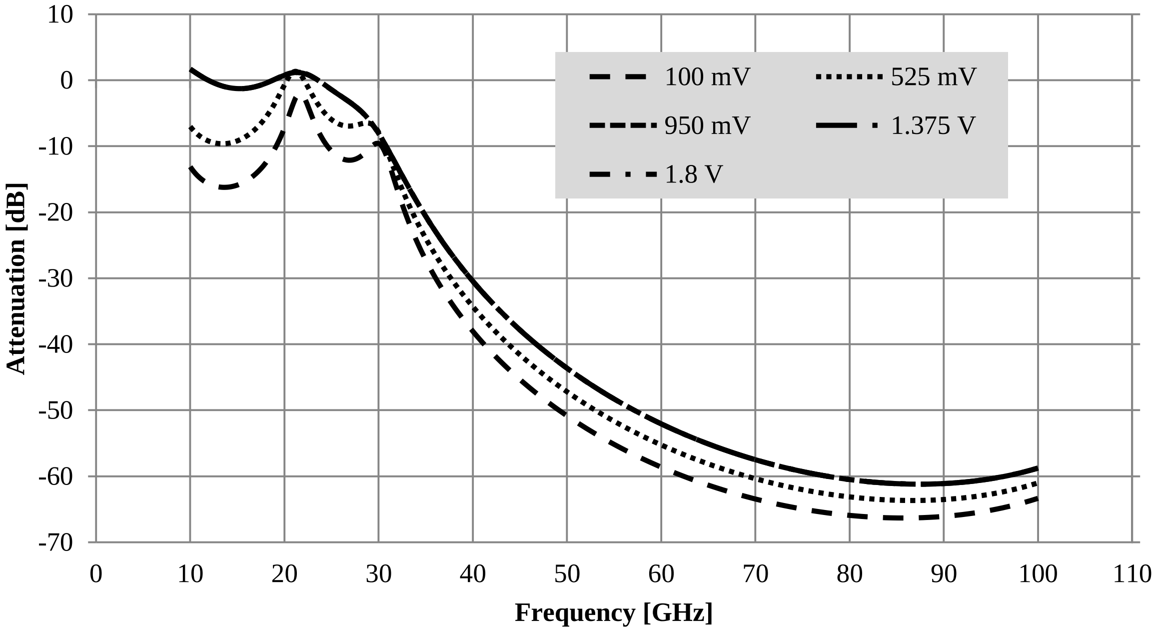

Figure 4.38: *Chebyshev* LPF variable transfer function with input DC supply varying from 100 mV to 1.8 V.

From Figure 4.38 similar results were encountered with -58.77 dB attenuation at 60 GHz using a 100 mV input to the transistor. This attenuation decreased to -52.24 dB with a 1.375 V and higher input to the base of the transistor at 60 GHz, constituting a difference of 6.53 dB in attenuation at 60 GHz, whereas only 0.28 dB change was possible using the hyperabrupt junction capacitor as a variable component to induce the change in transfer characteristics. Similar to the *Butterworth* LPF, the differences in the scenarios specified in section 4.4 can be tracked up to 7 m between all three scenarios, and up to 30 m when comparing scenario 1 and scenario 2, since $\left|s_{1,dB} - s_{2,dB}\right| < 6.53$ dB. The *Bessel* LPF results are given in Figure 4.39.

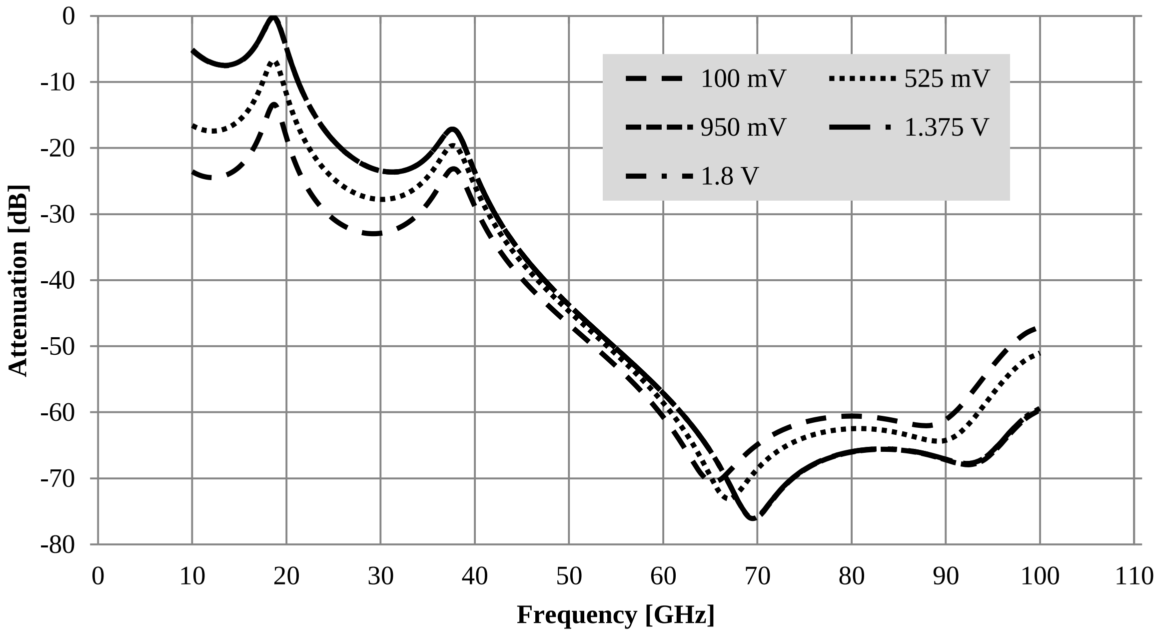

Figure 4.39: *Bessel* LPF variable transfer function with input DC supply varying from 100 mV to 1.8 V.

The *Bessel* LPF displayed the least amount of change in attenuation throughout the input voltage supply range (from 100 mV to 1.8 V). At 100 mV, with the transistor presenting a high attenuation of the input signal, an output attenuation of -61.20 dB at 60 GHz was achieved, and with input supply 1.375 V and higher, -57.49 dB was achieved, constituting a difference of 3.71 dB at 60 GHz. Due to the non-linear operation of the *Bessel* LPF beyond 65 GHz, small change in attenuation as a function of input voltage, and limited space on the 4 mm^2 IC, it was decided not to implement this filter on the prototype, and measurement results (refer to Chapter 5) are only obtained for the *Butterworth* and the *Chebyshev* LPFs. The smaller change in attenuation (3.71 dB) as a function of the DC input signal for frequencies from 40 GHz to 70 GHz (refer to Figure 4.39) only allowed simulating the difference between scenarios 1 to 3 up to approximately 4 m.

The variable attenuation of each filter structure could therefore be used to change the environmental conditions of a real-time mm-wave transmission, and from the results obtained in this section, the signal amplitude can be varied up to 6.59 dB around -60 dB (relaxed from -100 dB to accommodate technology limitations) attenuation using the *Butterworth* filter structure. To relate this to practical applications, section 4.6.6 summarizes the information supplied in section 2.1 based on the maximum obtainable amplitude variations for each filter structure.

4.6.6 Variable attenuation applications

The values provided in this section, for maximum obstruction thicknesses, path-loss exponent, *Fresnel* diffraction parameter, and rain-rate simulations, assume a stationary set-up and is not a function of time and speed of movement of the transmitter, receiver, or obstructions.

The measured material attenuations for obstructions breaking the LOS of the transmission were given in Table 2.2 in dB/cm. Table 4.7 summarizes the maximum thickness (in cm) for each material based on the maximum obtainable attenuation obtained in section 4.6.5 for each filter structure.

Table 4.7: Possible obstruction thicknesses (in cm) for each filter structure.

Material	***Butterworth* LPF [cm]**	***Chebyshev* LPF [cm]**	***Bessel* LPF [cm]**
Plywood panels	55	54	31
Brick wall (with paint and plasterboards)	3.13	3.1	1.77
Drywall	2.75	2.72	1.55
Whiteboard	1.32	1.31	0.74
Ordinary glass	0.94	0.93	0.53
Double glass	0.58	0.58	0.33
Mesh glass	0.21	0.20	0.12
Iron door (with plywood panels)	0.13	0.13	0.08

Table 4.7 serves as an estimation for material thicknesses and is based on measured results (therefore accounting for reflections, scattering, and diffraction) given in [**10**] and [**23**]. Combining more than one material (cascading) does not account for interaction between materials, and the attenuation should be verified through separate measurements.

From Figure 2.2, it was noted that for each filter structure, based on the maximum amount of variable attenuation, it was possible to determine a minimum distance at which the path-loss exponent could be simulated as an environmental change parameter. This distance (Table 4.8), specifies where the attenuation difference between $n = i$ and $n = i + 1$ for $i = 1, 2$, and 3 is equal to, or less than the maximum obtainable attenuation variation of each filter structure. Also specified in Table 4.8 is the *Fresnel* diffraction parameter that can be simulated to represent the knife-edge diffraction attenuation (refer to Figure 2.7).

Table 4.8: Possible path-loss exponent and *Fresnel* diffraction simulations.

Parameter	***Butterworth* LPF**	***Chebyshev* LPF**	***Bessel* LPF**
Maximum variable attenuation [dB]	6.59	6.53	3.71
Minimum distance for varying path-loss exponent [m]	8	8	13
Maximum *Fresnel* diffraction parameter	-0.48	-0.49	-0.56

From Table 4.8, the minimum distance for which the path-loss exponent can be varied in increments of 1, is similar for the *Butterworth* and *Chebyshev* filter structures (8 m) and is equal to 13 m for the *Bessel* filter structure. The Fresnel diffraction parameter can be varied between -0.75 (for which (2.9) is valid) up to -0.48, -0.49, and -0.56 for the *Butterworth*, *Chebyshev*, and *Bessel* filter structures respectively.

Based on the results obtained in Figure 2.9, it was possible to simulate the effect of rain-rate using each of the proposed filter structures up to the simulated distance of 30 m. The highest attenuation, for a rain-rate of R = 150 mm/h was 1.63 dB, therefore possible to simulate using the structure with lowest possible variable attenuation (*Bessel* filter with 3.71 dB maximum variable attenuation).

4.7 MATCHING NETWORK DESIGN

To maximize power transfer to the load (VNA and wafer prober, refer to section 3.8), a matching circuit was designed to match the output of the buffer circuit and GSG bonding pads to 50 Ω. The output impedance before the matching circuit was Z_{in} = 3 – j6 Ω. The *Smith* chart was used to determine the matching network circuit component values and is given in Figure 4.40.

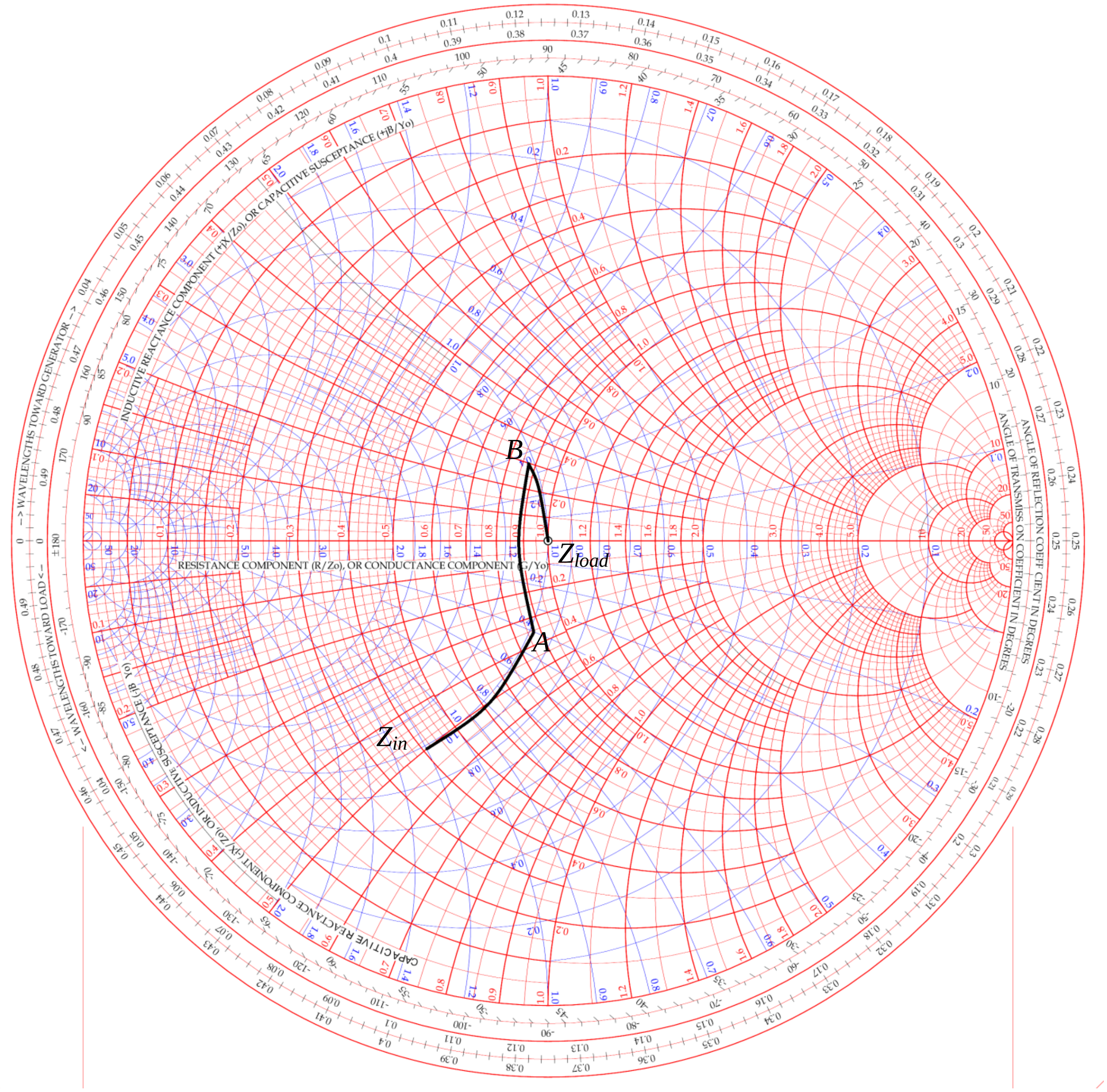

Figure 4.40: *Smith* chart and matching network design.

From Figure 4.40 the impedance matching was done by plotting the normalized value of Z_{in} and moving along the constant reactance circle up to its intersection with the constant resistance circle, thus moving a total of j0.72 Ω (towards point *A*). From this point, movement on the constant resistance circle (j0.68 Ω – point *B*) and finally on the constant reactance circle (-j0.34 Ω) completed the three-component (π) matching network. The movement across the

Smith chart translated into a shunt inductor (L_{shunt}), a series inductor (L_{series}) and a shunt capacitor (C_{shunt}). The matching circuit is depicted in Figure 4.41.

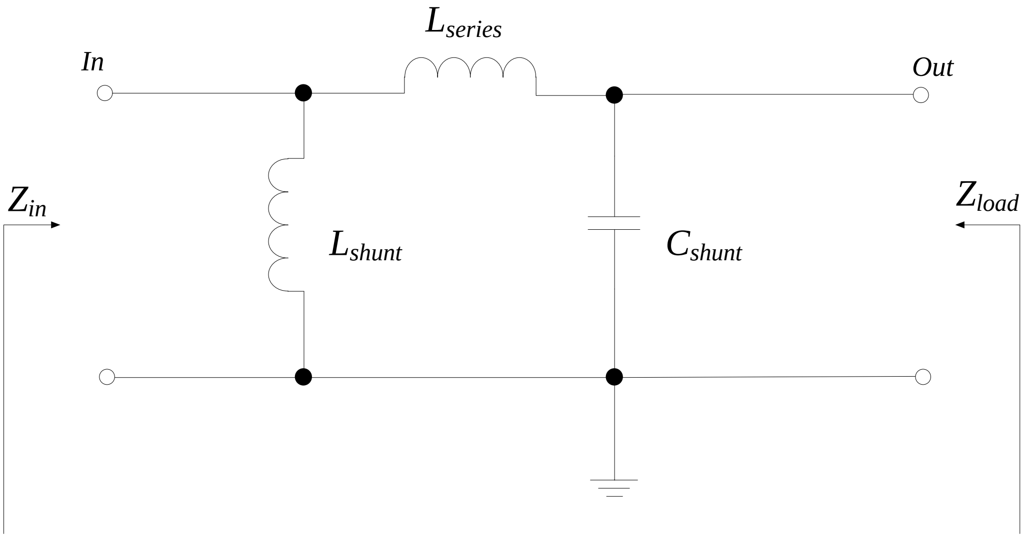

Figure 4.41: Matching network to match filter output to bonding pad impedance.

The de-normalized values of the circuit presented in Figure 4.41 were determined by the following equations, for the inductive and capacitive components respectively.

$$L = \frac{|\Gamma| \times Z_L}{2 \times \pi \times f} \tag{4.29}$$

$$C = \frac{|\Gamma|}{Z_L} \frac{1}{2 \times \pi \times f} \tag{4.30}$$

where $|\Gamma|$ is the distance moved along the *Smith* chart, Z_{load} is the output impedance to be matched to (50 Ω), and f is the operating frequency (60 GHz). From (4.29) and (4.30), the component values for Figure 4.41 are determined, and summarised in Table 4.9.

Table 4.9: Component values for the pi-matching circuit.

Component	Required value
L_{shunt}	96 pH
L_{series}	90 pH
C_{shunt}	18 fF

The values in Table 4.9 are attainable using the proposed 130 nm process components (transmission lines and capacitors – refer to sections 3.1.1 and 3.1.2) and used to design the output matching circuit. Figure 4.42 shows the results of the output impedance before and after the implementation of the matching network.

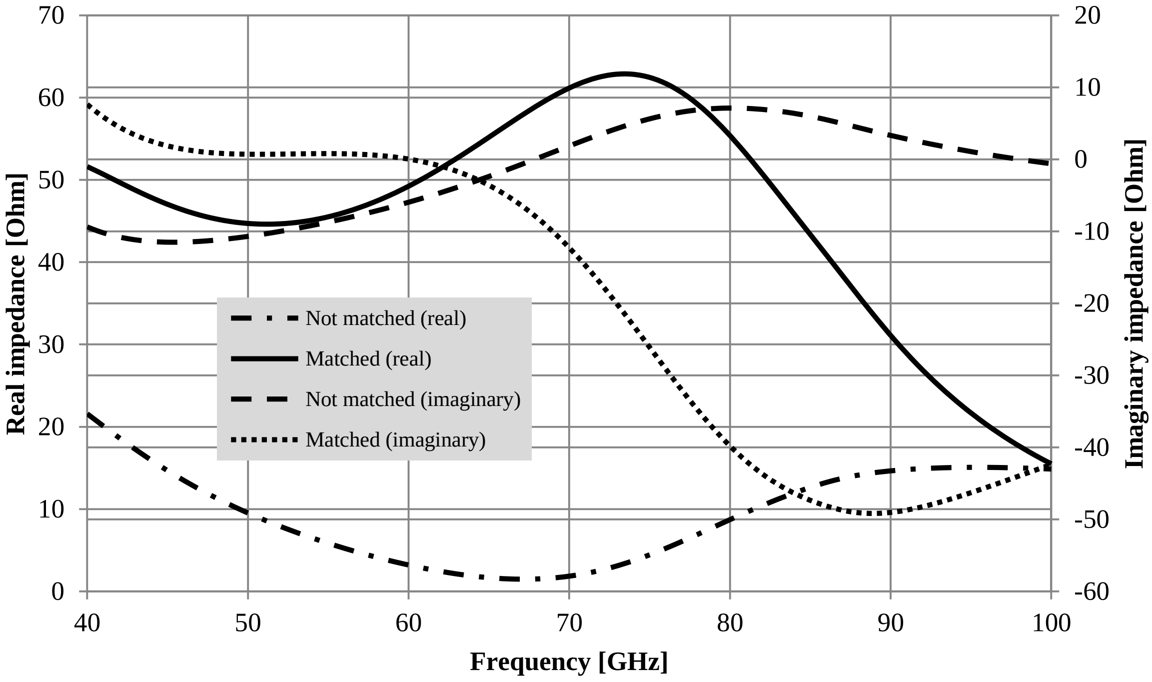

Figure 4.42: Output impedance before and after the output matching network.

From Figure 4.42, the real and imaginary impedance of the circuit without the implementation of the matching network, at 60 GHz, is seen to be Z_{in} = 3 – j6 Ω. The results also show the real and imaginary impedance of the output after the matching circuit, with an output impedance (as seen from Figure 4.42) of Z_{load} = 49.3 – j0.01 Ω. This impedance value as seen from the output of the circuit ensures that maximum power transfer is achieved to the measurement equipment and minimizes reflection losses at the output.

4.8 CONCLUSION

This chapter presented the design equations used during the development of the models pertaining to the experimental investigation of the research hypothesis (refer to section 1.2). In section 4.1 the design equations for a mm-wave (at 60 GHz) dipole antenna is presented. The EM simulation parameters of the dipole antenna are bounded by the chosen technology node and choice of material and dimensions is based on this node to provide future implementation of this antenna using the proposed technology. The radiating antenna can be manufactured using a different node and changes to parameters can be implemented in EM simulation. Simulated results in CST Microwave Studio ensured the correct implementation of the design equation in mm-wave frequencies. In section 4.2.1 the simulations were conducted without a substrate added below the dipole geometry. These results are required to determine if the dipole equations without taking into account any effects from the surrounding atmosphere are correct. Generally some form of antenna de-tuning occurs when implemented practically as a result of the surrounding environment, therefore it is important to first verify the results based on no interference. The input impedance (imaginary and real) are given in Figure 4.4 where the radiation resistance is R_r = 70.21 – j20.95 Ω, and therefore $|R_r|$ = 73.27 Ω. Theoretically, a dipole antenna with length $L = \lambda/2$ and 180° separation should have a radiation resistance of 73 Ω therefore this result confirms correct implementation of the design equations. The resonance of the antenna is verified with Figure 4.6 with S_{11} = -16.60 dB at 60 GHz. The VSWR of the antenna at 60 GHz was determined to be 1.35:1 which translates to a value of less than 4 % being reflected by input port of the antenna at the operating frequency.

The dipole equivalent model would be based on the practical implementation of the radiating antenna, designed on a substrate as supporting structure for the dipole elements. The interaction between the surrounding environment and the antenna is modelled through an equivalent circuit, and therefore this transfer characteristic was first modelled in EM simulations. In section 4.2.2 the results are given where the supporting substrate is included in the simulated results. Firstly the results are obtained with matching the ports to a 75 Ω load (approximately equal to the radiating resistance expected at the input). The results displayed a change in transfer characteristics and are documented in Figure 4.8 and Figure 4.9 with specific reference to the real and imaginary impedance. Further results displayed the changes in the reflection coefficient and VSWR, where results are also given when the antenna is matched to a 50 Ω load, since the changes in radiating resistance provided evidence that the resistance decreased to approximately 50 Ω with the substrate added. The results for the EM simulations are summarised in Table 4.2 with specific reference to the impedance, reflection coefficient, VSWR, and transmitted power.

The results obtained in section 4.1 forms the basis for the proposed circuits in section 4.3. In section 4.3 a preliminary equivalent circuit for the dipole presented in section 4.1 is proposed. The results for this circuit, based on the *Foster canonical form* for electrical antennas, are presented along with an analytical technique that estimates the initial circuit based on input parameters obtained from the EM simulations (refer to Appendix A for a MATLAB script that determines this initial approximation). The circuits are first simulated using ideal circuit components, after which limitations are incurred based on the 130 nm node used for this research. The research determines the validity of implementing such an equivalent circuit using the 130 nm node available during the time, where all findings during this work can be transferred to a smaller node. Limitations on passive component values and performance of the 130 nm node are investigated, and the conclusion that the mm-wave operation of a dipole antenna can in fact be modelled in the 130 nm node considering these limitations. In section 4.3.1 the results of the initial (preliminary) equivalent circuit are presented and compared to the results obtained in EM simulation. The correlation between the EM simulations and the equivalent circuit (ideal components and implemented using the 130 nm components) shows similar operation based on its frequency domain impedance and resulting reflection coefficients. The input impedance of the 130 nm equivalent circuit is 34.5 – j89.6 Ω including parasitic effects introduced by the 130 nm circuit components. The reflection coefficient in Figure 4.19 is similar to EM simulations at -16.60 dB at 60 GHz with a slight shift in resonance frequency (64.3 GHz) using the 130 nm components. Following the analysis of section 4.3.1 on the preliminary circuit, an improved equivalent circuit is presented in section 4.3.2 taking into account the effects of the non-ideal circuit components and the effects from the surrounding environment such as the substrate effects in the EM simulations. Similar analysis on this circuit is presented, and compared to the preliminary circuit; with the conclusion that the added degrees of freedom to the *Foster canonical form* circuit did not change the operation of the circuit in comparison to the antenna transfer characteristic, and improved the ratio obtainable between inductive and capacitive components within the circuit. The significance of this conclusion is that it was possible to improve the reflection coefficient at resonance based only on the added degrees of freedom to the circuit design, and still be able to ensure equivalent circuit operation when compared to the radiating dipole antenna. This was not possible with the preliminary circuit, as the limitations of the 130 nm node determined also the limited reflection coefficient at resonance. In Appendix C the temperature dependence of the passive circuit structure is given for temperatures 0, 27, and 85 °C, and concluded that since the circuit consists of passive components only, a small change in transfer characteristics is seen with change in temperature.

In section 4.4 the results for the proposed attenuation function (refer to section 2.1.7) at 60 GHz over a 30 m distance are given in Figure 4.28. The results are divided into three scenarios (refer to Table 4.3) and the attenuation experienced in the mm-wave spectrum over a short distance (practically measurable within a laboratory environment) shorter than 1 m is given. The attenuation over this distance is approximately -100 dB, and this value is used as baseline for the design of the variable LPFs in section 4.5 and 4.6. Section 4.5 analyses the mathematical approximations and design of the LPFs (*Butterworth*, *Chebyshev*, and *Bessel* structures) and provides transfer characteristics of the filter structures across a wide bandwidth (up to 70 GHz). The results also investigate the ripple factor in the *Chebyshev* filter and verify the attenuation of the mathematical approximations at 60 GHz to be within the -100 dB range. The cut-off frequencies of each structure are verified from the design equations in for each filter respectively. The filter structures are simulated in schematic simulations in section 4.6 and component values for each structure given in Table 4.4, Table 4.5, and Table 4.6. Based on the results in section 4.6.4 presented in Figure 4.34, it was concluded that in order to verify the research hypothesis that a variable filter can be implemented in the 130 nm process based on passive components available, the attenuation at 60 GHz had to be relaxed to approximately 60 dB since circuit operation when designing for a -100 dB attenuation resulted in inconsistent transfer characteristics due to large aspect ratios of transmission line geometries (*W/L* ratios) required. Additional parasitic inductances are introduced with such large aspect ratios as the transmission lines act as antennas on the structure and resonate with interfering magnetic waves within the structure itself. Simulation results on the variable attenuation range of each structure is presented in section 4.6.5 with applications based on commonly found materials provided in section 4.6.6. A variable attenuation at 60 GHz of between 3.57 dB and 6.59 dB could be achieved with the proposed common-base amplifier structure for the respective filter structures.

In section 4.7 the design procedure for the matching network to the output of the circuit is given, with a *Smith* chart analysis provided in Figure 4.40 and simulated results given in Figure 4.42.

CHAPTER 5: MEASUREMENT RESULTS

5. CHAPTER OVERVIEW

This chapter presents the measurement results of the dipole equivalent circuits (preliminary and improved), the LPF structures (*Butterworth* and *Chebyshev* – the *Bessel* filter was not implemented on the IC due to wafer size constraints), and the buffer circuit connected to the matching network and bonding pads. The PCB design to facilitate the measurements is described in section 3.7 and the measurement set-up and equipment is described in section 3.8.

The results presented in this chapter include the reflection coefficient (S_{11}), real and imaginary impedance (Z_{11}), and VSWR of the preliminary and improved dipole equivalent circuits. Each figure also presents the simulated results on the same graph for comparison to the measurement results. Discussions include comments on results with respect to obtained and expected results, and provide a perspective based on the validity of the research hypothesis (refer to section 1.2).

The circuit layouts and PCB configurations are given in Appendix B, and each prototype was measured from the wafer to the ceramic substrate (and PCB). Since the dipole equivalent circuits did not require any external routing (wire bonding), three prototypes were measured and the results compared for consistency. The LPF structures required a DC connection to be bonded from the IC and therefore only one structure per substrate was measured, and the results are presented in this chapter.

The chapter concludes with an interpretation of the measurement results of the dipole equivalent circuits, LPF structures, buffer and matching network. This conclusion serves as an introduction to Chapter 6 that discusses the interpretations and relevance based on the overall research hypothesis (with critical analysis presented) and scope limitations with recommendations for future improvements.

Although this chapter aims to verify the circuit operation as a function of its frequency behaviour and real and imaginary impedances, it should be noted that there are discrepancies between the simulated and the measured results presented in this chapter. The reasons for these discrepancies are two-fold and must be critically analysed to ensure that the result can in fact be used to prove the research hypothesis. During each measurement results, any offsets between simulated and measured results are discussed and identified. In order to draw the conclusion in section 5.4 regarding the individual circuits, a discussion on the common errors should be identified. The measurement setup limitations that are investigated and identified preceding the measurement results are the calibration techniques and structures used over the extremely wide bandwidth in which this research is presented and the grounding strategy applied to each individual circuit.

Calibration of the RF source that provides the stimulus to the DUT under testing operations is an important and involved procedure, and any information not provided to the measurement equipment (probe station and VNA) can lead to significant errors in measured results. Since the VNA measures vector ratios of reflected or transmitted energy to energy incident upon the DUT, the VNA determines the properties of the device rather than the properties of the signals. An accurate and well-defined reference plane is therefore required to ensure any errors introduced as parasitics, not only by the DUT but also by the external environment are accounted for and eliminated during *S*-parameter measurements. Errors introduced in a two-tier measurement system can be summarized through the following approach depicted in Figure 5.1.

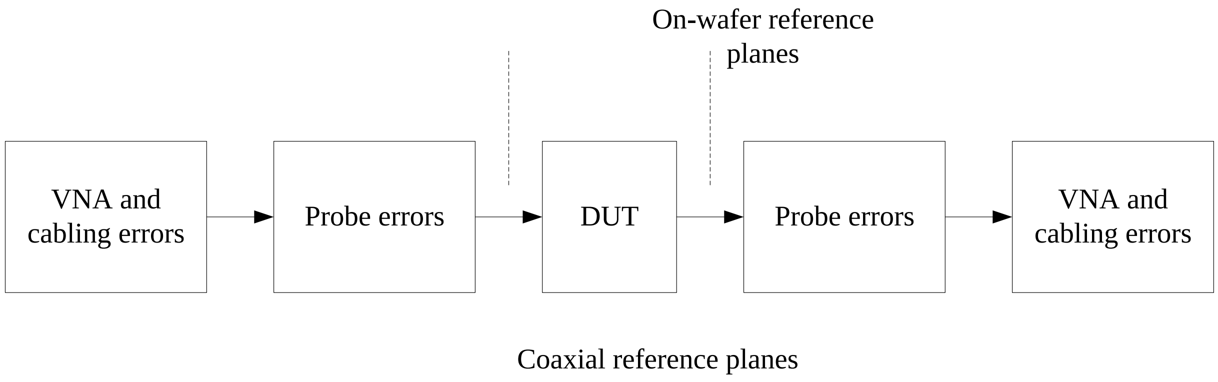

Figure 5.1: Introduced errors in a two-tier measurement setup.

Calibration structures are used to balance errors introduced specifically through the VNA, cables, and probes, and become more difficult to parameterize at high frequencies. The errors introduced through the DUT should also be very well characterized, however the data required to completely characterize the VNA is usually provided within a kit, referred to as the Impedance Standard Substrate (ISS) provided by the manufacturer of the thin-film structure.

The calibration kit used for these measurements were provided by GBB Industries Inc. ® suitable for Picoprobes® since high-performance and high frequency ISS load resistors are manufactured within a 0.3 % accuracy / tolerance of its desired DC value and all of the reflection standards (CalKit / AutoCal utility) provided by the factory are to be loaded into the VNA on a serial number basis. Although SOLT structures were designed on the DUT to ensure accurate measurements, these structures could not be used during calibration as not all information and data regarding the process were available as part of the technology's NDA. It was therefore decided, in order to calibrate the system as accurate as possible, the ISS SOLT calibration structures with provided data and parameters were used instead. The measurement facility was already set up to allow integration of these structures and advised its use, as opposed to SOLT structures on the DUT (see Appendix B) with unknown substrate parameters which are difficult to characterize as there exist right-angles (interconnects) that introduce reflections not quantized by these structures (capacitance and inductance values of *open* and *short*). These SOLT structures do however present lower accuracy at higher frequencies (> 60 GHz) as they generally require multiple algorithms to cover large bandwidth ranges and frequencies approaching 110 GHz where it is more difficult to characterise opens and loads. Additionally, the frequency up-conversion from 67 GHz to 100 GHz to allow measurements to be performed with the Picoprobe® 67a DP-type probes (see section 3.8) are assumed to have introduced some frequency and amplitude errors observed (commonly) in the measured results.

Secondly, the grounding strategy for each circuit on the DUT (see Figure 5.3 and Figure 5.4) was not connected to both AC ground planes (GSG) and therefore a significant error could be introduced if any difference in offset between these ground planes and DC ground was established. Since the ground planes itself must fill all available area in the circuit that is not used for circuit-related components, the probability of such an error commonly found in the measured results is increased.

The measured results for the dipole equivalent circuits are discussed in section 5.1.

5.1 DIPOLE MEASUREMENTS

The first measurement results for the dipole equivalent circuits depicted in Figure 5.2 are the reflection coefficient (S_{11}) for the simulated and measured circuits. These results are used to determine the resonant frequency of the prototyped circuits and compare these results with the simulated values.

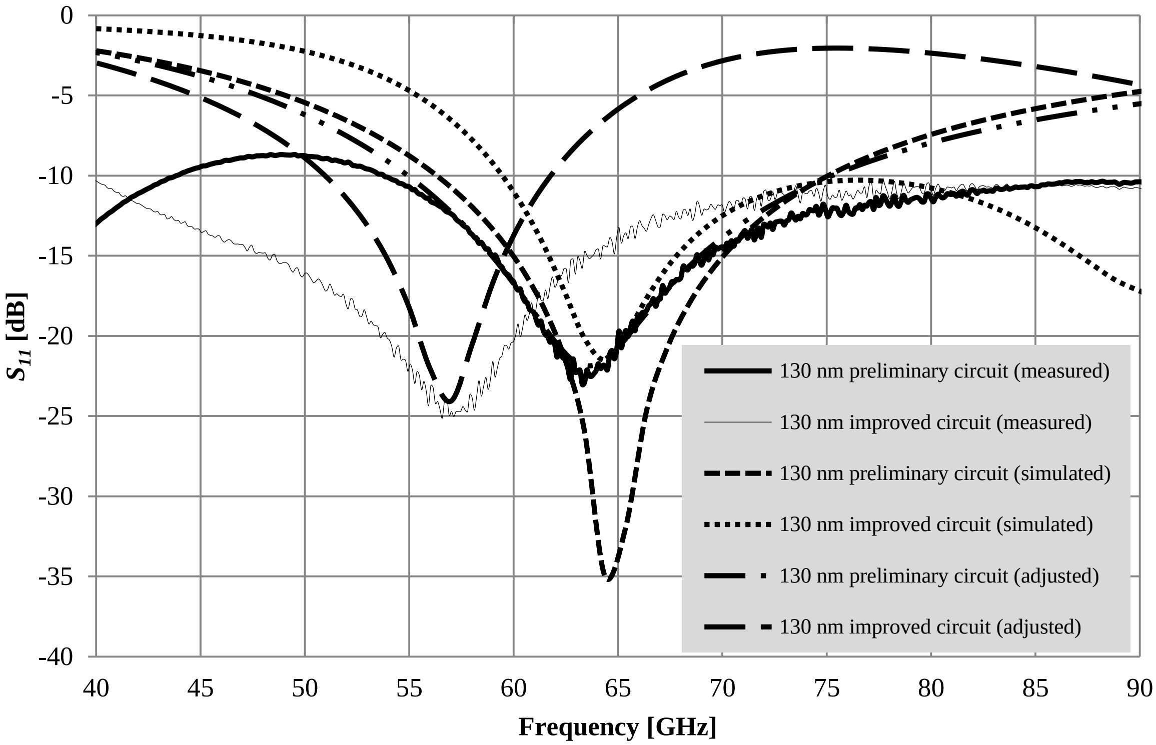

Figure 5.2: Reflection coefficient of simulated and measured dipole equivalent circuits.

From Figure 5.2, the S_{11} results of the simulated circuits (refer to section 4.3) are presented as the short dashed line (preliminary circuit) and the dotted line (improved circuit). The simulated preliminary circuit resulted in a S_{11} of -35 dB at 64.3 GHz, whereas the measured value (thick solid line) resulted in a value of -22.2 dB at 64 GHz. This measured result shows a good frequency correlation to the simulated value, with an increase in the reflection coefficient (from -35 dB to -22.2 dB as a result of mismatches introduced parasitically in the circuit layout). The reflection coefficient for both the measured and simulated results at 64.3 GHz are different by only 11 % (-22.2 dB versus -24.9 dB). The shift in resonance at these high frequencies is an important result used in future implementations to determine the accuracy of each component model as well as effective layout strategies during the design of mm-wave circuits to improve on the integrity of these results. Further investigation was done on this change in resonant frequency. Circuit operation was reconstructed in the ADS software suite to represent a similar transfer function as obtained in the measurement results. The corresponding component values are presented in Table 5.1. The results of the reflection coefficient for the preliminary dipole equivalent circuit using these values are also presented in Figure 5.2 with the dash-dot-dot line.

Table 5.1: Preliminary circuit component values adjusted to fit measured results.

Component	Original value	Practical value	Change in value
L_0	53 pH	26.5 pH	26.5 pH
L_1	60 pH	40.5 pH	19.5 pH
C_0	50 fF	50 fF	0.0 fF
C_1	88 fF	96.8 fF	8.8 fF

From Table 5.1, it can be noted that there is in fact a significant change in inductance of L_0 and L_1 in the measured results. Compared to the designed inductance values there is a 26.5 pH change in the inductance of L_0 and a 19.5 pH change for L_1. It was determined that a possible reason for these changes in inductance was the grounding strategy used during the layout of the circuit which was not optimal and could add parasitic inductances to the circuit. In Figure 5.3, the micrograph of the layout of the dipole equivalent circuit is depicted.

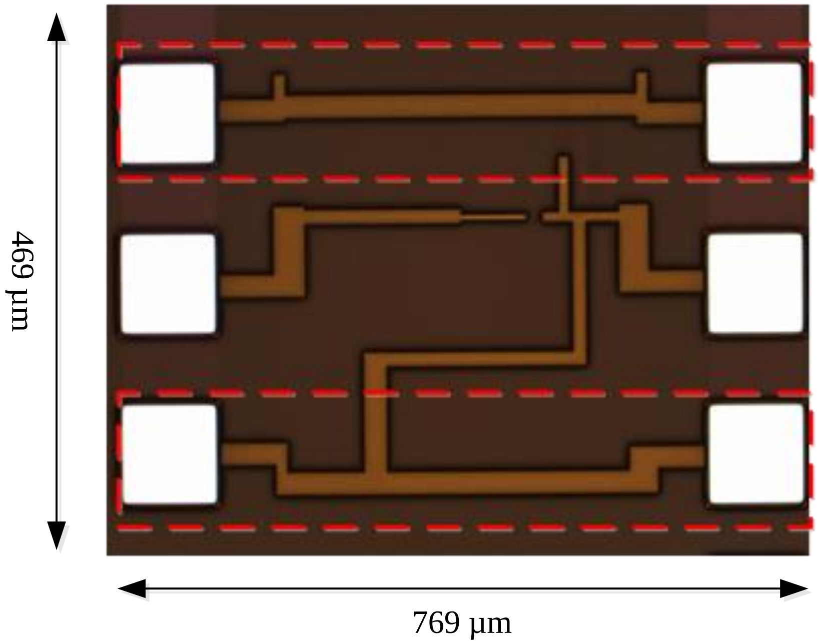

Figure 5.3: Layout of the preliminary dipole equivalent circuit with ground highlighted.

The ground planes of the dipole equivalent circuit in Figure 5.3 are highlighted in red blocks. Investigation during measurements suggested that the ground planes could be too thin and long (high aspect ratio) that could act as a transmission line itself, and add parasitic inductance to the overall design. The suggestion for future implementation is to increase the width of the ground planes as much as possible, and ensure that the entire circuit around the ground plane is enclosed in the ground structure (as opposed to the ground plane running on top and below the circuit as seen in Figure 5.3). Another recommendation is also to tie the top and bottom ground planes together, as this would ensure that there is no potential difference between the ground connections of the GSG probes. The parasitic changes in the required capacitance values (Table 5.1) of C_0 and C_1 are less significant (0 fF and 8.8 fF respectively) compared to the changes in inductance values (the capacitors are also grounded on the same ground plane).

Similar results are obtained for the improved dipole equivalent circuit, and given in Figure 5.2. The reflection coefficient (S_{11}) for the improved dipole equivalent circuit from Figure 5.2 represented as a dotted line (also presented in Figure 4.24) is -21.8 dB at 64 GHz. The measurement results, however, showed a shift in resonance frequency (thin solid line) with S_{11} of -24 dB at 56.7 GHz. It was again investigated what changes in components values could result in these changes in resonance, and the results are presented in Table 5.2.

Table 5.2: Improved circuit component values adjusted to fit measured results.

Component	Original value	Practical value	Change in value
L_0	240 pH	140 pH	100.0 pH
L_S	120 pH	141.6 pH	21.6 pH
L_{SUB}	160 pH	160 pH	0.0 pH
C_0	18 fF	14.8 fF	3.2 fF
C_S	104 fF	80.95 fF	23.05 fF
C_{SUB}	18 fF	16.9 fF	1.1 fF
C_P	18 fF	21.1 fF	3.1 fF
C_{P1}	450 fF	450 fF	0.0 fF
L_P	72 pH	119.3 pH	47.3 pH

The results of the adjusted (practical) component values to the transfer characteristic of the improved dipole equivalent circuit reflection coefficient are depicted with the (long) dashed line in Figure 5.2. This line shows the estimated resonance if the adjusted component values are used in simulation, and presents similar results compared to the measured results. It is again noticeable from Table 5.2 that the inductance values showed a significant change in value during simulation and measurements. The grounding strategy recommendation should also be adhered to for the improved circuit, and since there is a larger number of inductive components in this circuit compared to the preliminary circuit, the effects of the parasitic changes had a much larger effect in the shift in frequency. The micrograph of the improved dipole equivalent circuit layout, with ground planes highlighted in red, is displayed in Figure 5.4.

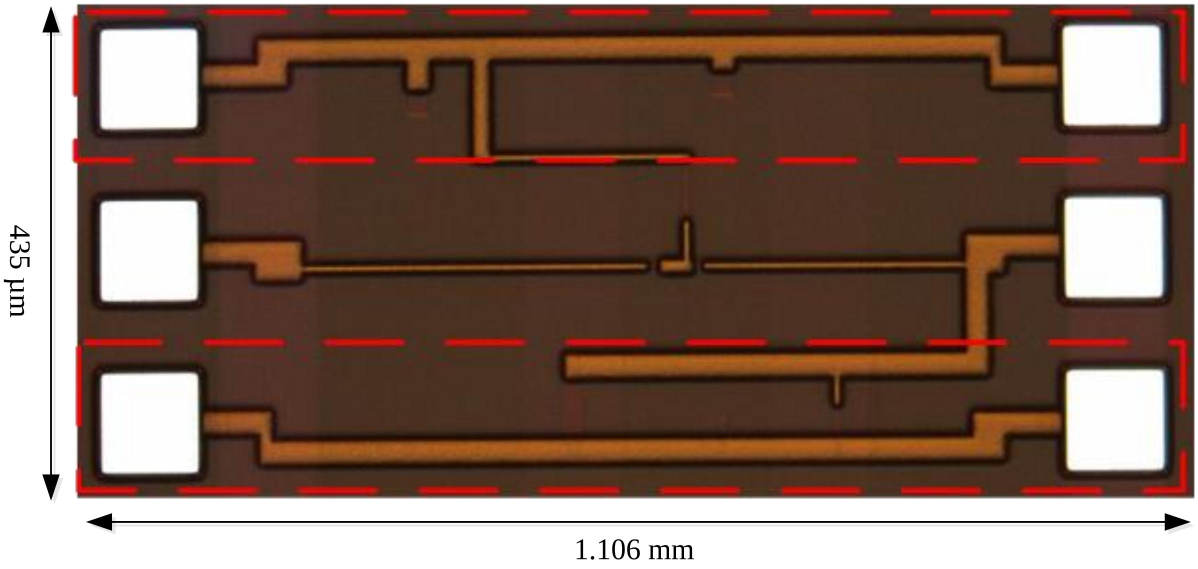

Figure 5.4: Layout of the improved dipole equivalent circuit with ground highlighted.

Figure 5.4 also highlights (similar to Figure 5.3) the ground planes as used on the circuit layout of the improved dipole equivalent circuit and emphasises the width of these planes to be too thin and long. Improvements in lowering the aspect ratio of the width and length of these planes would reduce parasitic inductances generated by interference around the ground planes. The top and bottom bonding pads should also be connected to avoid any potential difference generated with reference to ground. Modelling of these errors can become mathematically cumbersome with a large number of variables that need to be accounted for during simulation and analysis. Important to consider is that the research hypothesis investigates the possibility of obtaining a similar transfer function for the EM simulated dipole and equivalent circuits, in simulation and measurement. The simulation results have proved that this is in fact possible to obtain similar frequency operation (with limitations on the component value ratios) within the 130 nm technology. The measurement results confirm at this point that although a slight change in frequency occurred, these shifts can be attributed to the layout strategy (and changes in component values due to parasitics) and not as a result of technology limitations. Further analysis into the impedance (real and imaginary) of the equivalent circuits can also be used to analyse the performance of the circuits based on the simulated results.

The imaginary impedance for the simulated preliminary and improved equivalent circuits, the measured results for these components, and the results of the adjusted component values as presented in Table 5.1 and Table 5.2 are presented in Figure 5.5.

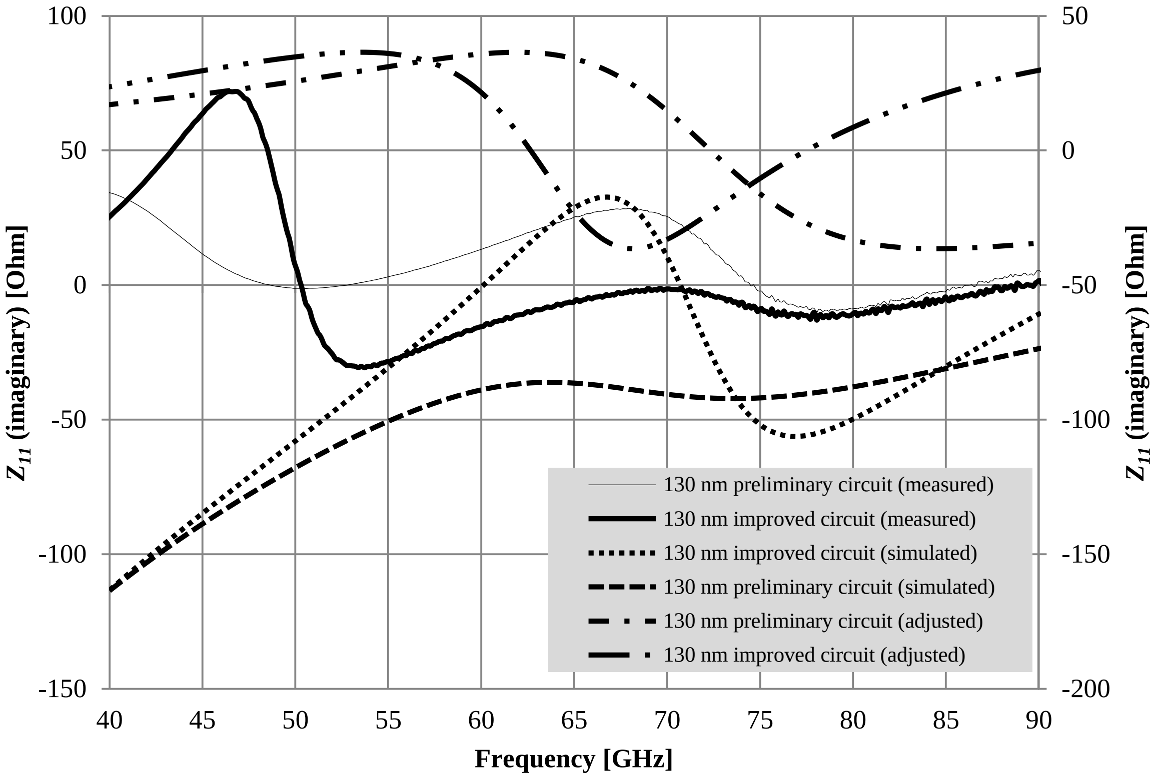

Figure 5.5: Imaginary impedance of simulated and measured dipole equivalent circuits.

From Figure 5.5 the simulated imaginary impedance for the preliminary dipole equivalent circuit is depicted by the short dashed line. These results are also given in Figure 4.16. The imaginary impedance of the simulated circuit at 60 GHz is –j89.6 Ω (read from the secondary *Y*-axis) with a local maximum and minimum at 63.4 GHz and 72.9 GHz respectively. The inclusion of the primary and secondary *Y*-axis is to allow for easier reading of the results if the obtained range differs significantly between results. For the measured results to be similar, a transfer characteristic that displays similar frequency operation (minimum and maximum) was required. The values of the measured imaginary impedances at these frequencies are expected to be different compared to the simulated results due to the difference in reflection coefficient

(-22.2 versus -24.9 dB). The measured result of the preliminary dipole equivalent circuit is given by the thin solid line in Figure 5.5. The measured imaginary impedance showed a local maximum of j31.8 Ω at 67 GHz and a local minimum of –j11.5 Ω at 78.2 GHz, with an impedance of j12.2 Ω at 60 GHz (read from the primary *Y*-axis). This result verified that the operation of the simulated preliminary equivalent circuit can be achieved through the 130 nm process and the slight shift in frequency is expected as a result of the improper grounding strategy as discussed in the reflection coefficient results. The change in impedance values at the specified frequencies (60 GHz and local maximum and minimum) is also a result of this occurrence as the ratio of inductance to capacitance changes due to the parasitic effects introduced within the circuit. The transfer characteristic for the adjusted values (refer to Table 5.1) is given by the dash-dot line within Figure 5.5 on the secondary *Y*-axis. The local maximum for this adjusted circuit is obtained at 63 GHz (j34.5 Ω) with its local minimum occurring at 83 GHz (-j36.5 Ω) and displays an impedance of j35.6 Ω at 60 GHz. The results for the improved dipole equivalent circuit simulation are given by the dotted line in Figure 5.5. These results are also available in Figure 4.21. The local maximum is situated at 67.4 GHz (j32.5 Ω) and the local minimum at 78.5 GHz (-j55.7 Ω), with an impedance of –j3.2 Ω at 60 GHz. The measured results obtained, displayed a local maximum at 69 GHz (-j1.33 Ω) and a local minimum at 76.5 GHz (-j11.6 Ω) and an impedance of –j17 Ω at 60 GHz. It was also noted that an additional resonance occurred between 45 GHz and 55 GHz which was close to the primary (required) resonance to influence the measurement results as this effect was not witnessed in simulation results. Simulation results, however, do not account for all parasitic effects that can be introduced in the circuit during measurement and therefore it was not possible to simulate this effect in software (software license limitations for post-layout simulations provided by additional Cadence tools (refer to section 3.6) prevented investigation of parasitic effects in final circuit layout). The adjusted circuit component (refer to Table 5.2) simulation also did not show this effect at these frequencies, with results of this circuit displayed by the dash-dot-dot line in Figure 5.5. The adjusted component value results did not show consistent results. The research hypothesis was valid taking into account the measurement results for the improved circuit, however, improvements to the frequency operation can still be made for measured results.

The real impedance results of the preliminary, improved, and adjusted equivalent dipole circuits at 60 GHz are given in Figure 5.6.

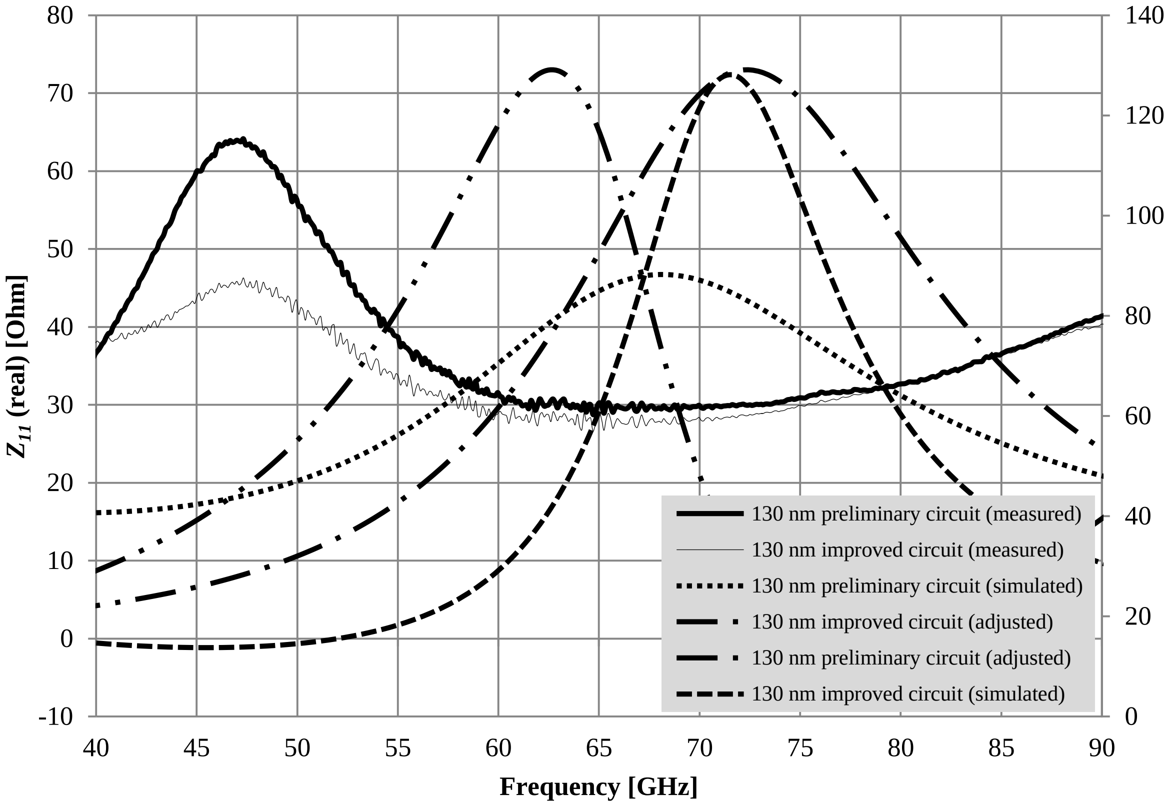

Figure 5.6: Real impedance of simulated and measured dipole equivalent circuits.

From Figure 5.6 the real impedance of the preliminary simulated circuit is given by the dotted line, and the measured results given by the thick solid line. The improved simulated circuit real impedance is given by the dashed line (read from the secondary *y*-axis) and its measured results given by the thin solid line. Both of these sets of results showed a similar tendency where the peak of the real impedance of the measurement results was found at a lower frequency compared to the simulated value (shift in frequencies presented in Figure 5.2). The real impedances at 60 GHz for these circuits (simulated and measured, preliminary and improved) were within the range of 27 Ω to 32 Ω which indicated that the measured prototype displayed consistent real impedances compared to its simulated counterpart at the (matched) 60 GHz frequency. The adjusted circuits (refer to Table 5.1 and Table 5.2) represented by the dash-dot and dash-dot-dot lines respectively, indicated a real impedance for the preliminary circuit of 28.2 Ω at 60 GHz, but a much larger 66.1 Ω for the improved circuit, which is consistent with the results obtained during the imaginary impedance results in Figure 5.5 where the complexity of a large number of circuit components influence circuit performance and these adjusted values increase the real impedance of the circuit. A comparison of the VSWR of each circuit (simulated and measured) is given in Figure 5.7.

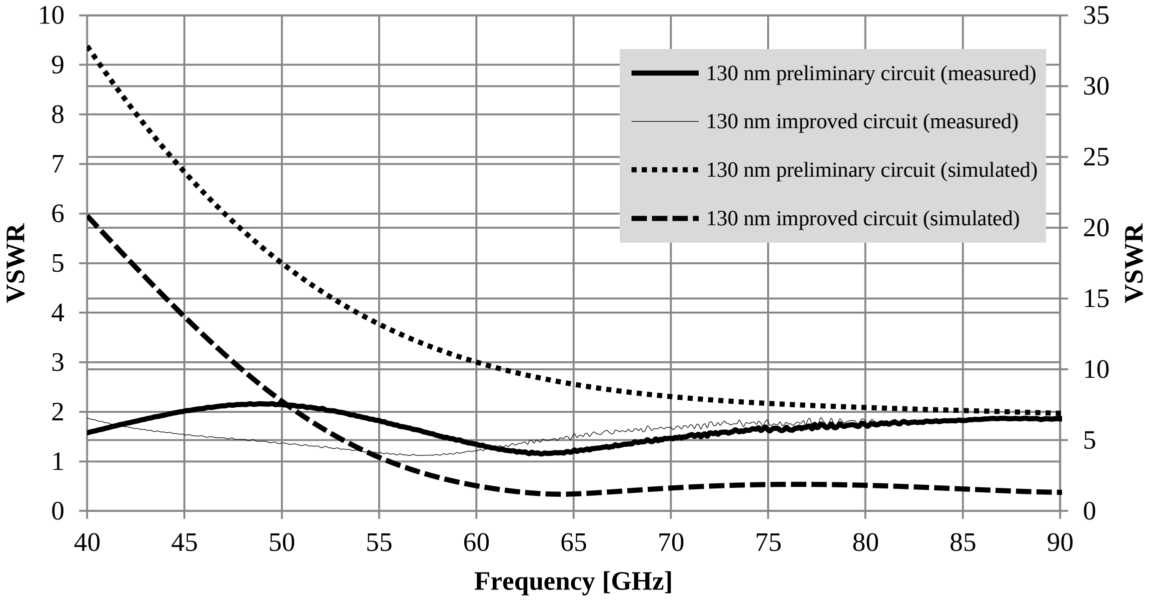

Figure 5.7: VSWR of simulated and measured dipole equivalent circuits.

The VSWR results in Figure 5.7 display a decrease (improvement) in VSWR beyond 60 GHz. The measurement results for the preliminary and improved circuits are displayed on the primary *Y*-axis with the simulated results on the secondary *Y*-axis. The simulated VSWR at 60 GHz for the preliminary circuit was determined to be 10.6:1 and the improved circuit 1.88:1 at 60 GHz. The measurement results displayed a similar tendency of the VSWR in the operating band, with the preliminary circuit VSWR measured at 60 GHz to be 1.88:1 and the improved circuit 1.86:1. Therefore, for both dipole circuits the reflected power at the input of the antenna is less than 10 % (2:1). The results are summarized in Table 5.3.

Table 5.3: Summary of simulated and measured results.

Component / circuit	**Imaginary impedance**			**Reflection coefficient [dB] at 60 GHz**	**VSWR at 60 GHz**
	Local minimum	**Local maximum**	**At 60 GHz**		
EM antenna (without substrate)	-98.13 Ω @ 83.8 GHz	-20.69 Ω @ 59 GHz	-j20.95 Ω	-16.60	1.35:1
EM antenna (with substrate)	-j439 Ω @ 74.5 GHz	+j300 Ω @ 68.8 GHz	+j2.30 Ω	-12.81	1.66:1
Preliminary circuit (simulated)	-j92.1 Ω @ 73 GHz	-j86.1 Ω @ 66 GHz	-j89.5 Ω	-16.10	10.67:1
Improved circuit (simulated)	-j55.7 Ω @ 78.5 GHz	+j32.5 Ω @ 67.4 GHz	-j3.2 Ω	-12.14	1.88:1
Preliminary circuit (measured)	-j11.6 Ω @ 76.5 GHz	-j1.33 Ω @ 69 GHz	-j17 Ω	-16.71	1.37:1
Improved circuit (measured)	+j1.69 Ω @ 52 GHz	+j26.9 Ω @ 68 GHz	+j12.5 Ω	-20.06	1.20:1
Adjusted preliminary (simulated)	-j36.5 Ω @ 83 GHz	+j34.5 Ω @ 63 GHz	+j35.6Ω	-16.7	-
Adjusted improved (simulated)	-j36.5 Ω @ 68 GHz	+j36.5 Ω @ 54 GHz	+j21.3 Ω	-13.7	-

From Table 5.3, the results for the EM antenna, preliminary circuit, improved circuit, as well as the circuit that contains adjusted component values with reference to the amount of error determined during measurements. The circuit operation can be defined by the characteristics of the frequency behaviour of each component. Additional degrees of freedom were implemented to maintain the transfer characteristics of the EM antenna. Ensuring similar frequency operation is crucial to accurately represent the antenna operation. The simulated and measured, preliminary and improved real impedances at 60 GHz for the circuits were within the range of 27 Ω to 32 Ω which indicated that the measured prototype displayed consistent real impedances compared to its simulated counterpart at the matched 60 GHz frequency. The adjusted circuits indicated a real impedance for the preliminary circuit of 28.2 Ω at 60 GHz, but a much larger 66.1 Ω for the improved circuit.

The results for the EM antenna with substrate included, the simulated results for the improved circuit, and the measured results for the improved circuit (greyed rows in Table 4) show similar frequency operation over a large bandwidth. The reflection coefficient and VSWR at 60 GHz show reflected power at the input of less than 10 % (VSWR of better than 2:1), constituting a good impedance matching [13].

The addition of components to quantify expected parasitic behaviour to the Foster canonical form for electrical antennas does enable antenna operation to be better estimated in an analogue circuit environment. The circuits can be transferred to smaller nodes to increase the minimum and maximum inductive and capacitive behaviour, since from Table 4, EM simulations, shows that these values can reach large positive and negative quantities.

The following section (refer to section 5.2) presents the measurement result for the LPF structures. These filters are variable with the use of a common-base transistor amplifier which does not add any gain to the output of the signal therefore taking advantage of the high reverse isolation and improved GBP compared to common-emitter and common-collector amplifiers (refer to section 4.6.5). The variable filter adds the functionality of changing environmental conditions within the IC based on a DC input as a function of attenuation required. The hypothesis states that if a variable attenuation of more than 10 dB can be achieved over the permitted DC input range, it can be used to simulate conditions within the environment that are commonly experienced during transmission. The *Butterworth* and *Chebyshev* LPF measurement results are presented.

5.2 PASSIVE FILTER MEASUREMENTS

The measurement results presented in this section are combined (on the same graphs) with the simulated results as a function of DC input signal to the base of the transistor. The input to the circuit is varied and the change in the filter attenuation is recorded and displayed. The passive filter transfer functions and circuit topologies are presented in section 4.5 and section 4.6 with the layout considerations and micrographs given in Appendix B. The *Bessel* filter was not implemented on the prototype IC since there was a limitation on the available area on the IC (recommended in future works in section 6.4) and to prove the hypothesis, the principles could be investigated using the *Butterworth* and *Chebyshev* filters.

The DC input signal for the simulated results are limited to 1.8 V as specified by the 130 nm technology and the simulations were performed only up to this value. For the measured results, this voltage was increased to approximately 50 % of its open emitter breakdown voltage (VB_{CBO} = 5.5 V) of 2.5 V ± 0.2 V so as not to damage the circuit components and displayed a larger change in attenuation compared to 1.8 V. Since no components were damaged with this practise, the results were recorded and are presented on the same result graphs as the (1.8 V maximum) simulated results.

5.2.1 *Butterworth* filter

The simulated results for the *Butterworth* filter for a 0 V and 1.8 V DC input, as well as the measured results for the prototyped filter for a 0 V and 2.5 V DC input are given in Figure 5.8. The passive filter attenuation is expected to decrease (lower attenuation) with an increasing DC supply, therefore at 0 V the largest attenuation achieved and at 1.8 V (2.5 V) the lowest attenuation should be achieved.

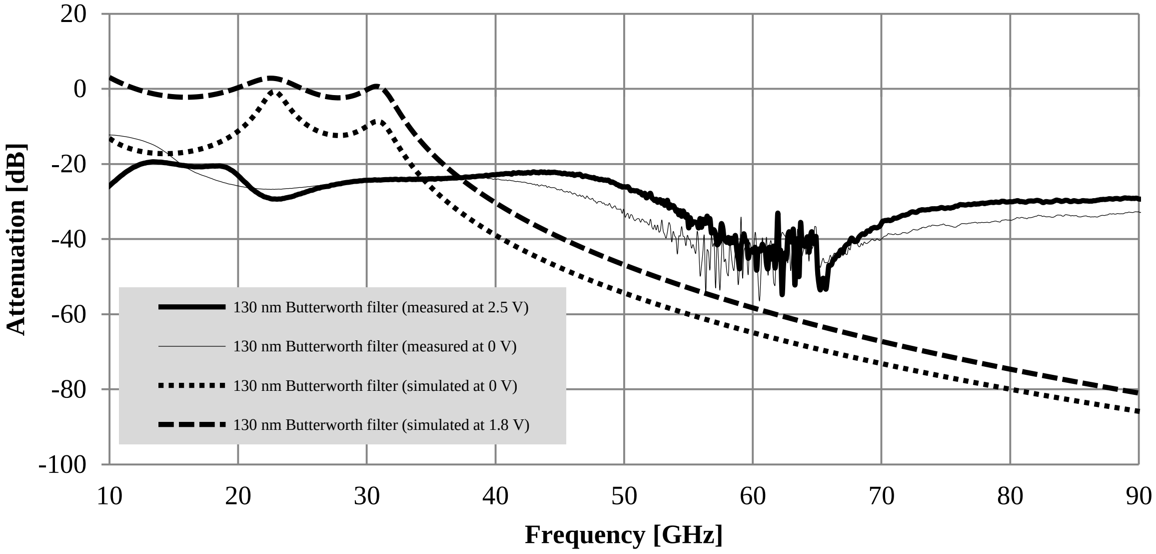

Figure 5.8: Simulated and measured results for the *Butterworth* LPF with varied DC input.

From Figure 5.8, the decrease in attenuation for the simulated results (dotted line at 0 V and dashed line at 1.8 V) is evident. The attenuation (1.8 V) at 60 GHz is approximately -57.6 dB, where the attenuation is increased (higher attenuation) at 0 V to -64.2 dB. This constitutes a 6.6 dB change in attenuation at 60 GHz with a 1.8 V (as specified for the 130 nm process) voltage span. The attenuation for the simulated filter, with a 1.8 V DC input also shows an approximately 0 dB attenuation of the input signal at low frequencies (< 30 GHz) (also refer to section 4.6.4 and section 4.6.5 for more detailed results). The measured results for the *Butterworth* LPF structure did show evidence of variable attenuation with a changing DC input in the frequency range higher than 40 GHz and below 70 GHz. The signal was, however, very noisy around the 60 GHz ± 5 GHz spectrum due to the frequency conversion allowing measurements up to 110 GHz (refer to section 3.8). The attenuation achieved on average around the 60 GHz frequency was -43 dB with a 2.5 V input signal to the circuit. Decreasing the input signal to 0 V allowed for an average attenuation at 60 GHz of -46 dB, constituting in a 3 dB (compared to the 6.6 dB for the simulated results) change in signal attenuation over the full voltage range. At lower frequencies (< 30 GHz) the attenuation transfer function of the filter displayed a higher attenuation compared to the simulated results by a value of approximately 20 dB. The circuit also did not display a similar slope (to determine the cut-off frequency and -3 dB bandwidth) at these lower frequencies which could point to insufficient modelling of the circuit layout (as opposed to library component schematic simulations) across the entire frequency spectrum (40 MHz to 110 GHz where measurements were conducted). Also evident from Figure 5.8 is that at high frequencies (> 70 GHz) the results do not follow the simulated results. At these frequencies, the transfer characteristics of the capacitors used (refer to section 3.1.2) are not available (defined) and only extrapolated based on its lower frequency operation, therefore the operation cannot be verified and alternative processes would be required for operation in this band. For this thesis, however, the operation is specified within the 57 GHz to 64 GHz band, and therefore these higher frequency anomalies do not influence the hypothesis. The possibility to model the IC layout was not possible within Cadence Virtuoso due to software license limitations. In section 5.3, the buffer and matching network is discussed and the discovery of the 20 dB attenuation is revisited in this section. To account for this 20 dB loss, the results for the *Butterworth* LPF were adjusted accordingly to present it such that the difference in attenuation of the 0 V and 2.5 V input are clearly visible. This adjustment is depicted in Figure 5.9.

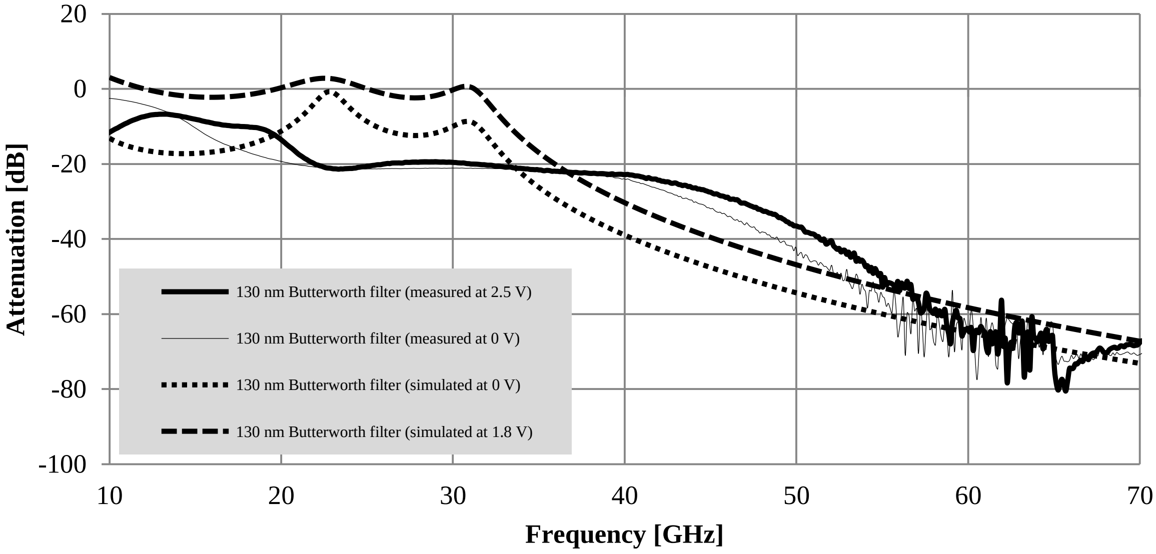

Figure 5.9: Simulated and measured results for the adjusted *Butterworth* LPF with varied DC input.

The adjustment of Figure 5.8 in Figure 5.9 accounts for the difference in attenuation at low frequencies and extrapolates the high-frequency conversion (from 67 GHz) based on the expected values from the simulated results. The adjusted results display the difference in attenuation based on its DC input, however, the presence of noise within the 55 GHz to 65 GHz band obstructs the true reading of the attenuation, and therefore an individual investigation for each measured result is presented in Figure 5.10 and Figure 5.11.

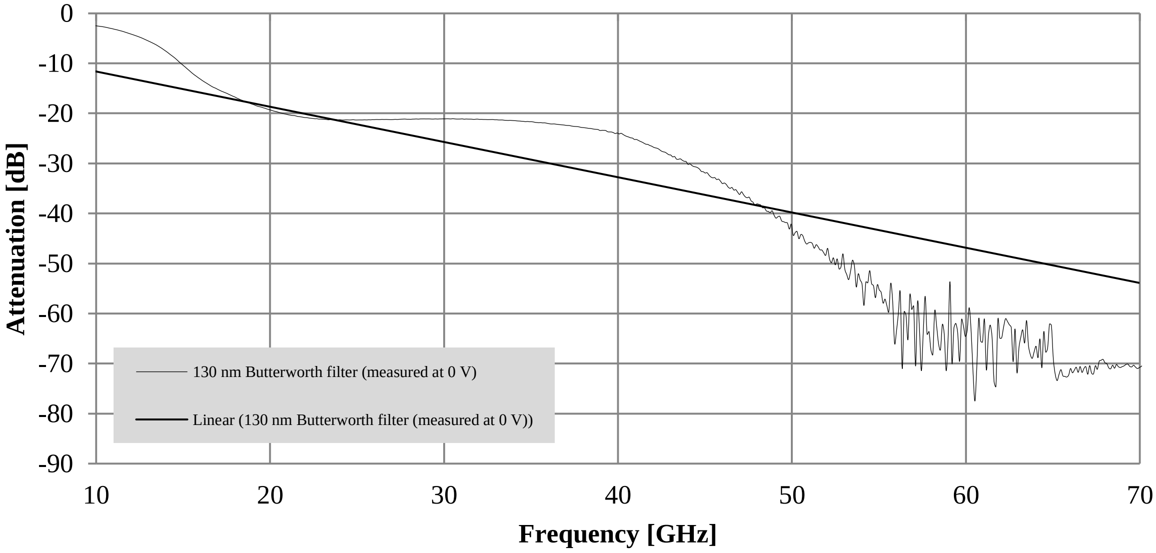

Figure 5.10: Measured results of the *Butterworth* filter (0 V input) with linear regression.

In Figure 5.10 the measured results for the *Butterworth* LPF is separated on a single graph in order to determine the multivariate linear regression of the function. This function (straight line in Figure 5.10) serves as a predictive model of the filter attenuation since the addition of noise to the system and high-frequency anomalies obstructs the readings. From Figure 5.10, the linear regression line at 60 GHz crosses the -47 dB mark when a 0 V DC signal is applied to the filter. The same analysis was done for the 2.5 V input signal, and the results are separated and displayed on Figure 5.11.

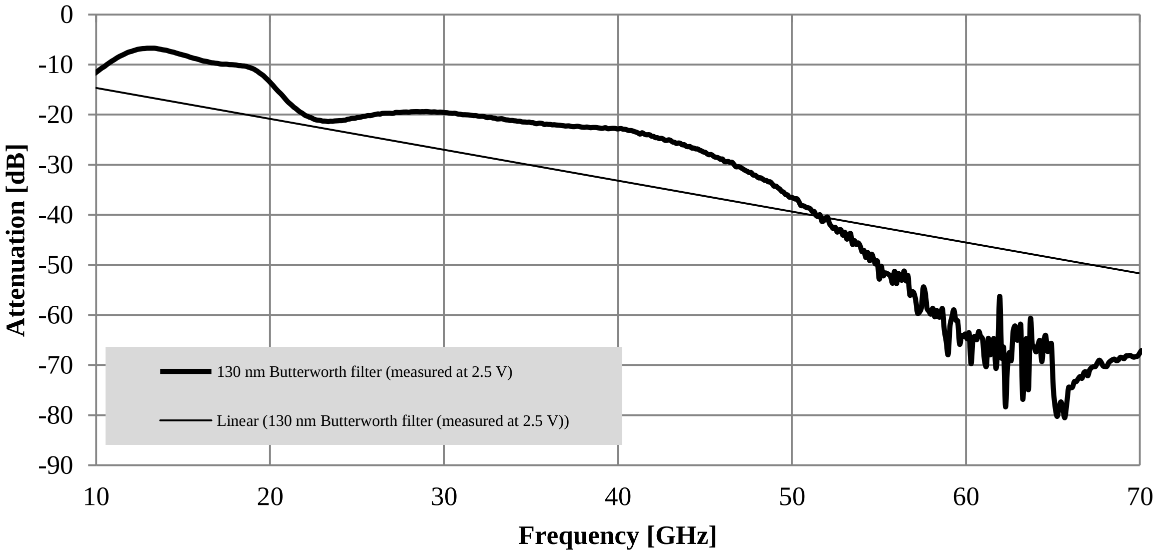

Figure 5.11: Measured results of the *Butterworth* LPF (2.5 V input) with linear regression.

From Figure 5.11, the linear regression model displays a similar trend compared to the 0 V input signal, however, it can be noted that the attenuation is slightly lower (-45 dB compared to -47 dB for the 0 V input). The results for the *Butterworth* LPF concluded that there is a difference (2 dB) in attenuation based on the DC input signal to the circuit, however the difference in attenuation (albeit the trend could be identified) was relatively small compared to the expected (from simulation) results. Similar analyses were done on the *Chebyshev* LPF and the results are discussed in section 5.2.2.

5.2.2 *Chebyshev* filter

The simulated and measured results for the *Chebyshev* LPF are given in Figure 5.12.

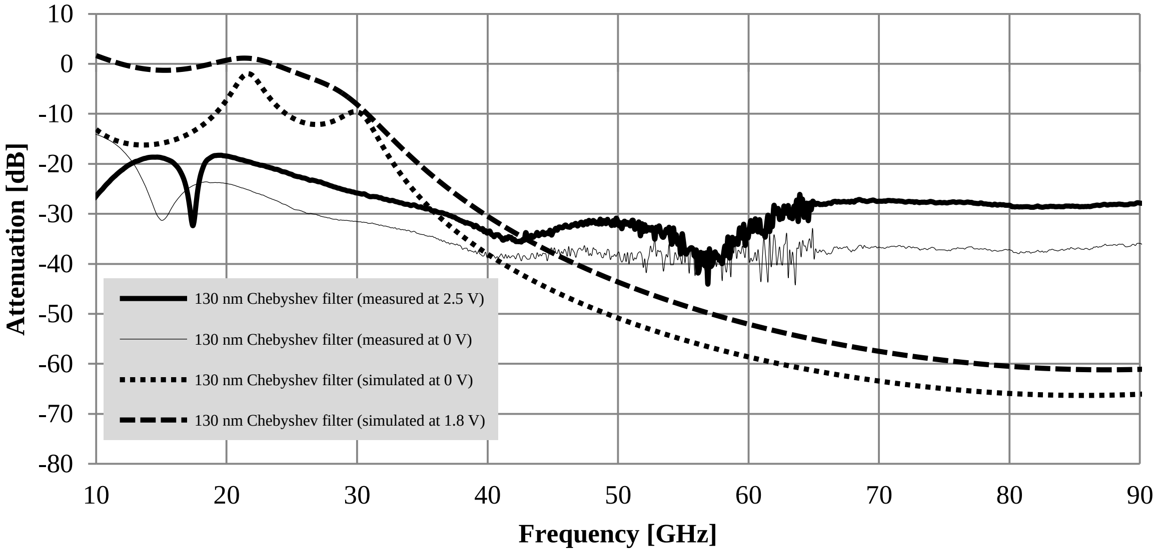

Figure 5.12: Simulated and measured results for the *Chebyshev* LPF with varied DC input.

From Figure 5.12 the simulated results for a 0 V and 1.8 V DC input is given by the dotted and dashed lines respectively. The measured results for the 0 V and 2.5 V DC input are given by the thin and thick solid lines respectively. The simulated results are discussed in section 4.6.4 and section 4.6.5. The change in DC input from 0 V to 1.8 V showed a decrease in attenuation from -58.2 dB to -51.6 dB at 60 GHz, constituting a 6.6 dB difference in attenuation. Similar to the *Butterworth* measured results, the attenuation of the filter at frequencies below 30 GHz was 20 dB higher compared to the simulated results. Inspection of the circuit layout showed no evidence of improper connections and this 20 dB attenuation below 30 GHz was further investigated. Noise in the system around the 60 GHz frequency also limited the accuracy of the readings close to the desired operating frequency. The trend showed that there was a definite increase in attenuation with lower DC input, but further analysis on the results were done to determine the validity of this statement. In Figure 5.13 an adjustment to the results to account for the inherent 20 dB attenuation below 30 GHz was made and depicted.

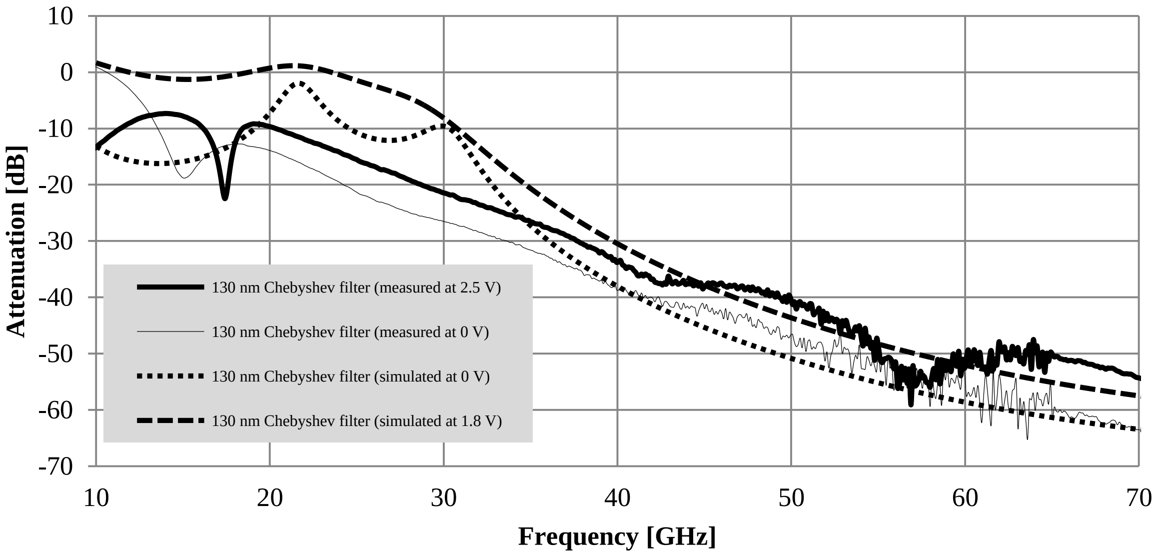

Figure 5.13: Simulated and measured results for the adjusted *Chebyshev* LPF with varied DC input.

From Figure 5.13 the simulated results are similar to the results in Figure 5.12 and used to determine the expected trend of the measured results displayed in the thin (0 V input) and thick (2.5 V input) solid lines respectively. The measured results display a similar trend in terms of attenuation based on input signal, where the 0 V DC input signal produced a higher attenuation (approximately -55 dB at 60 GHz) compared to the 2.5 V input which showed an attenuation of approximately -50 dB at 60 GHz. In order to view the trends of the transfer function more clearly, the linear regression prediction models for the 0 V and 2.5 V input signals are given in Figure 5.14 and Figure 5.15.

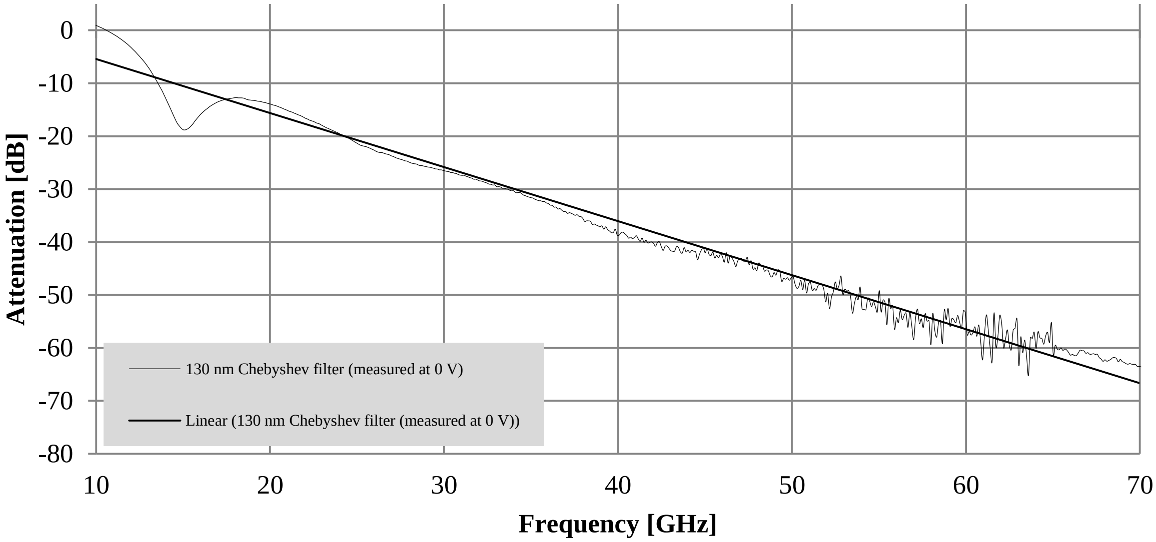

Figure 5.14: Measured results of the *Chebyshev* filter (0 V input) with linear regression.

From Figure 5.14 it can be seen that the regression prediction for the 0 V input signal for the *Chebyshev* LPF predicts an attenuation of approximately -55 dB at 60 GHz. This value is in accordance with the simulated value (-58.2 dB) and the expected results for the circuit with a 2.5 V input signal is that the attenuation should be less compared to the 0 V input signal. The results for the 2.5 V signal and its linear prediction is given in Figure 5.15.

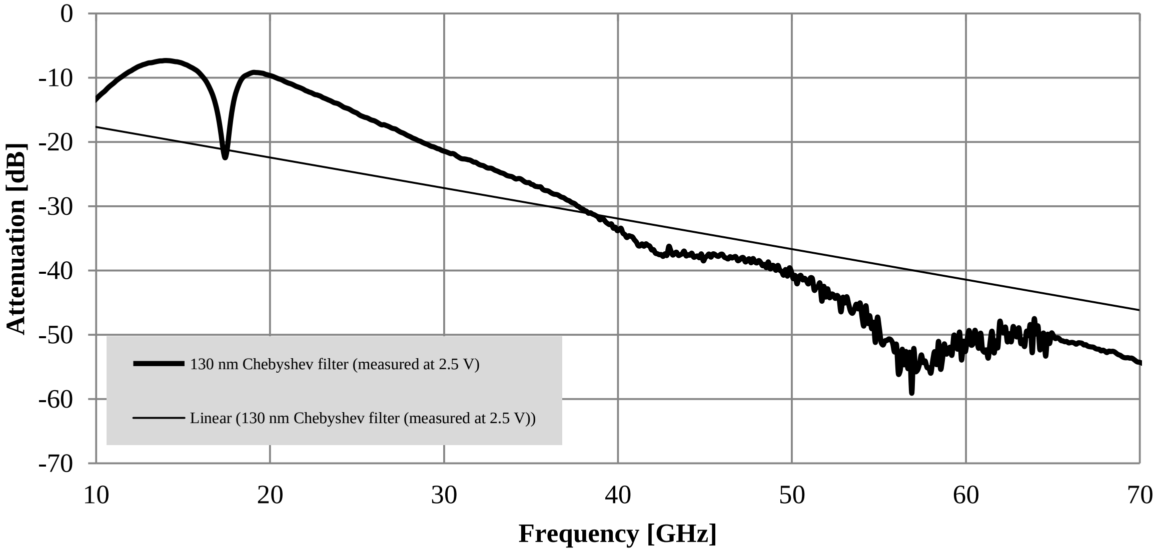

Figure 5.15: Measured results of the *Chebyshev* filter (2.5 V input) with linear regression.

From Figure 5.15, the prediction for attenuation at 60 GHz is approximately -41.5 dB (compared to -55 dB for a 0 V input) whereas the simulated results predicted an attenuation of -51.6 dB. These results confirmed that the attenuation of the *Chebyshev* LPF could be better controlled with varied DC input signal compared to the *Butterworth* circuit, since a clearer and higher difference in attenuation (14.5 dB versus 2 dB) could be achieved.

The measured results for the buffer circuit and matching network is given in section 5.3 and from these results further investigation into the -20 dB attenuation of the LPF circuits is introduced.

5.3 MATCHING NETWORK MEASUREMENTS

In Figure 5.16 the measured results for the buffer circuit and the results for the buffer circuit connected to the matching network (matched to provide maximum power transfer to the bonding pads on the IC) are presented.

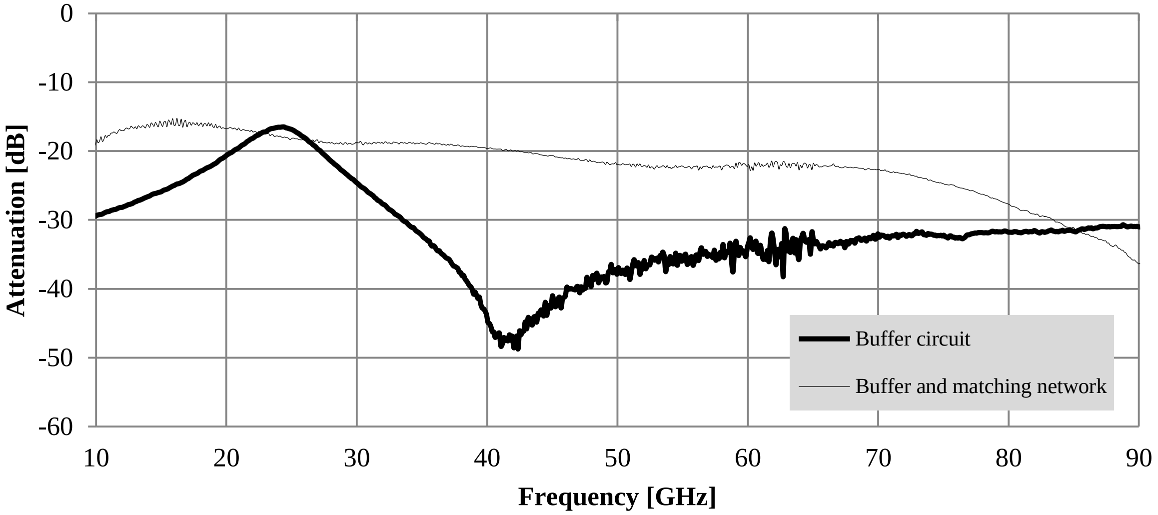

Figure 5.16: Output impedance before and after the output matching network.

The results in Figure 5.16 also showed a large attenuation in the measured output. The output of the buffer circuit and matching network should ideally pass all signals without any attenuation (constant 0 dB output for the entire frequency band), however, there is a significant attenuation of approximately -20 dB up to 70 GHz after which the attenuation increases due to the increased frequency and increased parasitic effects of the 130 nm components. The output (thin solid line) did show a relatively constant attenuation across the frequency spectrum which indicated correct circuit operation for the matched buffer circuit, and the -20 dB attenuation factor could have been as a result of the improper grounding strategy as presented in Figure 5.3. The adjusted results do confirm correct circuit operation when taking into account this anomaly present in the discussed circuits.

5.4 CONCLUSION

This chapter presented the measurement results of the preliminary and improved dipole equivalent circuits (refer to section 5.1), LPF structures (*Butterworth* and *Chebyshev*) (refer to section 5.2), and buffer circuit and matching network (refer to section 5.3) manufactured in the 130 nm process. The measured results are compared with the simulated results to determine the accuracy of the layout of each circuit and investigate the performance based on the research hypothesis presented in section 1.2. Circuit performance of the measured results are analysed in accordance with expected results from the simulated circuit (refer to Chapter 4) and discussed in each section respectively.

The dipole equivalent circuit measurement results (refer to section 5.1) reflection coefficient (S_{11}) results are presented in Figure 5.2. The results for the preliminary circuit showed a change in reflection coefficient from -35 dB to -22.2 dB but with only a small shift in resonance frequency from 64.3 GHz (simulated) to 64 GHz (measured) and therefore the hypothesis of this circuit operating within the desired frequency band was still valid. Further investigation into the practical (measured) values of the circuit components was done. These practical values are given in Table 5.1 and the simulated results with these practical values are also given on Figure 5.2. From Table 5.1 it was determined that the inductive components in the circuit showed the largest change in value on the layout of the IC and this was possibly due to the grounding strategy used. This strategy can be improved in future iterations of the circuit structure by increasing the width of the ground plane, ensuring that the ground plane fill up more of the circuit structure in terms of area covered with sufficient return-paths for ground currents to avoid common-mode currents that could act as a parasitic antenna. A larger ground plane can conduct significantly larger currents with low-voltage drops, ensuring the ground connection of all connected components are at the same reference potential. Connecting all ground planes of the GSG probe will also avoid potential differences in these planes. DUT calibration on the wafer substrate as opposed to ISS structures (discussed in the chapter overview for Chapter 5) would also eliminate frequency deviations at high (> 67 GHz) frequencies.

The improved dipole equivalent circuit structure results showed another shift in frequency from 64 GHz (-21.8 dB) to 56.7 GHz (-24 dB) as a result of the same grounding approach.

The larger number of passive components within this structure resulted in this larger shift in frequency; however, the research hypothesis was still valid since the resonance could be shifted back in future iterations of the IC layout. A similar investigation into the results (Table 5.2) again proved that the inductive components experienced the largest change in value and confirmed the interference from the ground plane contributing.

The results of the imaginary and real impedance for both structures are given in Figure 5.5 and Figure 5.6 respectively. The results are discussed in detail below each figure and good correlation between the simulated and measured results are presented, with small changes in frequency behaviour as a result of the ground plane discussion (discussed in the chapter overview for Chapter 5). VSWR measured results for both structures gave a ratio of less than 2:1 at 60 GHz (Figure 5.7).

The measured results compared with the simulated results for the LPF structures are given in section 5.2. The *Butterworth* filter results are depicted in Figure 5.8. During measurements it was decided to increase the voltage to the common-base amplifier (refer to section 4.6.5) responsible for the varied attenuation to 2.5 V (from 1.8 V) to increase the variable attenuation without damaging the circuit components. From Figure 5.8 it was seen that the results displayed an approximately 20 dB difference (< 30 GHz) when compared with the simulated results, and noisy results in the 55 GHz to 65 GHz band decreased the accuracy of the measurements. In order to investigate the results with improved accuracy, the results were adjusted taking into account the 20 dB difference for lower frequencies and the inaccurate results for high frequencies (as a result of incomplete modelling of the 130 nm circuit components above the specified working frequency) to determine a trend for the results and interpret the validity of the research hypothesis. In Figure 5.9, Figure 5.10, and Figure 5.11 the results are given with the adjusted values, and a linear regression trend line for the 0 V and 2.5 V DC input respectively. The research hypothesis could still be verified as the results displayed a change in attenuation for varied input signal. Similar analysis for the *Chebyshev* LPF was done and the measured results are depicted in Figure 5.12 with the adjusted values given in Figure 5.13. The trend-line analysis for the 0 V input and 2.5 V input are given in Figure 5.14 and Figure 5.15 respectively. Again, it was confirmed that there is a change in filter attenuation based on the input signal to the circuit.

During measurements of the buffer circuit and matching network (refer to Figure 5.16) it was determined that again -20 dB attenuation (from expected 0 dB) was experienced throughout the frequency band from 10 GHz to 70 GHz. This attenuation introduced parasitically, were losses that had to be adjusted to obtain measured results in accordance to simulations, however, no impact on the research hypothesis and overall operation of the circuits was experienced consequently.

CHAPTER 6: CONCLUSION

6. CHAPTER OVERVIEW

The conclusion to the research conducted in this thesis is summarized in this chapter and a critical analysis of the research hypothesis is presented, including scope delimitations and assumptions and possible future work implementations.

6.1 INTRODUCTION

This chapter investigates the validity of the research hypothesis proposed in Chapter 1 and provides a critical analysis of the gathered information, research, proposed techniques, and simulated and measured results throughout this thesis. The research hypothesis and research questions (refer to section 1.2) proposed an equivalent electrical circuit of a radiating antenna and variable filter in the mm-wave spectrum as building blocks for an analogue, real-time, path-loss prediction model. Chapter 1 investigated the possibility of this research hypothesis with justification for the research and provided a research methodology to be followed. In Chapter 2, this hypothesis was enforced with a literature review on the aspects involved in undertaking such a study in the mm-wave domain, and supporting literature reviews were presented regarding path-loss models and antenna theory compared with the current body of knowledge. Passive devices are the focus of this thesis and relevant modelling techniques and considerations are presented in this chapter. Chapter 3 presented the research methodology and summarized the techniques and software suites used during the course of this research. Measurement equipment was discussed and an explanation on the techniques used to do measurements is given. In Chapter 4 the mathematical modelling and analysis together with the simulated results are presented. The experiments were used to determine the validity of the hypothesis in a 130 nm process and ensure that the component limitations of this process are within bounds to allow modelling for the mm-wave spectrum. The measured results confirming operation are presented in Chapter 5 and an analysis of the results is given in this chapter to investigate and identify any unexpected results.

6.2 CRITICAL EVALUATION OF HYPOTHESIS

Relevant information gathered from the research presented in this thesis including comments on the research methodology, practical implementation from simulated circuits to a working prototype, and comments on the outcome of this study is presented in this section.

- Research into mm-wave applications has proven beneficial in recent years as the large bandwidth applications are a requirement for high data-rate wireless transmissions. Predicting the behaviour and operation of these systems often require down-conversion of analogue signals to the digital domain. The question was asked how to develop a model on an analogue level using passive components within a 130 nm technology for real-time analysis of the signal transfer on an IC.
- Not only would this method provide real-time analysis, it could allow emulating environmental conditions of a communication signal through application of a controlled varied analogue input to the system. The amount of attenuation experienced by a mm-wave signal is high over relatively short distances (< 1 m). It would be beneficial for communication engineers to not only have mathematical predictions of signal behaviour, but have the ability to quantise the attenuation based on electronic models and analyse the effects in real-time.
- A study into the current body of knowledge based on antennas operating in the mm-wave spectrum was conducted and presented in Table 2.6 with focus on the topology and type of antennas, reflection coefficients, gain, and efficiency to determine if the overall performance of the simulated antenna in CST Microwave Studio (refer to Table 3.5) presented comparable results. These results then formed the basis for comparison with the proposed electronic equivalent circuit presented in this thesis.
- An electrical equivalent model of a dipole antenna based on the *Foster canonical form* operating in the 60 GHz frequency band was studied to determine the effectiveness of this model at the specific frequency using a 130 nm process with component limitations as a function of the node. A model using ideal components (no limitations on component values or sizes) was presented and with good correlation to EM results for the dipole antenna. The limitations of the node were implemented for ideal components, and an improved model was developed to improve the accuracy of the transfer characteristics of the model.
- A software script was developed in MATLAB (refer to Table 3.5) that reads information supplied by the user in terms of the transfer characteristics of the radiating antenna and uses this information supplied to determine crucial parameters within the transfer function. This information is processed through an iterative process that

converges to a solution of the transfer functions, and displays the results in the form of a *Foster canonical form* equivalent circuit to be used as a first estimation for the circuit component values with accuracy within 10 % of the user specified function. These component values can be altered by the user to fit the transfer function with more accuracy.

- Simulated results for the electrical equivalent circuits are presented and analysis on the input impedance (Z_{11}) real and imaginary components are done with reference to the parameters obtained in EM simulation. Reflection coefficient parameters are also investigated to determine the resonance (series and parallel) of each circuit and if this result is in accordance with the EM simulation of the radiating dipole. VSWR results are used in comparative studies, and a conclusion for the proposed circuits with reference to its validity on the research hypothesis was drawn. Simulated results showed that the research questions and research hypothesis could in fact be further investigated with the 130 nm node and based on ideal component values, this method could be expanded to other technology nodes (smaller than 130 nm allowing for smaller dimensions at constant aspect ratios that translates into smaller component values with reduced manufacturing tolerances).
- LPF structures were investigated using only passive components to enable the ability to vary the amount of attenuation with reference to the path-loss prediction models discussed in section 2.1. The amount of attenuation required to depict different environmental conditions is investigated (around -100 dB attenuation with a ± 10 dB variable attenuation from a 0 V to 1.8 V DC input) and the possibility of providing this attenuation using passive components within the 130 nm structure is investigated. It was confirmed that the attenuation is in fact possible using a 10 GHz, 19 GHz, and 10 GHz cut-off frequency for the *Butterworth*, *Chebyshev*, and *Bessel* LPF respectively.
- The dipole equivalent circuits (preliminary and improved) based on the *Foster canonical form*, as well as the *Butterworth* and *Chebyshev* LPFs (not the *Bessel* filter due to limited chip area) were prototyped using a 130 nm process. The measurement set-up was done by mounting the IC on a ceramic substrate with Au-sputtered tracks and pads to allow wire bonding from the IC to the external pads. The substrates were

mounted on a Cu-PCB to allow easy access to connections from the measurement equipment (refer to sections 3.7 and 3.8).

- Measurements of the passive circuits were conducted and the results are used to verify the circuit operation based on the layout techniques. The measurements displayed good correlation with simulated results and the dipole equivalent circuits displayed a shift in frequency compared to simulated results. This shift could be as a result of improper grounding techniques as specified in Figure 5.3 but did not influence the validity of the research hypothesis in terms of circuit operation in comparison with the EM radiating antenna transfer functions.
- The LPF results also showed consistent difference in attenuation compared to simulation of approximately 20 dB. In the analysis of the buffer circuit and matching network, it was determined that the transfer of these functions which should display 0 dB attenuation across the frequency spectrum, also displayed -20 dB (approximately constant) attenuation. The losses incurred by the circuit (also could be a result of the grounding technique) could be adjusted to verify the operation of the circuits, with linear regression trend lines implemented to determine the predicted values of circuit attenuation at 60 GHz. The variable filters were also confirmed to vary attenuation based on the DC input signal supplied to the circuit. A 2.5 V DC input was supplied in measurements (as opposed to 1.8 V in simulation) to improve the range of attenuation without damaging any of the components.

The scope limitations and assumptions considered during the development of this thesis and required to prove its validity and effectiveness are discussed in section 6.3.

6.3 SCOPE LIMITATIONS AND ASSUMPTIONS

The path-loss prediction models were researched to determine specific applications and environmental conditions based on obstructions and reflections (and diffractions) of the mm-wave signal during transmission. The tests to verify the mathematical derivations for these conditions were not completed, using the simulated dipole antenna since this antenna was not prototyped practically and only simulated in CST Microwave Studio.

The *Bessel* LPF was simulated but not implemented on the final IC layout due to the limitations of the area available on the IC as part of the MPW run. All sub-circuits were separately placed on the layout to allow the possibility to test each circuit individually. The overall circuit was also placed on the IC (dipole equivalent circuit, LPF, buffer circuit, matching network, and bonding pads in cascade) but a DC connection between the filter circuit and buffer prevented correct biasing of the circuits and the final output was not measured. The overall circuit measurement results were not crucial to validate the research hypothesis.

Limitations on minimum component values as a function of the technology node (130 nm) and manufacturing tolerances (when operating on component minimum size boundaries) restricted the ability to represent local minimums and maximums of the preliminary dipole equivalent circuit imaginary impedance (with respect to its frequency operation). This limitation highlighted the need for an improved circuit as proposed in section 4.3.2. This improved equivalent circuit provided increased degrees of freedom for more accurate representation of the dipole frequency operation, without the necessity of using a smaller node that would relax the component value limitations of the 130 nm node.

Post-layout simulations were not performed before prototyping of the proposed IC as a result of software license limitations in the Cadence package (preventing possible misuse of educational licences). Analysis on the parasitic effects of the proposed layout structures was not done and had to be accounted for in measurements (refer to Chapter 5).

6.4 FUTURE WORK AND POSSIBLE IMPROVEMENTS

Prototyping the dipole antenna (refer to section 4.1) and adding measurements to the overall body of work would add another degree of certainty to the obtained results within the scope of the research.

Further studies on the actual attenuation of nLOS components using the abovementioned antenna prototype could benefit a separate scope of research in terms of measuring attenuation of obstructions within the mm-wave spectrum. Although measured data could be obtained from the current body of knowledge, it would be preferred to determine these values on an experimental level.

Future implementations could include the *Bessel* LPF to serve as a comparison of performance in the 130 nm technology. Area limitations during this MPW prototype resulted in the *Bessel*

LPF excluded from the final layout. To analyse simulated and measured results of this structure it can be included on the IC by replacing the full circuit structure which was not measured.

EM modelling of the transmission lines used within the circuits in this research was attempted (although not forming part of the scope of this research) in CST Microwave Studio in collaboration with an international institution (IMT-Bucharest). Future implementations can be related to this research to include prototyping transmission lines in the 130 nm process and extrapolating measured results to allow better modelling of the transmission lines as EM components. This process would improve the expected mm-wave operation of the inductive components and improve parasitic extraction and estimation.

Following EM simulations of circuit components used in this thesis, improvements to the grounding approach can be verified. The current strategy possibly introduces parasitic inductances to the circuits which have an effect on the resonance frequency of the circuits and the impedance (imaginary and real) at the circuit outputs (refer to Chapter 5). A connection between both ground planes of the GSG probes are required, and thicker ground planes that enclose more of the circuit structures is required for more accurate measurement results compared to simulated results. The post-layout simulations are software license limited (refer to section 3.6) therefore EM simulations could further improve the confidence levels for expected measured results.

REFERENCES

[1] C. Liu, E. Skafidas, and R. Evans, "Capacity and Data Rate for Millimeter Wavelength Systems in a Short Range Package Radio Transceiver," *IEEE Trans. on Wireless Communications*, vol. 9, no. 3, pp. 903-906, March 2010.

[2] J. Wells, "Faster than Fiber: The Future of Multi-G/s Wireless," *IEEE Microwave Magazine*, vol. 10, no. 3, pp. 104-112, May 2009.

[3] J. Wang, R. V. Prasad, and I. Niemegeers, "Analyzing 60 GHz Radio Links for Indoor Communications," *IEEE Trans. on Consumer Electronics*, vol. 55, no. 4, pp. 1832-1840, November 2009.

[4] HDMI. (2012, January) High Definition Multimedia Interface. [Online]. www.hdmi.org

[5] A. Yamamoto, K. Ogawa, T. Horimatsu, A. Kato, and A. Fujise, "Path-loss Prediction Models for Intervehicle Communication at 60 GHz," *IEEE Trans. on Vehicular Technology*, vol. 57, no. 1, pp. 65-78, January 2008.

[6] J. Park, B. Richards, and B. Nikolic, "A 2 Gb/s 5.6 mW Digital LOS/NLOS Equalizer for the 60 GHz Band," *IEEE Jour. of Solid-State Circuits*, vol. 46, no. 11, pp. 2524-2534, November 2011.

[7] E. Juntunen, M. C. Leung, F. Barale, A. Rachamadugu, D. A. Yeh, B. G. Perumana, P. Sen, D. Dawn, S. Sarkar, S. Pinel, and J. Laskar, "A 60 GHz 38 pJ/bit 3.5 Gb/s 90 nm CMOS OOK Digital Radio," *IEEE Trans. on Microwave Theory and Techniques*, vol. 58, no. 2, pp. 348-355, February 2010.

[8] P. Cheng, C. M. Grens, and J. D. Cressler, "Reliability of SiGe HBTs for Power Amplifiers - Part II: Underlying Physics and Damage Modeling," *IEEE Trans. on Device and Materials Reliability*, vol. 9, no. 3, pp. 440-448, September 2009.

[9] G. Avenier, M. Diop, P. Chevalier, G. Troillard, N. Loubet, J. Bouvier, L. Depoyan, N. Derrier, M. Buczko, C. Leyris, S. Boret, S. Montusclat, A. Margain, S. Pruvost, S. T. Nicolson, K. H. K. Yau, N. Revil, D. Gloria, D. Dutartre, and S. P. Voinigescu, "0.13 µm SiGe BiCMOS Technology Fully Dedicated to Millimeter-Wave Applications," *IEEE Jour. of Solid-State Circuits*, vol. 44, no. 9, pp. 2312-2321, September 2009.

[10] N. Moraitis and P. Constantinou, "Indoor Channel Measurements and Characterization at 60 GHz for Wireless Local Area Network Applications," *IEEE Trans. on Antennas and*

Propagation, vol. 52, no. 12, pp. 3180-3189, December 2004.

[11] M. A. Panjwani, A. L. Abbott, and T. S. Rappaport, "Interactive Computation of Coverage Regions for Wireless Communications in Multifloored Indoor Environments," *IEEE Jour. on Selected Areas in Communication*, vol. 14, no. 3, pp. 420-430, April 1996.

[12] B. T. Wang, A. M. Niknejad, and R. W. Brodersen, "Circuit Modeling Methodology for UWB Omnidirectional Small Antennas," *IEEE Jour. on Selected Areas in Communications*, vol. 24, no. 4, pp. 871-877, April 2006.

[13] J. Powel, H. Kim, and C. G. Sodini, "SiGe Receiver Front Ends for Millimeter-Wave Passive Imaging," *IEEE Trans. on Microwave Theory and Techniques*, vol. 56, no. 11, pp. 2416-2425, November 2008.

[14] S. Geng, J. Kivinen, X. Zhao, and P. Vainikainen, "Millimeter-Wave Propagation Channel Characterization for Short-Range Wireless Communication," *IEEE Trans. on Vehicular Technology*, vol. 58, no. 1, pp. 3-13, January 2009.

[15] C. H. Doan, S. Emami, A. M. Niknejad, and R. W. Brodersen, "Millimeter-Wave CMOS Design," *IEEE Jour. of Solid-State Circuits*, vol. 40, no. 1, pp. 144-155, January 2005.

[16] Y. Lin, J. Chang, C. Chen, H. Liang, P. Huang, T. Wang, G. Huang, and S. Lu, "Ultralow-Loss and Broadband Micromachined Transmission Line Inductors for 30-60 GHz CMOS RFIC Applications," *IEEE Trans. on Electron Devices*, vol. 54, no. 9, pp. 2512-2519, September 2007.

[17] J. Brinkhoff, K. Koh, K. Kang, and F. Lin, "Scalable Transmission Line and Inductor Models for CMOS Millimeter-Wave Design," *IEEE Trans. on Microwave Theory and Techniques*, vol. 56, no. 12, pp. 2954-2962, December 2008.

[18] G. Michel, "Numerical Modeling of Millimeter-Wave Transmission Lines," *IEEE Trans. on Plasma Science*, vol. 38, no. 6, pp. 1375-1384, June 2010.

[19] K. Kang, J. Brinkhoff, J. Shi, and F. Lin, "On-Chip Coupled Transmission Line Modeling for Millimeter-Wave Applications Using Four-Port Measurements," *IEEE Advanced Packaging*, vol. 33, no. 1, pp. 153-159, February 2010.

[20] T. Quemerais, L. Moquillon, J. Fournier, and P. Benech, "65-, 45-, and 32-nm Aluminium and Copper Transmission-Line Model at Millimeter-Wave Frequencies," *IEEE Trans. on Microwave Theory and Techniques*, vol. 58, no. 9, pp. 2426-2433, September 2010.

[21] T. S. Rappaport, *Wireless Communications: Principles and Practice*, 2nd ed.: Prentice Hall, 2002.

[22] H. Chuang, L. Yeh, P. Kuo, K. Tsai, and H. Yue, "A 60 GHz Millimeter Wave CMOS Integrated On-Chip Antenna and Bandpass Filter," *IEEE Trans. on Electron Devices*, vol. 58, no. 7, pp. 1837-1845, July 2011.

[23] C. R. Anderson and T. S. Rappaport, "In-Building Wideband Partition Loss Measurements at 2.5 and 60 GHz," *IEEE Trans. on Wireless Communications*, vol. 3, no. 3, pp. 922-928, May 2004.

[24] A. Natarajan, S. K. Reynolds, M. Tsai, S. T. Nicolson, J. C. Zhan, D. G. Kam, D. Liu, Y. O. Huang, A. Garcia, and B. A. Floyd, "A Fully-Integrated 16-Element Phased-Array Receiver in SiGe BiCMOS for 60-GHz Communications," *IEEE Jour. of Solid-State Circuits*, vol. 46, no. 5, pp. 1059-1075, May 2011.

[25] R. J. Hill, "Absorption by the Tails of the Oxygen Microwave Resonances at Atmospheric Pressures," *IEEE Trans. on Antennas and Propagation*, vol. AP-35, no. 2, pp. 198-204, February 1987.

[26] P. W. Rosenkranz, "Shape of the 5 mm Oxygen Band in the Atmosphere," *IEEE Trans. on Antennas and Propagation*, vol. AP23, no. 4, pp. 498-506, July 1975.

[27] J. H. Van Vleck, "The absorption of Microwaves by Oxygen," *Physical Review*, vol. 71, no. 7, pp. 413-424, April 1947.

[28] S. Hakusui. (2001, April) RF Globalnet. [Online]. www.rfglobalnet.com

[29] O. Landron, M. J. Feuerstein, and T. S. Rappaport, "A Comparison of Theoretical and Empirical Coefficients for Typical Exterior Wall Surfaces in a Mobile Environment," *IEEE Trans. on Antennas and Propagation*, vol. 44, no. 3, pp. 341-351, March 1996.

[30] M. Sarkar, D. San Segundo Bello, C. van Hoof, and A. Theuwissen, "Integrated Polarization Analyzing CMOS Image Sensor for Material Classification," *IEEE Sensors Journal*, vol. 11, no. 8, pp. 1692-1703, August 2011.

[31] S. J. Orfanidis, *Electromagnetic Waves and Antennas*, 1st ed. New Jersey, United States of America: Rutgers University, 2010.

[32] K. Sato, T. Manabe, T. Ihara, H. Saito, S. Ito, T. Tanaka, K. Sugai, N. Ohmi, Y. Murakami, M. Shibayama, Y. Konishi, and T. Kimura, "Measurements of Reflection and Transmission Characteristics of Interior Structures of Office Building in the 60-GHz

Band," *IEEE Trans. on Antennas and Propagation*, vol. 45, no. 12, pp. 1783-1792, December 1997.

[33] R. Piesiewicz, "Properties of Building and Plastic Materials in the THz Range," *International Journal of Infrared and Millimeter Waves*, vol. 28, no. 5, pp. 363-371, May 2007.

[34] C. Jansen, R. Piesiewicz, D. Mittleman, T. Kürner, and M. Koch, "The Impact of Reflections From Stratified Building Materials on the Wave Propagation in Future Indoor Terahertz Communication," *IEEE Trans. on Antennas and Propagation*, vol. 56, no. 5, pp. 1413-1419, May 2008.

[35] G. D. Durgin, "The Practical Behavior of Various Edge-Diffraction Formulas," *IEEE Antennas and Propagation Magazine*, vol. 51, no. 3, pp. 24-35, June 2009.

[36] M. Jacob, S. Priebe, R. Dickhoff, T. K. Ostmann, T. Schrader, and T. Kürner, "Diffraction in mm and Sub-mm Wave Indoor Propagation Channels," *IEEE Trans. on Microwave Theory and Techniques*, vol. 60, no. 3, pp. 833-844, March 2012.

[37] A. Bogush and R. Elkins, "Gaussian Field Expansions for Large Aperture Antennas," *IEEE Trans. on Antennas and Propagation*, vol. 34, no. 2, pp. 228-243, February 1986.

[38] L. Tsang, H. Braunisch, R. Ding, and X. Gu, "Random Rough Surface Effects on Wave Propagation in Interconnects," *IEEE Trans. on Advanced Packaging*, vol. 33, no. 4, pp. 839-856, November 2010.

[39] S. van den Buckle and A. Franchois, "A Full-Wave 2.5D Volume Integral Equation Solver for 3D Millimeter-Wave Scattering by Large Inhomogeneous 2D Objects," *IEEE Trans. on Antennas and Propagation*, vol. 57, no. 2, pp. 535-545, February 2009.

[40] R. L. Olsen, D. V. Rogers, and D. B. Hodge, "The aRb Relation in the Calculation of Rain Attenuation," *IEEE Trans. on Antennas and Propagation*, vol. AP-26, no. 2, pp. 318-329, March 1978.

[41] C. T. Mulangu and T. J. Afullo, "Variability of the Propagation Coefficients due to Rain for Microwave Links in Southern Africa," *Radio Science*, vol. 44, no. 3, p. RS 3006, May 2009.

[42] M. O. Fashuyi, P. A. Owolawi, and T. J. Afullo, "Rainfall Rate Modeling for LOS Radio Systems in South Africa," *SAIEE Transactions*, vol. 97, no. 1, pp. 74-81, March 2006.

[43] V. Dzhankhotov, J. Pyrhönen, P. Silventoinen, and M. Kuisma, "Hybrid LC Filter

Electrical Design Considerations," *IEEE Trans. on Industrial Electronics*, vol. 59, no. 2, pp. 762-768, February 2012.

[44] P. Artillan, M. Brunet, D. Bourrier, J. Laur, N. Mauran, L. Bary, M. Dilhan, B. Estibals, C. Alonso, and J. L. Sanchez, "Integrated LC Filter on Silicon for DC-DC Converter Applications," *IEEE Trans. on Power Electronics*, vol. 26, no. 8, pp. 2319-2325, August 2011.

[45] Z. Q. Zhang, X. P. Liao, and R. Wu, "RF on-chip LC Passive Bandpass Filter Based on GaAs MMIC Technology," *Electronics Letters*, vol. 46, no. 3, pp. 269-270, February 2010.

[46] T. E. Duncan, "Mutual Information for Stochastic Signals and Fractional Brownian Motion," *IEEE Trans. on Information Theory*, vol. 54, no. 10, pp. 4432-4438, October 2008.

[47] V. Sekar and K. Entesari, "Pole-Perturbation Theory for Nonlinear Noise Analysis of All-Pole RF MEMS Tunable Filters," *IEEE Trans. on Microwave Theory and Techniques*, vol. 58, no. 9, pp. 2475-2489, September 2010.

[48] C. A. Balanis, *Antenna Theory: Analysis and Design*, 2nd ed.: John Wiley and Sons, 1996.

[49] B. Levin, "About Antenna Gain Measurement in a Fresnel Zone," *IEEE Antennas and Propagation Magazine*, vol. 52, no. 2, pp. 64-70, April 2010.

[50] R. Suga, H. Nakano, Y. Hirachi, J. Hirokawa, and M. Ando, "Cost-Effective 60-GHz Antenna Package With End-Fire Radiation for Wireless File-Transfer System," *IEEE Trans. on Microwave Theory and Techniques*, vol. 58, no. 12, pp. 3989-3995, December 2010.

[51] A. L. Amadjikpe, D. Choudhury, G. E. Ponchak, and J. Papapolymerou, "Location Specific Coverage With Wireless Platform Integrated 60-GHz Antenna Systems," *IEEE Trans. on Antennas and Propagation*, vol. 59, no. 7, pp. 2661-2671, July 2011.

[52] K. K. Huang and D. D. Wentzloff, "A 60 GHz Antenna-Referenced Frequency-Locked Loop in 0.13 µm CMOS for Wireless Sensor Networks," *IEEE Jour. of Solid-State Circuits*, vol. 46, no. 12, pp. 2956-2965, December 2011.

[53] G. Felic, C. Thomas, and E. Skafidas, "Design of co-planar waveguide-fed slot/patch antenna with wire bond for a 60-GHz complementary metal-oxide-semiconductor

transceiver," *IET Microwaves, Antennas and Propagation*, vol. 5, no. 4, pp. 490-494, March 2011.

[54] Y. P. Zhang, M. Sun, K. M. Chua, L. L. Wai, and L. Duixian, "Antenna-in-Package Design for Wirebond Interconnection to Highly Integrated 60-GHz Radios," *IEEE Trans. on Antennas and Propagation*, vol. 57, no. 10, pp. 2842-2852, October 2009.

[55] R. A. Alhalabi, Y Chiou, and G. M. Rebeiz, "Self-Shielded High-Efficiency Yagi-Uda Antenna for 60 GHz Communications," *IEEE Trans. on Antennas and Propagation*, vol. 59, no. 3, pp. 742-750, March 2011.

[56] Y. Guo, J. Wang, B. Luo, and E. Liao, "Development of a 60-GHz Bandpass Filter and a Dipole Antenna Using Wafer Transfer Technology," *IEEE Electron Device Letters*, vol. 30, no. 7, pp. 784-786, July 2009.

[57] Xuan Hui Wu, A. A. Kishk, and A. W. Glisson, "Modeling of Wideband Antennas by Frequency-Dependant Hertizan Dipoles," *IEEE Trans. on Antennas and Propagation*, vol. 56, no. 8, pp. 2481-2489, August 2008.

[58] A. Levy, R. Shavit, and L. Habib, "Optimisation of a microstrip left-handed transmission line using circuit modelling," *IET Microwaves, Antennas and Propagation*, vol. 4, no. 12, pp. 2133-2143, December 2010.

[59] S. Palud, F. Colombel, M. Himdi, and C. Le Meins, "Circuit Modeling of a Small Broadband Conical Antenna," *IEEE Antennas and Wireless Propagation*, vol. 8, pp. 96-99, 2007.

[60] O. O. Olaode, W. D. Palmer, and W. T. Joines, "Effects of Meandering on Dipole Antenna Resonant Frequency," *IEEE Antennas and Wireless Propagation*, vol. 11, pp. 122-125, 2012.

[61] J. Oh and K. Sarabandi, "Low Profile, Miniaturized, Inductively Coupled Capacitively Loaded Monopole Antenna," *IEEE Trans. on Antennas and Propagation*, vol. 60, no. 3, pp. 1206-1213, March 2012.

[62] M. Thompson and J. K. Fidler, "Determination of the Impedance Matching Domain of Impedance Matching Networks," *IEEE Trans. on Circuits and Systems - I: Regular Papers*, vol. 51, no. 10, pp. 2098-2106, October 2004.

[63] C. Bowick, C. Ajluni, and J. Blyler, *RF Circuit Design*, 2nd ed. United States of America: Elsevier Inc., 2008.

[64] D. A. Chan and M. Feng, "A Compact W-Band CMOS Power Amplifier With Gain Boosting and Short-Circuited Stub Matching for High Power and High Efficiency Operation," *IEEE Microwave and Wireless Components Letters*, vol. 21, no. 2, pp. 98-100, February 2011.

[65] T. Yao, M. Q. Gordon, K. K. W. Tang, K. H. K Yau, M. Yang, P. Schvan, and S. P. Voinigescu, "Algorithmic Design of CMOS LNAs and PAs for 60-GHz Radio," *IEEE Jour. of Solid-State Circuits*, vol. 42, no. 5, pp. 1044-1057, May 2007.

[66] S. Chaki, T. Ishida, T. Mizukoshi, H. Yumoto, Y. Sasaki, M. Komaru, and Y. Matsuda, "A Short Stub-Matching 77-GHz-Band Driver Amplifier With an Attenuator Compensating Temperature Dependance of a Gain," *IEEE Trans. on Microwave Theory and Techniques*, vol. 53, no. 6, pp. 2073-2081, June 2005.

[67] T. O. Dickson, M. LaCroix, S. Boret, D. Gloria, R. Beerkens, and S. P. Voinigescu, "300-100-GHz Inductors and Transformers for Millimeter-Wave (Bi)CMOS Integrated Circuits," *IEEE Trans. on Microwave Theory and Techniques*, vol. 53, no. 1, pp. 123-133, January 2005.

[68] A. L. Franc, E. Pistono, D. Gloria, and P. Ferrari, "High-Performance Shielded Coplanar Waveguides for the Design of CMOS 60-GHz Bandpass Filters," *IEEE Trans. on Electron Devices*, vol. PP, no. 99, pp. 1-8, February 2012.

[69] A. M. Niknejad and H. Hashemi, Eds., *mm-Wave Silicon Technology: 60 GHz and Beyond*.: Springer, 2008.

[70] B. C. Wadell, *Transmission Line Handbook*. Norwood, Massachusetts: Artech House, 1991.

[71] R. L. Bunch and S. Raman, "Large-Signal Analysis of MOS Varactors in CMOS -Gm LC VCOs," *IEEE Jour. of Solid-State Circuits*, vol. 38, no. 8, pp. 1325-1332, August 2003.

[72] D. G. Kam, D. Liu, A. Natarajan, S. K. Reynolds, and B. A. Floyd, "Organic Packages with Embedded Phased-Array Antennas for 60-GHz Wireless Chipsets," *IEEE Trans. on Components, Packaging and Manufacturing Technology*, vol. 1, no. 11, pp. 1806-1814, November 2011.

[73] J. Kim, Y. Qian, G. Feng, P. Ma, J. Judy, M. F. Chang, and T. Itoh, "A Novel Low-Loss Low-Crosstalk Interconnect for Broad-Band Mixed-Signal Silicon MMIC's," *IEEE Trans. on Microwave Theory and Techniques*, vol. 47, no. 9, pp. 1830-1835, September 1999.

[74] M. F. Chang, Y. Qian, P. Ma, and T. Itoh, "Silicon/metal/polyimide (SIMPOL) interconnects for broadband signal silicon MMICs," *Electronics Letters*, vol. 34, no. 17, pp. 1670-1671, August 1998.

[75] B. D. Popovic, *CAD of Wire Antennas and Related Radiated Structures*. Bristol, United States of America: Taylor and Francis, 1991.

[76] R. M. Golden and J. F. Kaiser, "Root and Delay Parameters for Normalized Bessel and Butterworth Low-Pass Transfer Functions," *IEEE Trans. on Audio and Electronics*, vol. AU-19, no. 1, pp. 64-71, March 1971.

[77] S. V. Thyagarajan, S. Pavan, and P. Sankar, "Active-RC Filters Using the Gm-Assisted OTA-RC Technique," *IEEE Jour. of Solid-State Circuits*, vol. 46, no. 7, pp. 1522-1533, July 2011.

[78] C. W. Solomon, "Switched-capacitor Filters: Precise, Compact, Inexpensive," *IEEE Spectrum*, vol. 25, no. 6, pp. 28-32, June 1988.

[79] J. Lee, M. D. Johnson, and D. R. Kipke, "A Tunable Biquad Switched-Capacitor Amplifier-Filter for Neural Recording," *IEEE Trans. on Biomedical Circuits and Systems*, vol. 4, no. 5, pp. 295-300, October 2010.

[80] W. B. Kuhn, F. W. Stephenson, and A. Elshabini-Riad, "A 200 MHz CMOS Q-enhanced LC Bandpass Filter," *IEEE Jour. of Solid-State Circuits*, vol. 31, no. 8, pp. 1112-1122, August 1996.

[81] X. Qi, C. P. Yue, T. Arnborg, H. T. Soh, H. Sakai, Z. Yu, and R. W. Dutton, "A Fast 3-D Modeling Approach to Electrical Parameters Extraction of Bonding Wires for RF Circuits," *IEEE Trans. on Advanced Packaging*, vol. 23, no. 3, pp. 480-488, August 2000.

[82] C. Schuster, G. Leonhardt, and W. Fichtner, "Electromagnetic Simulation of Bonding Wires and Comparison with Wide Band Measurements," *IEEE Trans. on Advanced Packaging*, vol. 23, no. 1, pp. 69-79, February 2000.

[83] H. Wu, M. Tekle, C. S. Nallani, N. Zhang, and K. O. Kenneth, "Bond Wire Antenna/Feed for Operation Near 60 GHz," *IEEE Trans. on Microwave Theory and Techniques*, vol. 57, no. 12, pp. 2966-2972, December 2009.

[84] J. G. Linvill, "RC Active Filters," in *Proc. of the IRE*, 1954, pp. 555-564.

[85] M. O. Odedina and T. J. O. Afullo, "Rain Attenuation Prediction along Terrestrial Paths in South Africa Using Existing Attenuation Models," in *Proc.: IEEE Africon 2007*,

Windhoek, 26-28 September 2007.

APPENDIX A: MATLAB CODE FOR DIPOLE MODELLING

The MATLAB functions that were used to determine the first-order approximation of the dipole model are given in this appendix. Comments next to coded lines briefly describe the functionality of the lines / functions.

```
%MAIN MATLAB FUNCTION WITH USER DEFINED VALUES%

clear all;
clc;
G=0; %Set initial value for type of output zero

w1 = 1e9 * (str2double(input('Enter the frequency of the first maximum (GHz):
','s')));
e1 = 1e9 * (str2double(input('Enter the maximum permitted error for this maximum
(GHz): ','s')));
w2 = 1e9 * (str2double(input('Enter the frequency of the midpoint (GHz): ','s')));
w3 = 1e9 * (str2double(input('Enter the frequency of the first minimum (GHz):
','s')));
e2 = 1e9 * (str2double(input('Enter the maximum permitted error for this minumum
(GHz): ','s')));
w4 = 1e9 * (str2double(input('Enter the frequency of the asymptotic zero (GHz):
','s')));
acc = 1e9 * (str2double(input('Enter the required accuracy of the asymptotic zero
(GHz): ','s')));
x1 = (str2double(input('Enter the value of the imaginary axis at 40 GHz: ','s')));
e3 = (str2double(input('Enter the maximum permitted error for this value: ','s')));
x = (str2double(input('Enter the maximum number of iterations allowed before
stopping the simulation: ','s')));
w4_or = w4; %Set original value of asymptotic zero in GHz
y = 10; %variable to determine average (not use x which could be 100)

clc;
%% Main function called using user input values
[X, Fave, fmax, c0, c1, cp, l0, l1] = RoundX(w1, e1, w2, w3, e2, w4, w4_or, acc, x1,
e3, y);

if X < y %If a desired convergence has been achieved by the script
    fprintf('The desired circuit was achieved in %d iterations\n',X);
    G = (str2double(input('Press 1 for Z11 graph and 2 for S11 graph: ','s')));
    O = outputfunc(fmax, c0, c1, cp, l0, l1, G); %User defined output function
end

if X == y %If a desired convergence has not been achieved by the script
    fprintf('The iterations have been done %d times and has not converged\n', X);
    fprintf('The analysis was stopped\n');
    fprintf('The analysis will be done with the average of %d Hz\n', Fave);
    fprintf('\n');

    %[X, Fave, fmax, c0, c1, cp, l0, l1] = RoundX(w1, e1, w2, w3, e2, w4, w4_or,
acc, x1, e3, x);
    [X, Fave, fmax, c0, c1, cp, l0, l1] = RoundX(w1, e1, w2, w3, e2, Fave, w4_or,
acc, x1, e3, x);

    if X < x %Repeat output functions until user selects "3"
    fprintf('The desired circuit was achieved in %d iterations\n',X);
        while G ~= 3
        G = (str2double(input('Press 1 for Z11 graph, 2 for S11 graph and 3 to exit:
','s')));
        fprintf('Enter 3 to exit\n');
```

```
        O = outputfunc(fmax, c0, c1, cp, l0, l1, G); %Display generated transfer
function
        end
    end
end

if X == x
    fprintf('The iterations have been done %d times and has not converged\n', X);
    fprintf('The analysis was stopped\n');
    fprintf('Try decreasing the accuracy\n');
    fprintf('\n');
end

%FUNCTION DETERMINING FIRST APPROXIMATION AND ERROR%

function [X, Fave, fmax, c0, c1, cp, l0, l1] = RoundX(w1, e1, w2, w3, e2, w4, w4_or,
acc, x1, e3, x)

syms Cp C1 %Define variables used in this function

f = 40e9:10e6:200e9; %Define frequency range up to 200 GHz for test purposes
%%Define initial values used in function - will be outputs as iterated
%%values
X = 0;
Ftot = 0;
ctot = 0;
fmax = w4;
Fave = w4;
Fhigh = w3;
%%
[S1] = compvalues(w1, w2, w3, w4_or); %used in this function to calculate component
values first iteration
[S2] = compiterate(w1, w2, w3); %not used here

cp = 1 / (2 * pi * 40e9 * abs(x1)); %Set initial value for cp based on analytical
model
%Compute component values based on initial approximation
c0 = subs(S1.C0, Cp, cp);
c1 = subs(S1.C1, Cp, cp);
l0 = subs(S1.L0, Cp, cp);
l1 = subs(S1.L1, Cp, cp);

%Find the highest value (slope equal to zero) of approximated function
[Fhigh, Fave, ctot, Ftot] = findFhigh(f, fmax, c0, c1, cp, l0, l1, w3, Fhigh, ctot,
Ftot, Fave);
%Determine the error of approximation using computed results
[error] = errorfunction(fmax, c0, c1, cp, l0, l1, w1, w3, x1);

%Test if error is within specified boundaries and iterate to new values if
%larger than specified
  while (error(1) > e1) || (error(2) > e2) || (error(3) > e3) || (abs(Fhigh - w4) >
acc)
      %[c0, c1, cp, l0, l1] = compvalues(w1, w2, w3, w4_or, x1);
      cp = 1 / (2 * pi * 40e9 * abs(x1));
      c0 = subs(S1.C0, Cp, cp);
      c1 = subs(S1.C1, Cp, cp);
      l0 = subs(S1.L0, Cp, cp);
      l1 = subs(S1.L1, Cp, cp);

      %%Continue process until error is within specified boundaries
      [Fhigh, Fave, ctot, Ftot] = findFhigh(f, fmax, c0, c1, cp, l0, l1, w3, Fhigh,
ctot, Ftot, Fave);
      [error] = errorfunction(fmax, c0, c1, cp, l0, l1, w1, w3, x1);

      if (error(1) > e1) || (error(2) > e2) || (error(3) > e3) || (abs(Fhigh - w4) >
acc)
```

```
          cp = 1 / (2 * pi * 40e9 * abs(x1));
          A = ((subs(S2.L0, C1, 1)) / (10*cp));
          maks1 = abs(A - l0);
          l0_new = abs(l0 + (maks1)*(rand(1) - rand(1)));
          c1 = (subs(S2.L0, C1, 1)) / l0_new; %Test if C1 > 10Cp
          c0 = subs(S2.C0, [Cp, C1], [cp, c1]);
          l0 = l0_new;
          l1 = subs(S2.L1, C1, c1);

          [Fhigh, Fave, ctot, Ftot] = findFhigh(f, fmax, c0, c1, cp, l0, l1, w3,
Fhigh, ctot, Ftot, Fave);
          [error] = errorfunction(fmax, c0, c1, cp, l0, l1, w1, w3, x1);
      end

      if (error(1) > e1) || (error(2) > e2) || (error(3) > e3) || (abs(Fhigh - w4) >
acc)
      %[c0, c1, cp, l0, l1] = compiterateCp(w1, w2, w3, w4_or, x1);
      %compiterateCp same as compvalues, just Cp randomized!

          cp_original = 1 / (2 * pi * 40e9 * abs(x1));
          cp = abs(cp_original + (cp_original)*(rand(1) - rand(1)));
          c0 = subs(S1.C0, Cp, cp);
          c1 = subs(S1.C1, Cp, cp);
          l0 = subs(S1.L0, Cp, cp);
          l1 = subs(S1.L1, Cp, cp);

      [Fhigh, Fave, ctot, Ftot] = findFhigh(f, fmax, c0, c1, cp, l0, l1, w3, Fhigh,
ctot, Ftot, Fave);
      [error] = errorfunction(fmax, c0, c1, cp, l0, l1, w1, w3, x1);
      end

      if (error(1) > e1) || (error(2) > e2) || (error(3) > e3) || (abs(Fhigh - w4) >
acc)
      %[c0, c1, cp, l0, l1] = compiterateL1(l1, w1, w2, w3, x1);
      %same as iterated L0 - only changed to L1 - use S2!!

          cp = 1 / (2 * pi * 40e9 * abs(x1));
          B = ((subs(S2.L1, C1, 1)) / (10*cp));
          maks2 = abs(B - l1);
          l1_new = abs(l1 + (maks2)*(rand(1) - rand(1)));
          c1 = (subs(S2.L1, C1, 1)) / l1_new;
          c0 = subs(S2.C0, [Cp, C1], [cp, c1]);
          l1 = l1_new;
          l0 = subs(S2.L0, C1, c1);

          [Fhigh, Fave, ctot, Ftot] = findFhigh(f, fmax, c0, c1, cp, l0, l1, w3,
Fhigh, ctot, Ftot, Fave);
          [error] = errorfunction(fmax, c0, c1, cp, l0, l1, w1, w3, x1);
      end
%%
      X = X + 1; %increase amount of iterations by one

      if X == x %if iterations more than user specified amount, break function
          break
      end

  end

 %FUNCTION TO DETERMINE COMPONENT VALUES FROM USER SPECIFIED INPUTS%

function [S1] = compvalues(w1, w2, w3, w4_or)

%This function computes the values of the components with the given input
%variables for the graph mins and max
```

```
syms C0 C1 Cp L0 L1

f1 = 1 / (w1 * 2 * pi)^2;
f2 = 1 / (w2 * 2 * pi)^2;
f3 = 1 / (w3 * 2 * pi)^2;
f4 = 1 / (w4_or * 2 * pi)^2;


F1 = (L0 + L1)*(C0 + Cp) - f1;
F2 = L0*(C0 + Cp) - f2;
F3 = L1*C1 - f3;
F4 = L0*Cp - f4;

S1 = solve(F1, F2, F3, F4);

%FUNCTION DETERMINES IF ANY VALUES HIGHER THAN USER SPECIFIED FREQUENCY AND
%SETS THIS AS LOCAL MAXIMUM
function [Fhigh, Fave, ctot, Ftot] = findFhigh(f, fmax, c0, c1, cp, l0, l1, w3,
Fhigh, ctot, Ftot, Fave)

     z =  find(diff(sign(diffzero(f, c0, c1, cp, l0, l1, 74.86))));
     c =  numel(find(diff(sign(diffzero(f, c0, c1, cp, l0, l1, 74.86)))));

for j = 1:c
    if f(z(j)) > w3 && transferTestsign(fmax, c0, c1, cp, l0, l1, w3) < 0
            Fhigh = f(z(j));
            [Fave, ctot, Ftot] = averageF(ctot, Ftot, Fhigh);
            break
        else
        Fhigh = w3;
    end
end

%DETERMINES THE SIGN OF THE TRANSFER FUNCTION SLOPE
function [w3_val] = transferTestsign(fmax, c0, c1, cp, l0, l1, w3)

F = 40e9:1e6:fmax; %sets frequency between 40 GHz and user specified maximum
w3_num = (w3 - 40e9) / 1e6;

%%This paragraph determines the mathematical transfer function based on the
%%Foster canonical form equivalent circuit
xC0 = 1 ./ (2*pi*F*c0);
tC0 = xC0*-1i;

xCp = 1 ./ (2*pi*F*cp);
tCp = xCp*-1i;

xC1 = 1 ./ (2*pi*F*c1);
tC1 = xC1*-1i;

xL0 = 2*pi*F*l0;
tL0 = xL0*1i;

xL1 = 2*pi*F*l1;
tL1 = xL1*1i;

R = 74.86 + 0i;

aA = (tC1.^-1 + tL1.^-1 + R.^-1).^-1;
B = aA + tL0;
C = (B.^-1 + tCp.^-1).^-1;
D = C + tC0;
%%
%Determines the value of the imaginary impedance at the specified frequency
w3_val = imag(D(w3_num));
```

```
%FUNCTION TO DETERMINE THE AVERGAGE FREQUENCY USED IN DETERMINING THE
%HIGHEST IMPEDANCE VALUE (LOCAL MAXIMUM)
function [Fave, ctot, Ftot] = averageF(ctot, Ftot, Fhigh)

Ftot = Ftot + Fhigh;
ctot = ctot + 1;
Fave = Ftot / ctot;


%ERROR FUNCTION TO DETERMINE THE ERROR BASED ON USER SPECIFIED VALUES AND
%COMPUTED RESULTS
function [error] = errorfunction(fmax, c0, c1, cp, l0, l1, w1, w3, x1)

    Test(1) = 1e9; %to avoid Test not being created
    F = 40e9:1e6:fmax;
    Z11  = transferfunc(fmax,  c0,  c1,  cp,  l0,  l1);%seperately  determine  transfer
function
    dZz = diff(Z11);% determine slope of transfer function
    dZz(numel(F)) = dZz(numel(F)-1);%determine difference is consequetive slopes
    j = 1;

        for k = 2:numel(F)
            if  sign(imag(dZz(k)))  ~=  sign(imag(dZz(k-1)))%test  if  sign  changed  in
slope
            Test(j) = F(k);
            j = j + 1;
            end
        end
            %If it was determined that there were sign changes in the
            %consequetive points slope, compute the errors and output to
            %main function
            if numel(Test) > 1
            error(1) = abs(w1 - Test(1));
            error(2) = abs(w3 - Test(2));
            error(3) = abs(x1 - imag(Z11(1)));
            end

            if numel(Test) == 1
            error(1) = 5e9;
            error(2) = 5e9;
            error(3) = 200;
            end

function [zero] = imaginaryzero(F, C0, C1, Cp, L0, L1, R)

%This function only computes the transfer function with the
%supplied input variables

zC0 = (1 / (1i*2*pi*F*C0));
zC1 = (1 / (1i*2*pi*F*C1));
zCp = (1 / (1i*2*pi*F*Cp));
zL0 = 1i*2*pi*F*L0;
zL1 = 1i*2*pi*F*L1;

zT = (((zC1^-1 + zL1^-1 + R^-1)^-1 + zL0)^-1 + zCp^-1)^-1 + zC0;

zero = imag(zT);

%THIS FUNCTION OUTPUTS THE DETERMINED VALUES IF A RESULT WAS ACHIEVED THAT
%IS WITHIN THE USER DEFINED BOUNDARIES. IF A RESULT IS NOT FOUND IT IS
%SUGGESTED THAT THE USER DEFINES LESS STRINGENT BOUNDARIES AS A FIRST-ORDER
%APPROXIMATED EQUIVALENT CIRCUIT

function [O] = outputfunc(fmax, c0, c1, cp, l0, l1, G)

fprintf('The calculated value for C0 is %d\n', c0);
```

```
fprintf('The calculated value for C1 is %d\n', c1);
fprintf('The calculated value for Cp is %d\n', cp);
fprintf('The calculated value for L0 is %d\n', l0);
fprintf('The calculated value for L1 is %d\n', l1);

F = 40e9:1e6:fmax;
Z11 = transferfunc(fmax, c0, c1, cp, l0, l1);
S11 = (74.86 - Z11) ./ (74.86 + Z11);

if G == 1
    O = plot(F, imag(Z11));
    xlabel('Frequency [GHz]');
    ylabel('Imaginary impedance [Ohm]');
    title('Imaginary impedance VS frequency of dipole');
    grid on;
end

if G == 2
    O = plot(F, abs(S11));
    xlabel('Frequency [GHz]');
    ylabel('S11 [ ]');
    title('S11 scattering parameter VS frequency of dipole');
    grid on;
end

if G == 3
    fprintf('Exiting...\n');
    O = fprintf('Thank you\n');
end
```

The obtained component values, estimated parasitic capacitances, and simulated results for the acquired component values are presented below.

Table A.1: MATLAB computed values for initial electrical circuit.

Component	Required value	Estimated parasitic capacitance
L_0	53 pH	13.96 fF
L_1	60 pH	12.88 fF
C_0	50 fF	0.98 fF
C_1	88 fF	1.78 fF

From Table A.1 the inductance and capacitance values are small and approaching the limits of the technology node. The parasitic capacitances were already included in the component models and simulations and circuit matching included these effects. L_0 and L_1 had similar dimensions of 12 µm × 100 µm and are spaced 80 µm apart to reduce mutual coupling. Capacitor C_0 is connected between L_0 and L_1 and has square dimensions of 4 µm × 4 µm to comply with geometric recommendation of the 130 nm node. Capacitor C_1 has dimensions of 9.52 µm × 9 µm and is connected in parallel with the output load and ground plane. The complex impedance results of the transfer function as determined by the MATLAB script and the analytical approach is depicted in Figure A.1.

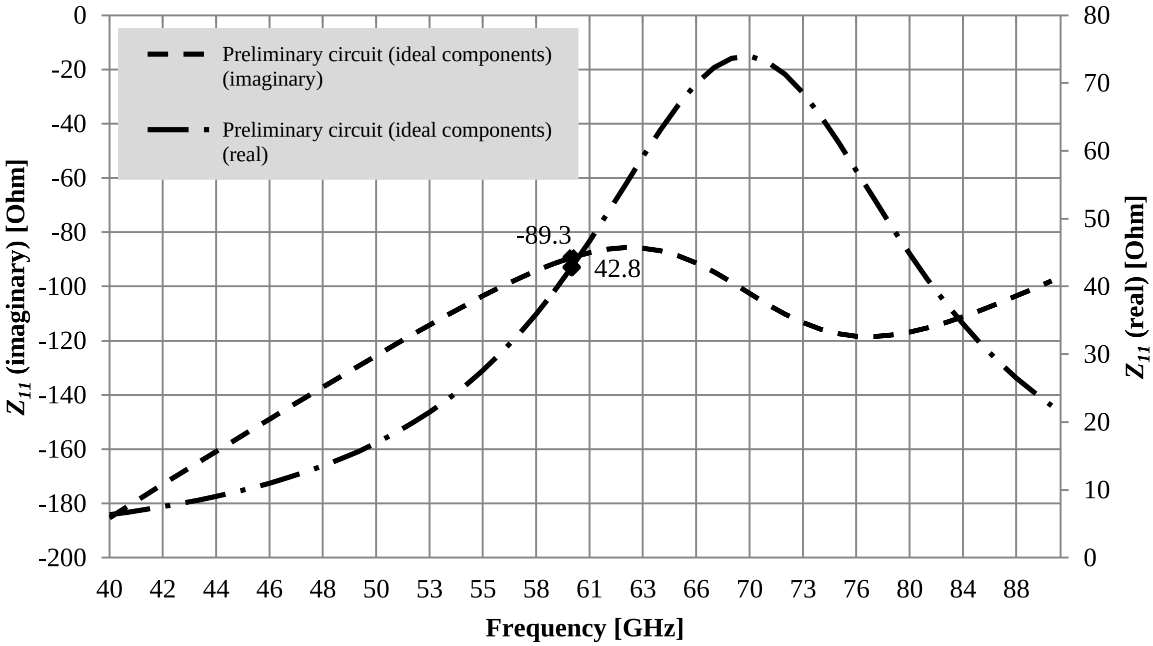

Figure A.1: Initial electrical circuit Z_{11} real and imaginary impedance.

From Figure A.1 it was noted that as an initial electrical circuit representation of the dipole antenna, the results were comparable with results obtained in Figure 4.4, where the middle of the local minimum and maximum (therefore the point of parallel resonance) was at a frequency of 70.6 GHz in both instances. The local maximum and minimum values were at 63.4 GHz and at 78.5 GHz (compared to 59 GHz and 83.2 GHz) and the circuit was evaluated based on this result. The frequency at which the local minimum and maximum of the complex impedance occurs is dependent on the ratio between inductive and capacitive components in the *Foster canonical form* initial circuit. Limitations on component values based on the chosen technology node confined the ability to represent these local minima and maxima accurately in terms of it frequencies, therefore highlighting the need for an improved circuit. The real impedance of the circuitis 42.8 Ω at 60 GHz (compared to 70.21 Ω in Figure 4.4); however, the local maximum of the slope is at 70.6 GHz in both instances (also evident from the peak real impedance at 70.6 GHz).

From the above results, it is confirmed that the initial electronic circuit can potentially represent the transfer function of the dipole antenna simulated in Figure 4.4, and that component value limitations such as the minimum obtainable inductance or capacitance (influencing the attainable inductance / capacitance ratio) based on the 130 nm process restricted the ability to obtain accurate impedance values of the electrical circuit.

The final result of the improved circuit compared to the initial *Foster canonical form* electrical circuit is given below. The component values and its respective parasitic capacitances (refer to section 2.6.1 and 2.6.2) of the improved circuit are given in Table A.2.

Table A.2: MATLAB computed values for improved electrical circuit.

Component	Required value	Estimated parasitic capacitance
L_0	240 pH	27.72 fF
L_S	120 pH	10.89 fF
L_{SUB}	160 pH	16.25 fF
C_0	18 fF	0.66 fF
C_S	104 fF	1.98 fF
C_{SUB}	18 fF	0.66 fF
C_P	18 fF	0.66 fF
C_{P1}	450 fF	5.35 fF
L_P	72 pH	17.03 fF

The component values presented in Table A.2 show some values (C_0, C_{SUB}, C_P, and L_P) approaching component value limitations (as a function of geometric limitations) of the technology node, however, the added degrees of freedom through the additional components (with capacitive values ranging from 104 fF to 450 fF and inductive values up to 240 pH) increased the range of component values and provided for greater flexibility. The four transmission lines, L_0, L_{SUB}, L_S and L_P had dimensions 4 µm × 260 µm, 4 µm × 100 µm, 4 µm × 151 µm, and 20 µm × 100 µm respectively. The minimum obtainable distance between all transmission lines with total area limitation is 40 µm to minimize mutual coupling between the inductive components. Capacitors C_0, C_{SUB}, $C_{S,}$ C_P, and C_{P1} have dimensions 4 µm × 4 µm, 4 µm × 4 µm, 10.14 µm × 10 µm, 4.24 µm × 4 µm, and 17.78 µm × 25 µm respectively. The parasitic capacitance values for the components were included in all simulations (through using supplied library components), and were accounted for in the output matching network. The complex real and imaginary impedance of the improved (ideal) electrical circuit used to represent the transfer function obtained by EM simulations of the dipole antenna (refer to Figure 4.8) with a substrate, matched to 75 Ω is given in Figure A.2.

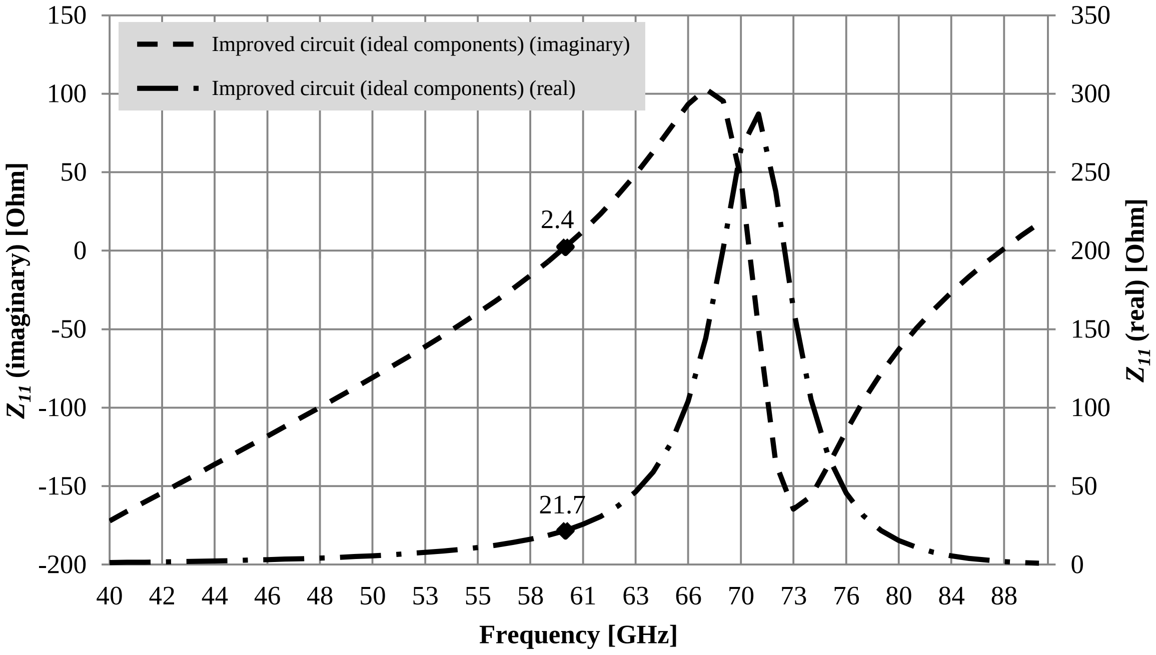

Figure A.2: Improved electrical circuit Z_{11} real and imaginary impedance.

Comparing the results obtained in Figure 4.8 and A.2 it was evident that a very strong relationship between the EM simulations and the equivalent, improved, electrical circuit now existed (refer to Figure 4.22 and Figure 4.23 for convenient comparative results). The local maximum (+j95.2 Ω) and minimum (-j164.6 Ω) of the electrical circuit for the imaginary impedance was situated at 68.4 GHz and 72.7 GHz respectively, compared to 67.4 GHz (+j302 Ω) and 74.6 GHz (-j444 Ω) for the EM dipole antenna (Figure 4.8). The frequency at which the slope becomes less negative ($X_C = |X_L|$) is situated at 72.7 GHz for both instances. The real impedance of the improved electrical circuit also showed similar performance compared to the EM dipole results, although the real value at 60 GHz was lower (21.7 Ω) compared to the dipole impedance of 45.04 Ω, the peak value of the real impedance was obtained at 72.7 GHz in both instances (as it was expected since the mid-point between the local maximum and minimum of the imaginary impedance ($X_C = |X_L|$) represents this point.

The MATLAB functions that were used to determine the total attenuation as a function of free-space loss, nLOS obstructions, oxygen absorption, reflection, and diffraction are given below. Detailed descriptions of each term are given in sections 2.1.1 to 2.1.5. Comments next to coded lines briefly describe the functionality of the lines / functions.

```
clear all;
clc;
%%
%THIS PART ACCEPTS USER ENTRIES REGARDING THE DISTANCE BETWEEN THE RECEIVER
%AND TRANSMITTER, THE FREE-SPACE ATTENUATION CONSTANT n, AND THE TYPE OF
%OBSTRUCTING MATERIAL BETWEEN THE TRANSMITTER AND RECEIVER
%THE SCRIPT IS NOT OPTIMIZED FOR ANY GIVEN SITUATION AND IS BASED ON THE
%DEDICATED SCENARIOS DESCRIBED IN SECTION 4.4

%Free space loss at reference distance(s) only:
d = (str2double(input('Please enter the distance between Rx and Tx: ','s')));
n = (str2double(input('Please enter the value of n (usually 2 in free space):
','s')));
f = 1e9 * (str2double(input('Please enter the operation frequency (GHz): ','s')));
fprintf('Please choose the obstructing material: \n');
fprintf('Type 1 for paper: \n');
fprintf('Type 2 for normal glass: \n');
fprintf('Type 3 for alumina: \n');
m = (str2double(input('Please enter your choice: ','s')));
v = (str2double(input('Please enter the Fresnel diffraction parameter: ','s')));
clc;
fprintf('The file has been written as TOTAL in downloads \n');
fprintf('Please run the rain-rate simulation and copy into same Excel file and add
\n');
if m == 1
    NLOS = -1;
    reflection = -13;
end
if m == 2
    NLOS = -3.5;
    reflection = -10;
end
if m == 3
    NLOS = -12;
    reflection = -7;
end

if v == -1
    diffraction = -3;
end
if v == 0
    diffraction = -10;
end
if v == 1
    diffraction = -17.5;
end

c = 3e8;
d0 = 1:1:d;

oxygen = -0.01 * d0;

LS = 20*log10(4*pi*d*f/c);
LSt = -1*(LS - 10*n*log10(d ./ d0));
%plot(d0, LSt);

TOTAL = LSt + NLOS + oxygen + reflection + diffraction;
plot(d0, TOTAL);
```

```
dlmwrite('C:\Users\WynandDV6\Downloads\SignalAttenuation.txt', LSt, '-append',
'newline', 'pc', 'delimiter', ' ');

dlmwrite('C:\Users\WynandDV6\Downloads\TOTAL.txt', TOTAL, '-append', 'newline',
'pc', 'delimiter', ' ');

title('Signal losses as a function of distance');
xlabel('Reference distance [m]');
ylabel('Signal attenuation [dB]');
grid on;

%%
```

The MATLAB functions that were used to determine the attenuation as a function of rain-rate (refer to section 2.1.6) are given below. This function is created separately from the functions above and added externally (in Microsoft Excel) to the above results to obtain the final attenuation results as displayed in Figure 4.28. Comments next to coded lines briefly describe the functionality of the lines / functions.

```
clear all;
clc;
Ga = 4.09e-2;
Ea = 0.699;
f = 60;
a = Ga.*(f.^Ea);%DETERMINE COEFFICIENT a
%plot(f, a);
Gb = 2.63;
Eb = -0.272;
b = Gb.*(f.^Eb);%DETERMINE COEFFICIENT b
%plot(f, b);
R = 150; %RAIN-RATE CHANGED IN THIS LINE DEPENDING ON SCENRAIO
K0 = a.*(R.^b);
d0 = 1:1:30;%SPECIFIED DISTANCE BETWEEN TRANSMITTER AND RECEIVER CAN BE CHANGED
Kd0 = -1*(K0 * (d0)) / 1000; %CONVERSION FROM KM TO M (/1000)

dlmwrite('C:\Users\WynandDV6\Downloads\RainRatedeltaD.txt', Kd0, '-append',
'newline', 'pc', 'delimiter', ' '); %WRITE TO SEPARATE TEXT FILE TO COMBINE IN EXCEL

plot(d0, Kd0); %PLOT IN MATLAB FOR VISUAL RESULTS
```

The method for determining the transfer function $H(j\omega)$ given in (2.22) in section 2.4 (Chapter 2) is expanded in this section.

The transfer function $h(t)$, in the time domain, can be transformed to the frequency domain by the single-sided *Laplace* transform

$$h(t) = \mathcal{L}\{h(t)\} = \int_0^\infty e^{-st}\, h(t)dt \tag{A.1}$$

where s is a complex number, $s = \sigma + j\omega$. By applying the *Laplace* transform solutions for electric circuits, **Error! Reference source not found.** can be redrawn as in Figure A.1.

Figure A.1. Laplace transformation of electrical antenna at first resonance.

Using Kirchhoff's voltage law around the circuit loop, collecting terms and rewriting the circuit equation, the system frequency response $H(s)$, is derived as

$$H(s) = \frac{V_{out(s)}}{V_{in(s)}} \tag{A.2}$$

and can be rewritten to include all the impedance terms of the circuit in Figure A.1 as

$$H(s) = sL_0 + \frac{1}{sC_0} + \left(sL_1 \parallel \frac{1}{sC_1} \parallel G_1\right) \tag{A.3}$$

Multiplying by the common denominator and collecting terms, it follows that the transfer function can be expressed as

$$H(s) = \frac{s^2C_0L_1G_1+s^2C_1L_1G_1+G_1+sL_1+sL_0\{sC_0(s^2C_0L_1G_1+s^2C_1L_1G_1+G_1)\}}{sC_0(s^2C_0L_1G_1+s^2C_1L_1G_1+G_1)} \tag{A.4}$$

which can be simplified to

$$H(s) = \frac{s^4(L_0L_1C_0C_1G_1)+s^3(L_0L_1C_0)+s^2(C_0L_1G_1+C_1L_1G_1+L_0C_0G_1)+sL_1+G_1}{s^3(C_0C_1L_1G_1)+s^2(L_1C_0)+s(C_0G_1)}. \tag{A.5}$$

Substituting the complex number $s = \sigma + j\omega$ where the real component $\sigma = 0$, and grouping the real and imaginary parts of the transfer function, it follows that

$$H(s = j\omega) = \frac{j[\omega(L_1)-\omega^3(L_0L_1C_0)]+[\omega^4(L_0L_1C_0C_1G_1)-\omega^2(C_0L_1G_1+C_1L_1G_1+L_0C_0G_1)]}{j[\omega(C_0G_1)-\omega^3(C_0C_1L_1G_1)]-\omega^2(L_1C_0)}. \tag{A.6}$$

In order to determine the separate equations for the real and imaginary impedance of the derived transfer function, the following theorem is applied. If dividing complex numbers in the form $(a + bj)/(c + dj)$, the real and imaginary part is given by

$$\frac{a+bj}{c+dj} = \left(\frac{ac+bd}{c^2+d^2}\right) + \left(\frac{bc-ad}{c^2+d^2}\right)j. \tag{A.7}$$

Therefore, the imaginary part of the transfer function $H(j\omega)$ is given by

$$H(j\omega)_{Im} = \frac{-\omega C_0G_1(1-\omega^2C_1L_1)\times G_1(\omega^2C_0L_0(\omega^2C_1L_1-1)-\omega^2L_1(C_0+C_1)+1)+\omega^3C_0L_1^2(1-\omega^2C_0L_0)}{(\omega G_1C_0(1-\omega^2C_1L_1))^2+(\omega^2C_0L_1)^2} \tag{A.8}$$

Equation (A.8) is used for circuit analysis in section 2.4.1.

APPENDIX B: DETAILED CIRCUIT LAYOUTS

The circuit layout of each subsystem is included in this appendix. Circuit layouts of the matching network, buffer circuit, *Butterworth* filter, *Chebyshev* filter, and *Bessel* filter are given in Figures B.1 to B.4. The SOLT calibration structures layouts are given in Figure B.5 and Figure B.6. The initial dipole equivalent circuit based on the *Foster canonical form*, and the improved dipole equivalent circuits are presented in Figure B.7 and B.8, with the full circuit layout depicted in Figure B.9.

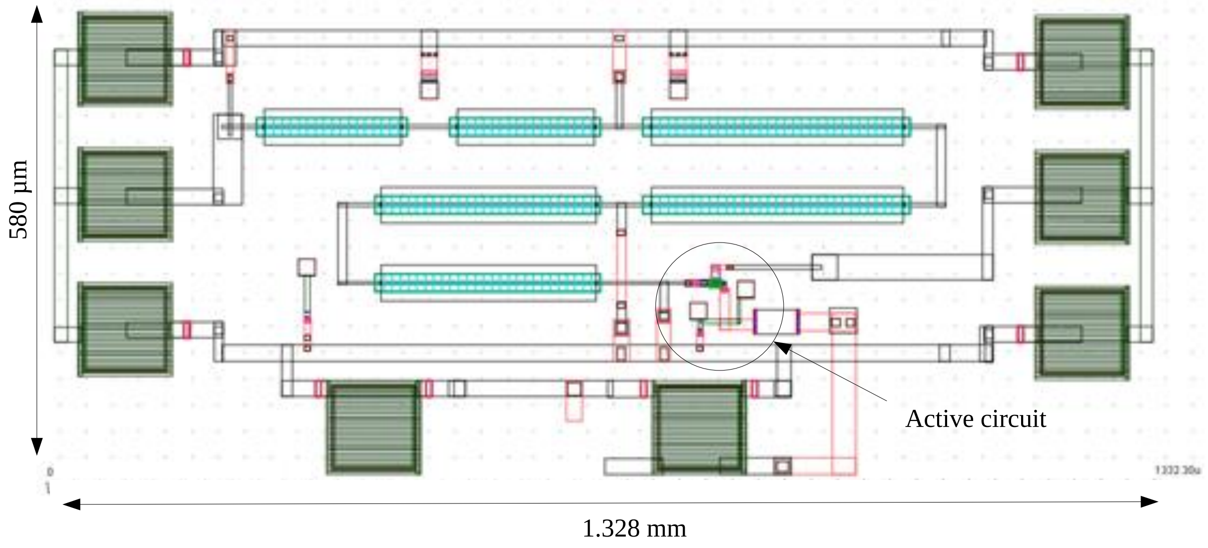

Figure B.1a. The circuit layout of the *Butterworth* LPF with GSG bonding pads for wafer-probing on left and right. Transmission lines are meandered to minimize chip area and active circuitry included to vary attenuation through an external bias.

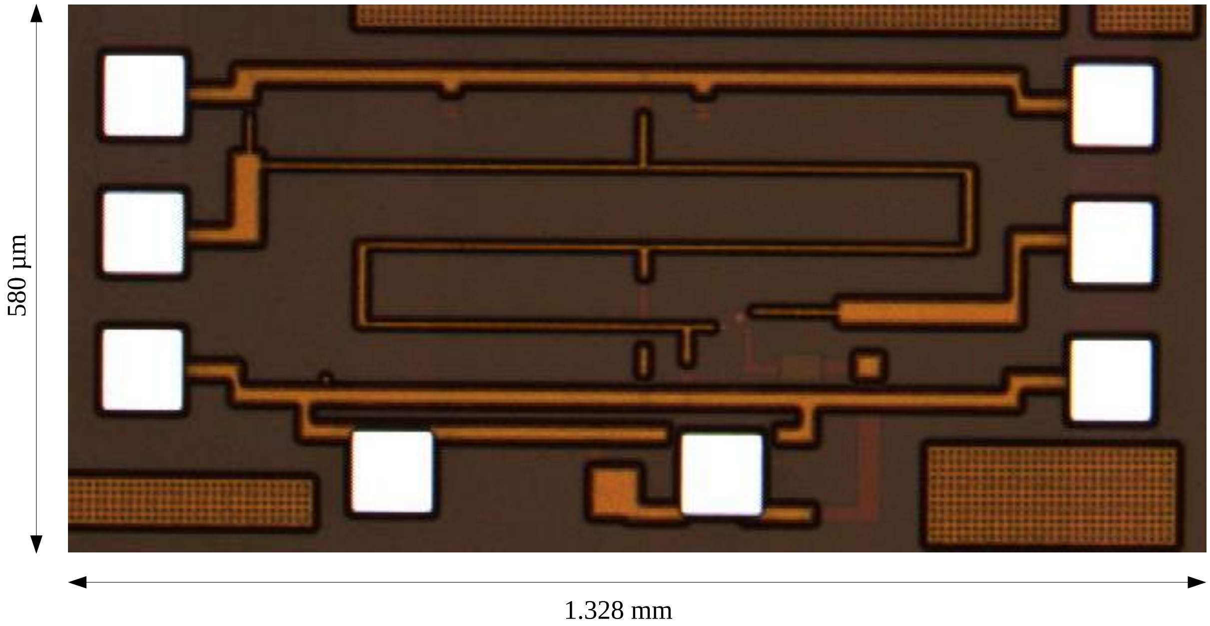

Figure B.1b. The micrograph of the *Butterworth* LPF.

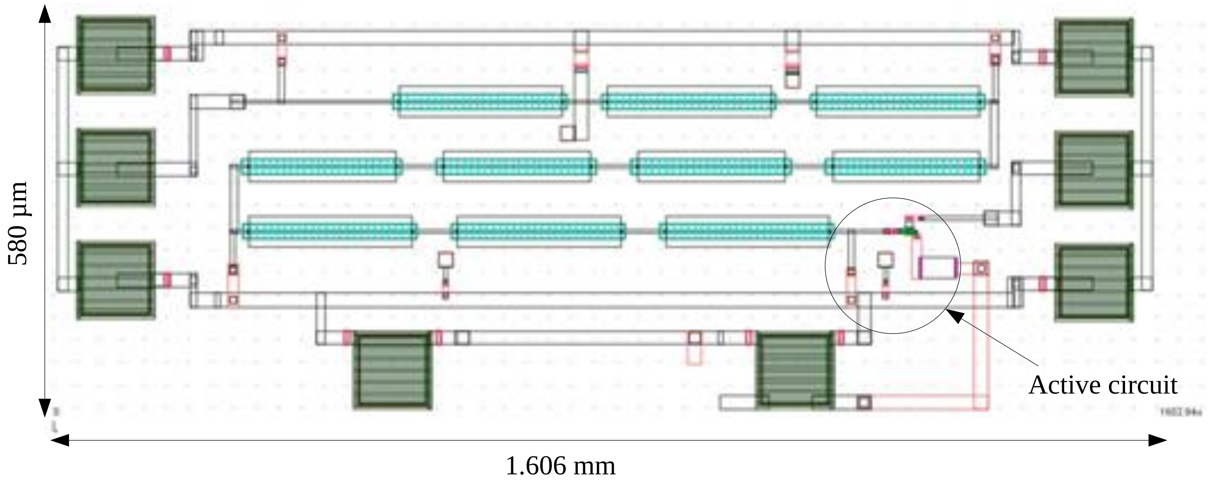

Figure B.2a. The circuit layout of the *Chebyshev* LPF with GSG bonding pads for wafer-probing on left and right. Transmission lines are meandered to minimize chip area and active circuitry included to vary attenuation through an external bias.

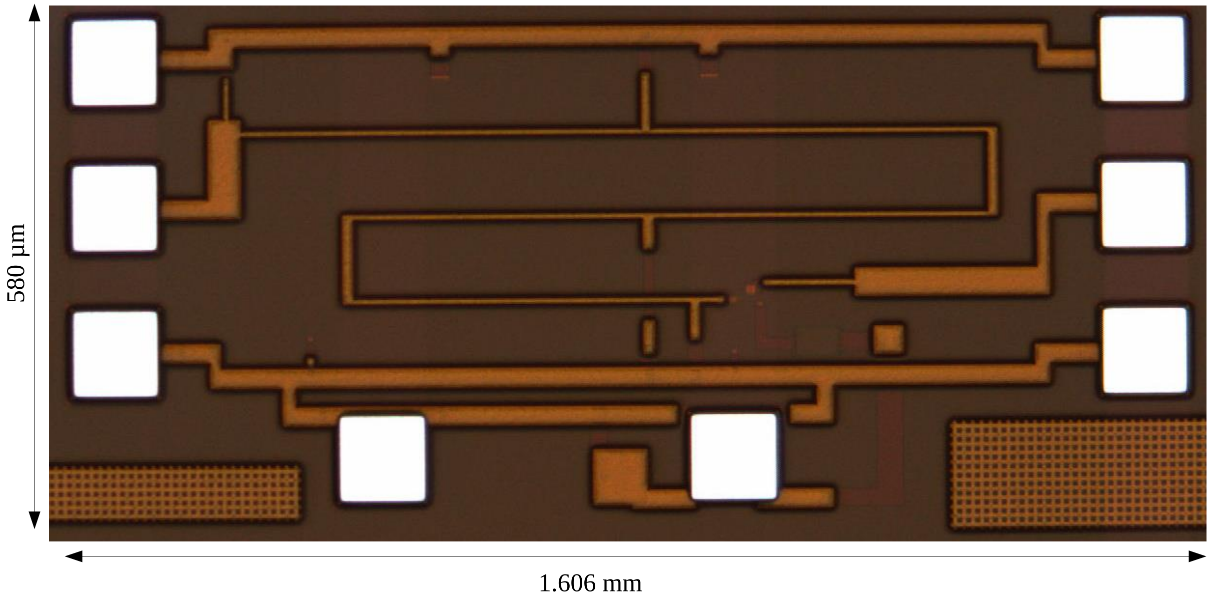

Figure B.2b. The micrograph of the *Chebyshev* LPF.

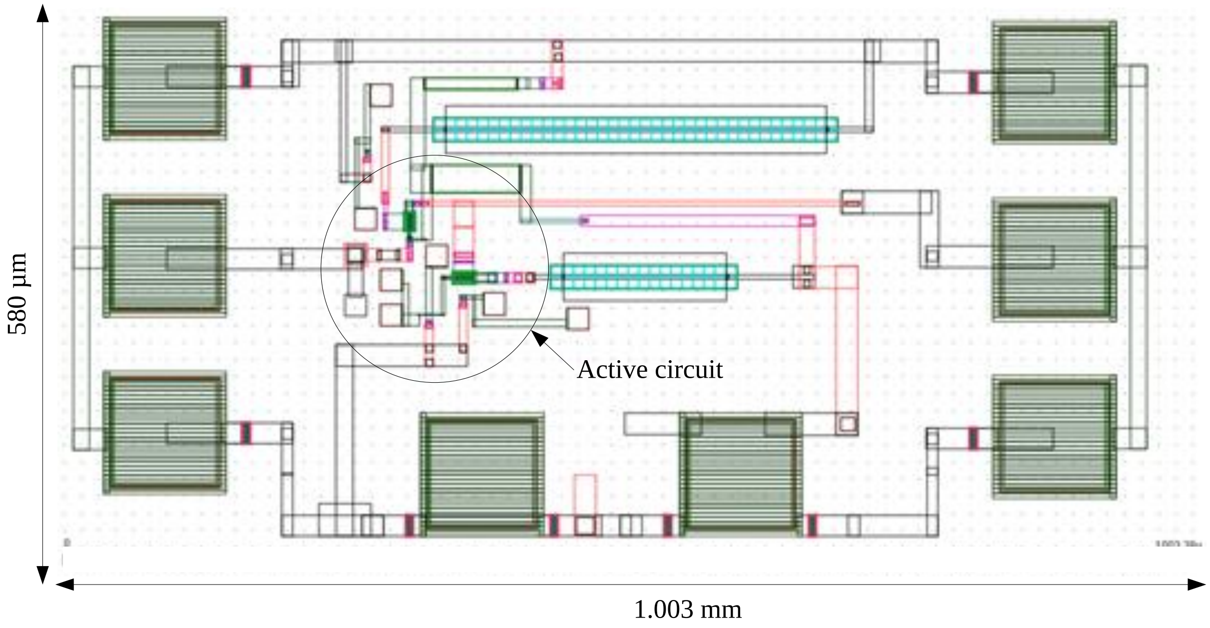

Figure B.3a. The circuit layout of the buffer circuit to avoid overloading and parasitic components influencing measurements when probes are connected to the GSG bonding pads. Active circuitry is depicted and DC supply and ground are connected to the bottom two bonding pads.

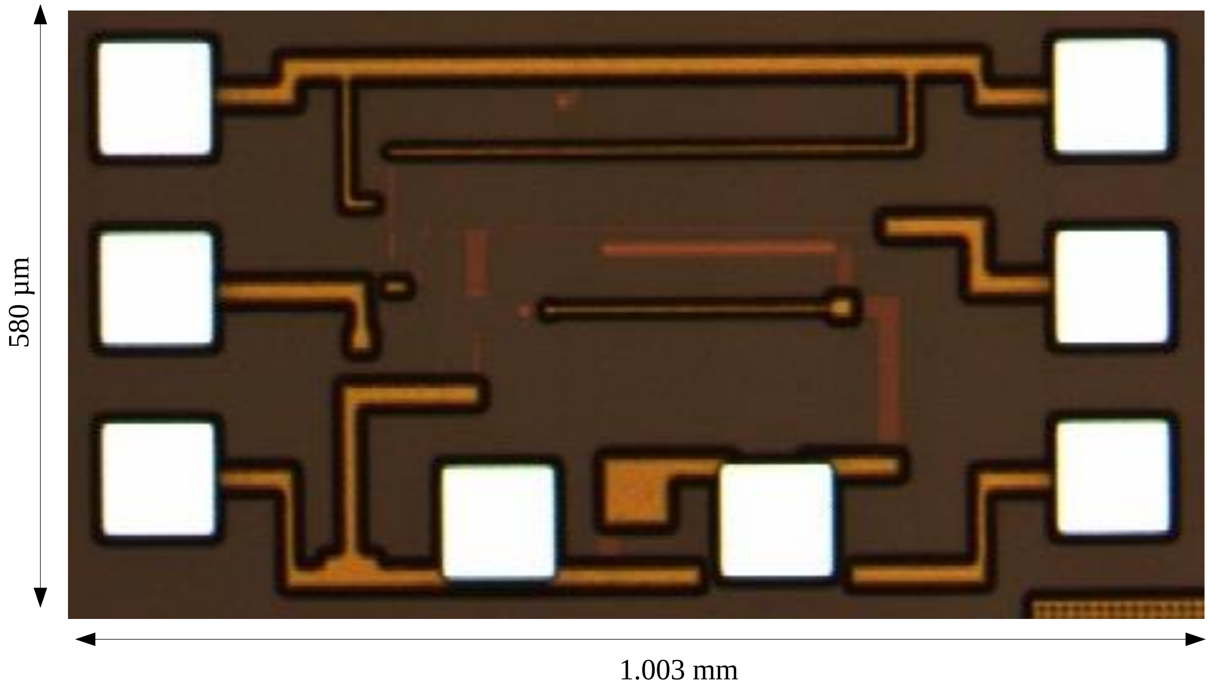

Figure B.3b. The micrograph of the buffer circuit.

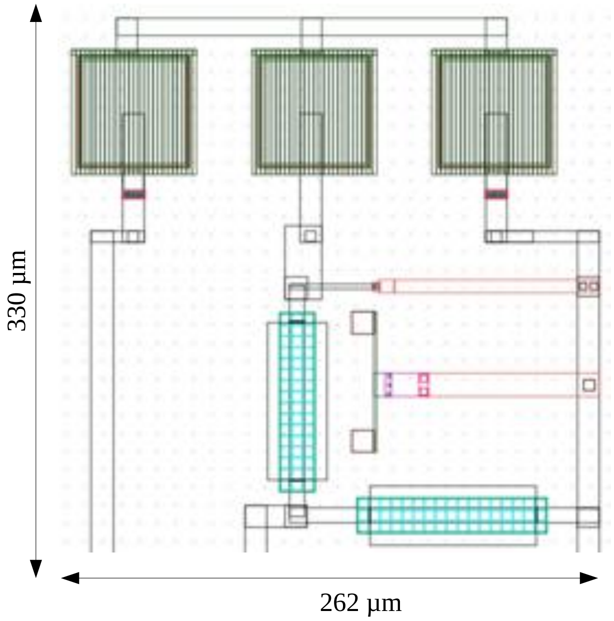

Figure B.4. Layout of the π-network matching circuit to match the output from the buffer to the 50 Ω probe impedances.

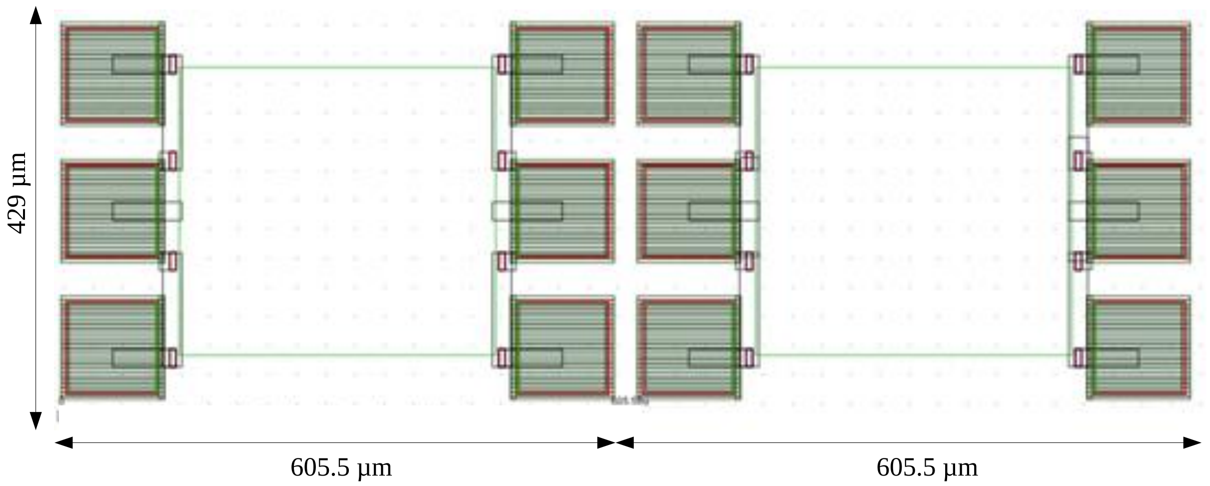

Figure B.5a. Circuit layout of the calibration structures (SOLT) displaying the load (left) and the short (right) topologies.

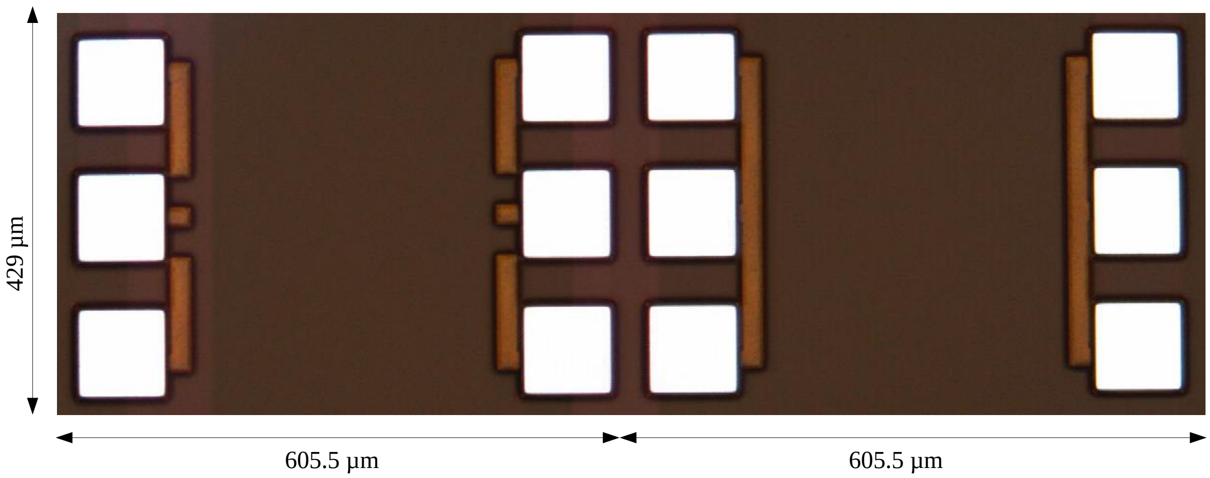

Figure B.5b. Micrograph of the load (left) and the short (right) topologies.

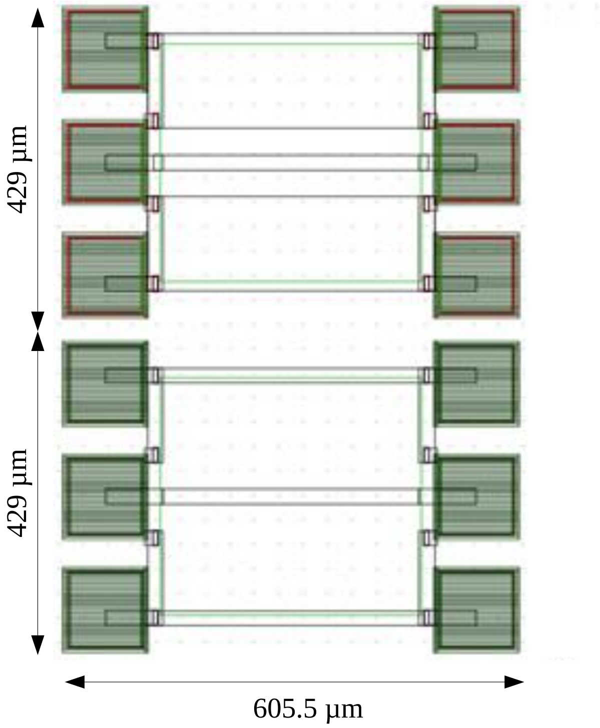

Figure B.6a. Circuit layout of the calibration structures (SOLT) displaying the open (top) and the through (bottom) topologies.

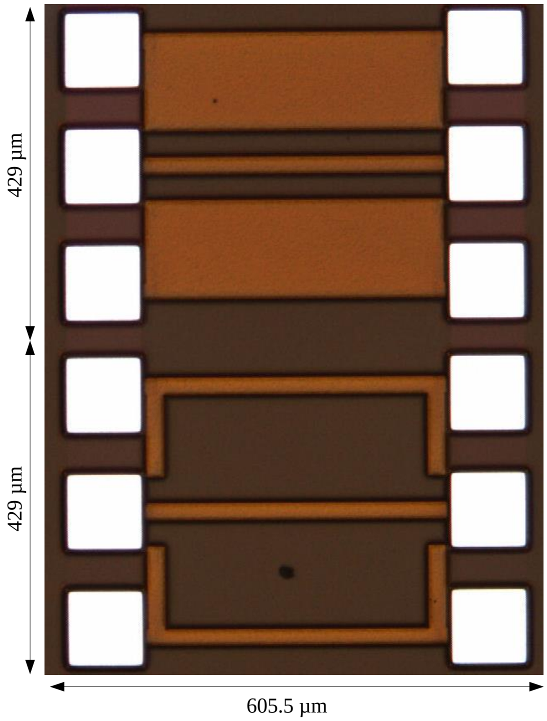

Figure B.6b. Micrograph of the open (top) and the through (bottom) topologies.

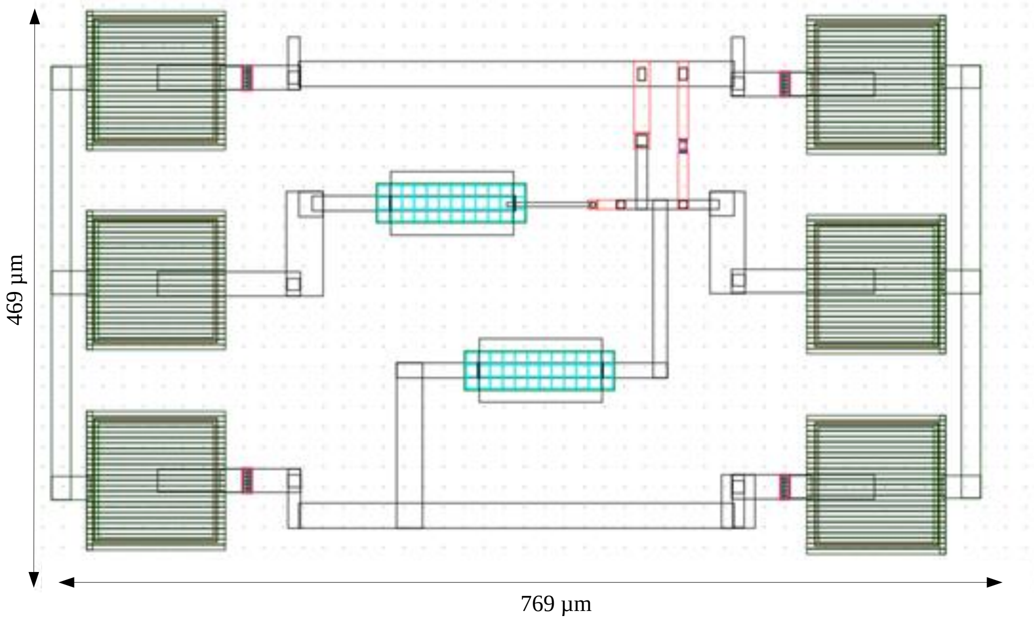

Figure B.7a. Circuit layout of the (initial) dipole equivalent circuit based on the *Foster canonical form*. The circuit contained two transmission lines and two capacitors.

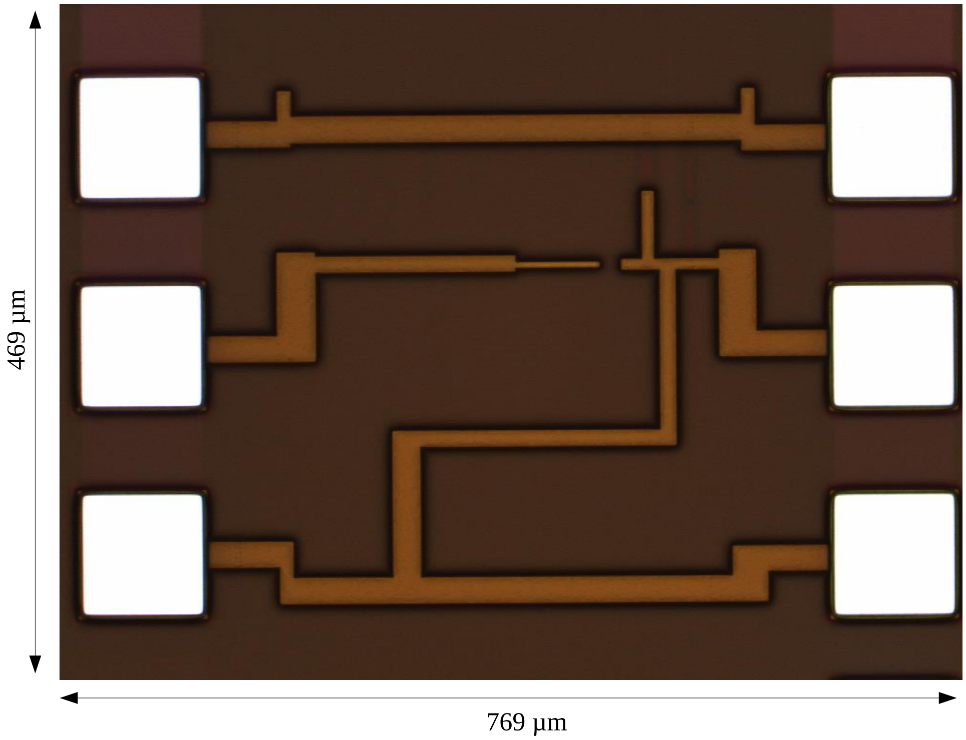

Figure B.7b. Micrograph of the initial dipole equivalent circuit.

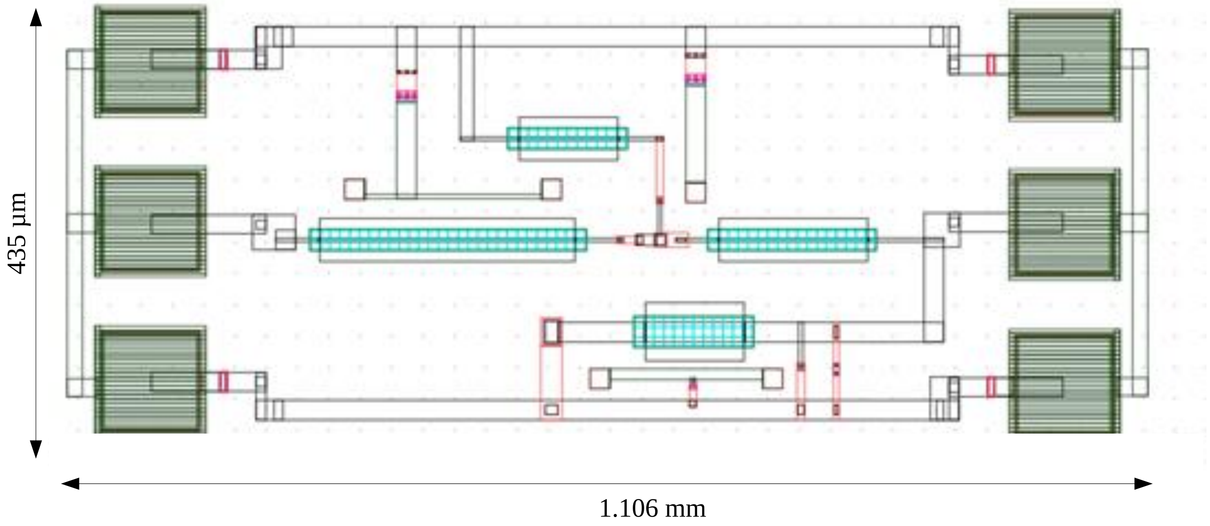

Figure B.8a. Circuit layout of the improved dipole equivalent circuit. The circuit contained four transmission lines and five capacitors.

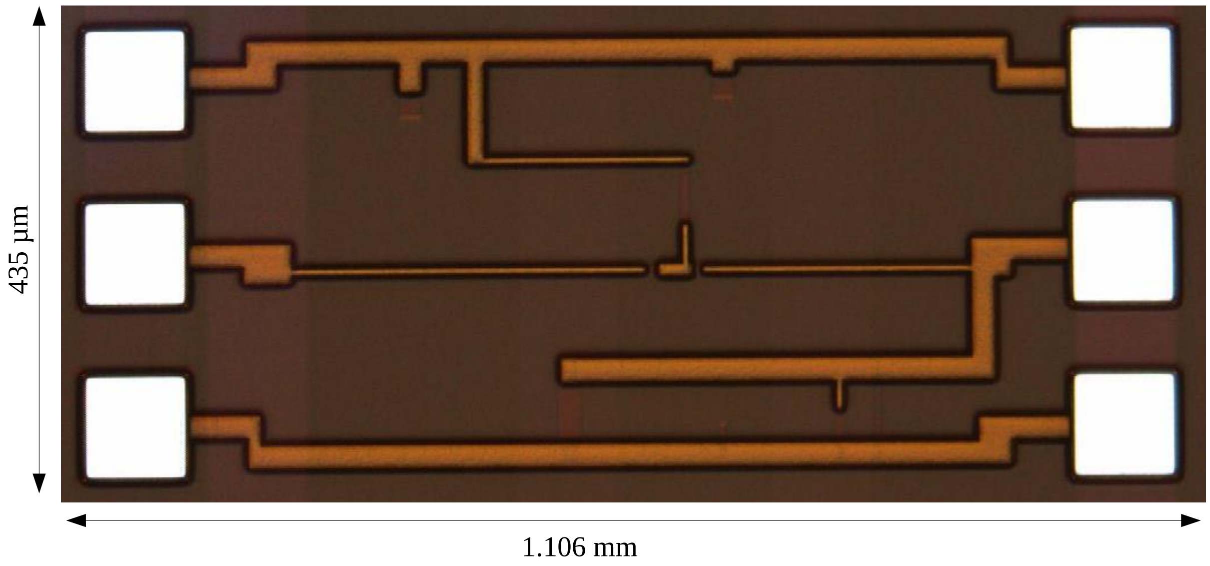

Figure B.8b. Micrograph of the improved dipole equivalent circuit.

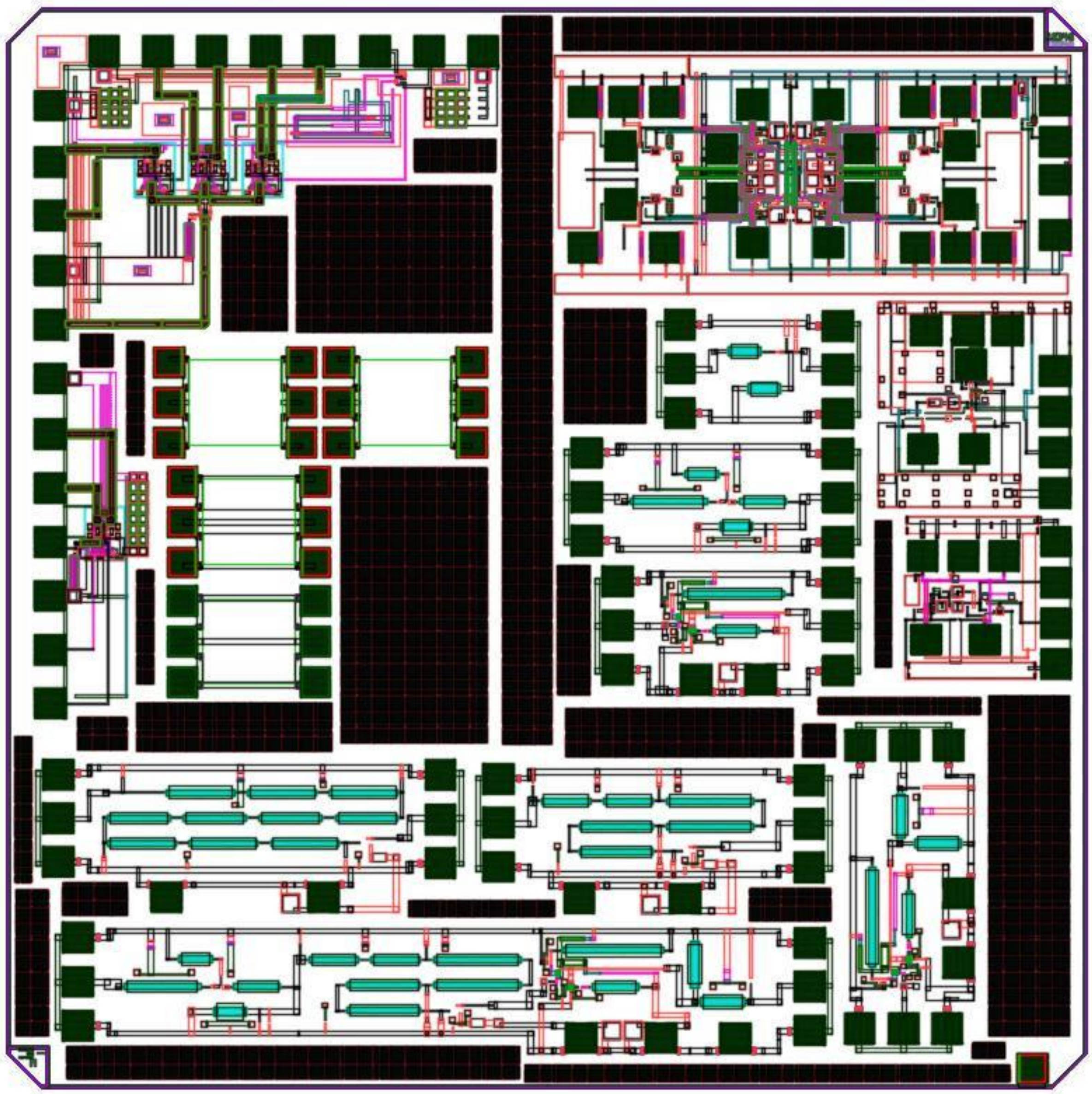

Figure B.9a. Floor planning of the shared MPW run IC (4 mm × 4 mm).

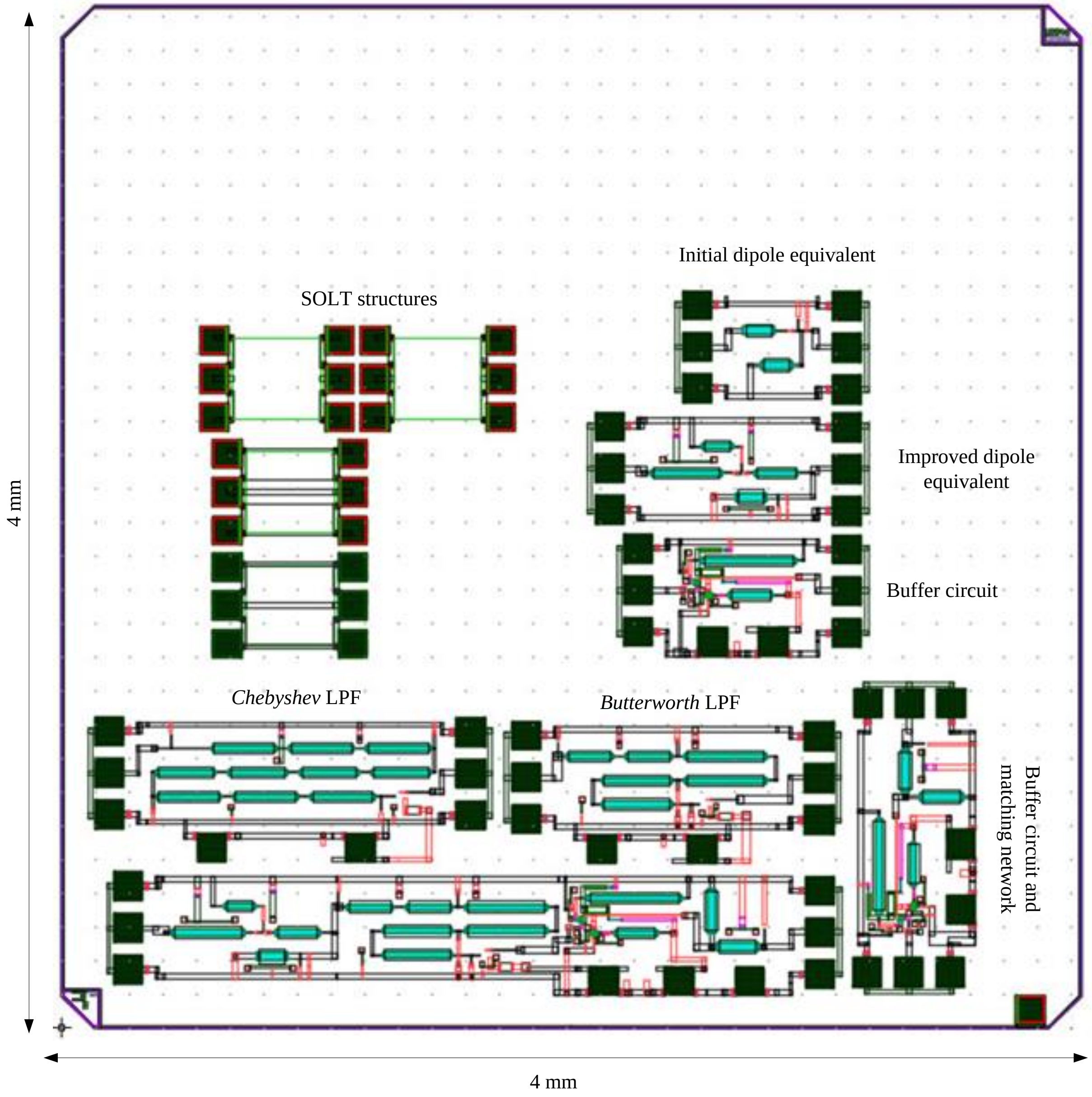

Figure B.9b. Floor planning of the shared MPW run IC (4 mm × 4 mm) where collaborated circuits are omitted.

The placement of the DUT on the substrate and PCB had to be done on three separate substrates. In order to avoid bonding wires from the DUT to the Au tracks obstructing the GSG wafer probes, the placement had to be optimized and subdivided. The floor planning for each substrate is given in Figures B.10 to B.12, accompanied with a photograph of each set-up.

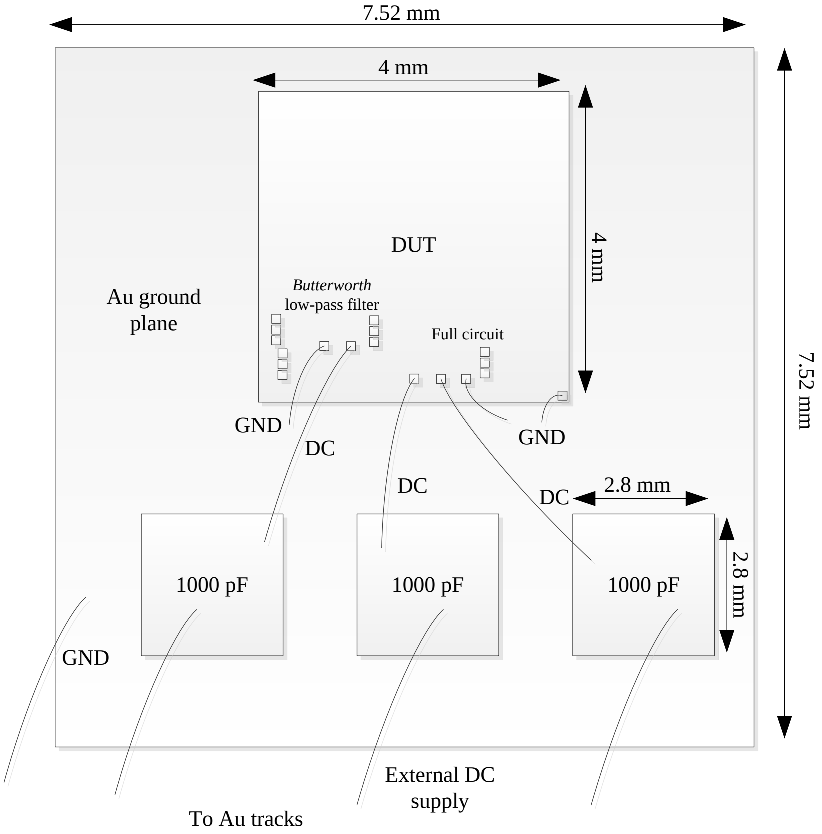

Figure B.10a. Substrate 1 – the DUT placement for measurements of the *Butterworth* LPF and full circuit. Coupling capacitors (3 × 1000 pF) included on each external DC connection.

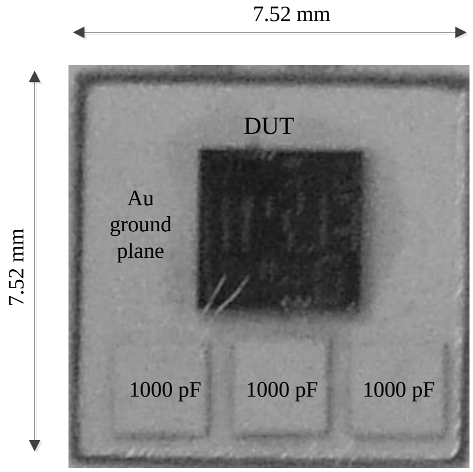

Figure B.10b. Photograph of substrate 1 (refer to Figure B.10a for additional specifications).

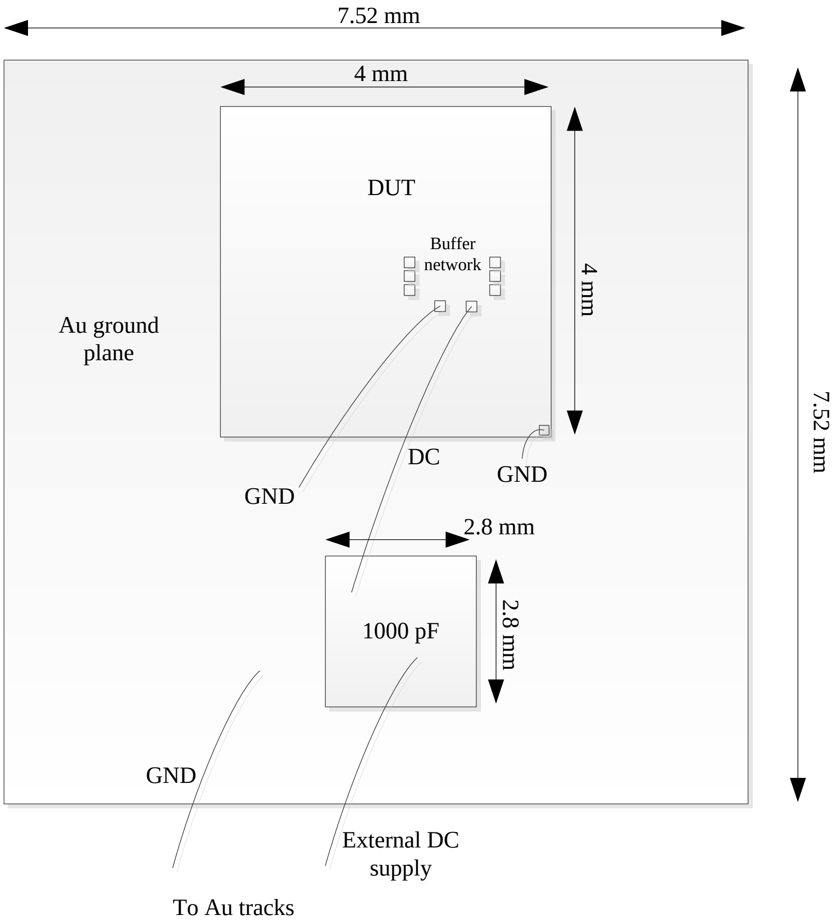

Figure B.11a. Substrate 2 - the DUT placement for measurements of the buffer circuit. Coupling capacitor (1000 pF) included on the external DC connection.

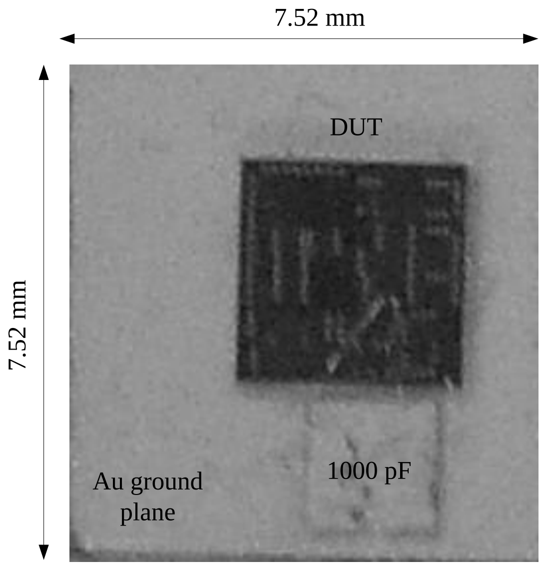

Figure B.11b. Photograph of substrate 2 (refer to Figure B.11a for additional specifications).

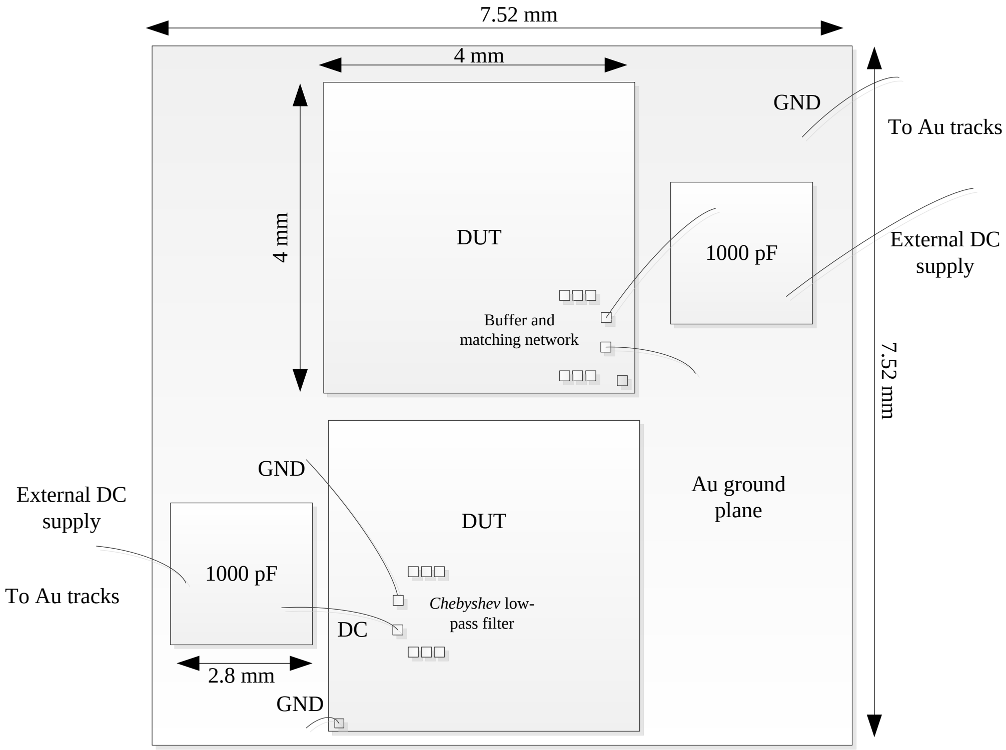

Figure B.12a. Substrate 3 – two DUTs placed on one substrate with considerations for bonding wires and wafer probe. Measurements for the *Chebyshev* LPF and the buffer and matching network (combined) possible. Each DUT DC connection contains a coupling capacitor (1000 pF).

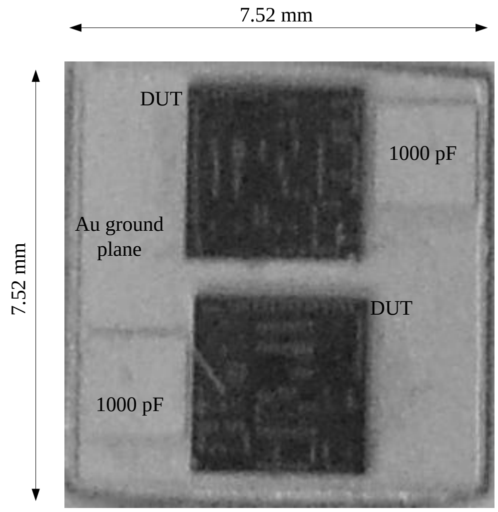

Figure B.12b. Photograph of substrate 3 (refer to Figure B.12a for additional specifications).

APPENDIX C: TEMPERATURE DEPENDENCE

This appendix investigates the changes of transfer characteristics of the initial dipole circuit (*Foster canonical form*) and the improved dipole circuit as a function of temperature. The imaginary impedance (Z_{11}) and insertion loss (S_{11}) are simulated at 0, 27, and 85 °C to investigate the possible change in circuit characteristics. The results are given in Figures C.1 to C.4. Figure C.1 depicts the imaginary input impedance of the initial dipole circuit at the defined temperatures.

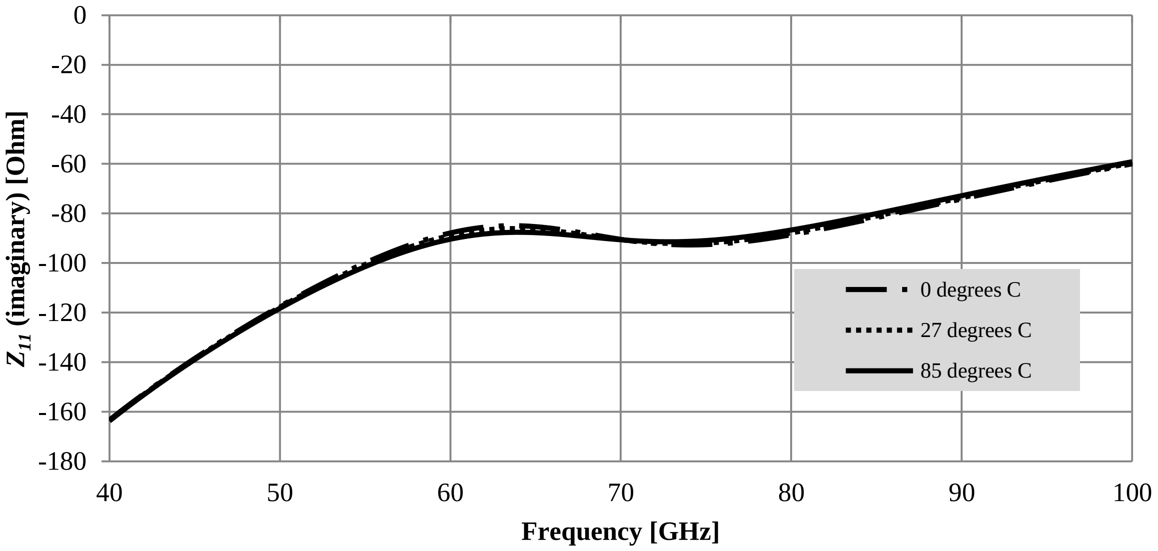

Figure C.1. Input impedance (Z_{11}) of the initial dipole circuit as a function of temperature.

From Figure C.1 it can be seen that the imaginary input impedance of the initial dipole circuit displays a small change in impedance (< 3 Ω) at the local maximum (63 GHz) and minimum (76 GHz). Evident from Figure C.1 is that the imaginary impedance does not shift in frequency, which indicates that there should be no change in resonant frequency, as confirmed by the insertion loss simulation in Figure C.2 for the initial dipole.

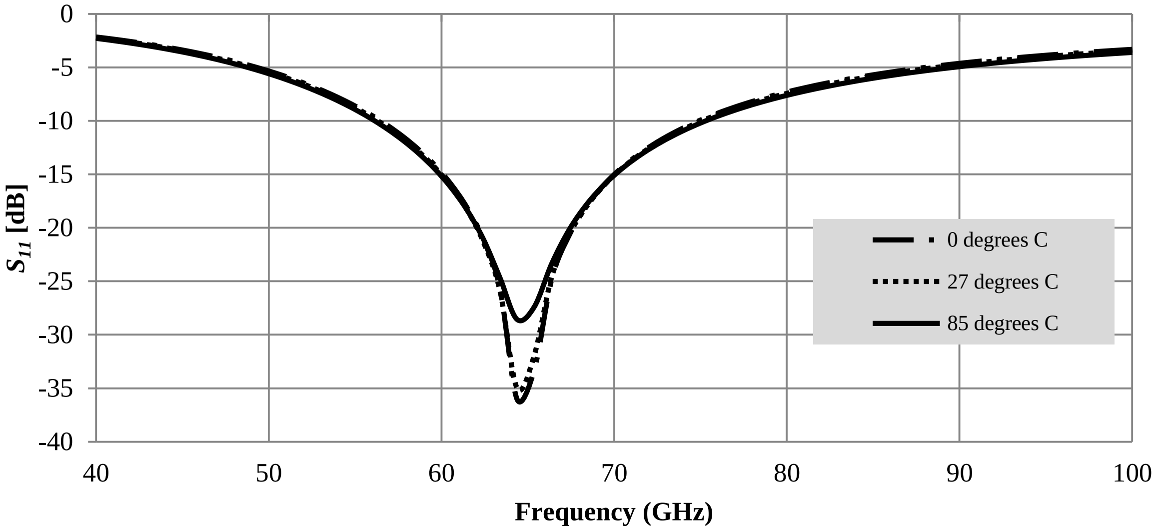

Figure C.2. Insertion loss (S_{11}) of the initial dipole as a function of temperature.

From Figure C.2 it can be seen that there is no change in resonant frequency with decreased and increased temperature of the (passive) dipole circuit. Since the ratio of capacitive and inductive components display a change as seen in Figure C.1 (with changes in peak impedance values), there is a change of insertion loss at varied temperature. At room temperature (27 °C), the insertion loss is -35 dB, and this value decreases to -36 dB at 0 °C (therefore improved insertion loss), and increases (reduced insertion loss) to -28 dB at a high temperature (85 °C). The resonant peak is constant at 64.3 GHz. Similar results are obtained for the improved dipole equivalent circuit, with the imaginary impedance simulation for the change in temperature given in Figure C.3.

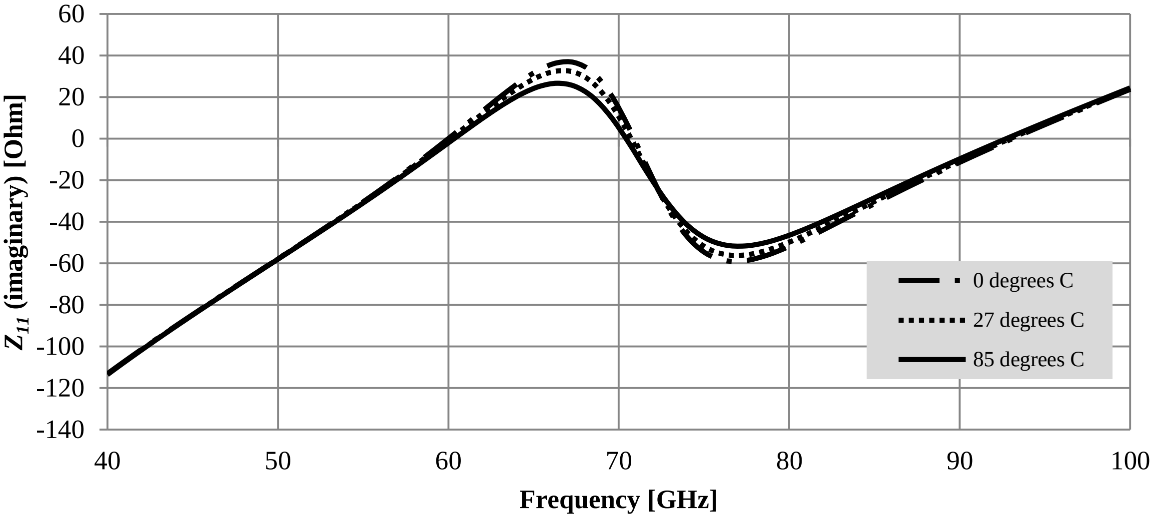

Figure C.3. Input impedance (Z_{11}) of the initial dipole circuit as a function of temperature.

From Figure C.3 it can be seen that, similar to Figure C.1, there is change in input imaginary impedance at the local maximum (66 GHz) and minimum (76 GHz) frequencies. The change in impedance is larger (|j10| Ω from 0 to 85 °C) compared to the initial dipole (< 3 Ω) circuit, as a result of the increased amount of passive components used in the circuit. This result again suggests that there is no shift in resonant frequency, however, due to the decreased ratio of inductive and capacitive components at higher temperature; this suggests a degraded insertion loss. The results for the insertion loss for the improved dipole at varied temperatures are given in Figure C.4.

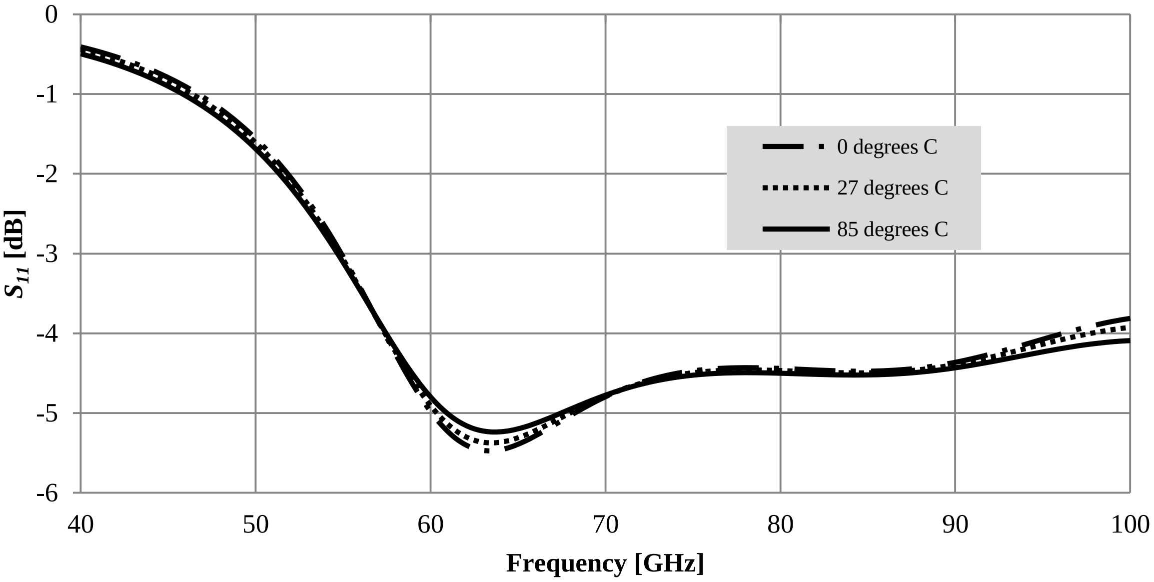

Figure C.4. Insertion loss (S_{11}) of the improved dipole as a function of temperature.

From Figure C.4 it is verified that although there is a change in insertion loss at the resonant frequency (1.5 dB increase from 0 to 85 °C at 63.3 GHz) and no shift in this resonant frequency.

The passive components (transmission lines and capacitors) used in the designs of the initial dipole and improved dipole equivalent circuits display a small change in impedance as a function of temperature, but this effect does not impact the operation of the respective equivalent circuits.